Ocular imaging technology and application

Edited by
Xinyu Liu, Bingyao Tan, Leopold Schmetterer
and Xiaojun Yu

About Frontiers

Frontiers is more than just an open access publisher of scholarly articles: it is a pioneering approach to the world of academia, radically improving the way scholarly research is managed. The grand vision of Frontiers is a world where all people have an equal opportunity to seek, share and generate knowledge. Frontiers provides immediate and permanent online open access to all its publications, but this alone is not enough to realize our grand goals.

Frontiers journal series

The Frontiers journal series is a multi-tier and interdisciplinary set of open-access, online journals, promising a paradigm shift from the current review, selection and dissemination processes in academic publishing. All Frontiers journals are driven by researchers for researchers; therefore, they constitute a service to the scholarly community. At the same time, the *Frontiers journal series* operates on a revolutionary invention, the tiered publishing system, initially addressing specific communities of scholars, and gradually climbing up to broader public understanding, thus serving the interests of the lay society, too.

Dedication to quality

Each Frontiers article is a landmark of the highest quality, thanks to genuinely collaborative interactions between authors and review editors, who include some of the world's best academicians. Research must be certified by peers before entering a stream of knowledge that may eventually reach the public - and shape society; therefore, Frontiers only applies the most rigorous and unbiased reviews. Frontiers revolutionizes research publishing by freely delivering the most outstanding research, evaluated with no bias from both the academic and social point of view. By applying the most advanced information technologies, Frontiers is catapulting scholarly publishing into a new generation.

What are Frontiers Research Topics?

Frontiers Research Topics are very popular trademarks of the *Frontiers journals series*: they are collections of at least ten articles, all centered on a particular subject. With their unique mix of varied contributions from Original Research to Review Articles, Frontiers Research Topics unify the most influential researchers, the latest key findings and historical advances in a hot research area.

Find out more on how to host your own Frontiers Research Topic or contribute to one as an author by contacting the Frontiers editorial office: frontiersin.org/about/contact

Ocular imaging technology and application

Topic editors

Xinyu Liu — Singapore Eye Research Institute (SERI), Singapore
Bingyao Tan — Nanyang Technological University, Singapore
Leopold Schmetterer — Medical University of Vienna, Austria
Xiaojun Yu — Northwestern Polytechnical University, China

Table of contents

Check for updates

Editorial: Ocular imaging technology and application

Xinyu Liu[1,2]*

[1]Institute of Medical Technology, Peking University, Beijing, China, [2]Ocular Imaging Group, Singapore Eye Research Institute, Singapore, Singapore

Editorial on the Research Topic
Ocular imaging technology and application

Ocular imaging plays an essential role in contemporary clinical diagnosis and vision care. Advancements in technology have enabled more clinical studies to investigate detailed structural and functional changes in the eye. The widespread clinical adoption of these imaging techniques not only accelerates the discovery of relevant biomarkers but also reciprocally drives further improvements in imaging instrumentation. This positive feedback loop, which is precisely what this Research Topic aims to promote, will ultimately lead to enhanced vision healthcare and tangible benefits for patients.

This Research Topic on "*Ocular Imaging Technology and Application,*" comprising submissions from Frontiers in Photonics and Frontiers in Medicine, was expertly organized by Associate Editors Dr. Xinyu Liu (Peking University, China), Dr. Binyao Tan (Singapore Eye Research Institute, Singapore), and Dr. Xiaojun Yu (Northwestern Polytechnical University, China), under the supervision of Dr. Leopold Schmetterer (Medical University of Vienna, Austria). This Research Topic has been highly successful, publishing 14 articles—including original research (10), mini-reviews (2), and case reports (2)—selected from a total of 31 submissions.

Key highlights include studies by Wang et al., who utilized non-invasive imaging technologies for faster and less invasive diagnosis of polypoidal choroidal vasculopathy. Yang et al. observed subclinical retinal perfusion loss and choroidal thickening in acute myeloid leukemia, which partially resolved upon remission. Pieklarz et al. reported that reduced peripapillary choroidal vascularity may increase the risk of glaucomatous optic neuropathy. Cai et al. demonstrated the effectiveness of *in vivo* confocal microscopy in characterizing conjunctival nevi. Farias et al. evaluated machine learning algorithms for sex classification from retinal thickness data, highlighting total retinal thickness and RNFL as significant markers. Yao et al. found that uncomplicated phacoemulsification increased retinal and choroidal thickness in early diabetic retinopathy patients. Kaushik et al. reviewed advances in two-photon excitation fluorescence imaging, emphasizing adaptive optics and laser safety improvements. Liao et al. showed partial recovery of retinal vein diameter post-ranibizumab injections in retinal vein occlusion patients. Zhang et al. described recovery in peripapillary RNFL thickness following scleral buckling in rhegmatogenous retinal detachment. Liu et al. associated optic disc

swelling in Vogt–Koyanagi–Harada disease with delayed treatment but fewer retinal exudations. Shi et al. highlighted the superiority of ultra-widefield SS-OCT in imaging vitreous cysts. Finally, Recchioni et al. confirmed SS-OCT's reliability in anterior segment measurements across diverse ocular surface disorders.

Overall, this Research Topic featured the application of novel ocular imaging technologies, including OCT, OCTA, confocal microscopy, and two-photon imaging across various eye conditions. The emerging applications of artificial intelligence (AI) in ocular imaging analysis are particularly noteworthy, highlighting the field's progression toward more precise, efficient, and personalized vision care.

Author contributions

XL: Writing–review and editing, Writing–original draft.

Funding

Conflict of interest

The author declares that the research was conducted in the absence of any commercial or financial relationships that could be construed as a potential conflict of interest.

The author(s) declared that they were an editorial board member of Frontiers, at the time of submission. This had no impact on the peer review process and the final decision.

Generative AI statement

The author declares that Gen AI was used in the creation of this manuscript. Generative AI is used to improve the language and to help writing summaries of articles.

Publisher's note

Check for updates

*CORRESPONDENCE
Xi Shen
✉ carl_shen2005@126.com
Ting Shen
✉ st12660@rjh.com.cn

†These authors share first authorship

Changes in retinal circulation and choroidal thickness in patients with acute myeloid leukemia detected by optical coherence tomography angiography

Ling Yang[1†], Yanwei Chen[2†], Yunxiang Zhang[3], Ting Shen[2]* and Xi Shen[1,2]*

[1]Department of Ophthalmology, RuiJin Hospital Lu Wan Branch, Shanghai Jiaotong University School of Medicine, Shanghai, China, [2]Department of Ophthalmology, RuiJin Hospital, Shanghai Jiaotong University School of Medicine, Shanghai, China, [3]Department of Hematology, RuiJin Hospital, Shanghai Jiaotong University School of Medicine, Shanghai, China

Purpose: To investigate changes in retinal circulation and the choroid in patients with acute myeloid leukemia (AML) in the acute and remission stages, to analyze the correlation between retinal circulation and laboratory parameters, and to assess risk factors associated with leukemic retinopathy.

Methods: Forty-eight patients (93 eyes) with AML were enrolled and divided into two groups according to fundus examination findings: the retinopathy and no retinopathy groups. Patients underwent eye measurements before treatment and after remission. Macular vessel density (VD), perfusion density (PD), foveal avascular zone (FAZ), and choroidal thickness (ChT) were measured using optical coherence tomography angiography. Patients with healthy eyes were recruited as control participants.

Results: Patients with leukemic retinopathy had higher measurements of white blood cells (WBCs), circulating blasts, fibrin degradation products, and cross-linked fibrin degradation products (D-dimer) and a lower hemoglobin (HB) count ($p < 0.05$). In the acute phase of the disease, the VD and PD were lower and the ChT was thicker in patients with AML than in controls ($p < 0.05$), irrespective of the presence of leukemic retinopathy; however, the patients were partially recovered in the remission stage. The VD was lower in patients with higher WBC ($r = -0.217$, $p = 0.036$), D-dimer ($r = -0.279$, $p = 0.001$), fasting blood glucose (FBG) ($r = -0.298$, $p = 0.004$) and triglyceride ($r = -0.336$, $p = 0.001$) levels. The FAZ area was negatively correlated with HB ($r = -0.258$, $p = 0.012$).

Conclusion: Patients with AML appear to have subclinical retinal perfusion loss and choroidal thickening in the acute phase of the disease, but this is reversible. Injury to bone marrow function may cause a decrease in retinal perfusion. Leukemic retinopathy is associated with abnormal hematologic parameters and coagulopathy.

KEYWORDS

acute myeloid leukemia, leukemic retinopathy, retinal circulation, choroidal thickness, optical coherence tomography angiography

Introduction

Leukemia is a malignant tumor of the bone marrow that causes an abnormal production of white blood cells (WBCs), affecting multiple organs (1). Ocular complications are common in patients with leukemia, especially acute myeloid leukemia (AML) (2). The retina is the most frequently affected site. Direct infiltration of tumor cells or hematologic abnormalities (thrombocytopaenia, anemia, and high viscosity) can lead to leukemic retinopathy (3–5). Retinal hemorrhage is the most common sign (2, 6, 7), and retinal vein dilation, cotton lint spots, vitreous hemorrhage, and papilledema can also manifest. Previous *ex vivo* studies have demonstrated retinal microvascular involvement (8). The choroid is also constantly affected by leukemic cell infiltration and can present as a serous retinal detachment (9). Ocular involvement may be the initial manifestation or first sign of systemic disease recurrence (10). To obtain more subclinical evidence of ocular involvement and early detection of disease progression, we used the quantitative analysis function of optical coherence tomography (OCTA) to investigate the changes in retinal circulation and the choroid in patients with AML in the acute and remission stages, correlated retinal circulation with laboratory parameters, and assessed some risk factors associated with leukemic retinopathy.

Method

Study design and participants

This was a prospective study. All patients with AML were recruited from the Department of Hematology at Ruijin Hospital, Shanghai Jiao Tong University School of Medicine from January 2021 to October 2021. Written informed consent was obtained from each participant. The design and procedure of this research adhered to the principles of the Declaration of Helsinki. The Institutional Review Board of Ruijin Hospital Luwan Branch authorized this study.

All patients with AML were aged >18 years, newly diagnosed, and to undergo systemic chemotherapy with idarubicin combined with cytarabine (IA regimen). The exclusion criteria were as follows: (1) opacity of the refractive stroma or macular lesions affecting fundus imaging; (2) fundus vascular diseases such as glaucoma, uveitis, high myopia, diabetic retinopathy, and age-related macular degeneration; (3) history of ocular surgical procedures; and (4) other severe systemic diseases. Age-matched healthy volunteers seeking physical examinations were enrolled as the control group during the same time period. According to fundus examination findings, patients with AML were divided into two groups: the retinopathy and no retinopathy groups. All patients were followed up until they completed chemotherapy. After hematologists' evaluation, patients who achieved complete remission (CR) were selected for further research.

Measurement of clinical examination

All participants underwent a complete ophthalmic examination, including best-corrected visual acuity, computer optometry, intraocular pressure (IOP) measurement with Goldmann applanation tonometry, axial length (AL), slit lamp examination, fundus examination in artificial mydriasis, fundus photography, and OCTA

scans of the macular area. Fundus photography and OCTA scans were repeated after CR.

Age, sex, and medical and ocular history were recorded. Laboratory parameters from peripheral blood samples, including WBCs (×109/L), circulating blasts (blast) (%), hemoglobin (HB) (g/dL), platelets (PLTs) (g/L), fibrinogen (Fg) (g/L), fibrin degradation products (FDP) (mg/L), cross-linked fibrin degradation products (D-dimer) (mg/L), fasting plasma glucose (FPG) (mmol/L), triglyceride (TG) (mmol/L), and total cholesterol (TC) (mmol/L) levels were recorded.

Macular OCTA scans were captured using Cirrus HD Oct 5,000 software version 9.5.2. (Carl Zeiss Meditec) and analyzed using software version 10.0. The superficial macular vessel density (VD) was obtained by angiography (6×6 mm), and choroidal thickness (ChT) was obtained using the HD Cross mode. To reduce the influence of motion artifacts, a tracking technique was used. Parameters, including the foveal avascular zone (FAZ), VD, and perfusion density (PD), were calculated to assess the superficial retinal vessels (from the inner limiting membrane layer to the inner plexiform layer) using the manufacturer's vascular measurement software. VD is the linear length of the vessel divided by the selected area, and PD is the area of vessel distribution divided by the selected area. ChT is the distance from the high reflection line of the Bruch membrane to the line of the inner surface of the sclera. ChT was measured manually in both the horizontal and vertical directions including points of the fovea, 1.0 mm from the fovea in the superior,

FIGURE 1
(A) A demonstration diagram of the partition in macular area.
(B) Example images of macular vessel density measurement based on optical coherence tomography angiography (OCTA).
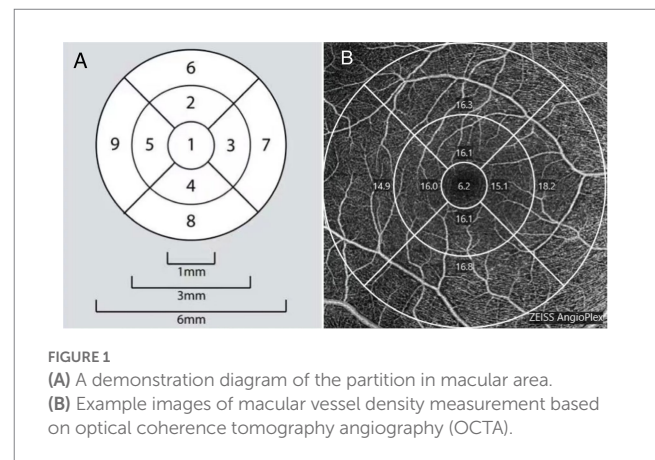
inferior, nasal, and temporal directions. Each point was measured three times and averaged. One skilled doctor who was masked to the patient's systemic and ocular data performed the measurements.

The VD map of the macula was a 6-mm-diameter circular area divided into nine sections with three concentric rings according to the Early Treatment Diabetic Retinopathy Study map. The inner ring was 1.0 mm in diameter, middle ring was 3 mm, and outer ring was 6 mm. VD and PD were automatically calculated. The central subfield was defined as a disk-shaped region of 1-mm diameter centered on the fovea (region 1). The value of the inner subfield was the average of each inner quadrant of an annulus centered on the fovea with an inner diameter of 1 mm and an outer diameter of 3 mm (regions 2, 3, 4, and 5). The value of the outer subfield was the average of each outer quadrant of an annulus centered on the fovea with an inner diameter of 3 mm and an outer diameter of 6 mm diameter (regions 6, 7, 8, and 9; Figure 1). One skilled doctor obtained all OCT scans. Images with signal intensities higher than six were selected for the analysis.

Statistical analysis

Statistical analysis was performed using SPSS 20.0 (IBM Corporation, Chicago, IL, USA). All data were tested for normality using the Kolmogorov–Smirnov test. Normally distributed data are presented as means ± standard deviations (SD), and partial non-normally distributed data are presented as medians with interquartile ranges. One-way analysis of variance was used to compare data with a normal distribution and equal variance among the three groups. The least SD test was subsequently performed for group comparisons. Otherwise, a Kruskal–Wallis test was adopted, and a Mann–Whitney U test was used for group comparisons. The paired t-test or Wilcoxon signed-rank test was used to assess the differences in data before and after chemotherapy. Spearman's correlation coefficients were calculated to evaluate the relationships between different clinical parameters. A chi-square test was used to assess the female to male ratio differences among the three groups. Results were considered statistically significant at $p < 0.05$.

Result

A total of 71 participants were enrolled, including 23 healthy individuals (46 eyes) and 48 patients with AML (93 eyes). Forty eyes belonging to 21 patients with AML were diagnosed with leukemic retinopathy. Fundus examination showed varying degrees of fundus bleeding and tortuous venous dilatation in all these eyes, some accompanied by cotton wool spots, hard exudation, and optic disc edema. None of the macular regions were involved. Only one patient complained of vision loss, and only six had symptoms of shadows or flying mosquitoes. The other 27 patients (53 eyes) had no leukemic retinopathy. The best-corrected visual acuity was 1.0 in 86 eyes (92.5%), 0.9 in two eyes (0.02%), and 0.8 in five eyes (0.05%).

The basic characteristics of all participants are shown in Table 1. There were no statistically significant differences in age, sex distribution, IOP, and AL among the three groups ($p = 0.714$, $p = 0.994$, $p = 0.306$, and $p = 0.155$, respectively).

Compared with patients without leukemic retinopathy, patients with leukemic retinopathy had a higher count of WBCs ($p = 0.03$) and circulating blasts ($p = 0.023$), and a lower count of HB ($p < 0.001$). Moreover, the FDP and D-dimer levels in the retinopathy group were also higher ($p = 0.038$ and $p = 0.046$, respectively). No significant differences were observed in bleeding symptoms, and PLT, FPG, TG and TC levels (Table 2).

The assessment of superficial retinal vessels measured using OCTA is summarized in Table 3. Patients with AML had lower VD and PD measurements than did healthy individuals (all $p < 0.05$), irrespective of the presence of leukemic retinopathy, but no significant difference in the central subfield was observed. ChT was thicker in patients with AML ($p < 0.05$), regardless of the presence or absence of leukemic retinopathy, except in the superior. The FAZ areas among the three groups were not significantly different.

After chemotherapy, the patients underwent OCTA and fundus photography again before discharge. The mean follow-up period was 46 days. Two patients died, and 15 were lost to follow-up during this period. Eight patients did not achieve CR before being discharged according to the hematologists' assessment. Finally, 23 patients (44 eyes) were enrolled for longitudinal comparison. Among them, 18 eyes were from the retinopathy group, and the rest were from the no retinopathy group. After remission, fundus

TABLE 1 Characteristics of the study population.

	Retinopathy	No retinopathy	Normal	P-value
Age (years)	43.2 ± 13.6	45.0 ± 13.2	46.2 ± 10.0	0.714
Sex (F/M)	9/12	12/15	10/13	0.994
IOP (mmHg)	16.2 ± 2.2	16.6 ± 2.0	16.7 ± 1.9	0.306
AL (mm)	23.50 ± 1.22	23.72 ± 0.94	23.19 ± 1.02	0.155

TABLE 2 Comparison of basic information and hematologic parameters between the retinopathy and no retinopathy group.

	Retinopathy	No retinopathy	P-value
Other bleeding Symptoms(with/without)	10/11	8/19	0.164
WBC	13.67(4.3,24.8)	3.9(2,10.5)	0.03*
HB	74 ± 23	100 ± 23	<0.001*
PLT	48(23,80)	75(27,147)	0.122
Blast(%)	46 ± 27	29 ± 23	0.023*
Fg	3.1 ± 0.9	3.2 ± 1.0	0.895
FDP	6.1(2.8,10.1)	3.0(2.5,5.9)	0.038*
D-dimer	1.7(0.51,3.13)	0.6(0.36,1.53)	0.046*
FBG	5.19 ± 0.62	5.38 ± 1.34	0.567
TG	1.45 ± 0.62	1.46 ± 0.66	0.951
TC	3.51 ± 0.90	3.86 ± 1.13	0.255

TABLE 3 Optical coherence tomography angiography (OCTA) analysis results in different study groups.

	Retinopathy	No retinopathy	Normal	P-value	P1	P2	P3
Vascular density (mm^{-1})							
Central	6.5 ± 2.9	5.6 ± 2.5	6.9 ± 4.6	0.425			
Inner	14.8 ± 2.5	15.3 ± 2.9	16.9 ± 1.9	<0.001*	0.173	<0.001*	0.003*
Outer	16 ± 2.1	16.4 ± 2.1	17.6 ± 1.6	<0.001*	0.159	<0.001*	0.001*
Perfusion density							
Central	0.160 ± 0.101	0.144 ± 0.087	0.166 ± 0.107	0.575			
Inner	0.340 ± 0.071	0.362 ± 0.077	0.390 ± 0.068	0.001*	0.073	<0.001*	0.034*
Outer	0.396 ± 0.062	0.399 ± 0.055	0.441 ± 0.039	<0.001*	0.759	<0.001*	<0.001*
FAZ area (mm^2)	0.24 ± 0.11	0.25 ± 0.13	0.26 ± 0.13	0.687			
Choroidal thickness (um)							
Subfoveal	266 ± 49	257 ± 45	238 ± 36	0.012*	0.341	0.004*	0.038*
Superior	249 ± 48	240 ± 48	224 ± 26	<0.024*	0.330	0.008*	0.066
Temporal	250 ± 45	242 ± 42	223 ± 27	<0.005*	0.369	0.002*	0.016*
Inferior	245 ± 49	244 ± 46	226 ± 26	<0.062	0.914	0.042*	0.041*
Nasal	237 ± 47	232 ± 43	212 ± 23	<0.01*	0.592	0.016*	0.02*

P1: P-value for the comparison group between retinopathy group and no retinopathy group.
P2: P-value for the comparison group between retinopathy group and normal controls.
P3: P-value for the comparison group between no retinopathy group and normal controls.
*Statistically meaningful.

hemorrhage decreased in two eyes, increased in one eye, and showed no significant change in 41 eyes. VD in the inner and outer subfields increased ($p = 0.043$ and $p = 0.036$, respectively), but no substantial change in the central subfield was observed. PD increased only in the outer subfield ($p = 0.04$), and the ChT decreased at most of the measurement points, except for the nasal and inferior subfields ($p = 0.001$, $p = 0.016$, $p = 0.023$; Figure 2). Figure 3 shows a clinical example of the macular perfusion and choroid changes in a patient imaged with OCTA in the active phase of AML and after remission. This patient was a 20-year-old boy. The first inspection time was July 21 and the review time was August 19. The visual acuity of his left eye was 1.2 in both exams. No leukemic retinopathy was observed before and after treatment. A1, A2, B1 and B2 show that macular perfusion normalized with remission of AML. C1 and C2 show that the thickening of choroid was reversed after remission of AML.

To determine the potential influencing factors associated with the above parameters, Spearman's correlation coefficient was calculated using the clinical variables from all 93 eyes. VD in the macular region was lower in patients with higher WBC ($r = -0.217$, $p = 0.036$), D-dimer ($r = -0.279$, $p = 0.001$), FBG ($r = -0.298$, $p = 0.004$), and TG ($r = -0.336$, $p = 0.001$) levels. FAZ area was negatively correlated with HB ($r = -0.258$, $p = 0.012$; Figure 4).

Discussion

Most ocular manifestations in patients with leukemia are not due to direct infiltration of the disease but rather changes in hematologic parameters that may lead to hemorrhage [11]. Our study showed that among patients with AML, those who developed leukemic retinopathy had lower HB counts, higher WBC counts, and higher percentages of circulating blasts. Nevertheless, PLT counts did not appear to be related. In previous research, some results were consistent with ours, but some differed [12]. El-asrar et al. found that patients with AML with Roth plaques had significantly higher WBC counts than did those without hemorrhage and that thrombocytopaenia was not associated with retinal hemorrhage [13]. Some researchers have suggested that low HB in patients with AML is associated with intraretinal hemorrhage [3, 14]. According to Guyer et al. patients with acute leukemia and retinopathy have higher levels of anemia and percentages of circulating blasts and lower PLT counts than do those without retinopathy [15]. Contrary to our findings, Wechsler et al. and Zhuang et al. found a statistically significant association between retinal hemorrhage and thrombocytopaenia [16, 17]. A recent study of acute leukemia showed that patients with clinically visible leukemic retinopathy had higher WBC counts and fewer PLTs than did those without retinal signs [18]. The sample size and classification of leukemia may be a result of differences in findings. A high proportion of patients in our study had abnormally high FDP and D-dimer levels. The onset of leukemia was associated with hemostatic derangement, favoring hypercoagulability. Coagulopathy was due to thrombin activation. This is evidenced by the increased D-dimer level [19]. A higher D-dimer level may be a risk factor for leukemic retinopathy. Further research is required to obtain more conclusive data.

Optical coherence tomography can identify the blood flow information of the retina and choroid with high resolution, image retinal and choroidal microvascular circulation in living tissue [20, 21], require no contrast agent, and avoid allergies and various contraindications. OCTA may have unique advantages in the
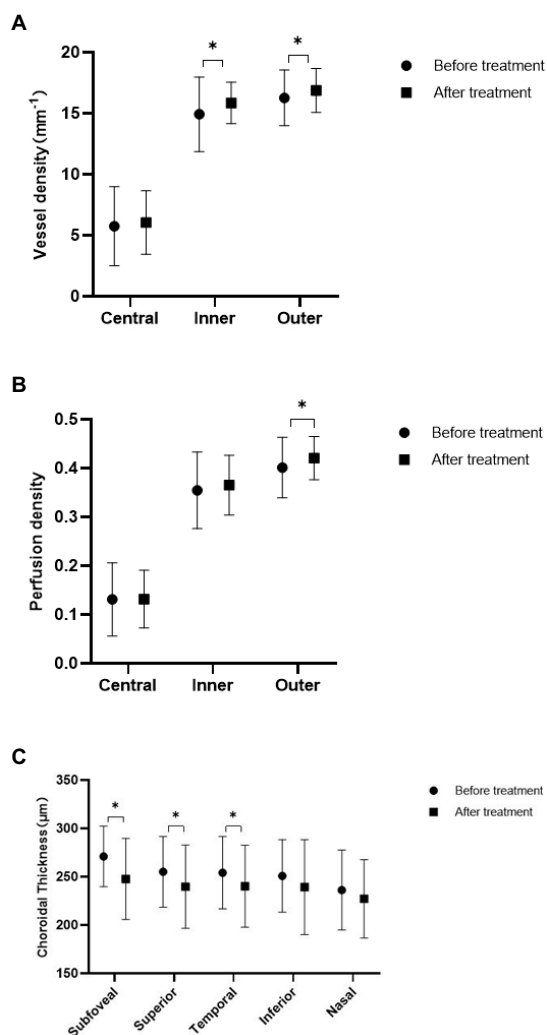
FIGURE 2
Comparison of acute myeloid leukemia (AML) patients before and after treatment. **(A)** Three zones of macular vessel density before and after treatment. **(B)** Three zones of macular perfusion density before and after treatment. **(C)** Choroidal thickness at five measurement points before and after treatment.

management and follow-up of patients with leukemia with its non-invasive and quantitative analysis function.

This study evaluated changes in superficial retinal perfusion in patients with AML. We found that retinal perfusion in the macular region was significantly reduced in the acute phase of the disease, except for the central subfield, in patients with AML than in individuals with healthy eyes, which is consistent with the findings of Cicinelli et al. (18); they also found lower VD in the SCP adjacent to the fovea in patients with acute leukemia, with no significant change in the fovea. This change was less pronounced in the central subfield, possibly because there are fewer vessels. Acute leukemic anemia, thrombocytopaenia, and a high-viscosity state due to an increased WBC count result in an abnormal expansion of retinal capillaries and loss of physiological branching patterns. The velocity of blood in the vasculature has an inverse relationship with the vessel cross-sectional area (volumetric flow rate = flow velocity × cross-sectional area). We hypothesized that a decrease in blood flow velocity below the

minimum OCTA detection threshold might cause loss of blood flow signals (22).

Comparing fundus photographs before and after treatment, we found that most patients had no significant changes, but their retinal perfusion had begun to improve. Previous studies have also suggested that retinal changes secondary to leukemic retinopathy are mostly transient and will subside without permanent damage. Abnormal retinal venous blood flow velocity was observed in patients with chronic myeloproliferative neoplasms which returned to normal levels after cytoreductive therapy (23). After leukemia remission, the perfusion of the capillaries in the macula and peripapillary areas improved (18), suggesting that the damage might be reversible. These studies revealed subclinical changes in the eyes of patients with acute leukemia, which can reflect the progression of systemic disease and may be helpful for the evaluation of patient efficacy and follow-up.

In addition, VD decreased significantly in patients with higher WBC counts, and the FAZ area was larger in patients with lower HB. This indicates that patients with more severe bone marrow damage have a greater reduction in retinal perfusion. VD decreased as D-dimer levels increased. Elevated D-dimer levels are common in acute leukemia, and their relationship with retinal circulation requires further clarification (24, 25). Elevated blood glucose and TG levels can also lead to a decrease in VD. VD is known to decrease in patients with diabetes (26). A drop in blood flow caused by hyperlipidemia has also been confirmed. This suggests that maintaining normal blood glucose and lipid levels also benefits patients with AML.

Histologic examination revealed choroidal leukemic infiltrates in the eyes of up to 65% of patients with leukemia and 31% of patients with fatal leukemia (27). This makes it the most common site of ocular involvement in leukemia (28). Previous studies have shown that the choroid in patients with acute leukemia thickened owing to leukocyte infiltration and became thinner after chemotherapy (29, 30). None of the patients with AML in our study had significant clinical signs in the macular region, but an increase in ChT was observed. In the acute phase of leukemia, choroidal invasion results in reduced capillary blood flow and increased ChT (31, 32). The causes of choroidal thickening can be explained as follows: leukemic cells adhere to the inner wall of choroidal vessels; extravasated leukemic cells compress the vessels, resulting in a reduction in choroidal blood flow velocity; and an increased inflow of fluids into the choroidal interstitial tissue due to blood flow congestion and choroidal infiltration of leukemia cells occurs, causing choroidal thickening. During the active phase of the disease, leukemic cells may lie dormant in the choroid and then subside as the treatment progresses. In patients with Vogt-Koyanagi-Harada syndrome, the choroid thickens almost a month before an anterior uveal recurrence in the context of recurrence, even before the appearance of any fundus signs of posterior involvement (33). A longer follow-up is needed to determine whether choroidal changes in patients with acute leukemia have similar clinical values.

In conclusion, patients with AML appeared to have subclinical retinal perfusion loss and choroidal thickening in the acute phase of the disease, and they partially recovered with remission. Injury to the bone marrow function may cause a decrease in retinal perfusion. Leukemic retinopathy is associated with abnormal hematologic parameters and coagulopathy. Because of the short follow-up period in this study, these changes could not be traced when the patients relapsed. The utility of OCTA in revealing subclinical ocular involvement and monitoring treatment response and the risk of
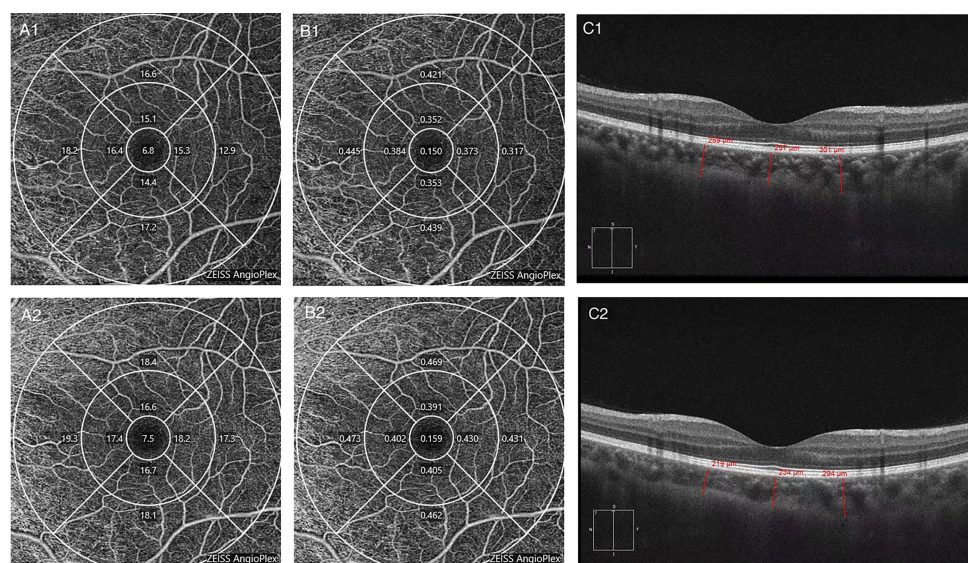
FIGURE 3
The changes in a patient imaged with optical coherence tomography angiography (OCTA) in the active phase of acute myeloid leukemia (AML) and after remission. **(A1)** Macular vessel density before treatment. **(A2)** Macular vessel density after treatment. **(B1)** Macular perfusion density before treatment. **(B2)** Macular perfusion density after treatment. **(C1)** Choroidal thickness before treatment. **(C2)** Choroidal thickness after treatment.
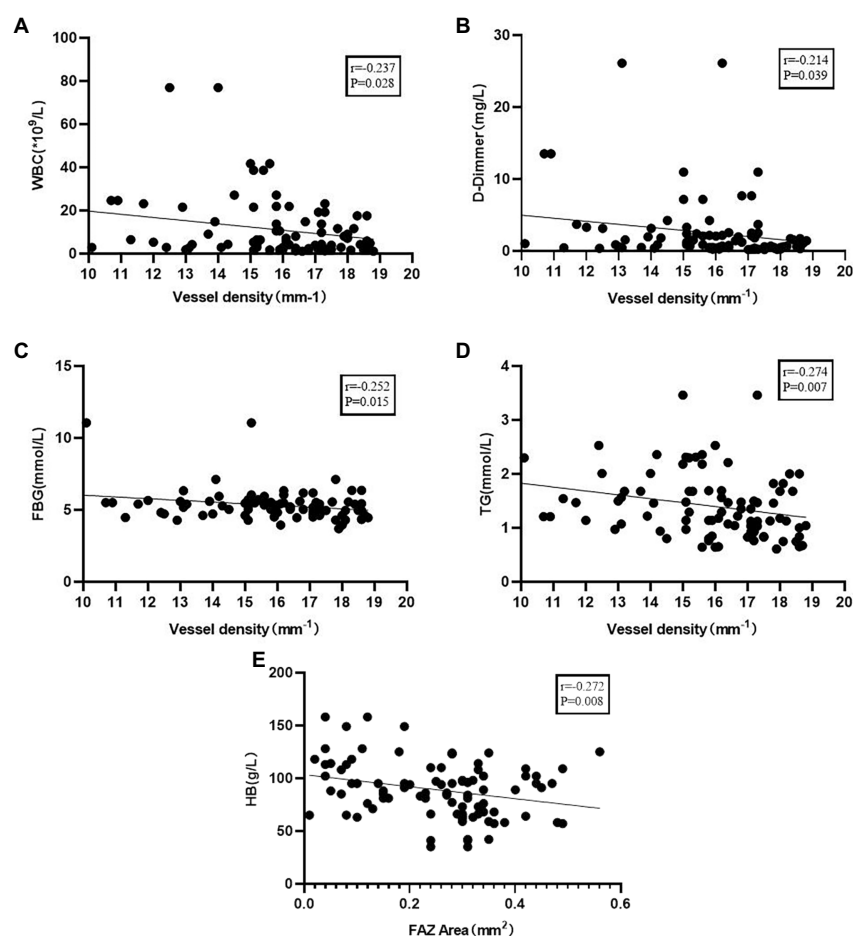
FIGURE 4
(A) Correlation of vessel density with white blood cells (WBC). **(B)** Correlation of vessel density with D-dimmer. **(C)** Correlation of vessel density with fasting plasma glucose (FBG). **(D)** Correlation of vessel density with triglyceride (TG). **(E)** Correlation of foveal avascular zone (FAZ) area with HB.

relapse in patients with acute leukemia requires further evidence. Owing to the limitations of the OCTA software version, only superficial VD was analyzed, which was a disadvantage of this study.

Data availability statement

The raw data supporting the conclusions of this article will be made available by the authors, without undue reservation.

Ethics statement

The studies involving human participants were reviewed and approved by the Ethics Committee of the Ruijin Hospital Luwan Branch. The patients/participants provided their written informed consent to participate in this study. Written informed consent was obtained from the individual(s) for the publication of any potentially identifiable images or data included in this article.

Author contributions

LY designed the study, analyzed the data, and wrote the manuscript. YC, TS, and YZ recruited the patients and collected the data. XS conceived the study and performed a critical revision of the manuscript for intellectual content. All authors contributed to the article and approved the submitted version.

Conflict of interest

The authors declare that the research was conducted in the absence of any commercial or financial relationships that could be construed as a potential conflict of interest.

Publisher's note

All claims expressed in this article are solely those of the authors and do not necessarily represent those of their affiliated organizations, or those of the publisher, the editors and the reviewers. Any product that may be evaluated in this article, or claim that may be made by its manufacturer, is not guaranteed or endorsed by the publisher.

References

1. Arber DA, Orazi A, Hasserjian R, Thiele J, Borowitz MJ, Le Beau MM, et al. The 2016 revision to the World Health Organization classification of myeloid neoplasms and acute leukemia. *Blood*. (2016) 127:2391–405. doi: 10.1182/blood-2016-03-643544

2. Hafeez MU, Ali MH, Najib N, Ayub MH, Shafi K, Munir M, et al. Ophthalmic manifestations of acute leukemia. *Cureus*. (2019) 11:e3837. doi: 10.7759/cureus.3837

3. Dhasmana R, Prakash A, Gupta N, Verma SK. Ocular manifestations in leukemia and myeloproliferative disorders and their association with hematological parameters. *Ann Afr Med*. (2016) 15:97–103. doi: 10.4103/1596-3519.188887

4. Reddy SC, Jackson N, Menon BS. Ocular involvement in leukemia–a study of 288 cases. *Ophthalmologica*. (2003) 217:441–5. doi: 10.1159/000073077

5. Eze BI, Ibegbulam GO, Ocheni S. Ophthalmic manifestations of leukemia in a tertiary hospital population of adult Nigerian Africans. *Middle East Afr J Ophthalmol*. (2010) 17:325–9. doi: 10.4103/0974-9233.71599

6. Russo V, Scott IU, Querques G, Stella A, Barone A, Delle NN. Orbital and ocular manifestations of acute childhood leukemia: clinical and statistical analysis of 180 patients. *Eur J Ophthalmol*. (2008) 18:619–23. doi: 10.1177/112067210801800420

7. Ilo OT, Adenekan AO, Alabi AS, Onakoya AO, Aribaba OT, Kehinde MO, et al. Ocular manifestations of leukemia: a teaching hospital experience. *Niger Postgrad Med J*. (2019) 26:205–10. doi: 10.4103/npmj.npmj_50_19

8. Allen RA, Straatsma BR. Ocular involvement in leukemia and allied disorders. *Arch Ophthalmol*. (1961) 66:490–508. doi: 10.1001/archopht.1961.00960010492010

9. Sharma H, Majumder PD, Rao C, Biswas J. A case of acute myeloid leukemia masquerading as unilateral exudative detachment. *Am J Ophthalmol Case Rep*. (2016) 4:47–9. doi: 10.1016/j.ajoc.2016.08.004

10. Kincaid MC, Green WR. Ocular and orbital involvement in leukemia. *Surv Ophthalmol*. (1983) 27:211–32. doi: 10.1016/0039-6257(83)90123-6

11. Soman S, Kasturi N, Srinivasan R, Vinod KV. Ocular manifestations in leukemias and their correlation with hematologic parameters at a tertiary care setting in South India. *Ophthalmol Retina*. (2018) 2:17–23. doi: 10.1016/j.oret.2017.05.009

12. Bukhari ZM, Alzahrani A, Alqarni MS, Alajmi RS, Alzahrani A, Almarzouki H, et al. Ophthalmic manifestations in acute leukemia patients and their relation with hematological parameters in a tertiary care center. *Cureus*. (2021) 13:e19384. doi: 10.7759/cureus.19384

13. Abu El-Asrar AM, Al-Momen AK, Kangave D, Harakati MS, Ajarim DS. Correlation of fundus lesions and hematologic findings in leukemic retinopathy. *Eur J Ophthalmol*. (1996) 6:167–72. doi: 10.1177/112067219600600213

14. Holt JM, Gordon-Smith EC. Retinal abnormalities in diseases of the blood. *Br J Ophthalmol*. (1969) 53:145–60. doi: 10.1136/bjo.53.3.145

15. Guyer DR, Schachat AP, Vitale S, Markowitz JA, Braine H, Burke PJ, et al. Leukemic retinopathy. Relationship between fundus lesions and hematologic parameters at diagnosis. *Ophthalmology*. (1989) 96:860–4. doi: 10.1016/S0161-6420(89)32809-0

16. Wechsler DZ, Tay TS, McKay DL. Life-threatening hematological disorders presenting with opthalmic manifestations. *Clin Exp Ophthalmol*. (2004) 32:547–50. doi: 10.1111/j.1442-9071.2004.00878.x

17. Zhuang I, Gupta I, Weng CY. Retinal hemorrhages in a patient with petechiae. *JAMA Ophthalmol*. (2019) 137:459–60. doi: 10.1001/jamaophthalmol.2018.6220

18. Cicinelli MV, Mastaglio S, Menean M, Marchese A, Miserocchi E, Modorati G, et al. Retinal microvascular changes in patients with acute leukemia. *Retina*. (2022) 42:1762–71. doi: 10.1097/IAE.0000000000003504. PMID: 35446824

19. Sehgal S, Sharma S, Chandra J, Nangia A. Coagulation profile at diagnosis in patients with acute lymphoblastic leukemia. *Indian J Pediatr*. (2016) 83:1082–6. doi: 10.1007/s12098-016-2114-2

20. Kashani AH, Chen CL, Gahm JK, Zheng F, Richter GM, Rosenfeld PJ, et al. Optical coherence tomography angiography: a comprehensive review of current methods and clinical applications[J]. *Prog Retin Eye Res*. (2017) 60:66–100. doi: 10.1016/j.preteyeres.2017.07.002

21. Falavarjani KG, Sarraf D. Optical coherence tomography angiography of the retina and choroid; current applications and future directions. *J Curr Ophthalmol*. (2017) 29:1–4. doi: 10.1016/j.joco.2017.02.005

22. Cheung CM, Teo KY, Tun SB, et al. Differential reperfusion patterns in retinal vascular plexuses following increase in intraocular pressure an OCT angiography study. *Sci Rep*. (2020) 10:16505. doi: 10.1038/s41598-020-73585-0

23. Willerslev A, Hansen MM, Klefter ON, Bjerrum OW, Hasselbalch HC, Clemmensen SN, et al. Non-invasive imaging of retinal blood flow in myeloproliferative neoplasms. *Acta Ophthalmol*. (2017) 95:146–52. doi: 10.1111/aos.13249

24. Shahmarvand N, Oak JS, Cascio MJ, Alcasid M, Goodman E, Medeiros BC, et al. A study of disseminated intravascular coagulation in acute leukemia reveals markedly elevated D-dimer levels are a sensitive indicator of acute promyelocytic leukemia. *Int J Lab Hematol*. (2017) 39:375–83. doi: 10.1111/ijlh.12636

25. Wang P, Zhang Y, Yang H, Hou W, Jin B, Hou J, et al. Characteristics of fibrinolytic disorders in acute promyelocytic leukemia. *Hematology*. (2018) 23:756–64. doi: 10.1080/10245332.2018.1470069

26. Zsoter T, Wm F, Mcgregor M. The effect of LIPEMIA on peripheral blood flow. *Can Med Assoc J*. (1964) 90:1203–5. PMID: 14146862

27. Kassam F, Gale JS, Sheidow TG. Intraocular leukemia as the primary manifestation of relapsing acute myelogenous leukemia. *Can J Ophthalmol*. (2003) 38:613–6. doi: 10.1016/S0008-4182(03)80120-5

28. Thill M, Schwartz R, Fiedler W, Linke S. Bilateral retinal pigment epithelial detachment as the presenting symptom of acute myeloid leukemia. *Eye*. (2006) 20:851–2. doi: 10.1038/sj.eye.6702025

29. Bajenova NV, Vanderbeek BL, Johnson MW. Change in choroidal thickness after chemotherapy in leukemic choroidopathy. *Retina*. (2012) 32:203–5. doi: 10.1097/IAE.0b013e31822b1f68

30. Adam MK, Pitcher JD, Shields CL, Maguire JI. Enhanced depth imaging optical coherence tomography of precursor cell leukemic choroidopathy before and after chemotherapy. *Middle East Afr J Ophthalmol*. (2015) 22:249–52. doi: 10.4103/0974-9233.150630

31. Naseripour M, Abdolalizadeh P, Abdi F, Mehrvar A, Tashvighi M. Serous retinal detachment as an initial presentation of childhood acute myeloid leukemia. *Can J Ophthalmol*. (2019) 54:e170–3. doi: 10.1016/j.jcjo.2018.10.008

32. Takita A, Hashimoto Y, Saito W, Kase S, Ishida S. Changes in blood flow velocity and thickness of the choroid in a patient with leukemic retinopathy. *Am J Ophthalmol Case Rep*. (2018) 12:68–72. doi: 10.1016/j.ajoc.2018.09.001

33. Takahashi H, Takase H, Ishizuka A, Miyanaga M, Kawaguchi T, Ohno-Matsui K, et al. Choroidal thickness in convalescent Vogt-Koyanagi-Harada disease. *Retina*. (2014) 34:775–80. doi: 10.1097/IAE.0b013e3182a6b3f6

Morphological characterization of nevi on the caruncle conjunctiva under *in vivo* confocal microscopy

Jianhao Cai[1]*, Cangeng Xu[1], Tsz Kin Ng[1,2,3] and Zeyi Li[1]

[1]Joint Shantou International Eye Centre of Shantou University and The Chinese University of Hong Kong, Shantou, Guangdong, China, [2]Shantou University Medical College, Shantou, Guangdong, China, [3]Department of Ophthalmology and Visual Sciences, The Chinese University of Hong Kong, Hong Kong, Hong Kong SAR, China

Objective: This study aimed to investigate the microscopic structure and characteristics of nevi on the conjunctiva of the lacrimal caruncle by *in vivo* confocal microscopy.

Methods: In total, four patients with nevi growing on the lacrimal caruncle conjunctiva were recruited. The morphological characteristics of the nevi were evaluated by *in vivo* confocal microscopy before excision surgery; the results were compared with histopathological analyses of the surgical specimens.

Results: The nevi of the four patients were all located at the conjunctiva of the lacrimal caruncle, with a slightly nodular surface, mixed black and brown color, and clear boundary. The nevi were round and highly protruded on the surface of the lacrimal caruncle, with an average diameter of 4.5 ± 1.29 mm. Under *in vivo* confocal microscopy, the pigmented nevus cells on the conjunctiva of the lacrimal caruncle were observed to be clustered in nests with irregular boundaries. The cells were round or irregular, with clear cell boundaries, hyper-reflective at the periphery, with low reflectivity in the center. Vascular crawling was observed in some regions. Histopathological analysis showed that nevus cells were roughly equal in size and distributed in a nodular pattern. Melanin granules were observed in the cytoplasm. No atypia or mitotic figures of the cells were found.

Conclusion: This study revealed that the microstructure of nevi growing on the conjunctiva of the lacrimal caruncle can be identified by *in vivo* confocal microscopy.

KEYWORDS

pigmented nevus, lacrimal caruncle, conjunctiva, *in vivo* confocal microscopy, histopathology

1. Introduction

Conjunctival melanocytic lesions are the most common tumors of the conjunctiva, accounting for 52% of all conjunctival tumors. Among all conjunctival melanocytic lesions, conjunctival nevi are the most common, accounting for 45% (1). A conjunctival nevus is a freckle or mole-like spot on the conjunctiva. Clinical diagnosis of conjunctival nevus can be challenging under some conditions. Histopathological examination is still the gold standard for diagnosis of melanocytic lesions, but this requires surgical excision. A potential diagnostic tool to allow for earlier diagnosis, before surgical operation, could be *in vivo* confocal microscopy (IVCM), which is a real-time, non-invasive form of high-resolution

microscopy. At present, IVCM imaging is mainly used for corneal diseases, and it has also been applied in the study of neoplasms of the ocular surface (2, 3). Morphological changes in lesions at the cellular level can be observed via IVCM, but only a small number of studies have presented IVCM images of nevi in the caruncle conjunctiva (4, 5). Here, we present a series of lacrimal caruncle conjunctival nevi investigated via IVCM before surgery, with these investigations compared with the histopathology analysis.

2. Methods

2.1. Study subjects

This study was approved by the Human Medical Ethics Committee of the Joint Shantou International Eye Center of Shantou University and the Chinese University of Hong Kong (approval number: EC20171103(6)-P01). Written informed consent was obtained from all study subjects after explanation of the nature and possible consequences of the study. In total, four patients (one male subject and three female subjects) were recruited between August 2018 and November 2021; all were undergoing surgical removal of a lacrimal caruncle conjunctival pigmented nevus. The exclusion criteria were: (1) the patient did not agree to undergo Heidelberg Retinal Tomography (HRT3) examination; and (2) acute inflammation on the ocular surface.

2.2. *In vivo* confocal microscopy examination

IVCM examination was carried out using a HRT3/Rostock Cornea Module (RCM; Heidelberg Engineering, Germany) equipped with a 670-nm laser (Supplementary Figure 1). The resolution of the IVCM output image was 384 pixels × 384 pixels, with 800× magnification. Each image corresponded to a horizontal section of 400 μm × 400 μm, with a high resolution of up to 1 μm.

Before IVCM examination, topical anesthesia was applied to the inferior conjunctival fornix of the eye with 0.5% proparacaine eye drops, administered three times at 5-min intervals. Carbomer eye gel was applied to the tip of the IVCM, which was then covered with a disposable sterile transparent shade. In order to display the detected image more clearly, the outer layer of the contact sleeve was evenly coated with carbomer eye gel. After sufficient ocular surface anesthesia, the chin and forehead of the subject were fixed in the corresponding positions of the IVCM machine. The ophthalmologist (C.X.) extended the upper and lower eyelids of the examined eye with the middle finger and thumb, respectively. The IVCM lens was then advanced by the other hand of the ophthalmologist so that it touched the edge of the pigmented nevus under examination. The scanning depth was adjusted, and the scan was performed gradually, moving from shallow to deep. Horizontal scanning was performed from the temporal side of lesion to the nasal side, and IVCM images were captured at any time during the

---

Abbreviations: IVCM, *in vivo* confocal microscopy; HRT3, Heidelberg Retinal Tomography 3; RCM, Rostock Cornea Module; HE, Hematoxylin and eosin; CT: computed tomography.

scanning process. The five clearest images from each patient were selected for analysis.

2.3. Excision surgery

All operations were carried out by a single surgeon (J.C.). Before surgery, topical anesthesia was applied to the inferior conjunctival fornix of the eye with 0.5% proparacaine eye drops, administered three times at 5-min intervals. Local anesthetic was administered to the caruncle subconjunctival tissue by injection with 0.5 ml of 2% lidocaine. The conjunctival tissue was incised by 1 mm beyond the edge of the nevus. The nevus and a small amount of subconjunctival tissue were completely removed and sent for histopathological examination. The conjunctival incision of the lacrimal caruncle was released and closed intermittently with 10-0 nylon suture. Attention was paid to avoid injury of the lacrimal canaliculus during the operation.

2.4. Histopathological examination

Histopathological examination was performed for all four specimens. The tissues of the caruncle conjunctival nevus were fixed in 10% paraformaldehyde, dehydrated, and embedded in paraffin according to the conventional procedure. The tissue sections (5 μm) were sliced, spread, baked, and stained with hematoxylin and eosin. Briefly, after deparaffinization at 60°C, the sections were incubated twice in xylene, then re-hydrated by passing them through decreasing concentrations of alcohol baths and water. The sections were stained for 8 min with Harris hematoxylin staining solution, followed by incubation with 1% hydrochloric acid in ethanol for 10 s. After washing, the blue-promoting solution appeared blue after 10 s. The sections were then washed with tap water, stained with 1% eosin iron-red, dehydrated in graded alcohol solutions increasing in concentration, and cleared in xylene. The HE-stained sections were imaged and analyzed via light microscopy by a pathologist to determine the morphological changes in the caruncle conjunctival nevus.

3. Results

3.1. Clinical diagnosis

Four patients, one male subject and three female subjects, were recruited. The ages of the four enrolled patients ranged from 14 to 24 years (mean: 17.75 ± 2.08). All lesions occurred only in one eye, with two occurring in the right eye and two in the left. The nevi of the four patients were all located at the conjunctiva of the lacrimal caruncle, with a slightly nodular surface, mixed black and brown color, and clear boundary (Figure 1). The nevi were round and highly protruded on the surface of the lacrimal caruncle, with an average diameter of 4.5 ± 1.29 mm (range: 3–6 mm).
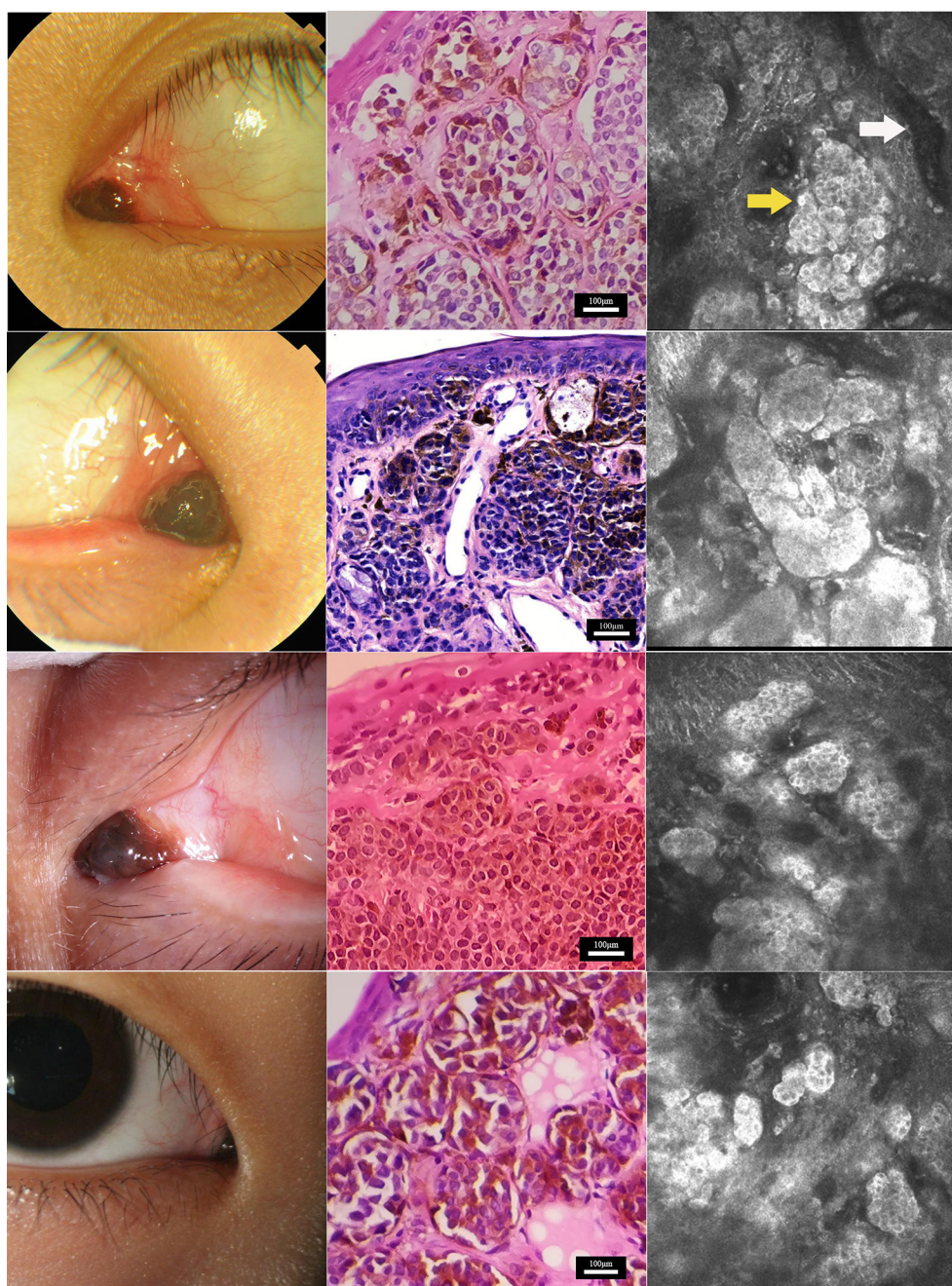
FIGURE 1
Characterization of nevus on the caruncle conjunctiva by histopathological and *in vivo* confocal microscopy analyses. Clinical **(left)**, histopathological **(center)**, and *in vivo* confocal microscopy **(right)** analyses of nevi at the caruncle conjunctiva in the four study subjects. Confocal microscopy showed that nevus cells (yellow arrow) in the conjunctiva of the lacrimal mound were clustered in nests with clear boundaries. The reflectivity of the nest was significantly increased compared with normal lacrimal mound tissue. Each single nevus cell was round or irregular, with clear cell boundaries. The periphery of the cell was hyper-reflective, and the center was hypo-reflective. Blood vessels (white arrow) were seen around the nevus cell nest in some areas. Scale bar for histopathological analysis: 100 μm. Depths of the *in vivo* confocal microscopy images captured: row 1, 14 μm; row 2, 50 μm; row 3, 23 μm; row 4, 25 μm.

3.2. Histopathological examination

The four surgical specimens from the patients were all diagnosed as pigmented nevus in the histopathology analysis. Microscopically, the pigmented nevi were completely removed, and no nevus cells were seen at the edges of the specimens.

Hematoxylin and eosin staining showed that nevus cells were located within the epidermis and dermis (Figure 1). The nevus cells were roughly equal in size and distributed in a nodular pattern. Melanin granules were observed in the cytoplasm. No atypia or mitotic figures of the cells were found in any of the four samples.
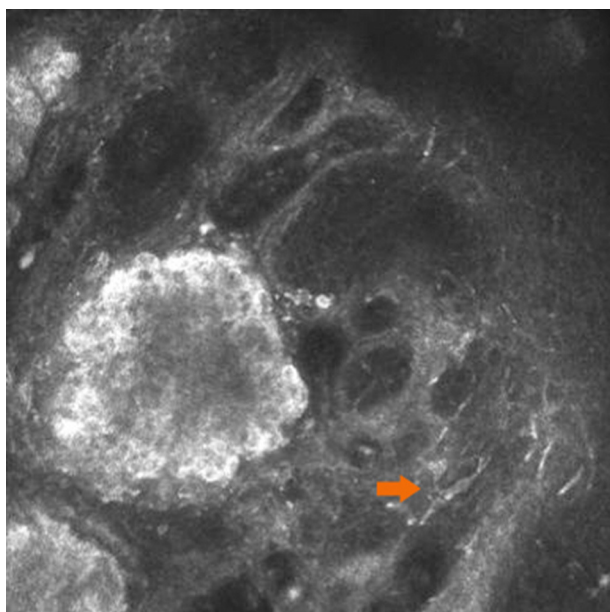
FIGURE 2
Langerhans cells around the lesions. Thick Langerhans cells (orange arrow) with irregular morphology were observed around the lesions in one of the four cases.

3.3. *In vivo* confocal microscopy examination

Under IVCM, nevus cells on the conjunctiva of the lacrimal caruncle were observed to be clustered in nests with clear and irregular boundaries, and reflectivity was significantly increased as compared to that of normal lacrimal caruncle tissue (Figure 1). Each single nevus cell was round or irregular, with clear cell boundaries, hyper-reflective at the periphery, with low reflectivity in the center. Blood capillaries were observed around the nevus cell nest in some areas. Thick Langerhans cells with irregular morphology were observed around the lesions in one of the four cases (Figure 2). The structure of the lacrimal caruncle conjunctival nevus observed under IVCM was similar in appearance to that of the histopathological section.

4. Discussion

A pigmented nevus, also known as a melanocyte nevus, is a benign hyperplastic growth composed of nevus cells. Its distribution covers the skin of the entire body, including the face and eyelid skin, as well as the conjunctiva. A Korean study has reported that 76.5% of conjunctival pigmented lesions are located on the bulbar conjunctiva, 8.2% on the caruncle, and 1.2% on the fornix. Compound nevus is the most common type (67.1%) of conjunctival melanocytic tumor and has a benign course. In contrast, conjunctival malignant melanoma is rare (7.1%) and carries serious consequences (6). Clinical diagnosis mainly depends on the history of the morphological evolution of the skin lesion, and suspicious cases require histopathological examination.

Histopathological examination is still the gold standard for melanocytic lesions; however, it is invasive and cannot produce results in real time. New imaging techniques are of strong interest in the diagnosis of conjunctival pigmented neoplasms. IVCM is a non-invasive high-resolution imaging technique that has been demonstrated to be useful for the diagnosis of skin and ocular surface diseases (7).

There are two main kinds of IVCM device used in clinical settings. One is dedicated to the skin, with a handheld probe, and the other is applied to the ocular surface using the Rostock Cornea Module. Under IVCM, cells or tissues can have a similar appearance to the non-invasive optical slices visualized under CT scan. CT has been applied in dermatology for a significant period of time, and it can effectively identify the properties of lesions (8). However, the type of confocal microscope used for the skin cannot be used for the conjunctiva, especially the lacrimal caruncle, as there is a physiological depression in the lacrimal caruncle. It is difficult to achieve sufficient proximity to the larger probe, and lacrimal caruncle lesions cannot be detected (9).

The form of IVCM used in this study is a real-time, non-invasive, and high-resolution imaging method, providing magnification by up to 800 times, which can detect fine structures at the cellular level. In 1990, Cavanagh *et al.* reported the application of IVCM to observe and record human corneal stratification *in vivo* for the first time (10). Since then, with the continuous progress of science and technology, the research scope of IVCM has gradually expanded from initial application in the diagnosis of and research on corneal diseases to applications in other ocular surface diseases (11). At present, IVCM is mainly used in the examination and diagnosis of corneal diseases, meibomian gland dysfunction, and other related issues. Compared to skin CT, the IVCM probe used for ocular surface analysis is smaller, which makes it more suitable for examination of ocular surface diseases.

In this study, we found that IVCM images of lacrimal caruncle conjunctival pigmented nevi were highly similar to images of histopathological sections, demonstrating that IVCM can accurately visualize the microstructure of a lacrimal caruncle conjunctival pigmented nevus. We summarize the features of the IVCM images from the four patients as follows: (1) the boundaries of the lesions were clear, showing a nest distribution; and (2) dense, large, bright cells arranged in a honeycomb-like pattern with clear cell boundaries were observed within the lesions. The cell sizes were roughly uniform. Our findings were consistent with previously reported IVCM images of dermal melanocytic nevi (12). However, they differed from IVCM images of conjunctival nevi, which have been found to exhibit lower reflectivity than the surrounding tissue (9). This might be due to the fact that the tissue at the lacrimal caruncle is closer to the skin tissue. Pigmented nevi at this site are also relatively more protruded and more similar to intradermal nevi of the skin. Not only does IVCM display the structure of the lesion at the cellular level, but it also produces these images in real time. During the examination, the probe angle and scanning depth can be adjusted at any time to evaluate the lesion in different dimensions in order to obtain more information.

There were several limitations to this study. First, a limited number of study subjects were included. Second, IVCM has limited penetration and is easily affected by the light transmittance of the

tissue. For superficial and transparent tissues, the imaging is clear, but for deep tissues or tissues with poor light transmittance, the imaging is fuzzy. Third, the resolution of IVCM is not comparable to that of conventional histopathological sections, although IVCM is non-invasive, real-time, and dynamic as compared to traditional histopathology, which is time-consuming and invasive. In addition, the examination process for IVCM requires the cooperation of the patient (12). Finally, IVCM is not able to distinguish activated Langerhans cells from dendritic melanocytes, since both are cells with prominent dendritic processes and they share similar refractive indices and morphological features. However, their distributions differ, in that Langerhans cells are more superficial and more common in the conjunctival tissue. The processes of Langerhans cells are also stouter than those of melanocytes.

5. Conclusion

This study revealed the ability of IVCM to display the microscopic structure of nevi of the lacrimal caruncle conjunctiva with a certain degree of recognition. Although the resolution of IVCM is not comparable to that of conventional histopathological sections, the non-invasive, *in situ*, real-time, and dynamic characteristics of IVCM enable it to overcome the disadvantages of traditional histopathological examination.

Data availability statement

The original contributions presented in the study are included in the article/Supplementary material, further inquiries can be directed to the corresponding author.

Ethics statement

The studies involving human participants were reviewed and approved by Human Medical Ethics Committee of Joint Shantou International Eye Center of Shantou University and The Chinese University of Hong Kong. The patients/participants provided their written informed consent to participate in this study. Written informed consent was obtained from the individual(s) for the publication of any potentially identifiable images or data included in this article.

Author contributions

JC: conception and design, data collection and surgical operation, and drafting of the manuscript. CX: IVCM examination. JC, CX, and ZL: analysis and interpretation of data. TN: critical revision of the manuscript. All authors read and approved the final manuscript.

Conflict of interest

The authors declare that the research was conducted in the absence of any commercial or financial relationships that could be construed as a potential conflict of interest.

Publisher's note

All claims expressed in this article are solely those of the authors and do not necessarily represent those of their affiliated organizations, or those of the publisher, the editors and the reviewers. Any product that may be evaluated in this article, or claim that may be made by its manufacturer, is not guaranteed or endorsed by the publisher.

Supplementary material

The Supplementary Material for this article can be found online at: https://www.frontiersin.org/articles/10.3389/fmed.2023.1166985/full#supplementary-material

References

1. Shields CL, Alset AE, Boal NS, Casey MG, Knapp AN, Sugarman JA, et al. Conjunctival tumors in 5002 cases. comparative analysis of benign versus malignant counterparts. the 2016 James D. Allen Lecture. *Am J Ophthalmol.* (2017) 173:106–33. doi: 10.1016/j.ajo.2016.09.034

2. Kymionis GD, Diakonis VF, Shehadeh MM, Pallikaris AI, Pallikaris IG. Anterior segment applications of *in vivo* confocal microscopy. *Semin Ophthalmol.* (2015) 30:243–51. doi: 10.3109/08820538.2013.839817

3. Cinotti E, Singer A, Labeille B, Grivet D, Rubegni P, Douchet C, et al. Handheld *in vivo* reflectance confocal microscopy for the diagnosis of eyelid margin and conjunctival tumors. *JAMA Ophthalmol.* (2017) 135:845–51. doi: 10.1001/jamaophthalmol.2017.2019

4. Messmer EM, Mackert MJ, Zapp DM, Kampik A. *In vivo* confocal microscopy of pigmented conjunctival tumors. *Graefes Arch Clin Exp Ophthalmol.* (2006) 244:1437–45. doi: 10.1007/s00417-006-0284-8

5. Venkateswaran N, Sripawadkul W, Karp CL. The role of imaging technologies for ocular surface tumors. *Curr Opin Ophthalmol.* (2021) 32:369–78. doi: 10.1097/ICU.00000000 00000771

6. Lee YJ, Lee C, Kim MK, Khwarg SI, Oh JY. Conjunctival pigmented lesion: clinicopathological analysis of 85 cases in Korean population. *Sci Rep.* (2019) 9:18204. doi: 10.1038/s41598-019-54786-8

7. Canadas P, Alberquilla Garcia-Velasco M, Hernandez Verdejo JL, Teus MA. Update on corneal confocal microscopy imaging. *Diagnostics*. (2022) 13:46. doi: 10.3390/diagnostics13010046

8. Broggi G, Verzì AE, Caltabiano R, Micali G, Lacarrubba F. Correlation between *in vivo* reflectance confocal microscopy and horizontal histopathology in skin cancer: a review. *Front Oncol*. (2021) 11:653140. doi: 10.3389/fonc.2021.653140

9. Cinotti E, Perrot JL, Labeille B, Campolmi N, Espinasse M, Grivet D, et al. Handheld reflectance confocal microscopy for the diagnosis of conjunctival tumors. *Am J Ophthalmol*. (2015) 159:324–33. doi: 10.1016/j.ajo.2014.10.031

10. Cavanagh HD. The magic mountain. *Cornea*. (1990) 9:183. doi: 10.1097/00003226-199007000-00001

11. Agin A, Kocabeyoglu S, Colak D, Irkec M. Ocular surface, meibomian gland alterations, and *in vivo* confocal microscopy characteristics of corneas in chronic cigarette smokers. *Graefes Arch Clin Exp Ophthalmol*. (2020) 258:835–41. doi: 10.1007/s00417-019-04547-0

12. Jing Y, Shen CB, Xue K, Li CX, Shen X, Wang ZY, et al. Reflectance confocal microscopy characteristics for melanocytic nevi. *Chin Med J*. (2019) 132:2510–1. doi: 10.1097/CM9.0000000000000440

Advances in multi-modal non-invasive imaging techniques in the diagnosis and treatment of polypoidal choroidal vasculopathy

Yuelin Wang[1,2], Xingwang Gu[1,2] and Youxin Chen[1,2]*

[1]Department of Ophthalmology, Peking Union Medical College Hospital, Chinese Academy of Medical Sciences, Beijing, China, [2]Key Laboratory of Ocular Fundus Diseases, Chinese Academy of Medical Sciences, Beijing, China

Polypoidal choroidal vasculopathy (PCV) is a disease characterized by subretinal pigment epithelium (RPE) orange-red polypoidal lesions and abnormal branching neovascular networks (BNNs). In recent years, various non-invasive imaging technologies have rapidly developed, especially the emergence of optical coherence tomography angiography (OCTA), multi-spectral imaging, and other technologies, which enable the observation of more features of PCV. In addition, these technologies are faster and less invasive compared to indocyanine green angiography (ICGA). Multi-modal imaging, which combined multiple imaging techniques, provides important references for the diagnosis and treatment of PCV with the assistance of regression models, deep learning, and other algorithms. In this study, we reviewed the non-invasive imaging techniques, multi-modal imaging diagnosis, and multi-scene therapeutic applications of PCV, with the aim of providing a reference for non-invasive multi-modal diagnosis and treatment of PCV.

KEYWORDS

polypoidal choroidal vasculopathy (PCV), multimodal, non-invasive imaging technology, diagnosis, treatment

1. Introduction

Polypoidal choroidal vasculopathy (PCV) is a disease characterized by orange-red polypoidal lesions (PLs) and abnormal branching neovascular networks (BNNs) (1–3). It was first described by Yannuzzi in 1982 and was officially published in 1990 (4). Compared to wet age-related macular degeneration (wAMD), PCV has the characteristics of recurrent hemorrhage, subretinal hemorrhage, lower age of onset, and poor response to anti-VEGF therapies. The mechanism of PCV is still unclear, and it is a difficult and hot topic in the field of retinal research due to its serious harm (5, 6).

The gold standard for the diagnosis of PCV in the past was indocyanine green angiography (ICGA) (7). This involves observing focal hyperfluorescent lesions within 6 min on ICGA, as well as at least one of the following: observation of BNN on ICGA, visible pulsation on dynamic ICGA, nodular appearance when ICGA viewed stereoscopically, hypofluorescent halo on ICGA, orange subretinal nodule on a color photograph, and massive subretinal hemorrhage. This examination requires venipuncture and the injection of contrast agents into the body, which carry risks such as systemic allergies and local infections. Therefore, it is a contradiction for some patients. In remote areas, many PCV patients have not been correctly diagnosed due to the lack of ICGA examination equipment.

In recent years, non-invasive imaging techniques have been rapidly developed. Some non-invasive imaging techniques, such as optical coherence tomography (OCT), optical coherence tomography angiography (OCTA), and multi-spectral imaging, have emerged through the limitations of traditional non-invasive imaging techniques (fundus photography, autofluorescence, etc.) and provided more observational dimensions for the diagnosis of PCV. In addition, with the advent of multi-modal imaging technology and the emergence of artificial intelligence algorithms, the diagnosis and treatment of PCV have gradually become less dependent on invasive ICGA examinations.

Therefore, we review recent literature and summarize the latest advances in imaging features, multi-modal diagnosis, and multi-scenario treatment applications of PCV under non-invasive imaging techniques.

2. Non-invasive imaging PCV techniques

2.1. Fundus photography

Fundus photography can be taken using a traditional camera to capture the patient's dilated fundus or using a non-dilated camera to record the characteristics of PCV in the fundus posterior pole (8). The polypoidal lesion of PCV (formerly known as a polyp) can appear as one or more orange-red nodules under the retina, which can occur in the locations of the macular area, near the optic disk, near the vascular arcade, and even in the mid-periphery, but most of the polypoidal lesions appear in the posterior pole. In addition to the polypoidal lesions, extensive subretinal hemorrhage is also an important feature of some PCV cases, with a range often >4 disk diameters (DDs), located under the retina or RPE, and sometimes combined with vitreous hemorrhage (9).

2.2. Autofluorescence

Fundus autofluorescence (FAF) is a non-invasive diagnostic technique based on the theory that pigments and molecules can emit autofluorescence when excited by light. FAF can provide information about RPE and photoreceptor cell metabolism and activity. Oztas et al. (10) found that PLs may appear as granular low autofluorescence. Zhao et al. (11) found that FAF features of PLs include 49.8% high fluorescence rings, 22.6% mixed fluorescence with low fluorescence, and 3.7% mixed fluorescence with polyps, but there are still some (8.2%) PCV polyps with no obvious FAF changes. Some studies have also reported that autofluorescence can observe more pachydrusen, accounting for 61.8% of PCV (12). Overall, FAF has lower diagnostic efficacy for PCV.

2.3. OCT

Optical coherence tomography (OCT) is a non-invasive imaging technique that uses light waves to capture detailed images of the retina and other structures in the eye (13). Initially, the scanning rate of OCT was only a few hundred times per second, and the imaging quality was low. However, recent OCT technology can achieve scanning speeds of up to 400,000 times per second, a scanning width of 24 mm, and a scanning depth of 6 mm, bringing new momentum to clinical research (14, 15).

In earlier years, time-domain OCT technology was able to roughly display the inverted V-shaped pigment epithelium detachment (PED) of PCV, but the detailed features of the polyps could not be shown (16). Swept-source OCT (SS-OCT) was introduced in 2012, which used a longer wavelength light source and a tunable laser to sweep through a range of frequencies, producing a high-resolution image of the eye.

Some retinal and choroidal measurements obtained from SS-OCT are important parameters for quantifying the anatomical structure of the PCV. The central macular thickness (CMT) refers to the distance between the inner limiting membrane (ILM) and the inner boundary of the RPE (17). Generally, active polyps may cause retinal edema and hemorrhage, leading to an increase in CMT values and affecting the patient's vision. After anti-VEGF treatment, the CMT of some patients may decrease, and thus monitoring the CMT can be used to evaluate treatment efficacy (18). The subfoveal choroidal thickness (SFCT) refers to the distance between the Bruch's membrane and the choroid–scleral interface of the central fovea of the macula. Currently, PCV can be classified into type 1 and type 2 based on SFCT and other parameters, and there are reports suggesting that type 2 PCV have a different genotype, thicker SFCT, and poor responsiveness to anti-VEGF therapy as compared with type 1 PCV (19, 20).

In 2022, the PCV working group of the Asia-Pacific Academy of Ophthalmology published the main OCT features of PCV in the journal Ophthalmology (21), which include the following: (1) Sub-RPE ring-like lesion, also known as bubble sign, refers to a round structure observed under PED and characterized by hyporeflective center and a hyperreflective outline; (2) Complex or multi-lobular PED, which is characterized by notches on the PED, resembling an "M" shape with visible multi-lobular PED; (3) Sharp peak PED, also known as a thumb-like protrusion, presents as a narrow-peaked PED with an inverted "V" configuration, with a peak angle of >70 degrees on at least one side and a base-to-width ratio of >1; (4) A double-layer sign refers to the separation of the undulating RPE line and the underlying Bruch's membrane, forming a double layer; (5) Thick choroid with dilated Haller's layer vessels, which are characterized by a choroidal thickness of ≥300 μm at the foveal center, Haller's layer vessel dilation occupying most of the choroidal thickness, and thinning of the choroidal capillaries above it; (6) Complex or multi-lobular PED is visible as multiple high-reflective branching vascular networks of PED on en face OCT; (7) Fluid compartment is characterized by obvious subretinal fluid, which may be accompanied by intraretinal fluid.

2.4. OCTA

The OCTA technology obtains three-dimensional data images by establishing an en face mode based on the traditional cross-sectional scan (B-scan) combined with a coronal scan (C-scan). By identifying the displacement changes in blood flow signals, it can

construct the morphology and structure of retinal vessels, choroidal blood flow, and neovascularization (22, 23).

In the past few years, SD-OCTA has provided important information on PLs and BNNs in PCV. For PLs, SD-OCTA showed that these lesions are often located between Bruch's membrane and the RPE layer. The lesion morphology is often "ring-shaped", but it can also be seen as "cluster-like", "dot-like", "ring-like", or "nodular". However, due to the variability of blood flow signals and the limitations of SD-OCTA scanning speed, the detection rate of PLs by SD-OCTA is approximately 17.0 to 92.3% (24). For BNNs, Huang et al. (25) proposed three types of BNN morphology, namely, "Trunk" pattern, "Glomeruli" pattern, and "Stick" pattern, with detection rates of approximately 70.0 to 100.0% and sensitivities of 0.67 and 0.86. Wang et al. (26) conducted a meta-analysis and discovered that the average detection rate of BNN (0.86) in PCV was higher compared to the detection rate of PLs (0.67) in studies primarily utilizing SD-OCTA as the detection tool. This difference in detection rates may be attributed to the faster blood flow velocity observed in BNN compared to that of the polypoidal lesions in PCV. Meanwhile, OCTA combined with enhanced depth imaging (EDI) technology can provide more information on PCV. The choroidal vascularity index (CVI) is defined as the ratio between vascular luminal area (LA) and total choroidal area (TCA), which is the sum of LA and choroidal stromal area (SA) on EDI-OCT. Batioglu et al. observed that typical PCV (a subtype of PCV) has a higher choroidal blood flow and CVI compared to polypoidal CNV (17). In addition, intervortex venous anastomoses were observed in PCV, and more dilated anastomotic vessels were observed in the typical PCV (17).

In recent years, SS-OCTA has been developed with advantages such as faster scanning speed and deeper scanning depth, providing new insights into the understanding of PCV. Bo et al. (27) analyzed 23 eyes diagnosed with PCV by ICGA and found that SS-OCTA was able to detect all 43 polypoidal lesions identified by ICGA, displaying them as tangled vessels. In addition, SS-OCTA detected 16 tangled vascular structures that were not observed on ICGA. Similarly, BNNs were detected in all eyes on SS-OCTA, while ICGA only identified BNNs in 17 eyes (74%). Kim et al. (28) also conducted a comparative study of ICGA and SS-OCTA in the diagnosis of PCV. They found that SS-OCTA could identify a larger number of polypoidal lesions than ICGA in 12 eyes and detect BNNs in all cases. There was no significant difference in the measurement of the PCV lesion area between ICGA and SS-OCTA images. These results suggest that SS-OCTA imaging is comparable to, and may even be superior to, ICGA for the detection of PLs and BNNs.

2.5. Multi-spectral imaging

Multi-spectrum imaging (MSI) is an imaging method that records images in spectral form and has been attempted for the diagnosis of PCV. Ma et al. (29) found that PLs can be observed at wavelengths of 680 nm and above as lobes of "hyperborder, hypocenter" pattern lesions, and BNN can be vaguely observed as an area of interlacing hyper-reflectance with linear or dot of signals. Subretinal fluid appears as local blurred hyperreflective areas under short wavelengths, and PED can appear as a slightly high-reflective border. The sensitivity and specificity of MSI for diagnosing PCV are 0.84 and 0.93, respectively, with positive and negative predictive values of 0.94 and 0.81, respectively. Therefore, multi-spectrum imaging has a certain diagnostic value for PCV.

3. Multi-modal non-invasive imaging diagnosis

3.1. Theoretical basis

Multi-modal imaging is a joint imaging diagnostic technique. It combines multiple imaging modalities, complementing each other's strengths, and achieves rapid and accurate diagnosis of complex and difficult fundus diseases through mutual "verification". For example, in the field of tumor radiology, integrating multiple modal magnetic resonance sequences can improve diagnostic efficiency. On the one hand, the data from multiple modalities come from different imaging devices, with large amounts of data and more comprehensive descriptions of diseases. On the other hand, in regression analysis, or even deep-learning analysis, the "interaction" between modalities can increase the amount of diagnostic information, especially in deep learning, where the connection layer between each vector connects the information, making the diagnostic ability more advantageous than single-modal imaging.

3.2. Combined diagnosis of PCV

Multi-modal diagnosis of PCV has various combinations, mainly including OCT combined with fundus photography and OCT combined with OCTA (8, 21, 30–36) (Table 1).

In a joint multi-modal study of fundus photography and OCT, Yang et al. (31) found that by incorporating features such as subretinal orange-red nodules on fundus photography, thumb-like PED, notched PED, bubble sign, and Bruch's membrane depression under serosanguinous PED on OCT, the diagnostic strategy using at least two of the five features had a sensitivity of 0.88 and specificity of 0.92 for diagnosing PCV. Chaikitmongkol et al. (30) observed that the presence of at least two of the four features (notched or hemorrhagic PED detected using color fundus photography, sharply peaked PED detected using OCT, notched or multi-lobulated PED detected using OCT, and hyperreflective ring underneath PED detected using OCT) could diagnose PCV with a sensitivity and specificity of over 90%. Using fundus photography and OCT manifestations, the Asia-Pacific Ocular Imaging Society PCV Workgroup found, through regression analysis, that the positive predictive value for diagnosing PCV reached 0.93 when sharp PED peak, sub-RPE ring-like lesion, and En face OCT complex RPE elevation were observed simultaneously. Adding one of the criteria of observation of an orange nodule on fundus photography, complex or multi-lobular PED, thick choroid with dilated Haller's layer vessels, and double-layer sign could increase the positive predictive value to 0.94.

In a multi-modal study combining OCT and OCTA, de Carlo et al. (34) found that the sensitivity and specificity of OCT for diagnosing PCV were 0.30 and 0.86, respectively, while the multi-modal combination of OCT and OCTA improved the sensitivity

TABLE 1 Diagnostic accuracy of multi-modal non-invasive imaging techniques for the diagnosis of PCV.

References	Non-invasive diagnostic combination	Diagnostic criteria	Meeting criteria	Sensitivity	Specificity	PPV	NPV	AUC
Chaikitmongkol et al. (30)	FP+OCT	Four diagnostic criteria: (1) notched or hemorrhagic PED on fundus photography; (2) sharply peaked PED detected on OCT; (3) notched or multi-lobulated PED on OCT; and (4) hyperreflective ring underneath PED detected on OCT.	≥1 criterion	0.98	0.67	0.76	0.98	0.83
			≥2 criteria	0.95	0.95	0.92	0.95	0.93
			≥3 criteria	0.84	0.95	0.95	0.85	0.90
			4 criteria	0.53	0.97	0.94	0.66	0.75
Yang et al. (31)	FP+OCT	Five diagnostic criteria: (1) subretinal orange nodule on FP; (2) thumb-like PED on OCT; (3) notched PED on OCT; (4) bubble sign on OCT; and (5) Bruch's membrane depression under serosanguinous PED on OCT.	≥1 criterion	0.92	0.75	0.79	0.90	0.83
			≥2 criteria	0.88	0.92	0.92	0.89	0.90
			≥3 criteria	0.81	0.96	0.95	0.83	0.88
			≥4 criteria	0.69	0.98	0.97	0.76	0.84
			5 criteria	0.46	1.00	1.00	0.65	0.73
Chaikitmongkol et al. (8)	FP+OCT	(1) Fundus photograph indications: orange-red nodules, or hemorrhagic or fibrovascular PED, or extensive subretinal hemorrhage, and other characteristics; (2) OCT indications: sharp PED peak, or PED notch, or circular lesion below RPE, or double-layer sign, and other features.	Meet both indications	0.83	0.83	0.77	0.88	0.83
Chong Teo et al. (32)	FP+OCT	Three diagnostic criteria: (1) sharp-peaked PED on OCT, (2) sub-RPE ring-like lesion on OCT, and (3) orange nodule on FP.	Meeting all criteria	0.65	0.82	0.68	0.88	0.85
Cheung et al. (21)	FP+OCT	Three major criteria: (1) sub-RPE ring-like lesion on OCT; (2) sharp-peaked PED on OCT; and (3) en face OCT complex RPE elevation. Four minor criteria: (1) orange nodule on FP; (2) complex or multi-lobular PED on OCT; (3) thick choroid with dilated Haller's layer on OCT; and (4) double-layer sign on OCT.	Meet three major criteria and one minor criterion	0.78	0.91	0.94	0.68	0.91

(Continued)

TABLE 1 (Continued)

References	Non-invasive diagnostic combination	Diagnostic criteria	Meeting criteria	Sensitivity	Specificity	PPV	NPV	AUC
Cheung et al. (33)	OCT+OCTA	Three OCT criteria: (1) notched/narrow-peaked PED; or (2) round sub-RPE hyporeflective lesion, or (3) any RPE detachment. Two OCTA criteria: (1) localized sub-RPE hyperflow lesion in the cross-sectional OCTA; or (2) nodular hyperflow lesion in the en face OCTA.	Meet both OCT and OCTA criteria.	0.82	1.00	1.00	0.87	—
de Carlo et al. (34)	OCT+OCTA	(1) OCT criteria: PCV complex with small highly reflective circles representing polyps adjacent to large highly reflective circles in a "snowman" sign or adjacent to geographically shaped BNNs, etc. (2) OCTA criteria: the presence of an inverted U shape (the polyp) next to a large serous PED or shallow elevation of the RPE above Bruch membrane ("double layer" sign), etc.	Meet both OCT and OCTA criteria.	0.44	0.87	—	—	—
Chou et al. (35)	FP+OCT+AI	—	—	0.81	0.85	—	—	0.84
Xu et al. (36)	FP+OCT+AI	—	—	0.89	0.96	—	—	0.87

AI, artificial intelligence; AUC, area under the curve; BNN, branching neovascular network; FP, false positive; NPV, negative predictive value; OCT, optical coherence tomography; OCTA, optical coherence tomography angiography; PED, pigment epithelial detachment; PPV, positive predictive value; RPE, retinal pigment epithelium.

to 0.44 with a specificity of 0.87. Similarly, Cheung et al. (33) found that the sensitivity for the combined diagnosis of PCV and CNV/AMD using a two-step diagnostic algorithm with OCT and OCTA was still 0.82 when adding OCTA information to the OCT diagnosis, but the specificity increased from 0.52 to 1.00. This suggests that the diagnostic efficiency of multi-modal non-invasive diagnosis of PCV improved compared to single-modality diagnosis.

3.3. Artificial intelligence assistant diagnosis

In the field of artificial intelligence, multi-modal machine learning combines the advantages of each modality through algorithms and other techniques. Single modality refers to the use of a single type of data or input modality to train a machine learning model. Multi-modal learning refers to the use of the complementarity between multiple modalities and the interaction between each fully connected layer to learn better features.

In some studies, artificial intelligence has been used in the non-invasive diagnosis of PCV. Wongchaisuwat et al. (37) developed a model that trained on 2,334 OCT images of PCV using ResNet. On the internal dataset, the model achieved a diagnostic sensitivity and specificity of 1.00 and 0.60, respectively, whereas, on the external dataset, the model achieved a sensitivity and specificity of 0.85 and 0.71, respectively. Chou et al. (35) trained a deep-learning model based on color fundus photography and OCT biomarkers. They introduced a multiple correspondence analysis algorithm to train the PCV diagnostic model with a transfer learning architecture on approximately 700 cases, achieving a sensitivity and specificity of 0.81 and 0.85, respectively. Xu et al. (36) developed a bimodal deep-learning convolutional neural network model (DCNN-Combo) based on color fundus photography and OCT that achieved a PCV diagnosis with an accuracy of 87.4%, which was even more consistent with the diagnostic gold standard than that of ophthalmologists.

4. Application of multi-modal non-invasive imaging in PCV treatment

4.1. Monitoring the treatment response of PCV

Multiple studies have reported the use of non-invasive methods, such as fundus photography, OCT, and OCTA, to evaluate the response to PCV treatment. Cho et al. (38) reported that based on the manifestation of fundus photography, 10% of eyes in PCV patients at 5 years and 30% of eyes at 10 years could observe subretinal hemorrhage in fundus photography, which is significantly higher than typical nAMD, indicating disease progression.

Using SS-OCT/SS-OCTA gives us the ability to measure the choroid in PCV before and after treatment. Tan et al. (39) reported the use of OCT to evaluate the treatment response of PCV patients and assessed whether the polyp was closed by monitoring the changes such as (1) the disappearance of subretinal fluid, (2) a

significant reduction of PED height, (3) an increased reflection within PED, (4) the disappearance of low-reflection ring, and (5) a reduction of thickened RPE structure. The diagnosis AUC reached 0.90 when the criteria of (1), (3), and (4) were met. Montorio et al. (40) used OCTA to evaluate changes in choroidal capillary flow density and SFCT and found that the choroidal capillary flow density in PCV treated with anti-VEGF drugs was significantly reduced, and the CMT and SFCT were also significantly decreased. Fukuyama et al. (41) found that the blood flow signal within the polyp on OCTA was related to the response of PCV to anti-VEGF drug treatment during a follow-up of more than 6 months, and a low blood flow signal within the polyp lasting for more than 2 weeks may indicate poor initial treatment response of PCV.

4.2. Monitoring of PCV recurrence

Some studies use OCT and fundus photography to monitor PCV recurrence. Bo et al. (42) defined exudative recurrence as the reappearance of IRF, SRF, or serous PED on OCT, or the appearance of new subretinal or RPE hemorrhage on fundus photography. Ma et al. (43) described the impact of different BNN patterns observed on OCTA on the treatment response and outcomes of PCV and found that type 2 ("Glomeruli" pattern) and type 3 ("Stick" pattern) were associated with thicker choroid and increased recurrence of PCV, while type 1 ("Trunk" pattern) was associated with thin choroid, vitelliform lesions, and AMD-like features. However, because OCTA cannot display vascular leakage, it is currently primarily used in combination with structural OCT for treatment monitoring and as a reference for recurrence treatment decisions.

4.3. Timing of rescue PDT

The APOIS PCV working group also reported the criteria for identifying PCV in eyes previously diagnosed with wAMD and with poor response to three injections of anti-VEGF treatment (32). When one of the following three criteria is met, supplementary PDT treatment may be considered: orange-red nodules observed on fundus photography, peaked PED observed on OCT, and low-reflectance ring structure observed on OCT. The combination of these three criteria has a specificity of 0.82 and a sensitivity of 0.65 (AUC of 0.85) for detecting PCV.

5. Limitations in non-invasive multi-modal imaging diagnosis of PCV

Although non-invasive multi-modal imaging has a certain value in the diagnosis and treatment of PCV, there are still several problems. First, the pathogenesis of PCV is not yet clear, and the disease classification is complex (44). Some scholars believe that the high fluorescence signal observed on ICGA may be a common manifestation of many diseases, so the use of other non-invasive imaging for the identification and diagnosis of PCV may lead to misdiagnosis (45). Second, the current diagnostic criteria

for a combined diagnosis are mostly for newly diagnosed PCV. However, many patients are misdiagnosed with other diseases, and the possibility of PCV is only considered after various treatments have been proven ineffective, which may affect the diagnosis of PCV by non-invasive multi-modal imaging due to changes in some PED and intraretinal fluid (46). Third, different non-invasive multi-modal detection instruments may have different parameters and may affect the accuracy of diagnosis, such as image quality rating, degree of ocular refractive media opacity, and instrument resolution (47).

6. Conclusion

In summary, non-invasive imaging diagnostic technologies provide fast and safe diagnostic methods with high accuracy and are comparable to or might be better than ICGA in some aspects. The superiority of multi-modal non-invasive imaging diagnostic technology, combined with multiple devices and special algorithms, fully leverages their interactive effects and has played an important role in the diagnosis and treatment of PCV.

Author contributions

YW and XG were involved in manuscript drafting. YC contributed to the manuscript revision. All authors have read and approved the final manuscript.

Funding

Acknowledgments

Conflict of interest

The authors declare that the research was conducted in the absence of any commercial or financial relationships that could be construed as a potential conflict of interest.

Publisher's note

All claims expressed in this article are solely those of the authors and do not necessarily represent those of their affiliated organizations, or those of the publisher, the editors and the reviewers. Any product that may be evaluated in this article, or claim that may be made by its manufacturer, is not guaranteed or endorsed by the publisher.

References

1. Sen P, Manayath G, Shroff D, Salloju V, Dhar P. Polypoidal choroidal vasculopathy: an update on diagnosis and treatment. *Clin Ophthalmol.* (2023) 17:53–70. doi: 10.2147/OPTH.S385827

2. Koh AH, Expert PCVP, Chen LJ, Chen SJ, Chen Y, Giridhar A, et al. Polypoidal choroidal vasculopathy: evidence-based guidelines for clinical diagnosis and treatment. *Retina.* (2013) 33:686–716. doi: 10.1097/IAE.0b013e3182852446

3. Xue Y, Qinhua C. Short-term efficacy in polypoidal choroidal vasculopathy patients treated with intravitreal aflibercept or conbercept. *Front Med (Lausanne).* (2022) 9:835255. doi: 10.3389/fmed.2022.835255

4. Yannuzzi LA, Sorenson J, Spaide RF, Lipson B. Idiopathic polypoidal choroidal vasculopathy (IPCV). *Retina (Philadelphia, Pa).* (1990) 10:1–8. doi: 10.1097/00006982-199001010-00001

5. Han J, Choi S, Park JI, Hwang JS, Han JM, Ko J, et al. Detecting macular disease based on optical coherence tomography using a deep convolutional network. *J Clin Med.* (2023) 12:1005. doi: 10.3390/jcm12031005

6. Ruamviboonsuk P, Cheung GCM, Chainakul M, Arjkongharn N, Chan HH, Ogura Y, et al. Updates on risk factors, diagnosis, and treatments of polypoidal choroidal vasculopathy. *Asia Pac J Ophthalmol.* (2023) 12:184–95. doi: 10.1097/APO.0000000000000573

7. Koh A, Lee WK, Chen LJ, Chen SJ, Hashad Y, Kim H, et al. EVEREST study: efficacy and safety of verteporfin photodynamic therapy in combination with ranibizumab or alone versus ranibizumab monotherapy in patients with symptomatic macular polypoidal choroidal vasculopathy. *Retina.* (2012) 32:1453–64. doi: 10.1097/IAE.0b013e31824f91e8

8. Chaikitmongkol V, Khunsongkiet P, Patikulsila D, Ratanasukon M, Watanachai N, Jumroendararasame C, et al. Color fundus photography, optical coherence tomography, and fluorescein angiography in diagnosing polypoidal choroidal vasculopathy. *Am J Ophthalmol.* (2018) 192:77–83. doi: 10.1016/j.ajo.2018.05.005

9. Li MS, Tsen CL. Clinical features and outcomes of breakthrough vitreous hemorrhage secondary to polypoidal choroidal vasculopathy. *PLoS ONE.* (2022) 17:e0279778. doi: 10.1371/journal.pone.0279778

10. Oztas Z, Mentes J, Nalcaci S, Baris M. Characteristics of fundus autofluorescence in active polypoidal choroidal vasculopathy. *Turk J Ophthalmol.* (2016) 46:165–8. doi: 10.4274/tjo.54280

11. Zhao X, Xia S, Chen Y. Characteristic appearances of fundus autofluorescence in treatment-naive and active polypoidal choroidal vasculopathy: a retrospective study of 170 patients. *Graefes Arch Clin Exp Ophthalmol.* (2018) 256:1101–10. doi: 10.1007/s00417-018-3980-2

12. Lai TYY, Tang Z, Lai ACW, Szeto SKH, Lai RYK, Cheung CY, et al. Association of fundus autofluorescence abnormalities and pachydrusen in central serous chorioretinopathy and polypoidal choroidal vasculopathy. *J Clin Med.* (2022) 11:5340. doi: 10.3390/jcm11185340

13. Permadi AC, Djatikusumo A, Adriono GA. Optical coherence tomography in diagnosing polypoidal choroidal vasculopathy. Looking into the future: a systematic review and meta-analysis. *Int J Retina Vitreous.* (2022) 8:14. doi: 10.1186/s40942-022-00365-5

14. Laíns I, Wang JC, Cui Y, Katz R, Vingopoulos F, Staurenghi G, et al. Retinal applications of swept source optical coherence tomography (OCT) and optical coherence tomography angiography (OCTA). *Prog Retin Eye Res.* (2021) 84:100951. doi: 10.1016/j.preteyeres.2021.100951

15. Yamashiro K, Yanagi Y, Koizumi H, Matsumoto H, Cheung CMG, Gomi F, et al. Relationship between pachychoroid and polypoidal choroidal vasculopathy. *J Clin Med.* (2022) 11:4614. doi: 10.3390/jcm11154614

16. Kumar A, Kumawat D, Sundar MD, Gagrani M, Gupta B, Roop P, et al. Polypoidal choroidal vasculopathy: a comprehensive clinical update. *Ther Adv Ophthalmol.* (2019) 11:2515841419831152. doi: 10.1177/2515841419831152

17. Batioglu F, Yanik O, Ozer F, Demirel S, Ozmert E. A comparative study of choroidal vascular and structural characteristics of typical polypoidal choroidal vasculopathy and polypoidal choroidal neovascularization: OCTA-based evaluation of intervortex venous anastomosis. *Diagnostics (Basel).* (2022) 13:138. doi: 10.3390/diagnostics13010138

18. Pant P, Kundu A, Rathinavelu JK, Wei X, Agrawal R, Stinnett SS, et al. Longitudinal assessment of the choroidal vascularity index in eyes with branch retinal vein occlusion-associated cystoid macular edema. *Ophthalmol Ther.* (2023) 12:2103–15. doi: 10.1007/s40123-023-00731-y

19. Miki A, Honda S, Kondo N, Negi A. The association of age-related maculopathy susceptibility 2 (ARMS2).and complement factor H (CFH).variants with two angiographic subtypes of polypoidal choroidal vasculopathy. *Ophthalmic Genet.* (2013) 34:146–50. doi: 10.3109/13816810.2012.749288

20. Tanaka K, Mori R, Kawamura A, Nakashizuka H, Wakatsuki Y, Yuzawa M, et al. Comparison of OCT angiography and indocyanine green angiographic findings with subtypes of polypoidal choroidal vasculopathy. *Br J Ophthalmol.* (2017) 101:51–5. doi: 10.1136/bjophthalmol-2016-309264

21. Cheung CMG, Lai TYY, Teo K, Ruamviboonsuk P, Chen SJ, Kim JE, et al. Polypoidal choroidal vasculopathy: consensus nomenclature and non-indocyanine green angiograph diagnostic criteria from the asia-pacific ocular imaging society PCV workgroup. *Ophthalmology.* (2021) 128:443–52. doi: 10.1016/j.ophtha.2020.08.006

22. Chen L, Yuan M, Sun L, Chen Y. Different morphology of branching neovascular network in polypoidal choroidal vasculopathy: a swept-source optical coherence tomography angiography study. *J Clin Med.* (2023) 12:742. doi: 10.3390/jcm12030742

23. Yuan MZ, Chen LL, Yang JY, Luo MY, Chen YX. Comparison of OCT and OCTA manifestations among untreated PCV, neovascular AMD, and CSC in Chinese population. *Int J Ophthalmol.* (2020) 13:93–103. doi: 10.18240/ijo.2020.01.14

24. Li B, Chen Y. Application and research progress of optical coherence tomography angiography in polypoidal choroidal vasculopathy. *Chinese J Ophthalmol.* (2020) 56:950–5. doi: 10.3760/cma.j.cn112142-20200509-00259

25. Huang CH, Yeh PT, Hsieh YT, Ho TC, Yang CM, Yang CH, et al. Characterizing branching vascular network morphology in polypoidal choroidal vasculopathy by optical coherence tomography angiography. *Sci Rep.* (2019) 9:595. doi: 10.1038/s41598-018-37384-y

26. Wang Y, Yang J, Li B, Yuan M, Chen Y. Detection rate and diagnostic value of optical coherence tomography angiography in the diagnosis of polypoidal choroidal vasculopathy: a systematic review and meta-analysis. *J Ophthalmol.* (2019) 2019:6837601. doi: 10.1155/2019/6837601

27. Bo Q, Yan Q, Shen M, Song M, Sun M, Yu Y, et al. Appearance of polypoidal lesions in patients with polypoidal choroidal vasculopathy using swept-source optical coherence tomographic angiography. *JAMA Ophthalmol.* (2019) 137:642–50. doi: 10.1001/jamaophthalmol.2019.0449

28. Kim K, Yang J, Feuer W, Gregori G, Kim ES, Rosenfeld PJ, et al. A comparison study of polypoidal choroidal vasculopathy imaged with indocyanine green angiography and swept-source optical coherence tomography angiography. *Am J Ophthalmol.* (2020) 217:240–51. doi: 10.1016/j.ajo.2020.05.017

29. Ma F, Yuan M, Kozak I, Zhang Q, Chen Y. Sensitivity and specificity of multispectral imaging for polypoidal choroidal vasculopathy. *Retina.* (2021) 41:1921–9. doi: 10.1097/IAE.0000000000003130

30. Chaikitmongkol V, Kong J, Khunsongkiet P, Patikulsila D, Sachdeva M, Chavengsaksongkram P, et al. Sensitivity and specificity of potential diagnostic features detected using fundus photography, optical coherence tomography, and fluorescein angiography for polypoidal choroidal vasculopathy. *JAMA Ophthalmol.* (2019) 137:661–7. doi: 10.1001/jamaophthalmol.2019.0565

31. Yang J, Yuan M, Wang E, Xia S, Chen Y. Noninvasive multimodal imaging in diagnosing polypoidal choroidal vasculopathy. *BMC Ophthalmol.* (2019) 19:229. doi: 10.1186/s12886-019-1244-5

32. Chong Teo KY, Sadda SR, Gemmy Cheung CM, Chakravarthy U, Staurenghi G, Invernizzi A, et al. Non-ICGA treatment criteria for Suboptimal Anti-VEGF Response for Polypoidal Choroidal Vasculopathy: APOIS PCV Workgroup Report 2. *Ophthalmol Retina.* (2021) 5:945–53. doi: 10.1016/j.oret.2021.04.002

33. Cheung CMG, Yanagi Y, Akiba M, Tan A, Mathur R, Chan CM, et al. Improved detection and diagnosis of polypoidal choroidal vasculopathy using a combination of optical coherence tomography and optical coherence tomography angiography. *Retina.* (2019) 39:1655–63. doi: 10.1097/IAE.0000000000002228

34. de Carlo TE, Kokame GT, Kaneko KN, Lian R, Lai JC, Wee R. Sensitivity and specificity of detecting polypoidal choroidal vasculopathy with en face optical coherence tomography and optical coherence tomography angiography. *Retina.* (2019) 39:1343–1352. doi: 10.1097/IAE.0000000000002139

35. Chou YB, Hsu CH, Chen WS, Chen SJ, Hwang DK, Huang YM, et al. Deep learning and ensemble stacking technique for differentiating polypoidal choroidal vasculopathy from neovascular age-related macular degeneration. *Sci Rep.* (2021) 11:7130. doi: 10.1038/s41598-021-86526-2

36. Xu Z, Wang W, Yang J, Zhao J, Ding D, He F, et al. Automated diagnoses of age-related macular degeneration and polypoidal choroidal vasculopathy using bi-modal deep convolutional neural networks. *Br J Ophthalmol.* (2020) 105:561–6. doi: 10.1136/bjophthalmol-2020-315817

37. Wongchaisuwat P, Thamphithak R, Jitpukdee P, Wongchaisuwat N. Application of Deep Learning for automated detection of polypoidal choroidal vasculopathy in spectral domain optical coherence tomography. *Transl Vis Sci Technol.* (2022) 11:16. doi: 10.1167/tvst.11.10.16

38. Cho JH, Ryoo NK, Cho KH, Park SJ, Park KH, Woo SJ. Incidence rate of massive submacular hemorrhage and its risk factors in polypoidal choroidal vasculopathy. *Am J Ophthalmol.* (2016) 169:79–88. doi: 10.1016/j.ajo.2016.06.014

39. Tan ACS, Jordan-Yu JM, Vyas CH, Gan ATL, Teo KYC, Chan CM, et al. Optical coherence tomography features of polypoidal lesion closure in

polypoidal choroidal vasculopathy treated with aflibercept. *Retina.* (2022) 42:114–22. doi: 10.1097/IAE.0000000000003285

40. Montorio D, Giordano M, Concilio M, Cennamo G. Structural and vascular changes of the choroid in polypoidal choroidal vasculopathy after intravitreal anti-VEGF therapy. *Ophthalmologica.* (2022) 245:173–8. doi: 10.1159/000521071

41. Fukuyama H, Komuku Y, Araki T, Gomi F. Association of flow signals within polyps on optical coherence tomography angiography with treatment responses after combination therapy for polypoidal choroidal vasculopathy. *Retina.* (2022) 42:942–8. doi: 10.1097/IAE.0000000000003395

42. Bo Q, Zhang M, Chen J, Jia H, Shen M, Sun M, et al. Progression of polypoidal lesions associated with exudative recurrence in polypoidal choroidal vasculopathy. *Ophthalmology.* (2023) 130:167–78. doi: 10.1016/j.ophtha.2022.09.013

43. Ma ST, Huang CH, Chang YC, Lai TT, Hsieh YT, Ho TC, et al. Clinical features and prognosis of polypoidal choroidal vasculopathy with different morphologies of branching vascular network on optical coherence tomography angiography. *Sci Rep.* (2021) 11:17848. doi: 10.1038/s41598-021-97340-1

44. Azar G, Vasseur V, Lahoud C, Favard C, De Bats F, Cochereau I, et al. Polypoidal choroidal vasculopathy diagnosis and neovascular activity evaluation using optical coherence tomography angiography. *Biomed Res Int.* (2021) 2021:1637377. doi: 10.1155/2021/1637377

45. Siedlecki J, Klaas J, Keidel L, Asani B, Schiefelbein J, Knebel D, et al. Optical coherence tomography-based misdiagnosis and morphological distinction in pachychoroid neovasculopathy vs. polypoidal choroidal vasculopathy. *Eye (Lond).* (2023). doi: 10.1038/s41433-023-02529-5. [Epub ahead of print].

46. Chaikitmongkol V, Chaovisitsaree T, Patikulsila D, Kunavisarut P, Phasukkijwatana N, Watanachai N, et al. Optical coherence tomography features for identifying posttreatment complete polypoidal regression in polypoidal choroidal vasculopathy. *Asia Pac J Ophthalmol (Phila).* (2022) 11:408–16. doi: 10.1097/APO.0000000000000551

47. Dat DT, Hien N, Quan NN, Tung MQ, Tam HC, Hung BV. Current trends in clinical characteristics, diagnosis, and treatment of polypoidal choroidal vasculopathy: a perspective from Vietnam. *J Clin Med.* (2022) 11:4678. doi: 10.3390/jcm11164678

Peripapillary choroidal vascularity index and thickness in patients with systemic sclerosis

Barbara Pieklarz[1]*, Ewa Gińdzieńska-Sieśkiewicz[2],
Izabela Zawadzka[1], Magdalena Bagrowska[2], Joanna Daniluk[2],
Patryk Sidorczuk[1], Otylia Kowal-Bielecka[2], Joanna Konopińska[1]
and Diana Anna Dmuchowska[1]*

[1]Ophthalmology Department, Medical University of Białystok, Białystok, Poland, [2]Department of
Rheumatology and Internal Diseases, Medical University of Białystok, Białystok, Poland

Introduction: Patients with systemic sclerosis (SSc) present an increased risk of developing glaucomatous optic neuropathy (GON). We investigated peripapillary choroidal parameters and peripapillary retinal nerve fiber layer (RNFL) thickness using spectral domain optical coherence tomography (SD-OCT) to determine the relationships of these factors with clinical variables.

Methods: A total of 33 patients with SSc were enrolled and compared to 40 controls. After obtaining circular scans around the optic disc, the global and quadrant peripapillary choroidal thickness (pCT) and RNFL thickness were measured. Additionally, the peripapillary choroidal vascularity index (pCVI), which allows for a quantitative analysis of the choroidal vasculature, was determined.

Results: No significant differences were found in pCT and RNFL thickness between patients with SSc and controls, or within SSc subtypes (diffuse cutaneous systemic sclerosis (dcSSc) compared to limited cutaneous systemic sclerosis (lcSSc)) ($p > 0.05$). The pCVI was significantly lower in patients with SSc than in control subjects (64.25 ± 1.94 vs. 65.73 ± 2.12, $p < 0.001$).

Conclusion: Our results suggest that the statistically significant decrease in pCVI in patients with SSc compared to the control group is probably due to a decrease in the vascular layer, which would partially explain an increased risk of GON in patients with SSc.

1. Introduction

Systemic sclerosis (SSc) is an autoimmune connective tissue disease characterized by chronic progressive tissue and organ fibrosis. Its pathophysiology is complex; however, the process initially involves microvascular damage, followed by an autoimmune response, inflammation, and diffuse fibrosis (1). SSc remains a major medical challenge. Multiple organ-based manifestations are important for its diagnosis and classification. The most common consequences of SSc are digital vasculopathy, gastrointestinal complications, lung fibrosis, pulmonary hypertension, cardiac fibrosis, and renal scleroderma crisis (2).

SSc can be classified into two major disease subsets based on the extent of skin involvement. Cases with proximal skin involvement are classified as diffuse cutaneous systemic sclerosis SSc (dcSSc), whereas cases with skin involvement affecting the limbs distal to the elbows and knees, with or without neck and face involvement, are classified as limited cutaneous systemic sclerosis SSc (lcSSc) (1). Both dcSSc and lcSSc may be associated with internal organ involvement (3).

Many ocular manifestations involving the anterior and posterior segments have also been reported in SSc patients (4–6), and some reports suggest that SSc is a high-risk factor for the development of glaucomatous optic neuropathy (GON), especially normal-tension glaucoma (NTG) (7–11).

The choroid has the highest blood flow in the human body and a high vascular content. The end-arterial nature of the choroidal vasculature and the existence of watershed zones render this layer susceptible to inflammation and ischemia in multisystemic diseases (12). Endothelial cell injury, basement membrane thickening, and pericyte loss in choroidal vessels have been reported in histological studies of SSc patients (13). Macular choroidal thickness has been discussed as a promising inflammatory biomarker in systemic autoimmune diseases, especially those with vascular components (14).

Retinal and choroidal microvascular impairments in SSc patients have been confirmed using fluorescence angiography (FA) (15), optical coherence tomography (OCT) (16–20), and OCT-angiography (OCT-A) (21–25). Most studies on choroidal macular thickness have found that patients with SSc have a significantly thinner macular choroid than healthy subjects, probably due to chronic vascular damage (16–18, 20, 24–26). There are two studies in the literature evaluating CVI in SSc; however, they refer to the macular area and, the results are inconsistent (21, 27). In the peripapillary region, only the vascular density parameters and optic nerve head (ONH) parameters obtained using OCT-A were examined in patients with SSc (17, 19, 23), which is associated mostly with retinal and not choroidal circulation due to the functional and structural heterogeneity of these circulatory systems (24). In recent years, interest in peripapillary choroid thickness has increased. However, the characteristics of the choroid in this area are much poorer than those of the macular area. Studies have revealed thinner peripapillary choroidal thickness not only among patients with NTG and primary open-angle glaucoma (POAG), (23–26), but also in other diseases, such as multiple sclerosis (27), chronic obstructive pulmonary disease (28), high myopia (29), or in patients with vitamin D deficiency (30). In contrary, other studies have shown a thicker peripapillary choroid in some diseases, such as nonarteritic anterior ischemic optic neuropathy (31), Parkinson's disease (32) and retinal vein occlusions at diagnosis, followed by a decrease at an early follow-up stage (33).

The aim of this study was to investigate peripapillary choroidal parameters and peripapillary retinal nerve fiber layer (RNFL) thickness, and to determine their relationships with clinical variables to gain insight into one of the pathophysiological aspects of SSc. To the best of our knowledge, the present study is the first to analyze peripapillary choroidal thickness together with the peripapillary choroidal vascularity index in patients with SSc, and there are no previous reports on peripapillary choroidal characteristics. With our study we aimed at filling this gap. It is worth noting that choroidal thickness is a rough estimate rather than an accurate marker of choroidal status; hence, we not only determined choroidal thickness, but also calculated the peripapillary choroidal vascularity index

(pCVI), a novel OCT-based choroidal quantitative parameter that provides more detailed information about the vascular component of the choroid. We hypothesized that patients with SSc would demonstrate alterations in peripapillary choroidal parameters, which would explain their increased risk of GON.

2. Materials and methods

This was a prospective single-center, cross-sectional study conducted between March 2021 and March 2022 at the Ophthalmology Department, Medical University of Bialystok. The protocol of the study was approved by the local Bioethics Committee at the Medical University of Bialystok (decision no APK.002.109.2021) and the study was conducted in accordance with the Declaration of Helsinki. Written informed consent was obtained from each subject before enrolment in the study.

A total of 66 eyes from 33 patients with SSc, diagnosed according to the 2013 ACR/EULAR SSc criteria (28), were enrolled in the study, and the patients were followed up by the Department of Rheumatology and Internal Diseases, Medical University of Bialystok. The control group comprised 80 eyes from 40 ophthalmologically and systemically healthy (self-reported) subjects undergoing routine ophthalmological assessments. The groups did not differ with regard to age, sex, or axial length (AL). All participants underwent ophthalmological examination, including refraction, best corrected visual acuity (BCVA) in Snellen converted into log MAR, slit lamp biomicroscopy, AL measurement (Tomey OA-2000 biometer, Nagoya, Japan), fundus examination, and peripapillary structural spectral domain OCT (SD-OCT, Heidelberg Engineering, Heidelberg, Germany). IOP was measured using a Pascal dynamic contour tonometer (DCT, Zeimer Ophthalmic Systems AG, Port, Switzerland). Blood pressure was measured immediately prior to obtaining the OCT images, after 5 min of rest in a sitting position.

In three eyes, RNFL thinning in the superior, inferior, and inferotemporal quadrants was found with no corresponding scotoma in visual field examination and was associated with a glaucomatous disc appearance (preperimetric glaucoma) (29). The exclusion criteria included: ametropia ≥3 diopters, the presence of fundus pathology, phacoemulsification less than 12 months prior to the examination, history of posterior segment surgery, diabetes, and insufficient quality of OCT images.

Data regarding age, sex, SSc subtype (diffuse and limited), disease duration, autoantibody profile, current smoking status, and systemic treatment were recorded. A history of digital ulcers (present or past), the presence of interstitial lung disease (ILD) confirmed via high-resolution computed tomography (HRCT) of the lungs, and cardiac [elevated N-terminal pro b-type natriuretic peptide (NT-proBNP) or heart fibrosis upon magnetic resonance imaging (MRI)] and joint involvement (arthralgia or joint swelling) were also included in the analysis.

Structural microvascular abnormalities related to the pathophysiological process of SSc were visualized noninvasively using nailfold capillaroscopy (NFC). This safe method is relevant for predicting disease progression and monitoring the effects of treatment (30). NFC was performed using a CapillaryScope 200 Dino-Lite Digital microscope (MEDL4N Pro) and stratified based on the characteristic SSc pattern (capillary density, capillary dimension, abnormal capillary morphology, and presence or absence of hemorrhages), categorized by Cutolo et al. as "early," "active" and "late"
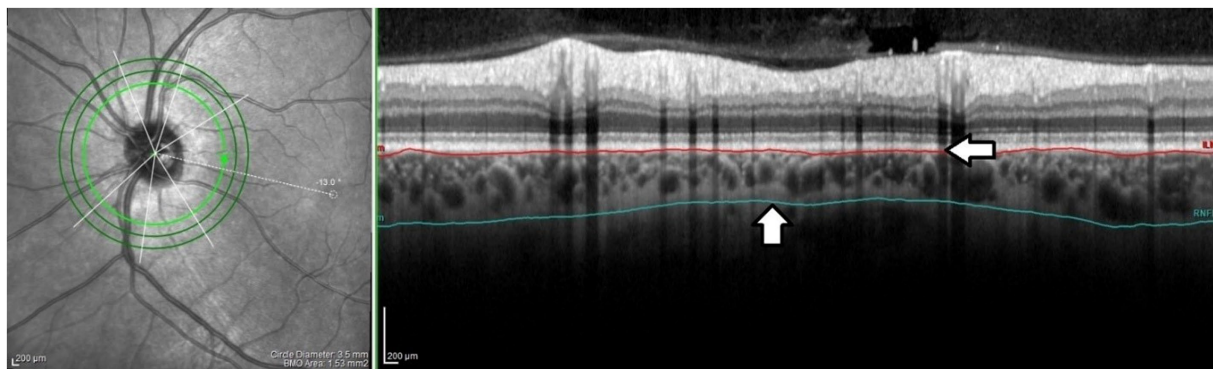
FIGURE 1
The peripapillary choroidal thickness. The internal limiting membrane (ILM) was manually shifted to Bruch's membrane (BM) (horizontal arrow) and the RNFL border to the choroidal–scleral junction (CSJ) (vertical arrow). The offset was performed on each scan by the same grader (PS). Peripapillary choroidal thickness was defined as the distance between the BM and the CSJ.

scleroderma patterns (30). Blood parameters including CRP, ESR (after 2 h), and NT-proBNP were measured.

2.1. OCT image acquisition and analysis

OCT images were taken in mydriasis within the same time interval (12 p.m.–3 p.m.) to avoid diurnal variation in choroidal thickness. Peripapillary OCT images were obtained using a 3.5 mm diameter, 360 degree circle scan centered on the optic nerve head carried out with glaucoma software SD-OCT (Heidelberg Engineering, Heidelberg, Germany). This scan pattern was used to determine the choroidal parameters: peripapillary choroidal thickness (pCT), peripapillary total choroidal area (pTCA), peripapillary luminal area (pLA), peripapillary stromal area (pSA), and retinal nerve fiber layer (RNFL) thickness. RNFL thickness was automatically measured by software and the distribution of the RNFL was displayed as an RNFL thickness map (superior, inferior, nasal, temporal quadrants, and global value). As there is no automatic tool for pCT measurement, pCT was obtained by manually shifting the internal limiting membrane (ILM) to Bruch's membrane (BM) and the RNFL border to the choroidal–scleral junction (CSJ) (Figure 1). The results were presented as global and quadrant values (superior, inferior, nasal, and temporal) in a thickness map.

Binarization of the peripapillary choroidal area (Figure 2) was performed by two authors (BP and PS). Images were analyzed using the public domain software ImageJ,[1] using the protocol previously described by Sonoda and Agrawal (31, 33) with a few modifications. The most important modification concerns the setting of the scale, which considered the stretching of the image (OCT sampling density is higher in the axial direction versus the transverse), to avoid erroneous quantification of the measured area (32). An image presented with a 1:1 pixel aspect ratio is stretched axially, but the detailed visualization of the structure is improved compared to a 1 × 1 μm image. Therefore, the scale was set considering the horizontal and vertical scale relationships between the distance and pitch of pixels (μm/pixel) to reflect the actual size of the measured area. A

detailed step-by-step image analysis algorithm is provided in the Supplementary material. In the next step, using the Polygon Selection tool, the pTCA was selected from the outer boundary of the RPE–Bruch's membrane layer to the choroidal–scleral border. The image was converted to an 8-bit image to allow the application of the Niblack Auto Local Threshold tool. The binarized image was reconverted to an RGB image. The vascularized area was highlighted using the Color Threshold tool and pLA and pTCA were measured. pSA was calculated by subtracting pLA from pTCA. The peripapillary choroidal vascularity index (pCVI) was determined as the pLA to pTCA ratio (%).The interobserver reproducibility of the measurements was assessed by measuring the intraclass correlation coefficient (ICC) and absolute agreement. The ICC values for the pCVI, pTCA, and pLA measurements were > 0.85 (95% CI, 0.723–0.986).

2.2. Statistical analysis

Analyses were performed using R 4.0.5. statistical software [R Core Team (2021). R: Language and environment for statistical computing by R Foundation for Statistical Computing, Vienna, Austria]. Data are presented as n (%) for nominal variables and as mean ± SD or median (Q1; Q3) for continuous variables, depending on the normality of distribution (validated with the Shapiro–Wilk test and based on skewness and kurtosis values). Comparison of groups was made using the chi-square test or the Fisher exact test for nominal data and with the t test, Mann–Whitney U test, ANOVA, or Kruskal–Wallis test for continuous variables, as appropriate. *Post hoc* comparisons were based on the Tukey or Dunn test with Bonferroni correction for multiple comparisons. The relationships between continuous variables were assessed using Pearson's or Spearman's correlation coefficients, as appropriate. Additionally, linear regression analysis was performed to verify the association between pCVI and demographic, clinical, and ocular features. All calculations were based on $\alpha = 0.05$.

3. Results

Sixty-six eyes of 33 SSc patients and 80 eyes of 40 healthy control subjects were enrolled in this study. The groups did not differ with

---

1 https://imagej.nih.gov/ij/
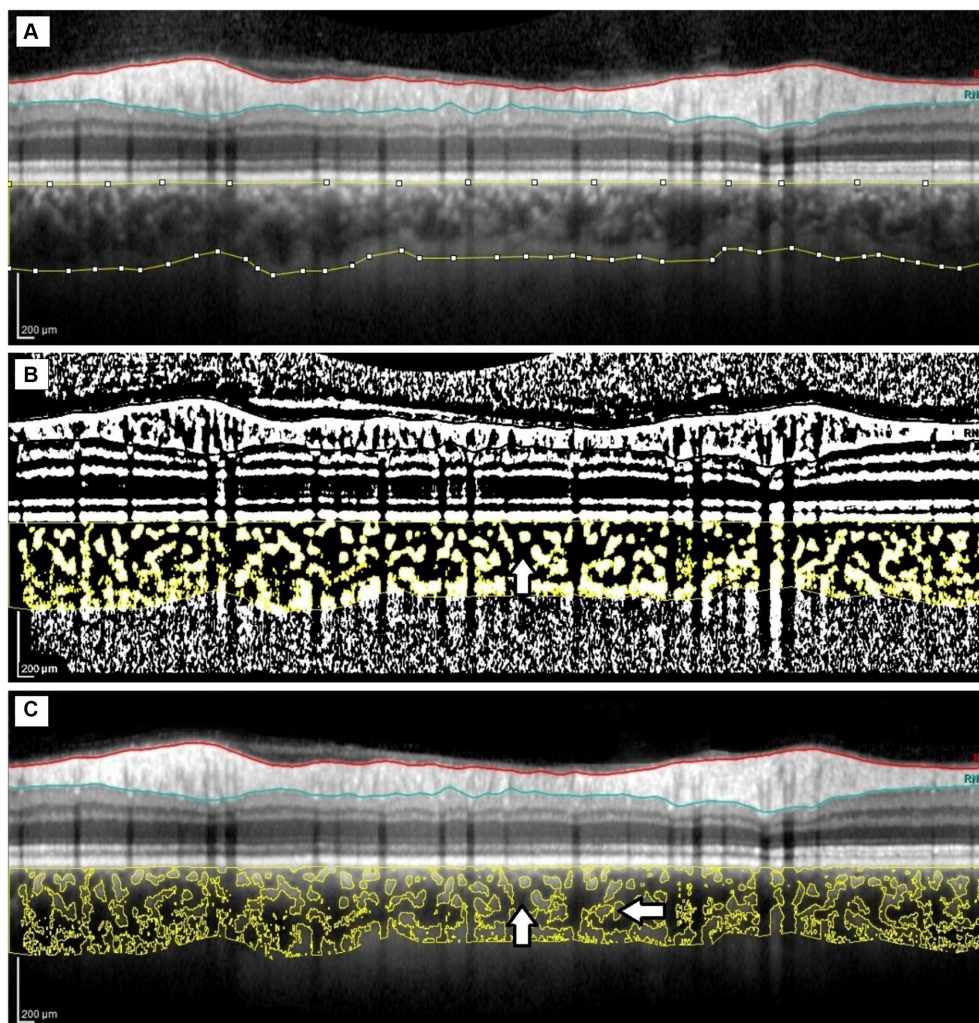
FIGURE 2
Image binarization of the peripapillary choroid. **(A)** Peripapillary total choroidal area marked on the original OCT circular scan. **(B)** Highlighted luminal area (vertical arrow) using the Color Threshold tool. **(C)**. Overlaying the luminal area on the original OCT scan; luminal area (vertical arrow) and stromal area (horizontal arrow).

regard to age, sex, axial length, smoking status, or BCVA; however, differences in mean arterial pressure (MAP) and IOP were found. A total of 22 (66.67%) patients presented with dcSSc and 11 (33.33%) had lcSSc. Similarly, there were no significant differences between the two subtypes in terms of age, sex, AL, smoking status, or BCVA, but significant differences existed in MAP and IOP. Detailed demographic and clinical data are reported in Table 1 (SSc group vs. control group) and Table 2 (control group vs. dcSSc vs. lcSSc).

Table 3 shows the choroidal parameters in detail for the SSc and control eyes. No significant differences were found in the peripapillary choroidal thickness (pCT), RNFL thickness (global and quadrants), peripapillary total choroidal area (pTCA), peripapillary luminal area (pLA), or peripapillary stromal area (pSA) parameters, nor were significant differences found in the aforementioned parameters within the SSc subtype groups ($p > 0.05$ for all). The pCVI was significantly lower in patients with SSc than in healthy control subjects (64.25 ± 1.94 vs. 65.73 ± 2.12, $p < 0.001$), while no significant difference in the pCVI was found between the SSc subgroups, as shown in Table 4.

No correlation between pRNFL G and pCVI or pRNFL G and pCT G was found between the SSc, dcSSc, or lcSSc groups and the controls, as shown in Supplementary Table S1. The univariate regression analyses of the association between pCVI and demographic, clinical, and ocular features are presented in Table 5 (control group) and Table 6 (SSc group). The univariate regression analysis revealed that in patients with SSc, pCVI was significantly associated with age, pTCA, pLA, global pCT, cardiac involvement, and diuretic use ($p < 0.05$ for all), which was not the case in the control group, for whom only pLA was significantly related to pCVI ($p = 0.035$).

Additional analysis of choroidal parameters was performed in SSc patients stratified according to SSc pattern using nailfold capillaroscopy. The pTCA, pLA, and pSA values were significantly higher in patients with "late" SSc patterns than those with "active" SSc patterns upon NFC ($p < 0.05$ for all), and the pCT was significantly thicker (Table 7). The temporal quadrant of pRNFL was significantly thicker in patients with "early" SSc patterns than those with "active" SSc patterns ($p = 0.009$). The groups ("early," "active," and "late" SSc patterns on NFC) did not differ with regard to age, sex, AL, MAP, IOP

TABLE 1 Demographic and clinical characteristics of SSc patients and control group.

Variable	Control group	SSc group	p
Number of patients	40	33	
Number of eyes	80	66	
Age, years, mean ± SD	50.43 ± 10.52	50.97 ± 12.27	0.841[2]
Sex, F, n (%)	22 (55.0)	24 (72.7)	0.188
Sex, M, n (%)	18 (45.0)	9 (27.3)	
MAP, mean ± SD	97.21 ± 12.43	86.47 ± 9.24	**<0.001[2]**
Nicotine, n (%)	6 (15.0)	3 (9.1)	0.484[1]
logMAR, median (Q1;Q3)	0.00 (0.00;0.00)	0.00 (0.00;0.00)	0.686[3]
IOP [mmHg], mean ± SD	15.37 ± 2.13	13.94 ± 3.22	**0.007[2]**
AL, [mm], mean ± SD	23.39 ± 0.97	23.15 ± 0.82	0.104[2]
Duration of the disease [years], median (Q1;Q3)		4.00 (2.00;10.00)	
Pulmonary Involvement, n (%)		22 (66.7)	
Cardiac involvement, n (%)		11 (33.3)	
Joint involvement, n (%)		16 (48.5)	
Digital ulcers (present/history), n%		11 (33.3)	
CRP [mg/L], median		1.45 (1.00;3.43)	
ESR [mm/2 h], median		27.00 (18.00;39.00)	
Anti-Scl70 positive, n (%)		16 (53.3)	
Anti-centromere positive, n (%)		7 (23.3)	
Other Abs positive, n (%)		13 (43.3)	
NFC (active/early/late; number of eyes)		30/18/18	

SSc, systemic sclerosis; F, female; M, male; MAP, mean arterial pressure; IOP, intraocular pressure; AL, axial length; CRP, C-reactive protein; ESR, erythrocyte sedimentation rate; h, hours; Abs, antibodies; NFC, nailfold capillaroscopy. Significant differences were tested using chi-square test or Fisher exact test[1] for nominal variables and with t-test[2] or Mann–Whitney U test[3] for continuous variables, $p < 0.05$ was considered statistically significant (highlighted with bold).

($p = 0.589$, $p = 0.484$, $p = 0.509$, $p = 0.07$, $p = 0.648$, respectively), or organ involvement (joint, pulmonary, and cardiac involvement; $p = 0.895$, $p = 0.669$, $p = 0.585$, respectively); however, a difference in the presence of digital ulcers (history or present) was found between the "active" SSc pattern group and the "late" SSc pattern group ($p = 0.003$).

4. Discussion

With mounting clinical evidence indicating the involvement of the peripapillary choroid in glaucoma (34–38), it has become increasingly important to detect changes in the choroid in patients with a high risk of developing of glaucomatous changes. As we mentioned above, there are no previous reports on peripapillary choroidal thickness in patients with SSc. Several pathophysiological pathways that might be involved in normal-tension GON have been discussed (39). As the blood supply of the prelaminar region partly derives from branches within the peripapillary choroid, the choroid has been implicated in the pathogenesis of GON and many studies have investigated this relationship (40–43). We not only investigated peripapillary choroidal thickness, but also determined the peripapillary choroidal vascularity index (pCVI) to characterize the choroid in detail in SSc patients. This index reflects the vascular content of the choroid. The CVI provides more detailed information about the vascular component of the choroid across all layers,

including the choriocapillaris, Sattler's layer, and Haller's layer. The current literature suggests that the CVI has less variability and is influenced by fewer physiological factors than choroidal thickness; therefore, it can be considered a relatively stable parameter for evaluating changes in choroidal vasculature in several chorioretinal and optic disc diseases, including glaucoma (44). The CVI has been proposed as a potential biomarker for establishing early diagnosis, monitoring disease progression, and prognosticating for these patients (45–47). As other authors have emphasized, CVI should be viewed not as an isolated marker, but as an addition to existing parameters such as CT. Specific data on the choroidal stromal and vascular area should also be analyzed (44). In our study, the pCVI was significantly lower in patients with SSc than in healthy control subjects, and no significant difference in pCVI was found between the SSc subtypes. Interestingly, no significant difference was found in pTCA, pLA, and pSA parameters between the SSc and control groups, nor between the SSc subtypes. However, the mean pTCA and pLA values were lower in the SSc group than in the control group, as were the global and quadrant pCT, but the differences were not statistically significant. No correlations were found between pCT, pCVI, and pRNFL within the two groups. The pSA values were comparable between the SSc and control groups. These differences were less pronounced in the SSc subtype groups. Increases or decreases in CVI may be due to various mechanisms; for example, an increase in CVI could be caused by an increase in the number or diameter of the vascular channels in the choroid. In turn, a decrease in CVI could be the result of attenuation

TABLE 2 Demographic and clinical characteristics of control group and SSc subtypes.

Variable	Control group	dcSSc	lcSSc	p	Post-hoc		
					Control group vs. dcSSc	Control group vs. lcSSc	dcSSc vs. lcSSc
Number of patients	40	22	11				
Number of eyes	80	44	22				
Age, years, mean ± SD	50.43 ± 10.52	51.41 ± 13.92	50.09 ± 8.55	0.933[2]			
Sex, F, n (%)	22 (55.0)	14 (63.6)	10 (90.9)	0.091[1]			
Sex, M, n (%)	18 (45.0)	8 (36.4)	1 (9.1)				
MAP, mean ± SD	97.21 ± 12.43	87.63 ± 10.44	84.13 ± 6.01	**0.001**[2]	**0.009**	**0.005**	0.694
Nicotine, n (%)	6 (15.0)	2 (9,1)	1 (9,1)	0.885[1]			
logMAR, median	0.00	0.00	0.00	0.919[3]			
IOP [mmHg], mean ± SD	15.37 ± 2.13	13.58 ± 3.38	14.76 ± 2.75	**0.005**[2]	**0.003**	0.682	0.294
AL [mm], mean ± SD	23.39 ± 0.97	23.23 ± 0.76	23.00 ± 0.94	0.179[2]			
Duration of the disease [years], median (Q1;Q3)	–	4.00 (2.00;10.00)	5.00 (2.00;10.00)	0.817[3]			
Pulmonary involvement, n (%)	–	18 (81.8)	4 (36.4)	**0.018**[1]			
Cardiac involvement, n (%)	–	8 (36.4)	3 (27.3)	0.709[1]			
Joint involvement, n (%)	–	8 (36.4)	8 (72.7)	0.071			
Digital ulcers (present/history), n (%)	–	9 (40.9)	2 (18.2)	0.259[1]			
Anti-Scl70 positive, n (%)	–	16 (80.0)	0 (0.0)	**<0.001**[1]			
Anti-centromere positive, n (%)	–	2 (10.0)	5 (50.0)	**0.026**[1]			
Other Abs positive, n (%)	–	8 (40.0)	5 (50.0)	0.091[1]			

SSc, systemic sclerosis; dcSSc, diffuse SSc; lcSSc, limited SSc; F, female; M, male; BP, blood pressure; IOP, intraocular pressure; AL, axial length; CRP, C-reactive protein; ESR, erythrocyte sedimentation rate; h, hours; Abs, antibodies. Groups compared with chi-square test or Fisher exact test[1] for nominal variables and with ANOVA[2] or Kruskal-Wallis test[3] for continuous variables. Post hoc tests used: Tukey test for ANOVA, Dunn test for Kruskal-Wallis test, $p < 0.05$ was considered statistically significant (highlighted with bold).

of the choriocapillaris, reduction in choroidal vessel size, or loss of large choroidal vessels (45). Our results suggest that the statistically significant decrease in pCVI in patients with SSc compared to the control group is probably due to a decrease in the vascular layer within the peripapillary area. A thinner choroid (global and quadrant) may support this hypothesis, although the differences were not statistically significant. Choroidal thickness is mainly determined by the thickness of Sattler's and Haller's layers (25). However, it is possible that changes in the vascular components of the peripapillary choroid in SSc patients may mainly result from damage to the choriocapillary layer, where the vessel lumen is smallest. There are two studies evaluating CVI in SSc, and the results are inconsistent; some authors found no significant differences (21), while others showed reduced CVI values, especially in the dSSc group, compared to the control group (27). However, they refer to the macular area. These results should not be directly compared with ours because they analysed a different area. The anatomy (the end-arterial nature of the choroidal vasculature with strictly segmental blood flow and the existence of watershed zones) and function of the choroid are very complex (12).

There is a discrepancy in the literature regarding the association between age and CVI. Agrawal et al. compared the factors affecting SFCT and CVI in healthy subjects and concluded that only SFCT was affected by age (48). In contrast, Kocak et al. demonstrated decreased LA, TCA, and CVI in healthy eyes with increasing age, with no significant differences in SA. The differences were more significant in the group 0–10 years old (49). The above studies refer to the different studied widths of the choroid in the macula. Guduru et al. stated that in healthy subjects, peripapillary CVI significantly increases after the age of 45 years, which introduces even greater ambiguities in the assessment and interpretation of the relationship between CVI and age, especially in the peripapillary area (50). In our study, the regression analysis revealed that in patients with SSc, pCVI was significantly associated with age, but this was not the case in the controls. Through regression analyses of the control group, we were able to identify pLA as a factor related to pCVI. Interestingly, in the SSc group, some variables, such as age, MAP, cardiac involvement, and diuretic use, were related to pCVI values. Consequently, CVI seemed to be more dependent on various factors in patients with SSc than in the controls.

No significant difference was found in pCT (global and quadrants) between the SSc and control groups, nor within the SSc subtypes. This is in contrast to previous reports that found thinner macular choroids in patients with SSc (16–18, 20, 24–26).

Significant differences were found between controls and patients with SSc in terms of MAP and IOP; however, the choroid shows some autoregulatory capacity during changes in ocular perfusion pressure, which depends on diastolic and systolic blood pressure and IOP (51). In another study, no associations were found between pCT and either MAP or IOP in healthy subjects (52) which is consistent with our analysis (Supplementary Table S2). The control group was comprised of ophthalmologically and systemically healthy patients; therefore, these factors seemed to have no impact on the final results.

TABLE 3 Peripapillary choroidal parameters and RNFL thickness comparison between eyes of SSc patients and control group.

Variable	SSc group	Control group	MD	95% CI	p
	Mean ± SD	Mean ± SD			
pTCA (μm^2)	2,403 261.14 ± 689 870.89	2,548 699.87 ± 631 981.03	−145438.73	−367085.20; 76207.75	0.197
pLA (μm^2)	1,549 602.62 ± 464 458.83	1,678 577.18 ± 430 596.33	−128974.56	−278905.43; 20956.31	0.091
pSA (μm^2)	853 658.52 ± 231 250.78	870 122.69 ± 210 444.28	−16464.16	−90569.55; 57641.23	0.661
pCVI (%)	64.25 ± 1.94	65.73 ± 2.12	−1.48	−2.15; −0.80	**<0.001**
pCT G (μm)	191.41 ± 59.49	203.05 ± 54.10	−11.64	−30.43; 7.14	0.223
pCT S (μm)	201.26 ± 61.08	218.24 ± 58.52	−16.98	−36.69; 2.73	0.091
pCT I (μm)	174.00 ± 61.13	177.43 ± 55.03	−3.43	−22.65; 15.80	0.725
pCT T (μm)	199.61 ± 70.71	213.36 ± 56.49	−13.76	−35.04; 7.53	0.203
pCT N (μm)	190.91 ± 56.56	203.44 ± 59.21	−12.53	−31.52; 6.46	0.194
pRNFL G (μm)	103.29 ± 10.69	101.33 ± 6.68	1.96	−1.04; 4.96	0.198
pRNFL S (μm)	126.95 ± 16.84	122.29 ± 10.92	4.67	−0.10; 9.43	0.055
pRNFL I (μm)	129.45 ± 18.85	131.25 ± 13.36	−1.8	−7.26; 3.67	0.517
pRNFL T (μm). median (Q1;Q3)	71.00 (65.00;78.00)	69.50 (63.75;75.25)	1.5	−1.00; 5.00	0.255[1]
pRNFL N (μm)	85.38 ± 16.65	82.10 ± 12.59	3.28	−1.64; 8.20	0.19

SSc, systemic sclerosis; pTCA, peripapillary total choroidal area; pLA, peripapillary luminal area; pSA, peripapillary stromal area; pCVI, peripapillary choroidal vascularity index; pCT, peripapillary choroidal thickness; pRNFL, peripapillary retinal nerve fiber layer; G, global; S, superior quadrant; I, inferior quadrant; T, temporal quadrant; N, nasal quadrant; MD, mean difference and CI, confidence interval. Data presented as mean ± SD, unless otherwise indicated. Groups compared with t-test or Mann–Whitney U test[1]. $p < 0.05$ was considered statistically significant (highlighted with bold).

The SSc and control groups differed significantly with regard to IOP, and further analyses showed that the dcSSc group differed in IOP compared to the control group. IOP was similar within the SSc subtypes and between eyes stratified according to SSc pattern using nailfold capillaroscopy. It seems that this difference did not affect the thickness of the peripapillary choroid. In a study by Huang et al., the average pCT in healthy controls decreased linearly with age, but other factors, such as IOP or MAP, were significantly related to average pCT (52). On the other hand, as patients with dcSSc presented with lower IOP values, one may speculate that this could have a protective effect, compensating for thinner choroids in the context of GON pathogenesis.

The thinning of RNFL as a result of progressive loss of ganglion cell axons is a cardinal feature of GON (53). Few studies have evaluated the structural glaucomatous abnormalities detected by OCT in patients with SSc; those that exist show conflicting results, but indicate that the detected abnormalities suggest SSc to be a major risk factor for the development of glaucomatous changes. Based on swept-source OCT (SS-OCT), Agapito Tito et al. observed a significant decrease in RNFL temporal quadrant thickness in patients with SSc compared to controls, but no differences were found in RNFL thickness and the macular ganglion cell complex (GCC) between the SSc subtypes. There was also an inverse correlation between disease duration and RNFL thickness and GCC. No significant correlations were found between NFC and OCT parameters. However, patients with osteoarthritis were included in the control group (7). In another study, the authors observed a thinner RNFL in the lower quadrant (SD-OCT) only in patients with an excavation/vertical disc ratio of 0.5 when compared with the control group (8). Hekimsoy et al. investigated OCT-A parameters of ONH and

RNFL thickness using SD-OCT in patients with lcSSc. No significant differences were found in peripapillary vessel density and RNFL thickness in lcSSc patients compared with controls (54). This finding is consistent with our results, although dcSSc patients were not enrolled in the above-mentioned study. Our study group was divided into SSc subtypes; no significant difference was found in RNFL thickness between the lcSSc and dcSSc groups and the control group. However, when groups were categorized according to NFC, the temporal quadrant of pRNFL was significantly thicker in patients with an "early" SSc pattern than in those with an "active" pattern. Gomes et al. evaluated the association between capillaroscopy patterns and the presence of glaucoma in patients with SSc, but found no significant differences, although the SSc patterns in that study were classified as mild or severe (11). However, the basis of the glaucoma diagnosis was not specified and the NFC classification differed from our study design. The mechanisms underlying the reduction in temporal RNFL thickness in SSc have not been entirely elucidated, but could be associated with greater susceptibility to vasoconstriction, endothelial damage, or ischemia in this region (7). Due to inconclusive data, further investigations focusing on the relationship between GON and SSc are required to address this issue.

The presence of giant capillaries is characteristic of "early" and "active" scleroderma patterns, while the presence of severely lowered density combined with abnormal shape is typical of "late" scleroderma patterns (30). The loss of capillaries, vascular architectural disorganization, and the presence of ramified/bushy capillaries ("late" SSc pattern) represents the clearest aspect of advanced SSc microvascular damage, regardless of the presence of a limited or diffuse subtype (55).

TABLE 4 Peripapillary choroidal parameters and RNFL thickness comparison between eyes of control group and SSc group stratified according to subtypes.

Variable	dcSSc group Mean ± SD	lcSSc group Mean ± SD	Control group	p	Post-hoc		
					Control group vs. dcSSc	Control group vs. lcSSc	dcSSc vs. lcSSc
pTCA (μm²)	2,425 826.32 ± 726 132.28	2,358 130.79 ± 625 499.99	2,548 699.87 ± 631 981.03	0.397			
pLA (μm²)	1,562 003.21 ± 488 305.14	1,524 801.43 ± 423 040.79	1,678 577.18 ± 430 596.33	0.224			
pSA (μm²)	863 823.11 ± 244 324.83	833 329.36 ± 206 769.39	870 122.69 ± 210 444.28	0.793			
pCVI (%)	64.13 ± 2.07	64.49 ± 1.67	65.73 ± 2.12	**<0.001**	**<0.001**	**0.038**	0.796
pCT G (μm)	195.89 ± 62.81	182.45 ± 52.45	203.05 ± 54.10	0.311			
pCT S (μm)	206.80 ± 63.57	190.18 ± 55.50	218.24 ± 58.52	0.135			
pCT I (μm)	177.50 ± 67.61	167.00 ± 46.12	177.43 ± 55.03	0.739			
pCT T (μm)	207.77 ± 72.92	183.27 ± 64.56	213.36 ± 56.49	0.143			
pCT N (μm)	191.82 ± 57.18	189.09 ± 56.59	203.44 ± 59.21	0.428			
pRNFL G (μm)	103.73 ± 10.46	102.41 ± 11.35	101.33 ± 6.68	0.343			
pRNFL S (μm)	127.45 ± 19.35	125.95 ± 10.46	122.29 ± 10.92	0.125			
pRNFL I (μm)	127.61 ± 20.72	133.14 ± 14.13	131.25 ± 13.36	0.337			
pRNFL T (μm). median (Q1;Q3)	72.50 (65.75;82.25)	70.00 (64.25;72.75)	70.00 (64.25;77.00)	0.128[1]			
pRNFL N (μm)	85.39 ± 16.15	85.36 ± 18.02	82.10 ± 12.59	0.405			

SSc, systemic sclerosis; systemic sclerosis; dcSSc, diffuse SSc; lcSSc, limited SSc; pTCA, peripapillary total choroidal area; pLA, peripapillary luminal area; pSA, peripapillary stromal area; pCVI, peripapillary choroidal vascularity index; pCT, peripapillary choroidal thickness; pRNFL, peripapillary retinal nerve fiber layer; G, global; S, superior quadrant; I, inferior quadrant; T, temporal quadrant; N, nasal quadrant. Data presented as mean ± SD, unless otherwise indicated. Groups compared with ANOVA or Kruskal-Wallis test[1]. *Post hoc* tests used: Tukey test for ANOVA, Dunn test for Kruskal-Wallis test. $p < 0.05$ was considered statistically significant (highlighted with bold).

TABLE 5 Regression analysis testing factors associated with pCVI in the control group.

	β	SE	B	p	R^2	Pseudo R^2
Age, years	0.013	0.025	0.080	0.624	0.007	−0.020
Sex. male	−0.376	0.533	–	0.486	0.013	−0.013
MAP	−0.010	0.024	−0.079	0.658	0.007	−0.027
Nicotine	0.248	0.741	–	0.740	0.003	−0.024
AL [mm]	−0.034	0.277	−0.020	0.903	0.000	−0.027
pTCA	0.000	0.000	0.246	0.126	0.062	0.037
pLA	0.000	0.000	0.335	**0.035**	0.115	0.091
pSA	0.000	0.000	0.061	0.709	0.004	−0.023
pCVI	–	–	–	–	–	–
pCT Global	0.006	0.005	0.204	0.206	0.043	0.017
pRNFL Global	−0.030	0.041	−0.127	0.436	0.016	−0.010

MAP, mean arterial pressure; AL, axial length, pTCA, peripapillary total choroidal area; pLA, peripapillary luminal area; pSA, peripapillary stromal area; pCVI, peripapillary choroidal vascularity index; pCT, peripapillary choroidal thickness; pRNFL, peripapillary retinal nerve fiber layer; G, global; β, beta coefficient; SE, standard error; B, standardised beta. Only one eye per patient included into the analysis (eyes with better quality of OCT images selected). $p < 0.05$ highlighted with bold.

Sub-analysis of scleroderma patients stratified according to NFC pattern showed interesting results. Statistically significant differences in pTCA, pLA, pSA, and pCT were observed. The higher values for TCA, LA, and SA, and a thicker peripapillary choroid (except for the nasal quadrant) in patients with a "late" capillaroscopy SSc pattern compared to those with an "active" SSc pattern were surprising. No

TABLE 6 Regression analysis testing factors associated with pCVI in SSc group.

	β	SE	B	p	R²	Pseudo R²
Age, years	−0.053	0.024	−0.367	**0.026**	0.134	0.106
Sex. male	0.291	0.705	–	0.683	0.005	−0.027
Nicotine	−0.743	1.087	–	0.500	0.015	−0.017
AL [mm]	−0.573	0.380	−0.261	0.142	0.068	0.038
MAP	−0.092	0.033	−0.477	**0.011**	0.208	0.179
pTCA	0.000	0.000	0.395	**0.023**	0.156	0.129
pLA	0.000	0.000	0.464	**0.006**	0.216	0.190
pSA	0.000	0.000	0.252	0.158	0.063	0.033
pCVI	–	–	–	–	–	–
pCT Global	0.012	0.005	0.412	**0.017**	0.169	0.143
pRNFL Global	0.012	0.031	0.072	0.700	0.005	−0.028
dcSSc/lcSSc. IcSSc	0.469	0.663	–	0.484	0.016	−0.016
NFC active = baseline						
Early	−0.384	0.766	–	0.620	0.023	−0.042
Late	−0.629	0.766	–	0.418		
Duration of the disease [years]	0.008	0.043	0.033	0.854	0.001	−0.031
ESR [mm/2 h]	0.008	0.025	0.058	0.759	0.004	−0.033
CRP [mg/L]	0.042	0.155	0.050	0.786	0.003	−0.034
Anti-Scl70 positive	−0.099	0.683	–	0.886	0.001	−0.035
Ant-centromere positive	−0.206	0.805	–	0.800	0.002	−0.033
Other Abs positive	0.515	0.681	–	0.456	0.020	−0.015
Joint involvement	0.337	0.627	–	0.596	0.009	−0.023
Pulmonary involvement	−0.209	0.667	–	0.757	0.003	−0.029
Cardiac involvement	−1.448	0.615	–	**0.025**	0.152	0.124
Digital ulcers (present/history)	0.093	0.668	–	0.890	0.001	−0.032
PDE inhibitors	−0.089	0.629	–	0.888	0.001	−0.032
Ca-blocker	0.767	0.694	–	0.284	0.037	0.006
Hydroxychoroquine	0.093	0.769	–	0.905	0.000	−0.032
Steroids	0.715	0.624	–	0.261	0.041	0.009
Diuretic	−1.320	0.643	–	**0.048**	0.120	0.092

MAP, mean arterial pressure; AL, axial length, pTCA, peripapillary total choroidal area; pLA, peripapillary luminal area; pSA, peripapillary stromal area; pCVI, peripapillary choroidal vascularity index; pCT, peripapillary choroidal thickness; pRNFL, peripapillary retinal nerve fiber layer; G, global; SSc, systemic sclerosis; dcSSc, diffuse SSc; lcSSc, limited SSc, CRP, C-reactive protein; ESR, erythrocyte sedimentation rate; h, hours; Abs, antibodies; PDE, phosphodiesterase; β, coefficient from the regression model; SE, standard error. $p < 0.05$ highlighted with bold. Only one eye per patient included into the analysis (eyes with better quality of OCT images selected).

significant difference in pCVI was found between "early," "active," and "late" SSc pattern groups. Due to the small number of patients in each group, this issue requires further investigation. Shenavandeh et al. assessed retinal vascular changes in SSc patients, but found no evidence of a relationship between retinal vascular changes seen on fundus photography and SSc patterns upon NFC (56). However, this cannot be related to our study due to the functional and structural heterogeneity of retinal and choroidal circulation (57, 58).

There is a discrepancy between peripapillary choroidal thickness found in our study and studies by Fard et al. (59) and Huang et al. (52). Choroidal thickness measurements can vary significantly using three different definitions of the choroidal-scleral junction as posterior boundaries (60). In our study, choroidal thickness measurements were based on the identification of the outer border of the choroid stroma (Figure 1) which was also clearly seen after binarization of the images

(Figure 2). Vuong et al. showed that this measurement method was more reproducible than the other methods (60).

The limitations of the present study, which must be taken into account when interpreting the results, are the relatively small number of patients due to the rarity of the disease. A technical limitation is the possibility of erroneously high CVI measurements due to shadowing of the large superficial retinal vessels on circle peripapillary OCT scans, but this would apply to all studied subjects. The study was conducted during the COVID-19 pandemic, causing the study period to be shortened, as scheduled hospital admissions were reduced. Additionally, except for three patients with SSc and preperimetric glaucoma, no patients with both SSc and more advanced glaucoma were included in the study. Such a group could potentially present more severe damage of the choroid. Although our study provides insight into the pathophysiology of the choroid in patients with systemic sclerosis,

TABLE 7 Comparison of peripapillary choroidal parameters and RNFL thickness between eyes stratified according to SSc pattern on nailfold capillaroscopy.

Variable	"Early" SSc pattern	"Active" SSc pattern	"Late" SSc pattern	p	Post hoc		
					Active vs. Early	Active vs. Late	Early vs. Late
pTCA (μm²)	2,316 186.00±707 103.21	2,238 800.32±542 810.82	2,766 335.00±787 284.69	**0.034**	0.921	**0.032**	0.119
pLA (μm²)	1,491 862.06±486 531.23	1,445 338.93±371 376.74	1,782 468.12±520 849.43	**0.048**	0.937	**0.046**	0.143
pSA (μm²)	824 323.94±226 247.40	793 461.39±177 865.52	983 866.88±272 261.92	**0.020**	0.888	**0.018**	0.090
pCVI (%)	63.99±2.17	64.38±1.94	64.31±1.78	0.796			
pCT G (μm)	181.72±62.76	176.47±44.21	226.00±67.07	**0.012**	0.948	**0.012**	0.055
pCT S (μm)	185.00±64.67	190.27±44.22	235.83±70.64	**0.016**	0.950	**0.028**	**0.029**
pCT I (μm)	171.44±61.40	154.10±44.78	209.72±70.98	**0.007**	0.572	**0.005**	0.121
pCT T (μm)	189.78±76.03	180.93±53.74	240.56±76.91	**0.012**	0.898	**0.011**	0.669
pCT N (μm)	180.94±59.74	180.43±48.94	218.33±59.02	0.052			
pRNFL G (μm)	105.50±9.80	102.03±12.04	103.17±9.28	0.560			
pRNFL S (μm)	128.83±12.94	125.43±21.12	127.61±12.13	0.785			
pRNFL I (μm)	131.61±13.37	129.63±20.04	127.00±21.98	0.768			
pRNFL T (μm), median (Q1;Q3)	74.50 (70.25;79.50)	69.00 (61.25;72.00)	71.50 (68.25;79.00)	**0.046**[1]	**0.009**	0.058	0.237
pRNFL N (μm)	85.89±18.26	85.17±17.57	85.22±14.14	0.989			

SSc, systemic sclerosis; pTCA, peripapillary total choroidal area; pLA, peripapillary luminal area; pSA, peripapillary stromal area; pCVI, peripapillary choroidal vascularity index; pCT, peripapillary choroidal thickness; pRNFL, peripapillary retinal nerve fiber layer; G, global; S, superior quadrant; I, inferior quadrant; T, temporal quadrant; N, nasal quadrant. Data presented as mean ± SD, unless otherwise indicated Groups compared with ANOVA or Kruskal-Wallis test[1]. *Post hoc* tests used: Tukey test for ANOVA, Dunn test for Kruskal-Wallis test. $p < 0.05$ was considered statistically significant (highlighted with bold).

longitudinal observation would facilitate future studies by documenting pRNFL changes over time and the possible development of GON in patients with SSc. Inclusion of not only RNFL, but also ganglion cell complexes [as a more sensitive parameter for risk/occurrence of glaucoma (61)] in the analysis could also be informative.

In conclusion, our cohort of patients with SSc presented alterations of choroidal characteristics. The differences were variable depending on the approach to patient stratification. A decrease in pCVI in patients with SSc compared to the control group reflects a decrease in the vascular layer within the peripapillary area, which would support the vascular hypothesis for an increased risk of GON in patients with SSc.

Data availability statement

The original contributions presented in the study are included in the article/Supplementary material, further inquiries can be directed to the corresponding authors.

Ethics statement

The studies involving humans were approved by Medical University of Białystok. The studies were conducted in accordance with the local legislation and institutional requirements. The participants provided their written informed consent to participate in this study.

Author contributions

BP: Conceptualization, Data curation, Formal analysis, Investigation, Methodology, Visualization, Writing – original draft. EG-S: Data curation, Investigation, Supervision, Writing – review & editing. IZ: Investigation, Writing – original draft. MB: Investigation, Writing – original draft. JD: Investigation, Writing – original draft. PS: Investigation, Methodology, Writing – original draft. OK-B: Project administration, Supervision, Writing – review & editing. JK: Project administration, Supervision, Writing – review & editing. DD: Conceptualization, Formal analysis, Funding acquisition, Investigation, Methodology, Project administration, Supervision, Writing – review & editing.

Funding

Conflict of interest

The authors declare that the research was conducted in the absence of any commercial or financial relationships that could be construed as a potential conflict of interest.

Publisher's note

All claims expressed in this article are solely those of the authors and do not necessarily represent those of their affiliated organizations, or those of the publisher, the editors and the reviewers. Any product that may be evaluated in this article, or claim that may be made by its manufacturer, is not guaranteed or endorsed by the publisher.

Supplementary material

The Supplementary material for this article can be found online at: https://www.frontiersin.org/articles/10.3389/fmed.2023.1273438/full#supplementary-material

References

1. Denton CP, Khanna D. Systemic sclerosis. *Lancet*. (2017) 390:1685–99. doi: 10.1016/S0140-6736(17)30933-9

2. Cutolo M, Soldano S, Smith V. Pathophysiology of systemic sclerosis: current understanding and new insights. *Expert Rev Clin Immunol*. (2019) 15:753–64. doi: 10.1080/1744666X.2019.1614915

3. Pearson DR, Werth VP, Pappas-Taffer L. Systemic sclerosis: current concepts of skin and systemic manifestations. *Clin Dermatol*. (2018) 36:459–74. doi: 10.1016/j.clindermatol.2018.04.004

4. Kreps EO, Carton C, Cutolo M, Cutolo CA, Vanhaecke A, Leroy BP, et al. Ocular involvement in systemic sclerosis: a systematic literature review, it's not all scleroderma that meets the eye. *Semin Arthritis Rheum*. (2019) 49:119–25. doi: 10.1016/j.semarthrit.2018.12.007

5. Kozikowska M, Luboń W, Kucharz EJ, Mrukwa-Kominek E. Ocular manifestations in patients with systemic sclerosis. *Reumatologia*. (2020) 58:401–6. doi: 10.5114/reum.2020.102004

6. Szucs G, Szekanecz Z, Aszalos Z, Gesztelyi R, Zsuga J, Szodoray P, et al. A wide spectrum of ocular manifestations signify patients with systemic sclerosis. *Ocul Immunol Inflamm*. (2021) 29:81–9. doi: 10.1080/09273948.2019.1657467

7. Agapito Tito CV, Silvatti J, de Almeida INF, Taniguchi EV, Prata TS, Paranhos A Jr, et al. Structural abnormalities associated with glaucoma using swept-source optical coherence tomography in patients with systemic sclerosis. *Int Ophthalmol*. (2022) 42:1369–80. doi: 10.1007/s10792-021-02124-1

8. Sahin-Atik S, Koc F, Akin-Sari S, Ozmen M. Retinal nerve fiber and optic disc morphology using spectral-domain optical coherence tomography in scleroderma patients. *Eur J Ophthalmol*. (2017) 27:281–4. doi: 10.5301/ejo.5000827

9. Allanore Y, Parc C, Monnet D, Brézin AP, Kahan A. Increased prevalence of ocular glaucomatous abnormalities in systemic sclerosis. *Ann Rheum Dis*. (2004) 63:1276–8. doi: 10.1136/ard.2003.013540

10. Kitsos G, Tsifetaki N, Gorezis S, Drosos AA. Glaucomatous type abnormalities in patients with systemic sclerosis. *Clin Exp Rheumatol*. (2007) 25:341.

11. Gomes BF, Souza R, Valadão T, Kara-Junior N, Moraes HV, Santhiago MR. Is there an association between glaucoma and capillaroscopy in patients with systemic sclerosis? *Int Ophthalmol*. (2018) 38:251–6. doi: 10.1007/s10792-017-0454-1

12. Hayreh SS. In vivo choroidal circulation and its watershed zones. *Eye (Lond)*. (1990) 4:273–89. doi: 10.1038/eye.1990.39

13. Farkas TG, Sylvester V, Archer D. The choroidopathy of progressive systemic sclerosis (scleroderma). *Am J Ophthalmol*. (1972) 74:875–86. doi: 10.1016/0002-9394(72)91208-1

14. Steiner M, Esteban-Ortega MDM, Muñoz-Fernández S. Choroidal and retinal thickness in systemic autoimmune and inflammatory diseases: a review. *Surv Ophthalmol*. (2019) 64:757–69. doi: 10.1016/j.survophthal.2019.04.007

15. Serup L, Serup J, Hagdrup H. Fundus fluorescein angiography in generalized scleroderma. *Ophthalmic Res*. (1987) 19:303–8. doi: 10.1159/000265512

16. Ingegnoli F, Gualtierotti R, Pierro L, Del Turco C, Miserocchi E, Schioppo T, et al. Choroidal impairment and macular thinning in patients with systemic sclerosis: the acute study. *Microvasc Res*. (2015) 97:31–6. doi: 10.1016/j.mvr.2014.08.008

17. Coşkun E, Zengin O, Kenan S, Kimyon G, Erdogan Er K, Okumus S, et al. Evaluation of choroidal thickness in patients with scleroderma. *Eye (Lond)*. (2016) 30:588–92. doi: 10.1038/eye.2015.287

18. Esen E, Tas DA, Sizmaz S, Turk I, Unal I, Demircan N. Evaluating choroidal characteristics in systemic sclerosis using enhanced depth imaging optical coherence tomography. *Ocul Immunol Inflamm*. (2017) 25:356–62. doi: 10.3109/09273948.2015.1129424

19. Aydin E, Atik S, Koc F, Balikoglu-Yilmaz M, Akin Sari S, Ozmen M, et al. Choroidal and central foveal thickness in patients with scleroderma and its systemic associations. *Clin Exp Optom*. (2017) 100:656–62. doi: 10.1111/cxo.12498

20. Kaymaz S, Halil Y, Kaya H, Karasu U, Cobankara V. The relationship of ocular parameters with clinical parameters and disease-related quality of life in patients with systemic sclerosis: a cross-sectional study. *Int J Rheum Dis*. (2021) 24:1308–16. doi: 10.1111/1756-185X.14216

21. Carnevali A, Giannaccare G, Gatti V, Battaglia C, Randazzo G, Yu AC, et al. Retinal microcirculation abnormalities in patients with systemic sclerosis: an explorative optical coherence tomography angiography study. *Rheumatology (Oxford)*. (2021) 60:5827–32. doi: 10.1093/rheumatology/keab258

22. Ranjbar M, Rothe M, Klapa S, Lange T, Prasuhn M, Grisanti S, et al. Evaluation of choroidal substructure perfusion in patients affected by systemic sclerosis: an optical coherence tomography angiography study. *Scand J Rheumatol*. (2020) 49:141–5. doi: 10.1080/03009742.2019.1641616

23. Küçük MF, Yaprak L, Erol MK, Ayan A, Kök M. Evaluations of the radial peripapillary, macular and choriocapillaris microvasculature using optical coherence tomography angiography in patients with systemic sclerosis. *J Fr Ophthalmol*. (2022) 45:81–92. doi: 10.1016/j.jfo.2021.06.009

24. Kılınç Hekimsoy H, Şekeroğlu MA, Koçer AM, Akdoğan A. Analysis of retinal and choroidal microvasculature in systemic sclerosis: an optical coherence tomography angiography study. *Eye (Lond)*. (2020) 34:763–70. doi: 10.1038/s41433-019-0591-z

25. Rommel F, Prangel D, Prasuhn M, Grisanti S, Ranjbar M. Correlation of retinal and choroidal microvascular impairment in systemic sclerosis. *Orphanet J Rare Dis*. (2021) 16:27. doi: 10.1186/s13023-020-01649-5

26. Kök M, Ayan A, Fatih Küçük M, Erol MK, Yaprak L. Evaluation of the direct effects on retinal and choroidal microvascularity of systemic scleroderma. *Microvasc Res*. (2021) 136:104166. doi: 10.1016/j.mvr.2021.104166

27. Ataş F, Kaya M, Ayhan Z, Ozkan O, Birlik M. Evaluation of choroidal vascularity index in systemic sclerosis patients. *Photodiagn Photodyn Ther*. (2023) 41:103297. doi: 10.1016/j.pdpdt.2023.103297

28. van den Hoogen F, Khanna D, Fransen J, Johnson SR, Baron M, Tyndall A, et al. 2013 classification criteria for systemic sclerosis: an American College of Rheumatology/European League against Rheumatism collaborative initiative. *Ann Rheum Dis*. (2013) 72:1747–55. doi: 10.1136/annrheumdis-2013-204424

29. Deshpande G, Gupta R, Bawankule P, Raje D, Chakarborty M. Structural evaluation of preperimetric and perimetric glaucoma. *Indian J Ophthalmol*. (2019) 67:1843–9. doi: 10.4103/ijo.IJO_1955_18

30. Smith V, Herrick AL, Ingegnoli F, Damjanov N, De Angelis R, Denton CP, et al. Standardisation of nailfold capillaroscopy for the assessment of patients with Raynaud's phenomenon and systemic sclerosis. *Autoimmun Rev*. (2020) 19:102458. doi: 10.1016/j.autrev.2020.102458

31. Sonoda S, Sakamoto T, Yamashita T, Shirasawa M, Uchino E, Terasaki H, et al. Choroidal structure in normal eyes and after photodynamic therapy determined by binarization of optical coherence tomographic images. *Invest Ophthalmol Vis Sci*. (2014) 55:3893–9. doi: 10.1167/iovs.14-14447

32. Sigal IA, Schuman JS, Ishikawa H, Kagemann L, Wollstein G. A problem of proportions in OCT-based morphometry and a proposed solution. *Invest Ophthalmol Vis Sci*. (2016) 57:484–5. doi: 10.1167/iovs.15-18570

33. Agrawal R, Salman M, Tan KA, Karampelas M, Sim DA, Keane PA, et al. Choroidal Vascularity Index (CVI) – a novel optical coherence tomography parameter for monitoring patients with panuveitis? *PLoS One*. (2016) 11:e0146344. doi: 10.1371/journal.pone.0146344

34. Zhang Z, Yu M, Wang F, Dai Y, Wu Z. Choroidal thickness and open-angle glaucoma: a meta-analysis and systematic review. *J Glaucoma*. (2016) 25:e446–54. doi: 10.1097/IJG.0000000000000275

35. Hirooka K, Tenkumo K, Fujiwara A, Baba T, Sato S, Shiraga F. Evaluation of peripapillary choroidal thickness in patients with normal-tension glaucoma. *BMC Ophthalmol*. (2012) 12:29. doi: 10.1186/1471-2415-12-29

36. Park JH, Yoo C, Kim YY. Peripapillary choroidal thickness in untreated normal-tension glaucoma eyes with a single-hemifield retinal nerve fiber layer defect. *Medicine (Baltimore).* (2018) 97:e11001. doi: 10.1097/MD.0000000000011001

37. Lin Z, Huang S, Huang P, Guo L, Shen X, Zhong Y. The diagnostic use of choroidal thickness analysis and its correlation with visual field indices in glaucoma using spectral domain optical coherence tomography. *PLoS One.* (2017) 12:e0189376. doi: 10.1371/journal.pone.0189376

38. Pablo LE, Cameo B, Bambo MP, Polo V, Larrosa JM, Fuertes MI, et al. Peripapillary choroidal thickness analysis using swept-source optical coherence tomography in glaucoma patients: a broader approach. *Ophthalmic Res.* (2018) 59:7–13. doi: 10.1159/000479877

39. Killer HE, Pircher A. Normal tension glaucoma: review of current understanding and mechanisms of the pathogenesis. *Eye (Lond).* (2018) 32:924–30. doi: 10.1038/s41433-018-0042-2

40. Wang W, Zhang X. Choroidal thickness and primary open-angle glaucoma: a cross-sectional study and meta-analysis. *Invest Ophthalmol Vis Sci.* (2014) 55:6007–14. doi: 10.1167/iovs.14-14996

41. Song YJ, Kim YK, Jeoung JW, Park KH. Assessment of open-angle glaucoma peripapillary and macular choroidal thickness using swept-source optical coherence tomography (SS-OCT). *PLoS One.* (2016) 11:e0157333. doi: 10.1371/journal.pone.0157333

42. Song YJ, Kim YK, Jeoung JW, Park KH. Assessment of peripapillary choroidal thickness in primary open-angle glaucoma patients with choroidal vascular prominence. *Jpn J Ophthalmol.* (2017) 61:448–56. doi: 10.1007/s10384-017-0535-8

43. Hayreh SS. Blood flow in the optic nerve head and factors that may influence it. *Prog Retin Eye Res.* (2001) 20:595–624. doi: 10.1016/S1350-9462(01)00005-2

44. Iovino C, Pellegrini M, Bernabei F, Borrelli E, Sacconi R, Govetto A, et al. Choroidal vascularity index: an in-depth analysis of this novel optical coherence tomography parameter. *J Clin Med.* (2020) 9:595. doi: 10.3390/jcm9020595

45. Agrawal R, Ding J, Sen P, Rousselot A, Chan A, Nivison-Smith L, et al. Exploring choroidal angioarchitecture in health and disease using choroidal vascularity index. *Prog Retin Eye Res.* (2020) 77:100829. doi: 10.1016/j.preteyeres.2020.100829

46. Dmuchowska DA, Sidorczuk P, Pieklarz B, Konopińska J, Mariak Z, Obuchowska I. Quantitative assessment of choroidal parameters in patients with various types of diabetic macular oedema: a single-centre cross-sectional analysis. *Biology (Basel).* (2021) 10:725. doi: 10.3390/biology10080725

47. Sidorczuk P, Pieklarz B, Konopinska J, Saeed E, Mariak Z, Dmuchowska D. Foveal avascular zone does not correspond to choroidal characteristics in patients with diabetic retinopathy: a single-center cross-sectional analysis. *Diabetes Metab Syndr Obes.* (2021) 14:2893–903. doi: 10.2147/DMSO.S318860

48. Agrawal R, Gupta P, Tan KA, Cheung CM, Wong TY, Cheng CY. Choroidal vascularity index as a measure of vascular status of the choroid: measurements in healthy eyes from a population-based study. *Sci Rep.* (2016) 6:21090. doi: 10.1038/srep21090

49. Koçak N, Subaşı M, Yeter V. Effects of age and binarising area on choroidal vascularity index in healthy eyes: an optical coherence tomography study. *Int Ophthalmol.* (2021) 41:825–34. doi: 10.1007/s10792-020-01636-6

50. Guduru A, Rasheed MA, Goud A, Vupparaboina KK, Agrawal R, Lupidi M. Peripapillary choroidal vascularity quantification and characterization in healthy individuals. *Nepal J Ophthalmol.* (2020) 12:48–55. doi: 10.3126/nepjoph.v12i1.25188

51. Polska E, Simader C, Weigert G, Doelemeyer A, Kolodjaschna J, Scharmann O, et al. Regulation of choroidal blood flow during combined changes in intraocular pressure and arterial blood pressure. *Invest Ophthalmol Vis Sci.* (2007) 48:3768–74. doi: 10.1167/iovs.07-0307

52. Huang W, Wang W, Zhou M, Chen S, Gao X, Fan Q, et al. Peripapillary choroidal thickness in healthy Chinese subjects. *BMC Ophthalmol.* (2013) 13:23. doi: 10.1186/1471-2415-13-23

53. Lin PW, Chang HW, Lin JP, Lai IC. Analysis of peripapillary retinal nerve fiber layer and inner macular layers by spectral-domain optical coherence tomography for detection of early glaucoma. *Int J Ophthalmol.* (2018) 11:1163–72. doi: 10.18240/ijo.2018.07.15

54. Kılınç Hekimsoy H, Şekeroğlu AM, Koçer AM, Hekimsoy V, Akdoğan A. Evaluation of the optic nerve head vessel density in patients with limited scleroderma. *Ther Adv Ophthalmol.* (2021) 13:251584142199538. doi: 10.1177/2515841421995387

55. Cutolo M, Sulli A, Pizzorni C, Accardo S. Nailfold videocapillaroscopy assessment of microvascular damage in systemic sclerosis. *J Rheumatol.* (2000) 27:155–60.

56. Shenavandeh S, Afarid M, Hasanaghaei T, Nazarinia MA. Prevalence of retinal changes in patients with systemic sclerosis: the association between retinal vascular changes and nailfold capillaroscopic findings. *Reumatologia.* (2021) 59:27–34. doi: 10.5114/reum.2021.103436

57. Yu DY, Yu PK, Cringle SJ, Kang MH, Su EN. Functional and morphological characteristics of the retinal and choroidal vasculature. *Prog Retin Eye Res.* (2014) 40:53–93. doi: 10.1016/j.preteyeres.2014.02.001

58. Delaey C, Van De Voorde J. Regulatory mechanisms in the retinal and choroidal circulation. *Ophthalmic Res.* (2000) 32:249–56. doi: 10.1159/000055622

59. Fard MA, Abdi P, Kasaei A, Soltani Mogaddam R, Afzali M, Moghimi S. Peripapillary choroidal thickness in nonarteritic anterior ischemic optic neuropathy. *Invest Ophthalmol Vis Sci.* (2015) 56:3027–33. doi: 10.1167/iovs.14-15661

60. Vuong VS, Moisseiev E, Cunefare D, Farsiu S, Moshiri A, Yiu G. Repeatability of choroidal thickness measurements on enhanced depth imaging optical coherence tomography using different posterior boundaries. *Am J Ophthalmol.* (2016) 169:104–12. doi: 10.1016/j.ajo.2016.06.023

61. Vidas S, Popović-Suić S, Novak Lauš K, Jandroković S, Tomić M, Jukić T, et al. Analysis of ganglion cell complex and retinal nerve Fiber layer thickness in Glaucoma diagnosis. *Acta Clin Croat.* (2017) 56:382–90. doi: 10.20471/acc.2017.56.03.04

Check for updates

*CORRESPONDENCE
Yuping Zheng
✉ zheng-tei@163.com
Jinying Li
✉ ljyszbdyy@163.com

†These authors have contributed equally to this work

Changes in foveal avascular zone area and retinal vein diameter in patients with retinal vein occlusion detected by fundus fluorescein angiography

Dingying Liao[1], Zixia Zhou[1], Fei Wang[1], Bin Zhang[1], Yanfen Wang[2], Yuping Zheng[2]*† and Jinying Li[1]*†

[1]Department of Ophthalmology, Shenzhen Hospital, Peking University, Shenzhen, China, [2]Department of Ophthalmology, Second Affiliated Hospital, Xi'an Jiaotong University, Xi'an, China

Purpose: To investigate changes in foveal avascular area (FAZ) and retinal vein diameter in patients with retinal vein occlusion (RVO) after intravitreal ranibizumab, and to analyze the correlation between ranibizumab therapy and visual gain.

Methods: This retrospective study enrolled 95 eyes of 95 patients who had accepted three consecutive monthly ranibizumab injections, including 50 branch RVOs (BRVOs) and 45 central RVOs (CRVOs). BRVOs were divided into ischemia group ($n = 32$) and non-ischemia group ($n = 18$), and CRVOs also had ischemia group ($n = 28$) and non-ischemia group ($n = 17$). Comprehensive ophthalmic examinations were performed before the first injection and after 6, 12, and 24 months. The FAZ was manually circumscribed on early-phase images of fundus fluorescein angiography. Retinal vein diameters were measured on fundus photographs.

Results: After three injections, the FAZ area was significantly enlarged firstly and then reduced in all ischemic RVOs and the non-ischemic BRVOs ($p < 0.05$), while the retinal vein diameter was significantly reduced firstly and then increased in all groups except for unobstructed branch veins of non-ischemic BRVOs ($p < 0.05$). The correlation between the FAZ area and best corrected visual acuity was statistically significant in all CRVOs (non-ischemic, $r = 0.372$; ischemic, $r = 0.286$; $p < 0.01$) and ischemic BRVOs ($r = 0.180$, $p < 0.05$). Spearman's correlation analysis revealed that the retinal vein diameter was significantly correlated to the larger FAZ area in obstructed branch veins of ischemic BRVOs ($r = -0.31$, $p < 0.01$), inferior temporal branch veins of non-ischemic CRVOs ($r = -0.461$, $p < 0.01$) and ischemia CRVO groups (superior temporal branch vein, $r = -0.226$, $p < 0.05$; inferior temporal branch vein, $r = -0.259$, $p < 0.01$).

Conclusion: After three consecutive monthly ranibizumab injections, the FAZ area was enlarged and retinal vein diameter reduced with gradual recovery to near baseline from 12 months. These results suggest that ranibizumab therapy can worsen macular ischemia and prevent visual gain in the short term. It has important significance for the treatment and prognosis of RVO, although the natural course of RVO may also affect ischemia and visual gain.

1. Introduction

Retinal vein occlusion (RVO) is a prevalent retinal vascular disorder, ranking second after diabetic retinopathy (1). Its incidence rises with age, affecting predominantly elderly individuals, with an estimated global prevalence of over 16 million people (2). RVO encompasses two main types: branch retinal vein occlusion (BRVO) and central retinal vein occlusion (CRVO). Common risk factors associated with RVO include diabetes, hypertension, dyslipidemia, and smoking. The condition manifests through retinal ischemia, vascular tortuosity, retinal hemorrhage, and macular edema due to obstruction of retinal veins at arteriovenous crossings (3).

Fundus fluorescein angiography (FFA) has long been established as the gold standard diagnostic tool for evaluating retinal vascular diseases, including RVO (4). This technique involves the intravenous injection of fluorescein dye, followed by capturing sequential images of the dye's circulation within the retinal vessels using a specialized camera (5). By analyzing the dynamics of the dye's distribution, FFA provides valuable information about the perfusion status, presence of vascular abnormalities, and alterations in the foveal avascular zone (FAZ) associated with RVO (6, 7).

The evaluation of RVO using FFA enables clinicians to visualize and assess the extent of retinal vascular involvement (8). The presence of venous obstruction, areas of non-perfusion, capillary leakage, and neovascularization can be detected, aiding in the accurate diagnosis and classification of RVO (9). Additionally, FFA allows for the precise assessment of FAZ alterations, which play a crucial role in determining visual outcomes in patients with retinal vascular diseases (10).

Through FFA, clinicians can analyze the FAZ area, which represents the central region of the retina devoid of blood vessels. Changes in FAZ area, such as enlargement or irregularity, have been associated with the severity and prognosis of RVO (11–13). These alterations can reflect the extent of retinal ischemia and provide insights into the functional impairment experienced by patients.

The combination of FFA with advanced image analysis techniques allows for a more comprehensive evaluation of RVO. Image analysis algorithms can provide quantitative measurements and objective assessments of FAZ area and other vascular parameters, reducing subjectivity and potential diagnostic errors associated with manual interpretation (14). This integration enhances the accuracy and reliability of RVO diagnosis and monitoring.

In this study, we aim to evaluate FAZ area and retinal vein diameter changes in eyes with RVO after ranibizumab therapy. We will utilize the gold standard FFA technique to assess the perfusion status, vascular abnormalities, and alterations in the FAZ. Incorporating advanced image analysis algorithms will enable us to obtain objective and quantitative measurements of these parameters. By investigating the correlations between FAZ area, retinal vein diameter, and best-corrected visual acuity (BCVA) following intravitreal ranibizumab treatment, we can gain a better understanding of the effects of anti-VEGF therapy on retinal vascular and structural parameters and their relationship with visual outcomes in RVO patients.

2. Materials and methods

2.1. Study population and design

In this retrospective, observational, and consecutive series study, 235 patients with RVO who visited the Ophthalmology Department of the Second Affiliated Hospital of Xi'an Jiaotong University (Shaanxi, China) were enrolled from August 2020 to September 2022. This study ultimately included 50 eyes of 50 patients with BRVO and 45 eyes of 45 patients with CRVO that were treated with ranibizumab (Lucentis; Genentech, San Francisco, CA, United States) by three consecutive intravitreal injection. These patients have received 6–8 injections (3 consecutive and 3–5 PRN treatments) within 24 months, with the decision for PRN treatments based on the degree of macular edema observed via OCT. In CRVO patients, an FFA result indicating a total area of non-perfusion in retinal capillaries greater than 10 DA (disc area) is classified as ischemic, while less than or equal to 10 DA is classified as non-ischemic. For BRVO patients, an FFA result demonstrating a total area of non-perfusion in retinal capillaries greater than 5 DA is considered ischemic, whereas less than or equal to 5 DA is categorized as non-ischemic. The 50 BRVOs were divided into an ischemia group ($n = 32$) and a non-ischemia group ($n = 18$). The 45 CRVOs were also divided into an ischemia group ($n = 28$) and a non-ischemia group ($n = 17$). These 95 patients accepted injections monthly for three consecutive months. All patients signed an informed consent form. This study procedure adhered to the tenets of the Declaration of Helsinki.

Demographic data and clinical records of systemic diseases, medical and ophthalmic histories were obtained from all patients. Each patient underwent comprehensive ophthalmic examinations the day before and the day after treatment. FFA was performed for each patient before 6, 12, and 24 months after the first intravitreal injection. The inclusion criteria were: (1) treatment-naive RVO patients; and (2) BCVA of 20/50 or worse if there were no other existing ocular diseases, including media opacity, uveitis, diabetic retinopathy, retinal arterial occlusion, glaucoma, and age-related macular degeneration. Patients with high myopia (over 8D), high astigmatism (over 3D), epiretinal membrane, or a history of pars plana vitrectomy were excluded. Eyes with poor-quality images on FFA due to eye movement were also excluded.

2.2. Ranibizumab injections

Intravitreal ranibizumab injections were administered in the operating room under strictly sterile conditions. Each patient was given an intravitreal injection of ranibizumab (0.05 mL), which was administered with a 30G needle inserted at 4 mm (phakic eyes) or 3.5 mm (pseudophakic eyes) from the limbus. The light perception of the eye was confirmed immediately after injection. In the following 3 days, the slit lamp examination was performed to check for any possible intraocular inflammation.

2.3. Fundus fluorescein angiography and measurement of the FAZ area

For the measurement of the FAZ area, FFA was performed with a scanning laser device known as the Heidelberg Spectralis HRA

(Heidelberg Retina Angiograph II; Heidelberg Engineering, Heidelberg, Germany) (Figure 1). RVO was defined by delayed venous filling in the region of retinal nonperfusion and obstructed veins, which may be caused by microvascular circulation abnormalities. The boundaries of the FAZ were manually delineated by two independent observers who were masked to the BCVA, and the area of FAZ was automatically measured by the software of the device in early-phase images after it was delineated (15).

2.4. Other ophthalmic parameters and their measurement

Fundus images were captured with a fundus camera (Topcon Imagenet, Tokyo, Japan). Two independent observers manually measured the vertical diameters of the superior and inferior temporal retinal veins using Adobe Photoshop CC (Adobe Systems, Inc. San Jose, CA, United States). The BCVA of each patient was measured at a distance of 4 m (or 1 m if necessary) following the guidance of the Early Treatment Diabetic Retinopathy Study (ETDRS) charts.

2.5. Statistical analyses

For statistical analysis, the BCVA was measured with ETDRS charts and converted to the logarithm of the minimal angle of resolution (LogMAR) scale. Comparisons between the BCVA before and after treatment were calculated using the nonparametric Wilcoxon signed rank tests. The bivariate relationships were assessed with the Spearman's correlational coefficient. All statistical analyses were performed using IBM SPSS Statistics version 21.0 (SPSS Inc., Chicago, IL, United States). A p value of <0.05 was considered statistically significant.

3. Results

3.1. Clinical characteristics of patients

A total of 235 patients with RVO were initially enrolled in this study, and 140 were excluded according to criteria. Therefore, 95 eyes of 95 subjects (50 BRVO patients and 45 CRVO patients) who received three consecutive and PRN ranibizumab injections met the criteria for the present study.

The clinical characteristics and outcomes of all patients are summarized in Table 1. The mean age of the patients with BRVO was 58.92 years (range, 35–82 years), and the mean age of the patients with CRVO was 63.20 years (range, 39–88 years). The mean BCVA was improved from 0.47 ± 0.21 before treatment to 0.45 ± 0.25 after follow-up in the BRVO group, and from 0.64 ± 0.23 before treatment to 0.61 ± 0.32 after follow-up in the CRVO group.

3.2. The trend of changes in the FAZ area from baseline to follow-up

The mean size of the FAZ changed from 0.44 ± 0.30 mm^2 to 0.48 ± 0.31 mm^2 in non-ischemia BRVO patients and from 0.61 ± 0.22 mm^2 to 0.67 ± 0.31 mm^2 in ischemia BRVO patients. For CRVO patients, the mean FAZ area changed from 0.60 ± 0.27 mm^2 to 0.61 ± 0.38 mm^2 in the non-ischemia group and from 0.69 ± 0.21 mm^2 to 0.76 ± 0.25 mm^2 in the ischemia group.

Most patients with ischemic and non-ischemic BRVO and CRVO had an obviously enlarged FAZ area after ranibizumab treatment, and a small number of patients had a reduced FAZ area, whereas only a few patients showed a stable FAZ area after three injections. The FAZ area was enlarged after ranibizumab treatment and persisted for a while, and then it reduced gradually. Compared with baseline, there was a significant increase in the size of the FAZ area at 6 and 12 months after the first injection. At the last FFA (24 months after the first injection), most cases showed an obvious decrease in the size of the FAZ, although it was still a little bigger than the pretreatment baseline value (Table 2; Figures 2, 3).

3.3. Changes of retinal vein diameter before treatment and follow-up

The retinal vein diameter data used in the present study were obtained by measuring the obstructed and unobstructed branch veins in BRVO patients and the superior and inferior temporal branch veins
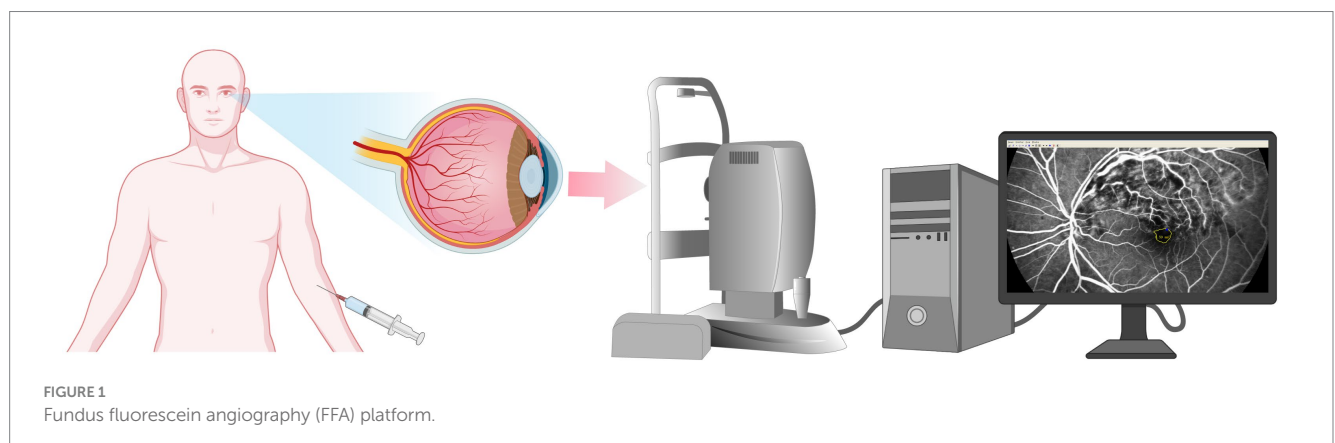

FIGURE 1
Fundus fluorescein angiography (FFA) platform.

TABLE 1 Baseline clinical characteristics and outcome of patients with retinal vein occlusion.

	BRVO (n = 50)	CRVO (n = 45)
Age (years)	58.92 ± 11.19	63.20 ± 12.18
Sex (n, F/M)	18/32	20/25
Period from onset to 1st injection treatment (weeks)	5.08 ± 3.80	3.56 ± 2.69
Systemic diseases		
Hypertension (n, %)	31, 62%	33, 73%
Diabetics mellitus (n, %)	26, 52%	28, 62%
Hypercholesteremia (n, %)	20, 40%	27, 60%
BCVA (logMAR)		
Before treatment	0.47 ± 0.21	0.64 ± 0.23
After follow-up	0.45 ± 0.25	0.61 ± 0.32
Foveal thickness (um)		
Before treatment	409.38 ± 182.48	410.17 ± 148.13
After follow-up	201.63 ± 86.57	343.83 ± 127.45

N, number of eyes; %, rate of eyes; BRVO, branch retinal vein occlusion; CRVO, central retinal vein occlusion; BCVA, best correct visual acuity; MAR, minimum angle of resolution; F, female; M, male.

TABLE 2 The trend of changes in FAZ area and retinal vein diameter before treatment and follow-up.

Parameter	Baseline	6 months	12 months	24 months	p
FAZ area(mm^2)					
BRVO					
Non-ischemia	0.44 ± 0.30	0.59 ± 0.39	0.66 ± 0.48	0.48 ± 0.31	0.256
Ischemia	0.61 ± 0.22	0.81 ± 0.29	0.92 ± 0.36	0.67 ± 0.31	0.000**
CRVO					
Non-ischemia	0.60 ± 0.27	0.83 ± 0.37	0.91 ± 0.45	0.61 ± 0.38	0.042*
Ischemia	0.69 ± 0.21	0.85 ± 0.20	0.92 ± 0.27	0.76 ± 0.25	0.001**
Vessel diameter ($\times 10^{-2}$ mm)					
BRVO					
Non-ischemia					
Obstructed BV	20.89 ± 1.74	19.00 ± 1.76	18.81 ± 2.20	19.69 ± 2.57	0.018*
Unobstructed BV	16.54 ± 2.93	14.46 ± 3.23	14.75 ± 2.25	16.06 ± 1.89	0.057
Ischemia					
Obstructed BV	20.33 ± 2.25	18.00 ± 2.12	17.93 ± 1.91	18.71 ± 3.39	0.000**
Unobstructed BV	17.05 ± 3.15	14.53 ± 3.01	14.53 ± 2.84	15.80 ± 2.84	0.002**
CRVO					
Non-ischemia					
Superior-temporal BV	18.42 ± 1.56	15.94 ± 1.53	16.62 ± 1.76	17.14 ± 1.99	0.001**
Inferior-temporal BV	19.68 ± 1.40	16.7 ± 1.59	17.82 ± 1.69	18.72 ± 1.92	0.000**
Ischemia					
Superior-temporal BV	20.33 ± 1.99	17.45 ± 1.85	16.97 ± 2.19	19.12 ± 2.37	0.000**
Inferior-temporal BV	21.96 ± 1.95	19.32 ± 2.12	18.21 ± 1.31	19.82 ± 2.03	0.000**

FAZ, foveal avascular zone; BRVO, branch retinal vein occlusion; CRVO, central retinal vein occlusion; BV, branch vein. * $p < 0.05$, ** $p < 0.01$.

in CRVO patients. Except for the unobstructed branch veins of the non-ischemic BRVO group, the retinal vein diameters were significantly reduced after ranibizumab treatment and then recovered gradually ($p < 0.05$), and these tendencies were the same with the FAZ area (Table 2; Figure 4).

3.4. Changes correlations between FAZ area, retinal vein diameter, and BCVA

After ranibizumab treatment, LogMAR visual acuity significantly reduced along with FAZ area enlargement in eyes with CRVO groups
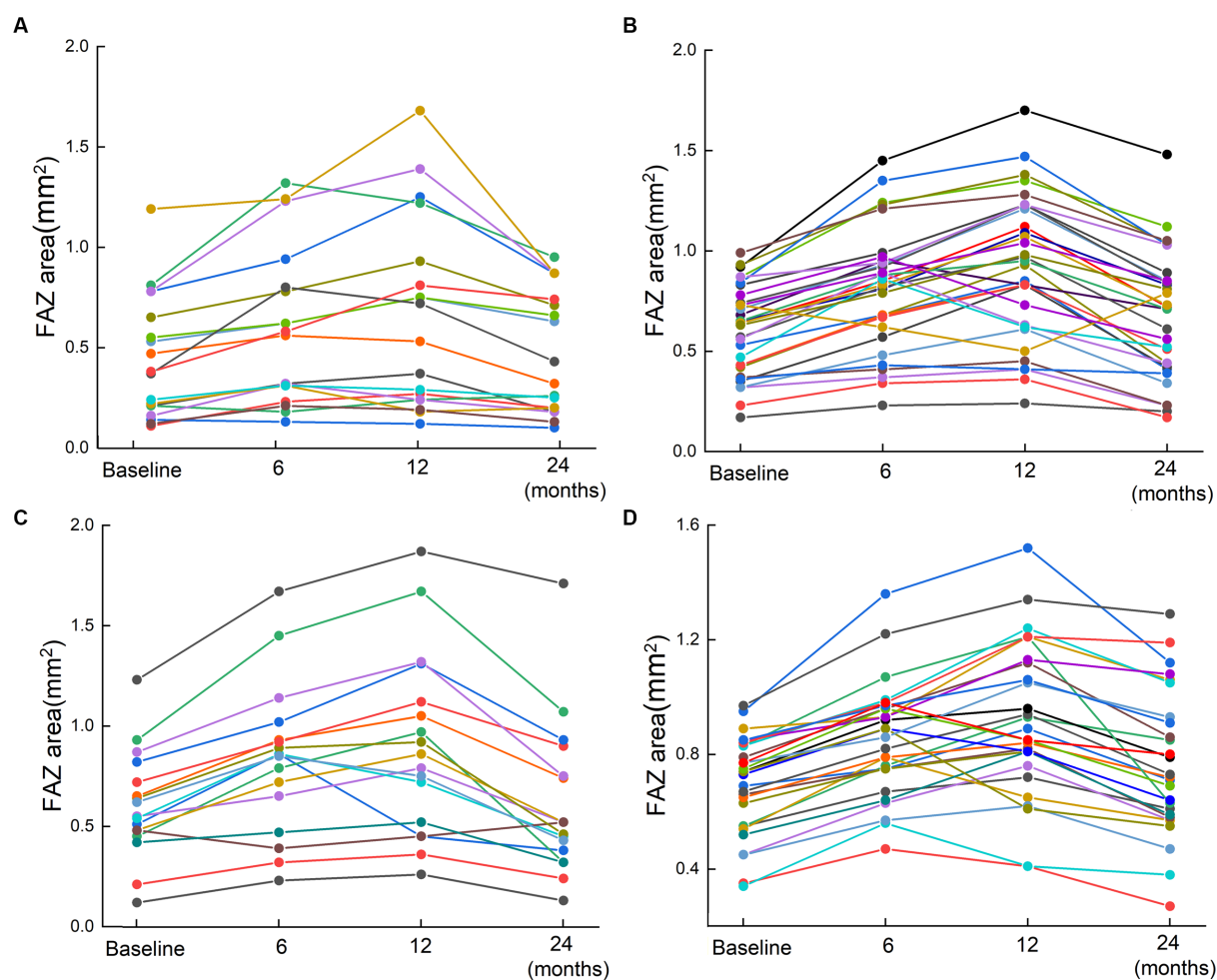
FIGURE 2
The changes of FAZ area for 95 patients based on FFA results. Scatter plots for the FAZ area in patients with RVO before the first injection and 6, 12, and 24 months after the first injection. **(A)** Non-ischemia BRVO; **(B)** Ischemia BRVO; **(C)** Non-ischemia CRVO; **(D)** Ischemia CRVO. Changes of the FAZ after treatment are represented by lines. Each line shows the trend of FAZ area changes for one patient. The four points indicated the FAZ area at baseline (before injection) and 6, 12, and 24 months after the first injection.
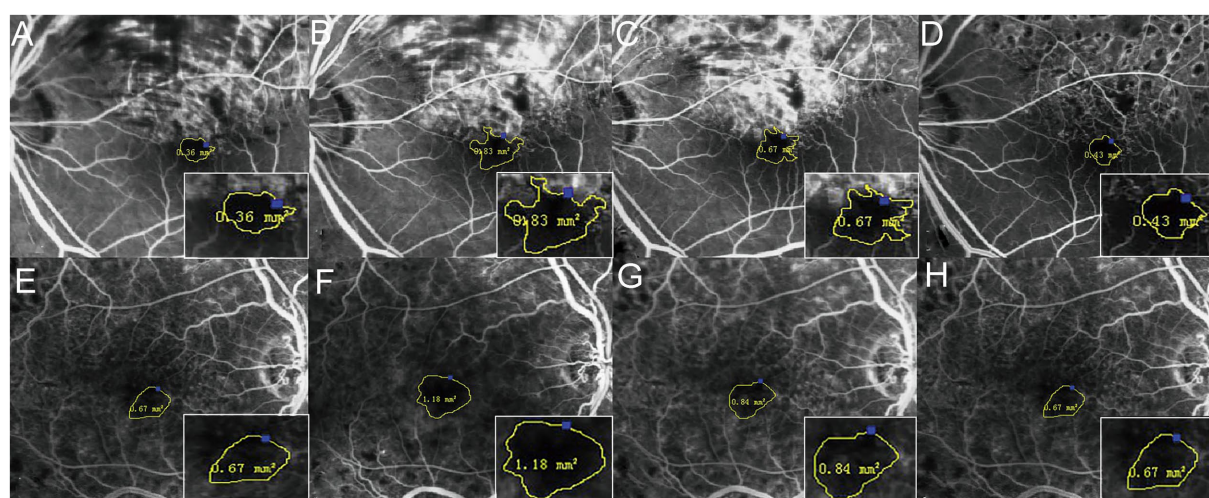
FIGURE 3
Changes of the FAZ area before and 6, 12, and 24 months after the first injection. The four times measurement of FAZ area for one of the BRVO patients **(A–D)** and one of the CRVO patients **(E–H)** by FFA. The FAZ area was enlarged until 12 months, and it then reduced gradually.
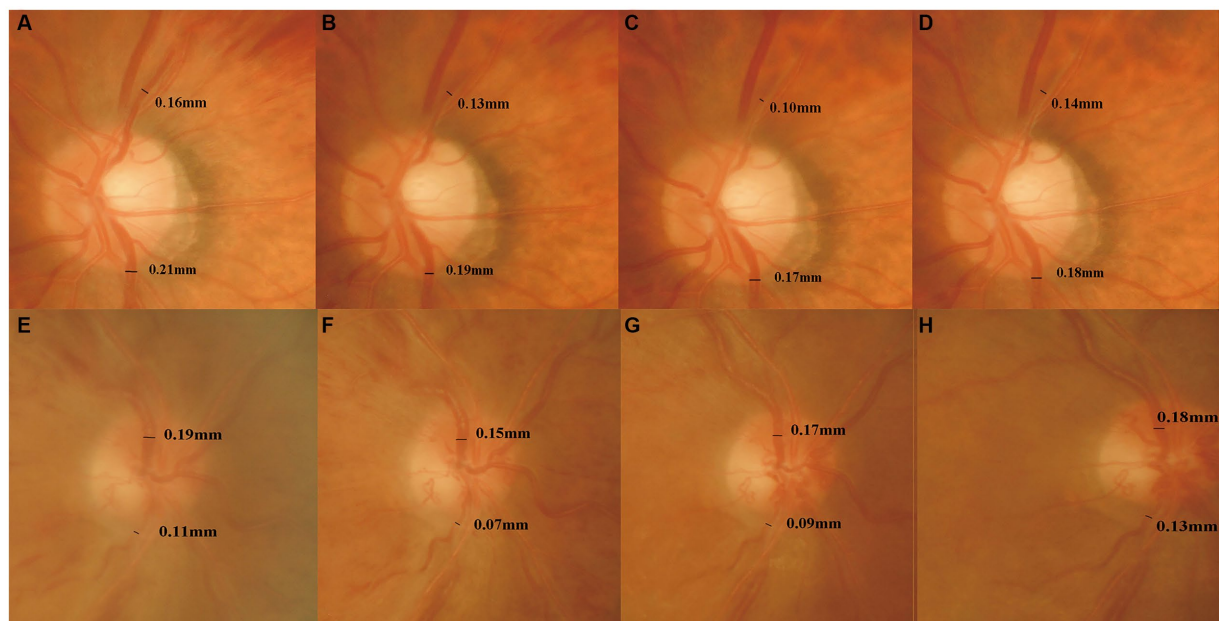
FIGURE 4
Changes of the retinal vein diameter before and 6, 12, and 24 months after the first injection. The four times measurement of retinal vein diameter for one of the BRVO patients **(A–D)** and one of the CRVO patients **(E–H)** in fundus photographs. The retinal vein diameter was decreased until 12 months, and then it increased gradually.

TABLE 3 The correlation between FAZ area and BCVA (LogMAR).

Parameter	FAZ area	BCVA (LogMAR)	r	p
BRVO				
Non-ischemia	0.54 ± 0.38	0.43 ± 0.20	0.200	0.092
Ischemia	0.75 ± 0.32	0.54 ± 0.24	0.180	0.041*
CRVO				
Non-ischemia	0.74 ± 0.39	0.60 ± 0.29	0.327	0.007**
Ischemia	0.81 ± 0.25	0.72 ± 0.27	0.286	0.002**

BRVO, branch retinal vein occlusion; CRVO, central retinal vein occlusion; BCVA, best corrected visual acuity; FAZ, foveal avascular zone; BV, branch vein. * $p < 0.05$, ** $p < 0.01$.

(non-ischemic, $r = 0.327$, $p < 0.001$; ischemic, $r = 0.286$, $p < 0.001$) and in eyes with ischemic BRVO group ($r = 0.180$, $p < 0.05$), but not in eyes with non-ischemic BRVO ($r = 0.200$, $p > 0.05$) (Table 3).

There was a significantly negative correlation between the FAZ area and the diameter of the obstructed branch veins in ischemic BRVO group ($r = -0.310$, $p < 0.01$), whereas the non-ischemia BRVO groups and the unobstructed branch veins of ischemia BRVO group did not show such correlation ($p > 0.05$). The branch vein diameter of ischemic CRVO groups and the inferior temporal branch vein diameter of non-ischemic CRVO group had a significant negative association with the FAZ area ($p < 0.05$), but the superior temporal branch veins of the non-ischemia CRVOs did not show the same tendency ($p > 0.05$) (Table 4).

4. Discussion

In patients with RVO, vein occlusion could lead to elevated venous pressure, turbulent blood flow, and overloading drainage capacity, which may cause dilation of retinal veins and capillaries (16). Simultaneously, the intraocular level of VEGF increases sharply during vein occlusion and is the most important mediator responsible for the development of neovascularization and macular edema. Thus, the VEGF inhibitor has been proven to be an effective first-line therapeutic strategy for treating neovascularization and macular edema secondary to RVO (17).

Several researchers hold a view that the VEGF blockade may lead to a poor progression of the retinal nonperfusion area (18, 19), while Campochiaro et al. have reported that the VEGF blockade not only prevented the worsening of retinal ischemia but also promoted the retinal reperfusion (20). The findings of this study were comparable to studies that similarly reported that the FAZ area changed after ranibizumab treatment in patients with RVO. If RVO patients who presented with macular edema already have severe parafoveal capillary dropout before treatment, the macular ischemia may not recover even after the resolution of the macular edema. Moreover, the present study showed that the enlargement of the FAZ area was transient and could return to near baseline at 24 months after injection. Samara et al.

TABLE 4 The correlation between FAZ area and retinal vessel diameter.

Parameter	FAZ area (mm^2)	Vessel diameter ($\times 10^{-2}$ mm)	r	p
BRVO				
Non-ischemia	0.54 ± 0.38			
Obstructed BV		19.60 ± 2.21	−0.058	0.628
Unobstructed BV		15.45 ± 2.72	0.226	0.056
Ischemia	0.75 ± 0.32			
Obstructed BV		18.74 ± 2.64	−0.310	0.000**
Unobstructed BV		15.48 ± 3.11	0.098	0.270
CRVO				
Non-ischemia	0.74 ± 0.39			
Superior-temporal BV		17.03 ± 1.91	−0.205	0.093
Inferior-temporal BV		18.23 ± 1.97	−0.461	0.000**
Ischemia	0.81 ± 0.25			
Superior-temporal BV		18.47 ± 2.48	−0.259	0.006**
Inferior-temporal BV		19.83 ± 2.30	−0.226	0.017*

BRVO, branch retinal vein occlusion; CRVO, central retinal vein occlusion; FAZ, foveal avascular zone; BV, branch vein. * $p < 0.05$, ** $p < 0.01$.

measured the FAZ area of healthy subjects (ranging from 0.21 to 0.41mm^2) by FFA (21). Feucht et al. and Erol et al. reported that enlargement of the FAZ area was observed on FFA images after intravitreal anti-VEGF treatment in patients with diabetic retinopathy or RVO (22, 23). However, other studies have arrived at a controversial conclusion that the FAZ area remained statistically unchanged before and after anti-VEGF therapy (24). Several possible factors contribute to these opposite results, including the follow-up of these studies varied from 6 months to 20 months, the different number of injections, and the patient sample size. The FAZ area of CRVO eyes was larger than that of BRVO eyes due to much greater VEGF activity in the vitreous of CRVO eyes, particularly in the ischemic type.

The present study found the retinal vein diameter of many RVO patients was significantly reduced after anti-VEGF treatment compared with baseline. This phenomenon could be explained by adverse vasoconstrictive effects of anti-VEGF therapy that were reduction of retinal flow velocity and vein diameter (25, 26). In addition, most of the retinal veins in RVO eyes were thicker than those in normal eyes mainly because VEGF could lead to vessel dilation and increased ocular blood flow by enhancing the endothelial nitric oxide synthetic rate and upregulating the activity of VEGF receptors in human endothelial cells (27). In normal eyes, the mean vessel diameters of the superior temporal veins and the inferior temporal veins were shown to be $17.15 \pm 1.56 \times 10^{-2}$ mm and $14.86 \pm 3.37 \times 10^{-2}$ mm, respectively, indicating that the inferior temporal vein diameter is normally thinner than that the superior temporal vein diameter, which was also proven by Ouyang et al. (28). The present study show that the diameter of superior temporal veins was thinner than that of the inferior ones in eyes with BRVO and CRVO, regardless of whether they were measured at baseline or after treatment. Retinal vein obstruction occurs easily in the superior temporal veins. Weinberg's study could also partially support the similar result that there was a greater proportion of vein-posterior crossing in superior temporal veins than in inferior temporal veins; thus, most BRVOs occurred in the retinal superior temporal quadrant (29).

As shown in the present study, the FAZ area had a negative correlation with BCVA (LogMAR) after treatment in eyes in both CRVO groups and in the ischemic BRVO group, but not in eyes with non-ischemic BRVO. This result was partially in line with a report from a previous study that an enlargement of the FAZ area correlated negatively with poor visual outcomes (30). However, the correlation of the FAZ area and BCVA was shown differently in many studies. Balaratnasingam et al. demonstrated that the FAZ area measured with FFA was significantly correlated with BCVA in eyes with RVO and diabetic retinopathy, and it was an important predictor for evaluating visual function after treatment of these diseases (14). On the contrary, Remky et al. postulated that the FAZ area was negatively correlated with BCVA in BRVO eyes but not in CRVO eyes (31). There are many reasons for the discrepancy in the relationship between the FAZ area and BCVA in the two types of RVO, which may be due to intraretinal cystic changes, degree of macular edema, disorganization of the retinal inner layers, length and integrity of the ellipsoid zone band. All these factors could affect the improvement of BCVA during follow-up.

In the present study, vein diameter reduced significantly along with the enlargement of the FAZ area after anti-VEGF treatment in eyes with RVO. The obvious vasoconstriction in retinal veins may be interpreted as a return to the normal diameter from a previously vasodilated status due to VEGF inhibition. After anti-VEGF therapy, the diameter of the obstructed branch veins in eyes with ischemic BRVO and the diameter of the branch veins in eyes with CRVO had negative correlations with the FAZ area, but this correlation was not observed in most of eyes with BRVO or the superior temporal branch veins of non-ischemic CRVO eyes. This finding indicated that the branch veins of non-ischemic BRVO eyes and the unobstructed branch veins of ischemic BRVO eyes may still have normal circulation and can maintain their filling degree without depending on the FAZ ischemia status. The obstructed branch veins of ischemic BRVO eyes already have impaired circulation, which can be affected by the adjacent branch retinal veins near the fovea. In the ischemic CRVO groups, the superior and inferior temporal branch veins were both affected by occlusion, and the circulation of inferior ones was weaker than that of superior ones due to anatomical characteristics.

Therefore, the diameter of the superior branch veins of non-ischemic CRVO eyes were rarely affected by the FAZ ischemia degree.

5. Conclusion

The integration of a FFA platform with image analysis techniques has provided valuable insights into the detection and evaluation of RVO. Consecutive intravitreal ranibizumab injections can cause significant short-term enlargement of the FAZ area and decreased retinal vein diameter in eyes with RVO, although the natural course of RVO may also affect ischemia and visual gain. After 12 months, the FAZ area and retinal vein diameter begin to recover and return to near baseline until 24 months. Ranibizumab therapy may cause macular ischemia to become more severe and affect BCVA for a short time. These findings highlight a potential adverse effect of consecutive ranibizumab therapy, which needs to be taken into consideration in the treatment and prognosis of RVO. The FFA platform with image analysis techniques offers a valuable tool for accurate detection, monitoring, and management of RVO, aiding clinicians in making informed treatment decisions for improved patient outcomes.

Data availability statement

The original contributions presented in the study are included in the article/supplementary material, further inquiries can be directed to the corresponding authors.

Ethics statement

The studies involving humans were approved by the Second Affiliated Hospital of Xi'an Jiaotong University of the Medical Ethics Committee. The studies were conducted in accordance with the local legislation and institutional requirements. Written informed consent for participation was not required from the participants or the participants' legal guardians/next of kin in accordance with the national legislation and institutional requirements.

Author contributions

DL: Investigation, Methodology, Writing – original draft. ZZ: Formal analysis, Writing – original draft. FW: Data curation, Writing – original draft. BZ: Formal analysis, Writing – original draft. YW: Data curation, Writing – original draft. YZ: Investigation, Writing – review & editing. JL: Investigation, Writing – review & editing.

Funding

Acknowledgments

Conflict of interest

The authors declare that the research was conducted in the absence of any commercial or financial relationships that could be construed as a potential conflict of interest.

Publisher's note

All claims expressed in this article are solely those of the authors and do not necessarily represent those of their affiliated organizations, or those of the publisher, the editors and the reviewers. Any product that may be evaluated in this article, or claim that may be made by its manufacturer, is not guaranteed or endorsed by the publisher.

References

1. Nicholson L, Talks S, Amoaku W, Talks K, Sivaprasad S. Retinal vein occlusion (RVO) guideline: executive summary. *Eye (Lond)*. (2022) 36:909–12. doi: 10.1038/s41433-022-02007-4

2. Romano F, Lamanna F, Gabrielle PH, Teo KYC, Battaglia Parodi M, Iacono P, et al. Update on retinal vein occlusion. *Asia Pac J Ophthalmol*. (2023) 12:196–210. doi: 10.1097/APO.0000000000000598

3. Khayat M, Williams M, Lois N. Ischemic retinal vein occlusion: characterizing the more severe spectrum of retinal vein occlusion. *Surv Ophthalmol*. (2018) 63:816–50. doi: 10.1016/j.survophthal.2018.04.005

4. Wilderson L, Moore DE. Fluorescein angiography detection of combined branch retinal vein and artery occlusion. *Asia Pac J Ophthalmol*. (2022) 11:295. doi: 10.1097/APO.0000000000000440

5. Schmidt-Erfurth U, Garcia-Arumi J, Gerendas BS, Midena E, Sivaprasad S, Tadayoni R, et al. Guidelines for the management of retinal vein occlusion by the European society of retina specialists (EURETINA). *Ophthalmologica*. (2019) 242:123–62. doi: 10.1159/000502041

6. Turczyńska MJ, Krajewski P, Brydak-Godowska JE. Wide-field fluorescein angiography in the diagnosis and management of retinal vein occlusion: a retrospective single-center study. *Med Sci Monit*. (2021) 15:e927782. doi: 10.12659/MSM.92778

7. Huang PW, Lai CC, Hwang YS, Wu WC, Wu CH, Huang JC, et al. Treatment responses for branch retinal vein occlusion predicted by semi-automated fluorescein angiography quantification. *BMC Ophthalmol*. (2022) 22:50. doi: 10.1186/s12886-022-02245-w

8. Fan W, Fleming A, Hemert JV, Wykoff CC, Brown D, Robertson G, et al. Retinal vascular bed area in eyes with retinal vein occlusion on ultra-widefield fluorescein angiography: wave study. *Retina*. (2022) 42:1883–8. doi: 10.1097/IAE.0000000000003549

9. Glacet-Bernard A, Miere A, Houmane B, Tilleul J, Souied E. Nonperfusion assessment in retinal vein occlusion: comparison between ultra-widefield fluorescein angiography and widefield optical coherence tomography angiography. *Retina*. (2021) 41:1202–9. doi: 10.1097/IAE.0000000000002993

10. Werner JU, Böhm F, Lang GE, Dreyhaupt J, Lang GK, Enders C. Comparison of foveal avascular zone between optical coherence tomography angiography and fluorescein angiography in patients with retinal vein occlusion. *PLoS One*. (2019) 14:e0217849. doi: 10.1371/journal.pone.0217849

11. Wons J, Pfau M, Wirth MA, Freiberg FJ, Becker MD, Michels S. Optical coherence tomography angiography of the foveal avascular zone in retinal vein occlusion. *Ophthalmologica*. (2016) 235:195–202. doi: 10.1159/000445482

12. Fan L, Zhu Y, Liao R. Evaluation of macular microvasculature and foveal avascular zone in patients with retinal vein occlusion using optical coherence tomography angiography. *Int Ophthalmol*. (2022) 42:211–8. doi: 10.1007/s10792-021-02015-5

13. Tang Z, Zhang X, Yang G, Zhang G, Gong Y, Zhao K, et al. Automated segmentation of retinal nonperfusion area in fluorescein angiography in retinal vein occlusion using convolutional neural networks. *Med Phys*. (2021) 48:648–58. doi: 10.1002/mp.14640

14. Balaratnasingam C, Inoue M, Ahn S, McCann J, Dhrami-Gavazi E, Yannuzzi LA, et al. Visual acuity is correlated with the area of the foveal avascular zone in diabetic retinopathy and retinal vein occlusion. *Ophthalmology*. (2016) 123:2352–67. doi: 10.1016/j.ophtha.2016.07.008

15. Zheng Y, Gandhi JS, Stangos AN, Campa C, Broadbent DM, Harding SP. Automated segmentation of foveal avascular zone in fundus fluorescein angiography. *Invest Ophthalmol Vis Sci*. (2010) 51:3653–9. doi: 10.1167/iovs.09-4935

16. Christoffersen NL, Larsen M. Pathophysiology and hemodynamics of branch retinal vein occlusion. *Ophthalmology*. (1999) 106:2054–62. doi: 10.1016/S0161-6420(99)90483-9

17. Leung DW, Cachiane G, Kuang WJ, Goeddel DV, Ferrara N. Vascular endothelial growth factor is a secreted angiogenic mitogen. *Science*. (1989) 246:1306–9. doi: 10.1126/science.2479986

18. Sabet-Peyman EJ, Heussen FM, Thorne JE, Casparis H, Patel SJ, Do DV. Progression of macular ischemia following intravitreal bevacizumab. *Ophthalmic Surg Lasers Imaging*. (2009) 40:316–8. doi: 10.3928/15428877-20090430-17

19. Mansour AM, Bynoe LA, Welch JC, Pesavento R, Mahendradas P, Ziemssen F, et al. Retinal vascular events after intravitreal bevacizumab. *Acta Ophthalmol*. (2010) 88:730–5. doi: 10.1111/j.1755-3768.2009.01535.x

20. Campochiaro PA, Bhisitkul R, Shapiro H, Rubio RG. Vascular endothelial growth factor promotes progressive retinal nonperfusion in patients with retinal vein occlusion. *Ophthalmology*. (2013) 120:795–802. doi: 10.1016/j.ophtha.2012.09.032

21. Samara WA, Say EA, Khoo CT, Higgins TP, Magrath G, Ferenczy S, et al. Correlation of foveal avascular zone size with foveal morphology in normal eyes using optical coherence tomography angiography. *Retina*. (2015) 35:2188–95. doi: 10.1097/IAE.0000000000000847

22. Feucht N, Schonbach EM, Lanzl I, Kotliar K, Lohmann CP, Maier M. Changes in the foveal microstructure after intravitreal bevacizumab application in patients with retinal vascular disease. *Clin Ophthalmol*. (2013) 7:173–8. doi: 10.2147/OPTH.S37544

23. Erol N, Gursoy H, Kimyon S, Topbas S, Colak E. Vision, retinal thickness, and foveal avascular zone size after intravitreal bevacizumab for diabetic macular edema. *Adv Ther*. (2012) 29:359–69. doi: 10.1007/s12325-012-0009-9

24. Falavarjani KG, Iafe NA, Hubschman JP, Tsui I, Sadda SR, Sarraf D. Optical coherence tomography angiography analysis of the foveal avascular zone and macular vessel density after anti-VEGF therapy in eyes with diabetic macular edema and retinal vein occlusion. *Invest Ophthalmol Vis Sci*. (2017) 58:30–4. doi: 10.1167/iovs.16-20579

25. Sacu S, Pemp B, Weigert G, Matt G, Garhofer G, Pruente C, et al. Response of retinal vessels and retrobulbar hemodynamics to intravitreal anti-VEGF treatment in eyes with branch retinal vein occlusion. *Invest Ophthalmol Vis Sci*. (2011) 52:3046–50. doi: 10.1167/iovs.10-5842

26. Fukami M, Iwase T, Yamamoto K, Kaneko H, Yasuda S, Terasaki H. Changes in retinal microcirculation after intravitreal Ranibizumab injection in eyes with macular edema secondary to branch retinal vein occlusion. *Invest Ophthalmol Vis Sci*. (2017) 58:1246–55. doi: 10.1167/iovs.16-21115

27. Mourad JJ, des GG, Debbabi H, Levy BI. Blood pressure rise following angiogenesis inhibition by bevacizumab. A crucial role for microcirculation. *Ann Oncol*. (2008) 19:927–34. doi: 10.1093/annonc/mdm550

28. Ouyang Y, Shao Q, Scharf D, Joussen AM, Heussen FM. Retinal vessel diameter measurements by spectral domain optical coherence tomography. *Graefes Arch Clin Exp Ophthalmol*. (2015) 253:499–509. doi: 10.1007/s00417-014-2715-2

29. Weinberg DV, Egan KM, Seddon JM. Asymmetric distribution of arteriovenous crossings in the normal retina. *Ophthalmology*. (1993) 100:31–6. doi: 10.1016/s0161-6420(13)31702-3

30. Chung EJ, Hong YT, Lee SC, Kwon OW, Koh HJ. Prognostic factors for visual outcome after intravitreal bevacizumab for macular edema due to branch retinal vein occlusion. *Graefes Arch Clin Exp Ophthalmol*. (2008) 246:1241–7. doi: 10.1007/s00417-008-0866-8

31. Remky A, Wolf S, Knabben H, Arend O, Reim M. Perifoveal capillary network in patients with acute central retinal vein occlusion. *Ophthalmology*. (1997) 104:33–7. doi: 10.1016/s0161-6420(97)30365-0

Macular changes following cataract surgery in eyes with early diabetic retinopathy: an OCT and OCT angiography study

Huiping Yao, Zijian Yang, Yu Cheng and Xi Shen*

Department of Ophthalmology, Ruijin Hospital, Shanghai Jiao Tong University School of Medicine,
Shanghai, China

Background: To evaluate changes in macular status and choroidal thickness (CT) following phacoemulsification in patients with mild to moderate nonproliferative diabetic retinopathy (NPDR) using optical coherence tomography.

Methods: In this prospective study, all of the patients underwent uncomplicated phacoemulsification. Retinal superficial capillary plexus vascular density (SCP-VD), macular thickness (MT), and CT were measured pre- and postoperatively.

Results: Twenty-two eyes of 22 cataract patients with mild to moderate NPDR without diabetic macular edema (DME) and 22 controls were enrolled. BCVA increased in two groups at 3 months postoperatively. At 1 and 3 months postoperatively, SCP-VD in the diabetic retinopathy (DR) group significantly increased; changes in SCP-VD in parafovea were significantly greater in the DR group than in the control group. MT and CT in the DR group significantly increased at all visits postoperatively in the fovea and perifovea. Changes in parafoveal MT were significantly greater in the DR group than in the control group at all visits postoperatively. Changes in CT and MT in the fovea were significantly greater in patients with DR than in the controls 1 and 3 months postoperatively.

Conclusion: Uncomplicated phacoemulsification resulted in greater increases in SCP-VD, MT and CT in patients with early DR without preoperative DME than in controls.

KEYWORDS

macular thickness, vascular density, choroidal thickness, optical coherence tomography, diabetic retinopathy, diabetic macular edema, optical coherence tomography angiography

Introduction

Cataract is a leading cause of blindness worldwide (1), and diabetes mellitus (DM) is one of the most common diseases and its prevalence is increasing (2, 3). People with DM are five times more likely to develop cataracts than those without DM (4, 5). Phacoemulsification is the most common, effective, and safe procedures for the treatment of cataract. However, it was reported that cataract surgery was a risk factor for postoperative macular edema and secondary progression in diabetic patients (6). Macular edema and DR progression are the major reasons for poor visual prognosis after cataract surgery in diabetic patients with or without DR (7). While, it has also been suggested that these complications may not be a direct effect of surgery

but rather a natural course of disease progression (8–10); therefore, it is clinically meaningful to determine the possible impact of cataract surgery on the occurrence of diabetic macular edema (DME) and/or the progression of DR. This may be related to the timing of cataract surgery as well as the treatment strategy for postoperative ME.

Fluorescent angiography (FA) and indocyanine green angiography (ICGA) are sensitive methods of detecting changes in the retinal and choroidal vasculature. FA is highly sensitive to retinal microvascular fluid leakage (11). However, there are many limitations to the clinical application of FA and ICGA owing to their invasive nature, the risk of allergic reactions, and the inability to achieve a good quantification of measurement. Optical coherence tomography (OCT) is thought to be more sensitive in detecting the presence of ME and is widely used to provide an objective and quantitative assessment of ME (12), providing more detailed images of the retinal and choroidal anatomy. Furthermore, optical coherence tomography angiography (OCTA) can help detect microvascular changes and assess retinal perfusion (13).

The aim of this study was to explore the influence of cataract surgery on macular microvasculature and macular and choroidal thicknesses in patients with mild/moderate DR through follow-up of changes in macular vascular density (VD), macular thickness (MT), and choroidal thickness (CT) using OCT and OCTA to evaluate the influence of phacoemulsification on retinal and choroidal microcirculation and structure.

Methods

Study subjects

This prospective observational case–control study included 22 eyes of 22 patients with cataract, who were clinically diagnosed with mild to moderate nonproliferative diabetic retinopathy (NPDR) without DME, and 22 age-matched non-diabetic patients with cataract. All patients underwent complete ophthalmologic examinations, including slit-lamp examination, best-corrected visual acuity (BCVA), dilated fundal examinations, intraocular pressure (IOP), and axial length (AL). Classification and diagnosis of DR and DME were evaluated according to the international clinical disease DR severity scale (14). If a patient underwent surgery on both eyes, the eye that underwent surgery first was included in this study. This study was approved by the Ethical Review Committee of Ruijin Hospital and adhered to the provisions of the Declaration of Helsinki. The consent forms were signed by all patients.

All patients were recruited consecutively from the Ophthalmology Department of Ruijin Hospital between October 2020 and October 2022. The inclusion criteria were: age ≥ 40 years, spherical diopter < −6 D, AL < 26 mm, no history of intraocular surgery or ocular trauma, no history of DME and DR treatment, and no history of glaucoma, uveitis, or other retinal diseases, such as vitreoretinal interface disorders, retinal vein occlusion, retinal artery occlusion, etc.

Optical coherence tomography measurement

Swept source (SS)-OCT (Triton DRI-OCT, Topcon, Inc., Tokyo, Japan) was used to obtain OCT B-scan and angiography images.

Angiography scans (3 × 3 mm) centered on the fovea and 12 radial scans through the center of the fovea were performed to obtain macular OCTA and B scan images. Images with a signal strength index >40 were saved for further analysis.

Superficial capillary plexus vascular density (SCP-VD), MT, and CT values were automatically provided by the built-in software of the SS-OCT device (Topcon FastMap, version 10.13.003.06). The macula was divided into three subfields according to the standard Early Treatment Diabetic Retinopathy Study (ETDRS) grid, as previously reported (15): foveal MT/VD were defined as values in the center circle (1.0 mm); parafoveal MT/CT/VD were defined as the arithmetic average values in the annular subfield with 1.0 mm inside and 3.0 mm outside diameter; and perifoveal MT/CT were defined as the arithmetic average values in the annular subfield with 3.0 mm inside and 6.0 mm outside diameter.

Surgery

One experienced surgeon performed all phacoemulsification procedures using the Infinity Vision System (Alcon Laboratories, Inc.). No surgery-related complications occurred, and intraocular lens was implanted into the capsular bag during surgery on each patient. The cumulative dissipated energy (CDE) data were collected. Tobramycin and dexamethasone eye drops 4 times per day were administered to all patients for 1 week after surgery, followed by 1.0% prednisolone acetate and 0.5% levofloxacin eye drops 3 times per day for 3 weeks.

Statistical analysis

Data were analyzed using GraphPad Prism 7.0 (GraphPad Software, CA) and expressed in the form of mean ± standard deviation (SD). The normal distribution of continuous variables was tested using D'Agostino & Pearson normality test. The differences between two groups were compared using independent t test. MT, CT, and SCP-VD at the four visits were compared using the repeated measures analysis of variance (ANOVA) with Bonferroni correction. Categorical variables were analyzed using Fisher's exact test. In addition, the repeated measures analysis of variance for the four visits with the inclusion of the CDE covariant (ANCOVA) was performed with SPSS software version 21.0 (SPSS, Inc., IL, Chicago, United States) to assess the effect of CDE on variations in OCTA parameter. $p < 0.05$ was considered statistically significant.

Results

Demographic and clinical characteristics

A total of 44 eyes of 44 participants were enrolled in the study; the DR group included 22 patients with mild to moderate NPDR (13 males and 9 females) and the control group included 22 nondiabetic patients (12 males and 10 females). There were no significant differences in age, sex, BCVA, IOP, CDE or AL between the two groups at baseline. The DR group included 3 patients with mild NPDR and 19 with moderate NPDR. BCVA at 3 months postoperatively

TABLE 1 Demographic and clinical characteristics.

		Controls (n = 22)	NPDR (n = 22)	p-value
Age, years (mean ± SD)		65.9 ± 1.43	65.1 ± 1.68	0.727
Gender (n)	Female	9	10	>0.999
	Male	13	12	
BCVA, log MAR (mean ± SD)	Baseline	0.75 ± 0.19	0.77 ± 0.21	0.710
	3 Mo postop	0.07 ± 0.13	0.09 ± 0.1	0.615
IOP, mmHg (mean ± SD)	Baseline	16.3 ± 2.31	16.1 ± 2.7	0.776
	1 Wk Postop	12.4 ± 3.46	12.9 ± 2.6	0.59
	1 Mo Postop	13.8 ± 1.92	13.4 ± 2.05	0.522
	3 Mo Postop	14.2 ± 2.05	14.1 ± 1.86	0.945
Axial length, mm(mean ± SD)		23.25 ± 0.94	23.31 ± 0.85	0.824
CDE(mean ± SD)		6.61 ± 4.9	5.86 ± 3.1	0.546

NPDR, nonproliferative diabetic retinopathy; BCVA, best-corrected visual acuity; IOP, intraocular pressure; Wk, week; Postop, postoperatively; Mo, month; CDE, cumulative dissipated energy; SD, standard deviation.

TABLE 2 Superficial capillary plexus vascular density of the two groups at four visits (mean ± SD).

		Baseline	Postop						p value
			1 Wk Postop		1 Mo Postop		3 Mo Postop		
		VD	VD	p value	VD	p value	VD	p value	
DR group (%)	Fovea	18.65 ± 2.05	18.23 ± 1.72	0.54	18.77 ± 1.64	>0.999	18.48 ± 1.78	>0.999	0.216
	Parafovea	46.63 ± 1.74	47.18 ± 1.35	0.339	49.11 ± 1.69	<0.001	48.67 ± 1.38	<0.001	<0.001
Control group (%)	Fovea	19.2 ± 2.6	18.6 ± 2.9	0.478	19.38 ± 3.01	>0.999	19.29 ± 2.9	>0.999	0.213
	Parafovea	48.28 ± 2	48.58 ± 1.86	>0.999	49.44 ± 1.69	0.122	49.05 ± 1.45	0.369	0.027

Wk, week; Postop, postoperatively; Mo, month; DR, diabetic retinopathy; VD, vascular density.

increased in DR and control groups (all $p < 0.001$). There was no significant difference in BCVA between the two groups at 3 months postoperatively ($p = 0.615$). In the control group, the IOP at 1 week, 1 month, and 3 months postoperatively was lower than at baseline ($p < 0.001$, $p < 0.001$, and $p = 0.003$, respectively), and in the DR group, the IOP at 1 week, 1 month, and 3 months postoperatively was also lower than at baseline ($p < 0.001$, $p < 0.001$, and $p = 0.006$, respectively) (Table 1). One patient progressed from mild NPDR to moderate NPDR, while the other patients showed no progression in the stage of DR and no occurrence of DME at the last visit.

Superficial capillary plexus vascular density

The microvasculature parameters obtained using OCTA at all visits are presented in Table 2. At baseline, there was no significant difference in foveal SCP-VD between the DR group and the control group ($p = 0.446$); however, parafoveal SCP-VD in the DR group was lower than that in the control group ($p = 0.005$).

In the DR group, there was no significant difference between postoperative foveal SCP-VD and baseline foveal SCP-VD at 1 week, 1 month, 3 months postoperatively; parafoveal SCP-VD at 1 week after surgery was not significantly different from baseline; parafoveal SCP-VD increased significantly at 1 and 3 months after surgery compared with baseline (Table 2). In the control group, SCP-VD after surgery was not significantly different from baseline at all visits postoperatively in fovea and parafovea (Table 2).

In DR group, there existed significant difference in parafoveal SCP-VD between 1 week and 1 months postoperatively ($p < 0.001$), and the same was true between 1 week and 3 months postoperatively ($p < 0.001$); other than that, there were no significant differences in SCP-VD between any two time points postoperatively in both fovea and parafovea (all $p > 0.05$). In the control group, there were no significant differences in SCP-VD between any two time points postoperatively in both fovea and parafovea (all $p > 0.05$).

Changes in SCP-VD in the DR group were significantly greater than those in the control groups 1 and 3 months postoperatively in the parafovea. Changes in SCP-VD in the DR group were not significantly different from those of the control group in the fovea at 1 week, 1 month and 3 months postoperatively (Table 3).

ANCOVA test did not show relationships between CDE and variations in SCP-VD in both DR and control groups. After adjusting for CDE, parafoveal SCP-VD increased significantly at 1 and 3 months after surgery compared with baseline in the DR group (Supplementary Tables S1, S2).

Macular thickness

At baseline, there was no significant difference between the DR and control group in the foveal, parafoveal, and perifoveal MT ($p = 0.637$, 0.927, and 0.773, respectively).

The MT of the DR group significantly increased at 1 week, 1 month, and 3 months postoperatively compared with baseline in all

TABLE 3 Changes in superficial capillary plexus vascular density after cataract surgery (mean ± SD).

		1 Wk Postop			1 Mo Postop			3 Mo Postop		
		Control	DR	p value	Control	DR	p value	Control	DR	p value
VD (%)	Fovea	−0.59 ± 1.51	−0.42 ± 1.1	0.671	0.18 ± 1.79	0.11 ± 1.67	0.895	0.09 ± 2.3	−0.17 ± 1.68	0.673
	Parafovea	0.3 ± 1.45	0.56 ± 1.3	0.529	1.16 ± 2.17	2.49 ± 1.96	0.038	0.77 ± 1.82	2.05 ± 1.35	0.011

Wk, week; Postop, postoperatively; Mo, month; DR, diabetic retinopathy; VD, vascular density.

TABLE 4 The macular thickness of the two groups at four visits (mean ± SD).

		Baseline	Postop						p value
			1 Wk Postop		1 Mo Postop		3 Mo Postop		
		MT	MT	p value	MT	p value	MT	p value	
Control (μm)	Fovea	219.3 ± 19.98	228.8 ± 21.38	0.004	244 ± 25.42	<0.001	236.5 ± 21.53	<0.001	<0.001
	Parafovea	292.2 ± 20.28	299.3 ± 18.54	0.014	311 ± 15.14	<0.001	303.9 ± 18.51	0.002	<0.001
	Perifovea	264.4 ± 16.03	271.2 ± 16.83	0.067	281.5 ± 23.78	<0.001	271.2 ± 17.45	<0.001	<0.001
DR (μm)	Fovea	222.3 ± 21.85	235.2 ± 20.21	<0.001	262.1 ± 31.15	<0.001	257.1 ± 28.92	<0.001	<0.001
	Parafovea	291.5 ± 25.07	306.9 ± 18.8	<0.001	318.8 ± 21.12	<0.001	314.1 ± 19.2	0.001	<0.001
	Perifovea	266 ± 18.97	277.9 ± 18.11	0.022	290 ± 20.04	<0.001	286.3 ± 17.87	<0.001	<0.001

Wk, week; Postop, postoperatively; Mo, month; DR, diabetic retinopathy; MT, macular thickness.

TABLE 5 Changes of macular thickness after cataract surgery (mean ± SD).

		1 Wk Postop			1 Mo Postop			3 Mo Postop		
		Control	DR	p value	Control	DR	p value	Control	DR	p value
MT (μm)	Fovea	9.5 ± 11.5	13.0 ± 11.1	0.323	24.68 ± 20.01	39.86 ± 19.34	0.014	17.23 ± 13.15,	34.86 ± 17.68	0.001
	Parafovea	7.16 ± 9.69	15.38 ± 13.91	0.028	18.87 ± 12.35	27.24 ± 12.64	0.032	11.69 ± 12.87	22.55 ± 13.95	0.01
	Perifovea	6.75 ± 11.38	11.9 ± 17.02	0.245	17.11 ± 17.32	24.06 ± 17.32	0.177	6.75 ± 6.21	20.38 ± 16.81	0.001

Wk, week; Postop, postoperatively; Mo, month; DR, diabetic retinopathy; MT, macular thickness.

subfields; in the control group, the MT significantly increased at 1 week, 1 month, and 3 months postoperatively in fovea and parafovea, and significantly increased at 1 and 3 months postoperatively compared with baseline in perifovea (Table 4).

In DR group, there existed significant difference between MT at 1 week and 1 month postoperatively in the fovea, parafovea, and perifovea ($p < 0.001$, $p < 0.001$, and $p < 0.001$, respectively); the same was true between MT at 1 and 3 months postoperatively in the fovea, parafovea ($p = 0.02$ and 0.02, respectively) and between MT at 1 week and 3 months postoperatively in the fovea, parafovea, and perifovea ($p = 0.001$, $p = 0.008$, and $p < 0.001$, respectively). In control group, there existed significant difference between MT at 1 week and 1 month postoperatively in the fovea, parafovea, and perifovea ($p < 0.001$, $p < 0.001$, and $p = 0.007$, respectively); the same was true between MT at 1 and 3 months postoperatively in the parafovea, perifovea ($p = 0.021$ and 0.032, respectively).

Changes in MT in the DR group were significantly greater than those in the control group at 1 and 3 months postoperatively in the fovea and parafovea, and the same was true for MT in the parafovea at 1 week postoperatively and in the perifovea at 3 months postoperatively (Table 5).

The distribution of foveal MT of the control and DR groups is shown in Table 6. The proportion of foveal MT >250 μm reached its maximum, up to 68.2%, at 1 month postoperatively and was 54.5% at

3 months postoperatively in the DR group, while in the control group it was highest at 1 month (40.9%). There was no significant difference in the distribution of foveal MT between the two groups (Table 6). No patient was found to develop to pseudophakic cystoid macular edema (PCME) during the follow-up period (Figure 1).

Choroidal thickness

At baseline, there were no significant difference between the DR and control groups in foveal, parafoveal and perifoveal CT ($p = 0.376$, 0.203, and 0.107, respectively).

The CT of the DR group increased significantly at 1 week, 1 month and 3 months postoperatively in the fovea and perifovea and 1 month and 3 months postoperatively in the parafovea compared with baseline (Table 7). In the DR group, there existed significant difference in CT between 1 week and 1 month postoperatively in the fovea ($p = 0.019$); other than that, there were no significant differences in CT between any two time points postoperatively in both fovea and parafovea (all $p > 0.05$). In the control group, there were no significant differences in CT between any two time points in all subfields (all $p > 0.05$).

Changes of CT in the DR group were significantly greater than those of the control group at 1 and 3 months postoperatively in the fovea, and at 3 months postoperatively in the parafovea (Table 8).

TABLE 6 Distribution of foveal macular thickness of the two groups at four visits (mean ± SD).

Foveal MT (µm)	Baseline		1 Wk Postop		1 Mo Postop		3 Mo Postop	
	≤250	>250	≤250	>250	≤250	>250	≤250	>250
DR(n, %)	20 (90.9%)	2 (9.1%)	16 (72.7%)	6 (27.3%)	7 (31.8%)	15 (68.2%)	10 (45.5%)	12 (54.5%)
Control(n, %)	22 (100%)	0	19 (86.4%)	3 (13.6%)	13 (59.1%)	9 (40.9%)	16 (72.7%)	6 (27.3%)
p-value	0.488		0.457		0.13		0.124	

Wk, week; Postop, postoperatively; Mo, month; MT, macular thickness.
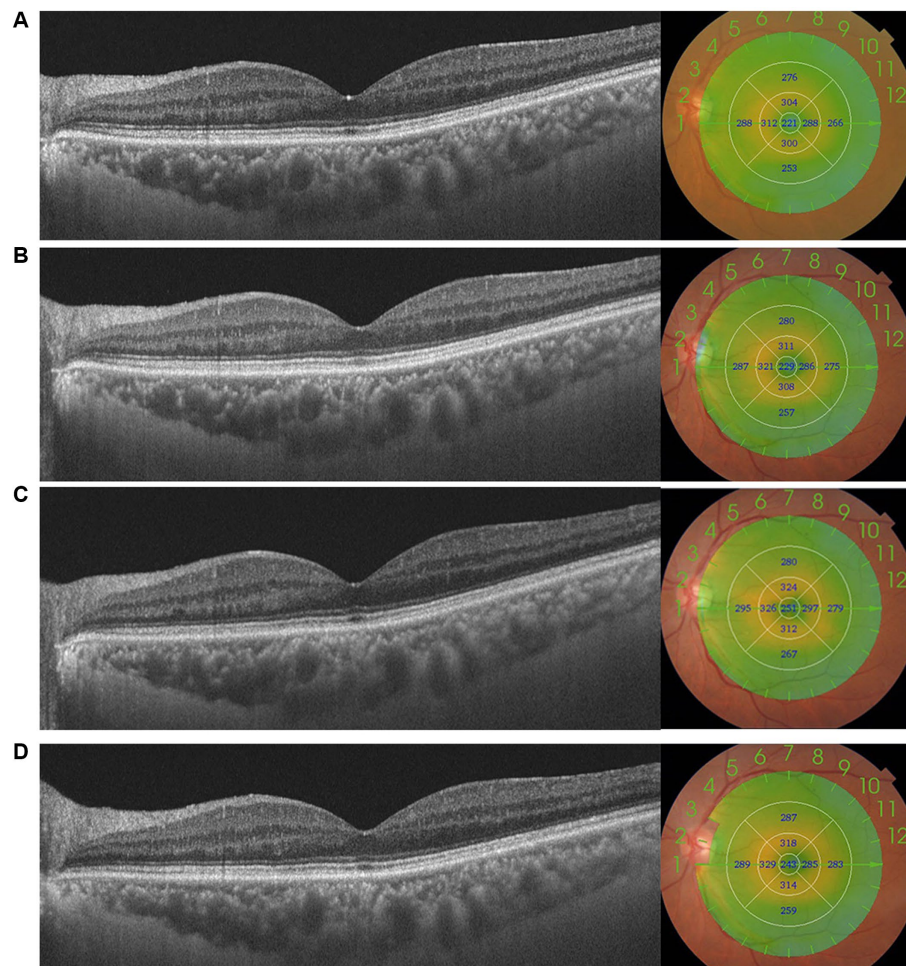
FIGURE 1
This figure shows the changes in macular thickness (MT) preoperatively **(A)** and 1 week **(B)**, 1 month **(C)**, and 3 months **(D)** postoperatively in a patient with moderate DR. MT in the central 1,000 µm increased after surgery, increasing to 251 µm, and absent of pseudophakic cystoid macular oedema (PCME).

TABLE 7 The choroidal thickness of the two groups at four visits (mean ± SD).

		Baseline	Postop						p-value
			1 Wk Postop		1 Mo Postop		3 Mo Postop		
		CT	CT	p-value	CT	p-value	CT	p-value	
Control (µm)	Fovea	222.6 ± 104.5	226.8 ± 107.8	0.57	228.8 ± 110.1	>0.999	229.5 ± 112.4	0.273	0.346
	Parafovea	220 ± 101.2	224.4 ± 105.9	0.667	228.6 ± 106.9	0.115	226.5 ± 105.4	0.21	0.022
	Perifovea	193.1 ± 84.98	198.3 ± 87.8	0.694	202.7 ± 87.35	0.066	201.8 ± 89.17	0.131	0.015
DR (µm)	Fovea	199.6 ± 59.2	211.4 ± 66.57	0.041	219.5 ± 64.53	<0.001	216.3 ± 62.61	<0.001	<0.001
	Parafovea	188.1 ± 56	199.2 ± 62.87	0.064	204.3 ± 57.48	<0.001	203.4 ± 57.48	0.001	<0.001
	Perifovea	158.8 ± 48.44	168.7 ± 53.78	0.039	174.7 ± 49.07	<0.001	172.4 ± 48.2	0.001	<0.001

Wk, week; Postop, postoperatively; Mo, month.

TABLE 8 Changes in choroidal thickness after cataract surgery (mean ± SD).

		1 Wk Postop			1 Mo Postop			3 Mo Postop		
		Control	DR	p value	Control	DR	p value	Control	DR	p value
CT (μm)	Fovea	4.25 ± 11.4	11.77 ± 18.42	0.111	6.21 ± 28.81	19.83 ± 12.06	0.035	6.93 ± 15.29	16.63 ± 13.38	0.031
	Parafovea	4.43 ± 12.5	11.13 ± 18.62	0.169	8.64 ± 15.95	16.24 ± 16.37	0.126	6.51 ± 13.54	15.34 ± 14.71	0.045
	Perifovea	5.17 ± 14.78	9.89 ± 15.32	0.305	9.56 ± 16.1	15.94 ± 10	0.121	8.67 ± 16.42	13.6 ± 14.23	0.293

Wk, week; Postop, postoperatively; Mo, month; DR, diabetic retinopathy; CT, choroidal thickness.

Discussion

Breakdown of the blood-retina barrier (BRB) can lead to the development of DR and ME (16). On the other hand, choroid is the only source of metabolic exchange for the avascular fovea (17). Postoperative inflammation may aggravate choroidal microvascular lesions, in addition to the retinal microcirculation (18). It is of great significance to clarify retinal and choroidal changes and the relationship with the occurrence of ME and deterioration of DR after cataract surgery in patients with DR, especially in early DR without DME, in which the occurrence of ME and the progression of retinopathy are crucial to postoperative visual prognosis.

Here, we report a significant increase in MT within 3 months after cataract surgery in a specific population with mild to moderate DR. George et al. observed hyperfluorescence of the macula and optic disc postoperatively on fluorescein angiography in the surgical eyes, which was greater than that in the nonsurgical eyes (19). Moreover, increased macular thickness has previously been reported in surgical diabetic eyes (18, 20), which is similar to the results of our research, although the population studied was not entirely consistent. We also observed a significant increase in CT after surgery in the DR group. This finding is consistent with the results of previous studies (15, 21–23). In addition, MT in the parafovea, and perifovea increased significantly in the control group at 1 week, 1 month, and 3 months postoperatively; while CT in the parafovea and perifovea slightly increased, though which was not significantly thicker than baseline in the control group at 1 month postoperatively. This indicates that surgical trauma itself induces a rapid increase in macular and choroidal thicknesses. To the best of our knowledge, this is the first observational follow-up study about macular microvasculature changes after phacoemulsification in this specific population of patients with mild to moderate DR using the OCTA-based VD calculation and analysis. SCP-VD in the parafoveal macula increased significantly at 1 and 3 months postoperatively compared with baseline in patients with DR in this study. This is consistent with a previous study that reported that vascular densities increased in both the SCP and deep capillary plexus (DCP) after cataract surgery (24–26). This may be due to postoperative inflammation. Inflammation is suspected to be involved in cataract surgery-mediated retinal complications. Cataract surgery induces markedly upregulated expression of IL-1 and CCL2 genes in the retina and choroid (27). In animal studies, breakdown of the inner BRB was observed after lens aspiration (28). And it was reported that decreased IOP resulted in an increase in leukocyte flow speed and choroidal thickness in the macula (22, 29). IOL decreased significantly after surgery in our study, which may be another cause of the increased VD and CT postoperatively.

What is more noteworthy is that, in our study, changes in foveal/parafoveal MT and foveal CT in patients with DR were significantly greater than those in controls at 1 and 3 months postoperatively; changes in SCP-VD in patients with DR were significantly greater than those in the control group in the parafovea at 1 and 3 months postoperatively. Presumably, it was suggested that cataract surgery might increase the risk of macular edema in patients with mild/moderate DR compared with patients without diabetes, which may be due to defects in blood-retinal barrier function in those patients with more advanced vascular changes caused by microvascular destruction in DR than in normal individuals. This finding is consistent with those of other studies. It has been reported that the retinal thickness of diabetic patients has a significantly increasing trend compared with that in non-diabetic patients (30). The presence of diabetes was a risk factor of pseudophakic macular edema (PME) and the risk increased approximately linearly with the severity of retinopathy (31). However, previous studies found no significant difference in the magnitude of changes after cataract surgery between diabetic and non-diabetic patients (32). This is inconsistent with our results and may be due to the inclusion of different patient population, and the patients enrolled in their study had less severe DR.

As is well-known, inflammation plays a role in retinal microvasculature damage and exists at different stages of DR. It plays a crucial role in the pathogenesis of DR by increasing retinal vascular permeability and promoting neovascularization, which leads to the occurrence and development of DME and DR (33–35). Diabetic patients exhibit an overall higher level of inflammatory activity than non-diabetic patients, according to previous clinical and laboratory studies (36–38). The expression of vascular endothelial growth factor (VEGF), which may be involved in increased vascular permeability and angiogenesis, is upregulated in the diabetic retina and choroid (39). And the levels of VEGF and IL-6 in aqueous humor are significantly correlated with macular edema severity in diabetic patients (40). The significantly greater changes in MT, foveal CT, and parafoveal VD observed at 1 and 3 months postoperatively in the DR group than in the control group may be due to the inflammation present in DR. Preexisting inflammatory activity caused by DR, as well as the surgery-induced inflammatory process, might be the cause of increased VD, MT, and CT in patients with mild/moderate NPDR in the present study.

In addition to postoperative inflammation, it was reported that anterior–posterior (AP) traction induced by the surgery procedure might also be a risk factor for macular edema after cataract surgery, and AP traction could disrupt the macular microcirculation, including blood–retinal barrier disfunction and increasing vascular permeability (41). In this study, MT and SCP-VD peaked 1 month postoperatively. Compared to macular thickening caused solely by mechanical traction

itself during the surgery, the disrupted macular microcirculation induced by surgery is more likely to be the direct cause of macular thickening. Furthermore, several studies have investigated the relationship between CDE and changes in retinal microcirculation after surgery. In some studies, patients with higher CDE values were reported to have a more significant reduction in VD after surgery (42, 43). In another study, it was found that changes in VD after surgery were not significantly correlated with CDE; therefore, they concluded that CDE had little effect on retinal microcirculation (32). This is consistent with our results. In the present study, there was no significant difference between the two groups, and ANCOVA test did not show relationships between CDE and variations in SCP-VD, which may imply that CDE had little effect on postoperative VD changes. There is some controversy among studies, and this may be due to the inclusion of different patient population and difference in levels of CDE between studies. Presumably, the CDE recorded in the present study was relatively small and insufficient to have a significant effect on OCT parameters. Randomized controlled trials with a large sample size should be needed in future.

In our study, MT, SCP-VD, and CT peaked 1 month after surgery. Previous reports have also shown that the incidence of ME peaks approximately 4–6 weeks after uneventful cataract surgery (44, 45). Temporally, the increases in CT，VD and MT seemed to coincide with the timing of the previously reported appearance of ME after surgery. Presumably, postoperative inflammation had the greatest impact on MT, SCP-VD, and CT at 1 month after surgery. From the point of view of time, it seems that choroidal and retinal microcirculation disorders might both be likely to be associated with the increase in MT postoperatively. Nevertheless, further research is required to determine whether the choroid is involved in the development of PME.

In this study, none of the patients developed to DME or PCME during the follow-up period. Foveal MT increased significantly after cataract surgery; foveal MT of more than 250 μm was as high as 68.2% at 1 month postoperatively. Central subfield thickness (CST), which is defined as average retinal thickness in the central 1,000 μm, corresponds to the foveal MT in this study, and 250 μm is usually the CST threshold value for diagnosing DME (46); however, no patients developed DME during the period of follow-up in our study. And in this study, BCVA of patients with DR was equivalent to that of nondiabetic individuals after surgery; therefore, increasing foveal MT could be considered a subclinical macular thickness thickening that did not affect visual acuity and was not a support of PCME, which is consistent with a previous study (10). In addition, DME and PCME after surgery were not be observed in this study, which might be due to the small size and short follow-up period. Moreover, it was reported that the risk of PME in patients with DR is high and increases with the severity of DR (31); preoperative noncenter-involved DME or a history of DME treatment may increase the risk of center-involved DME at 16 weeks after surgery (47). This study enrolled the patients with early DR and without a history of DME, which may be another reason for these observations.

Furthermore, at baseline, the parafoveal VD of DR patients was lower than that of the controls. It was previously reported that VD decreased in patients with DR without macular edema, and that VD parameters decreased with increasing DR severity (48). The foveal VD of patients with DR in our study was slightly lower than that of the controls, although the difference was not significant. This may be due to the small sample size or the fact that the population enrolled in our study included cataract patients with mild/moderate NPDR without preoperative DME, which does not reflect the full spectrum of patients with DR. However, there was no significant difference in MT between the DR and control groups at baseline. This may indicate that microvasculature changes occur before macular structural changes in patients with early DR.

This study had a few limitations. The sample size was relatively small, but the participants were homogeneous in terms of degree of retinopathy, ethnicity and sex, reducing some confounding effects. Moreover, the follow-up period was too short that we cannot observe the long-term effects on retina vessels and structural changes. Long-term follow-up is required to determine the duration of the increase in MT, CT, and VD after cataract surgery and its long-term relationship with the progression of DR severity and incidence of DME, which may be suggestive of a higher incidence of ME in this population. Future studies should enroll a larger sample of participants with longer follow-up periods.

Conclusion

Uncomplicated phacoemulsification results in a greater increase in MT, SCP-VD, and CT in patients with mild/moderate NPDR without preoperative DME than in controls. This may be suggestive of a predisposition to the occurrence of macular edema in this population, which may be due to the preexisting inflammatory activity caused by DR as well as cataract surgery trauma. However, the short-term postoperative visual prognosis of cataract patients with mild to moderate NPDR without preoperative DME is the same as that of healthy patients in this study.

Data availability statement

The original contributions presented in the study are included in the article/Supplementary material, further inquiries can be directed to the corresponding author.

Ethics statement

The studies involving humans were approved by the Ethical Review Committee of Ruijin Hospital. The studies were conducted in accordance with the local legislation and institutional requirements. The participants provided their written informed consent to participate in this study.

Author contributions

HY: Conceptualization, Data curation, Formal analysis, Investigation, Methodology, Writing – original draft. ZY: Data curation, Investigation, Writing – review & editing. YC: Methodology, Supervision, Validation, Writing – review & editing. XS: Conceptualization, Data curation, Investigation, Methodology, Supervision, Validation, Writing – review & editing.

Funding

Conflict of interest

The authors declare that the research was conducted in the absence of any commercial or financial relationships that could be construed as a potential conflict of interest.

Publisher's note

All claims expressed in this article are solely those of the authors and do not necessarily represent those of their affiliated organizations, or those of the publisher, the editors and the reviewers. Any product that may be evaluated in this article, or claim that may be made by its manufacturer, is not guaranteed or endorsed by the publisher.

Supplementary material

The Supplementary material for this article can be found online at: https://www.frontiersin.org/articles/10.3389/fmed.2023.1290599/full#supplementary-material

References

1. Flaxman SR, Bourne RRA, Resnikoff S, Ackland P, Braithwaite T, Cicinelli MV, et al. Global causes of blindness and distance vision impairment 1990-2020: a systematic review and meta-analysis. *Lancet Glob Health*. (2017) 5:e1221–34. doi: 10.1016/S2214-109X(17)30393-5

2. Yang W, Lu J, Weng J, Jia W, Ji L, Xiao J, et al. Prevalence of diabetes among men and women in China. *N Engl J Med*. (2010) 362:1090–101. doi: 10.1056/NEJMoa0908292

3. Saaddine JB, Honeycutt AA, Narayan KM, Zhang X, Klein R, Boyle JP. Projection of diabetic retinopathy and other major eye diseases among people with diabetes mellitus: United States, 2005-2050. *Arch Ophthalmol*. (2008) 126:1740–7. doi: 10.1001/archopht.126.12.1740

4. Javadi MA, Zarei-Ghanavati S. Cataracts in diabetic patients: a review article. *J Ophthalmic Vis Res*. (2008) 3:52–65.

5. Pollreisz A, Schmidt-Erfurth U. Diabetic cataract-pathogenesis, epidemiology and treatment. *J Ophthalmol*. (2010) 2010:608751:1–8. doi: 10.1155/2010/608751

6. Menchini U, Cappelli S, Virgili G. Cataract surgery and diabetic retinopathy. *Semin Ophthalmol*. (2003) 18:103–8. doi: 10.1076/soph.18.3.103.29805

7. Squirrell D, Bhola R, Bush J, Winder S, Talbot JF. A prospective, case controlled study of the natural history of diabetic retinopathy and maculopathy after uncomplicated phacoemulsification cataract surgery in patients with type 2 diabetes. *Br J Ophthalmol*. (2002) 86:565–71. doi: 10.1136/bjo.86.5.565

8. Brown JC, Solomon SD, Bressler SB, Schachat AP, DiBernardo C, Bressler NM. Detection of diabetic foveal edema: contact lens biomicroscopy compared with optical coherence tomography. *Arch Ophthalmol*. (2004) 122:330–5. doi: 10.1001/archopht.122.3.330

9. Browning DJ, McOwen MD, Bowen RM Jr, O'Marah TL. Comparison of the clinical diagnosis of diabetic macular edema with diagnosis by optical coherence tomography. *Ophthalmology*. (2004) 111:712–5. doi: 10.1016/j.ophtha.2003.06.028

10. Eriksson U, Alm A, Bjärnhall G, Granstam E, Matsson AW. Macular edema and visual outcome following cataract surgery in patients with diabetic retinopathy and controls. *Graefes Arch Clin Exp Ophthalmol*. (2011) 249:349–59. doi: 10.1007/s00417-010-1484-9

11. Hee MR, Puliafito CA, Wong C, Duker JS, Reichel E, Rutledge B, et al. Quantitative assessment of macular edema with optical coherence tomography. *Arch Ophthalmol*. (1995) 113:1019–29. doi: 10.1001/archopht.1995.01100080071031

12. Im JHB, Jin YP, Chow R, Yan P. Prevalence of diabetic macular edema based on optical coherence tomography in people with diabetes: a systematic review and meta-analysis. *Surv Ophthalmol*. (2022) 67:1244–51. doi: 10.1016/j.survophthal.2022.01.009

13. Ghassemi F, Fadakar K, Berijani S, Babeli A, Gholizadeh A, Sabour S. Quantitative assessment of vascular density in diabetic retinopathy subtypes with optical coherence tomography angiography. *BMC Ophthalmol*. (2021) 21:82. doi: 10.1186/s12886-021-01831-8

14. Wilkinson CP, Ferris FL 3rd, Klein RE, Lee PP, Agardh CD, Davis M, et al. Proposed international clinical diabetic retinopathy and diabetic macular edema disease severity scales. *Ophthalmology*. (2003) 110:1677–82. doi: 10.1016/S0161-6420(03)00475-5

15. Yao H, Gao S, Liu X, Zhou Y, Cheng Y, Shen X. Choroidal structural changes assessed with swept-source optical coherence tomography after cataract surgery in eyes with diabetic retinopathy. *J Ophthalmol*. (2020) 2020:1–9. doi: 10.1155/2020/5839837

16. Cunha-Vaz J, Bernardes R, Lobo C. Blood-retinal barrier. *Eur J Ophthalmol*. (2011) 21:3–9. doi: 10.5301/EJO.2010.6049

17. Mrejen S, Spaide RF. Optical coherence tomography: imaging of the choroid and beyond. *Surv Ophthalmol*. (2013) 58:387–429. doi: 10.1016/j.survophthal.2012.12.001

18. Brito PN, Rosas VM, Coentrão LM, Carneiro ÂV, Rocha-Sousa A, Brandão E, et al. Evaluation of visual acuity, macular status, and subfoveal choroidal thickness changes after cataract surgery in eyes with diabetic retinopathy. *Retina*. (2015) 35:294–302. doi: 10.1097/IAE.0000000000000298

19. Escaravage GK Jr, Cohen KL, Patel SB, Hartnett ME, Armstrong BD, Janowski CM. Quantification of macular and optic disc hyperfluorescence after phacoemulsification in diabetes mellitus. *J Cataract Refract Surg*. (2006) 32:803–11. doi: 10.1016/j.jcrs.2006.01.073

20. Kim SJ, Equi R, Bressler NM. Analysis of macular edema after cataract surgery in patients with diabetes using optical coherence tomography. *Ophthalmology*. (2007) 114:881–9. doi: 10.1016/j.ophtha.2006.08.053

21. Aslan Bayhan S, Bayhan HA, Muhafiz E, Kırboğa K, Gürdal C. Evaluation of choroidal thickness changes after phacoemulsification surgery. *Clin Ophthalmol*. (2016) 10:961–7. doi: 10.2147/OPTH.S94096

22. Ohsugi H, Ikuno Y, Ohara Z, Imamura H, Nakakura S, Matsuba S, et al. Changes in choroidal thickness after cataract surgery. *J Cataract Refract Surg*. (2014) 40:184–91. doi: 10.1016/j.jcrs.2013.07.036

23. Yılmaz T, Karci AA, Yilmaz İ, Yılmaz A, Yıldırım Y, Sakalar YB. Long-term changes in subfoveal choroidal thickness after cataract surgery. *Med Sci Monit*. (2016) 22:1566–70. doi: 10.12659/MSM.898714

24. Zhao Z, Wen W, Jiang C, Lu Y. Changes in macular vasculature after uncomplicated phacoemulsification surgery: optical coherence tomography angiography study. *J Cataract Refract Surg*. (2018) 44:453–8. doi: 10.1016/j.jcrs.2018.02.014

25. Yu S, Frueh BE, Steinmair D, Ebneter A, Wolf S, Zinkernagel MS, et al. Cataract significantly influences quantitative measurements on swept-source optical coherence tomography angiography imaging. *PLoS One*. (2018) 13:e0204501. doi: 10.1371/journal.pone.0204501

26. Jia X, Wei Y, Song H. Optical coherence tomography angiography evaluation of the effects of phacoemulsification cataract surgery on macular hemodynamics in Chinese normal eyes. *Int Ophthalmol*. (2021) 41:4175–85. doi: 10.1007/s10792-021-01987-8

27. Xu H, Chen M, Forrester JV, Lois N. Cataract surgery induces retinal pro-inflammatory gene expression and protein secretion. *Invest Ophthalmol Vis Sci*. (2011) 52:249–55. doi: 10.1167/iovs.10-6001

28. Liu H, Demetriades AM, Xiao WH, Campochiaro PA, Vinores SA. Mouse model of post-surgical breakdown of the blood-retinal barrier. *Curr Eye Res*. (2004) 28:421–6. doi: 10.1080/02713680490503769

29. Grunwald JE, Sinclair SH, Riva CE. Autoregulation of the retinal circulation in response to decrease of intraocular pressure below normal. *Invest Ophthalmol Vis Sci*. (1982) 23:124–7.

30. Degenring RF, Vey S, Kampmeter B, Budde WM, Jonas JB, Sauder G. Effect of uncomplicated phacoemulsification on the central retina in diabetic and non-diabetic subjects. *Graefes Arch Clin Exp Ophthalmol*. (2007) 245:18–23. doi: 10.1007/s00417-006-0377-4

31. Chu CJ, Johnston RL, Buscombe C, Sallam AB, Mohamed Q, Yang YC. Risk factors and incidence of macular Edema after cataract surgery: a database study of 81984 eyes. *Ophthalmology*. (2016) 123:316–23. doi: 10.1016/j.ophtha.2015.10.001

32. Feng L, Azhati G, Li T, Liu F. Macular vascular density changes following cataract surgery in diabetic patients: an optical coherence tomography angiography study. *J Ophthalmol*. (2021) 2021:1–7. doi: 10.1155/2021/6641944

33. Kaštelan S, Tomić M, Gverović Antunica A, Salopek Rabatić J, Ljubić S. Inflammation and pharmacological treatment in diabetic retinopathy. *Mediat Inflamm*. (2013) 2013:213130:1–8. doi: 10.1155/2013/213130

34. Gouliopoulos NS, Kalogeropoulos C, Lavaris A, Rouvas A, Asproudis I, Garmpi A, et al. Association of serum inflammatory markers and diabetic retinopathy: a review of literature. *Eur Rev Med Pharmacol Sci*. (2018) 22:7113–28. doi: 10.26355/eurrev_201811_16243

35. Capitão M, Soares R. Angiogenesis and inflammation crosstalk in diabetic retinopathy. *J Cell Biochem*. (2016) 117:2443–53. doi: 10.1002/jcb.25575

36. Dong N, Xu B, Wang B, Chu L, Tang X. Aqueous cytokines as predictors of macular edema in patients with diabetes following uncomplicated phacoemulsification cataract surgery. *Biomed Res Int*. (2015) 2015:126984:1–8. doi: 10.1155/2015/126984

37. Hernández C, Segura RM, Fonollosa A, Carrasco E, Francisco G, Simó R. Interleukin-8, monocyte chemoattractant protein-1 and IL-10 in the vitreous fluid of patients with proliferative diabetic retinopathy. *Diabet Med*. (2005) 22:719–22. doi: 10.1111/j.1464-5491.2005.01538.x

38. Dong N, Li X, Xiao L, Yu W, Wang B, Chu L. Upregulation of retinal neuronal MCP-1 in the rodent model of diabetic retinopathy and its function in vitro. *Invest Ophthalmol Vis Sci*. (2012) 53:7567–75. doi: 10.1167/iovs.12-9446

39. Lutty GA, McLeod DS, Merges C, Diggs A, Plouet J. Localization of vascular endothelial growth factor in human retina and choroid. *Arch Ophthalmol*. (1996) 114:971–7. doi: 10.1001/archopht.1996.01100140179011

40. Funatsu H, Yamashita H, Noma H, Mimura T, Yamashita T, Hori S. Increased levels of vascular endothelial growth factor and interleukin-6 in the aqueous humor of diabetics with macular edema. *Am J Ophthalmol*. (2002) 133:70–7. doi: 10.1016/S0002-9394(01)01269-7

41. Copete S, Martí-Rodrigo P, Muñiz-Vidal R, Pastor-Idoate S, Rigo J, Figueroa MS, et al. Preoperative vitreoretinal interface abnormalities on spectral domain optical coherence tomography as risk factor for PSEUDOPHAKIC cystoid macular EDEMA after phacoemulsification. *Retina*. (2019) 39:2225–32. doi: 10.1097/IAE.0000000000002298

42. Wang Z, Wang E, Chen Y. Transient reduction in macular deep capillary density on optical coherence tomography angiography after phacoemulsification surgery in diabetic patients. *BMC Ophthalmol*. (2020) 20:335. doi: 10.1186/s12886-020-01605-8

43. Tan LZ, Tian F, Chen L, Sun LN, Gong X, Liang JL, et al. Changes in the peripapillary vasculature and macular thickness after cataract surgery using two phacoemulsification systems with optical coherence tomography angiography. *Int J Ophthalmol*. (2022) 15:932–9. doi: 10.18240/ijo.2022.06.10

44. Perente I, Utine CA, Ozturker C, Cakir M, Kaya V, Eren H, et al. Evaluation of macular changes after uncomplicated phacoemulsification surgery by optical coherence tomography. *Curr Eye Res*. (2007) 32:241–7. doi: 10.1080/02713680601160610

45. Buyukyildiz HZ, Gulkilik G, Kumcuoglu YZ. Early serous macular detachment after phacoemulsification surgery. *J Cataract Refract Surg*. (2010) 36:1999–2002. doi: 10.1016/j.jcrs.2010.07.007

46. Wang YT, Tadarati M, Wolfson Y, Bressler SB, Bressler NM. Comparison of prevalence of diabetic macular Edema based on monocular fundus photography vs optical coherence tomography. *JAMA Ophthalmol*. (2016) 134:222–8. doi: 10.1001/jamaophthalmol.2015.5332

47. Arevalo JF. Diabetic macular edema: changing treatment paradigms. *Curr Opin Ophthalmol*. (2014) 25:502–7. doi: 10.1097/ICU.0000000000000102

48. Samara WA, Shahlaee A, Adam MK, Khan MA, Chiang A, Maguire JI, et al. Quantification of diabetic macular ischemia using optical coherence tomography angiography and its relationship with visual acuity. *Ophthalmology*. (2017) 124:235–44. doi: 10.1016/j.ophtha.2016.10.008

Sex-related difference in the retinal structure of young adults: a machine learning approach

Flávia Monteiro Farias[1,2], Railson Cruz Salomão[2],
Enzo Gabriel Rocha Santos[3], Andrew Sousa Caires[1],
Gabriela Santos Alvarez Sampaio[1],
Alexandre Antônio Marques Rosa[4], Marcelo Fernandes Costa[5]
and Givago Silva Souza[1,2]*

[1]Instituto de Ciências Biológicas, Universidade Federal do Pará, Belém, Brazil, [2]Núcleo de Medicina
Tropical, Universidade Federal do Pará, Belém, Brazil, [3]Instituto de Ciências Exatas e Naturais,
Universidade Federal do Pará, Belém, Brazil, [4]Instituto de Ciências da Saúde, Universidade Federal do
Pará, Belém, Brazil, [5]Departamento de Psicologia, Instituto de Psicologia, Universidade de São Paulo,
São Paulo, Brazil

Purpose: To compare the accuracy of machine learning (ML) algorithms to classify the sex of the participant from retinal thickness datasets in different retinal layers.

Methods: This cross-sectional study involved 26 male and 38 female subjects. Data were acquired using HRA + OCT Spectralis, and the thickness and volume of 10 retinal layers were quantified. A total of 10 features were extracted from each retinal layer. The accuracy of various algorithms, including k-nearest-neighbor, support vector classifier, logistic regression, linear discriminant analysis, random forest, decision tree, and Gaussian Naïve Bayes, was quantified. A two-way ANOVA was conducted to assess the ML accuracy, considering both the classifier type and the retinal layer as factors.

Results: A comparison of the accuracies achieved by various algorithms in classifying participant sex revealed superior results in datasets related to total retinal thickness and the retinal nerve fiber layer. In these instances, no significant differences in algorithm performance were observed ($p > 0.05$). Conversely, in other layers, a decrease in classification accuracy was noted as the layer moved outward in the retina. Here, the random forest (RF) algorithm demonstrated superior performance compared to the others ($p < 0.05$).

Conclusion: The current research highlights the distinctive potential of various retinal layers in sex classification. Different layers and ML algorithms yield distinct accuracies. The RF algorithm's consistent superiority suggests its effectiveness in identifying sex-related features from a range of retinal layers.

KEYWORDS

retina, retinal thickness, macula, machine learning, sex-related differences

Introduction

Over the past 30 years, optical coherence tomography (OCT) has been used as a non-invasive method for image acquisition to evaluate the anterior and posterior segments of the eye in both diseased and healthy conditions of the human retinal structure (1–3). The development of eye diseases can occur throughout life due to the natural aging process, exposure to unhealthy lifestyle habits, systemic disorders, or genetic inheritance. In addition to these factors, sex-related factors, such as the concentrations of sex hormones that vary throughout an individual's life, can also influence the development of eye diseases (4–6).

The existence of sexual dimorphism of the retina in humans has been investigated using OCT. The first findings of retinal sexual dimorphism pointed to a larger total retinal thickness in male subjects than in female subjects (7–12). However, the debate regarding retinal layers remains open, as some studies have observed that some retinal layers are thicker in male subjects than in female subjects, while other investigations have found no or few sex-related differences (13–19).

Overall, investigating sex-related features in the human retina is an important area of research that could lead to new insights into the causes of retinal diseases, the development of sex-specific treatments, and the design of more effective medical devices for the eye and the possible impact of postmenopausal hormone replacement anti-estrogenic therapy therapy (20).

Due to the large amount of data extracted from the retina during an OCT scan, the use of machine learning methods could be an alternative candidate for analyzing OCT data. Machine learning methods have been used due to their ability to capture complex relationships, work with high-dimensional data, generalize to new data, be flexible and adaptable, and perform automated learning of relevant features, reducing the need for human intervention (21–23). Compared to norms based on populational averages, which may not account for the significant individual variability that exists within each sex group, machine learning models can capture and leverage this variability, allowing for more precise and individualized assessments of retinal thickness. This individualized precision can be particularly valuable in clinical decision-making as it takes into account the uniqueness of each patient's condition. Additionally, retinal thickness datasets can exhibit complex patterns and subtle variations that may not be fully captured by simple norm-based criteria.

In the present study, we aimed to evaluate the performance of several machine learning algorithms to predict the sex of the participants based on information from retinal structure features. Our primary goal was to identify which retinal layers are best to correctly classify the sex of the participant and which machine learning algorithms are better for predicting the participant's sex in the different retinal layers.

Materials and methods

Ethical considerations

The present study was approved by the Ethical Committee for Research in Humans of the Universidade Federal do Pará (report number 3.285.557). All participants were informed about the experimental procedures and gave written consent to participate in the study.

Participants

The sample consisted of 26 male participants (mean age ± standard deviation: 26.19 ± 4.96 years) and 38 participants (mean age ± standard deviation: 26.05 ± 4.68 years). All participants had normal visual acuity or were corrected to 20/20 visual acuity using a refractive lens. Only two participants (one male and one female) used optical corrections of −0.5 and −0.7 diopters and we considered that any imprecision of their OCT measurements had little or no influence on the results. Participants with neurological, systemic, eye, or retinal diseases that affected the structure or function of the visual system were excluded.

OCT imaging

Retinal OCT imaging was performed using the Spectralis HRA + OCT system (Heidelberg Engineering GmbH, Heidelberg, Germany). Each session consisted of a 25-line horizontal raster scan in a $20° \times 20°$ area centered on the fovea, followed by 24 automated real-time repetitions. The Heidelberg Eye Explorer software (Heidelberg Engineering GmbH, Heidelberg, Germany) was used to segment retinal layers [total retina (TR), retinal nerve fiber layer (RNFL), ganglion cell layer (GCL), inner plexiform layer (IPL), inner nuclear layer (INL), outer plexiform layer (OPL), outer nuclear layer (ONL), and retinal pigmented epithelium (RPE)] and three combinations of retinal layers [overall retinal, outer retinal layers (ORL), which range from the external limiting membrane to Bruch's membrane, and inner retinal layers (IRL), which range from the inner limiting membrane to the external limiting membrane]. The thickness and volume of each layer were quantified. Visual inspection of the segmentation was performed to avoid possible errors. The outcome of the image segmentation of retinal layers was the mean thickness of nine macular subfields (central, nasal inner, temporal inner, superior inner, inferior inner, nasal outer, temporal outer, superior outer, and inferior outer), following the Early Treatment Diabetic Retinopathy Study (ETDRS) grid. The volume of each layer was also extracted.

For each participant, the examination was performed by the same operator following the manufacturer's guidelines. Two images were obtained in sequence for each eye on the same day. The first image was used as a reference to scan the same parts of the retina during the second image (device's follow-up mode). The thickness of both images was averaged for subsequent analysis. Data were acquired from 128 eyes with the Spectralis HRA + OCT system, and 64 eyes were randomly selected for analysis.

Machine learning algorithms

Prior to the application of ML algorithms, a bootstrap resampling method was employed, utilizing 200 replications for each feature derived from OCT readings. A total of 10 features were used for each retinal layer, comprising nine subfield thicknesses and the volume of the retinal layer. Python scripts were utilized for data

analysis and normalization, feature selection, and the execution of ML algorithms through the training and testing phases. The performance of the ML was subsequently evaluated.

We utilized the *StandardScaler* function from the sklearn. Preprocessing package to standardize the features into standard deviation units, as shown in Equation 1.

$$\text{Standardized\_feature} = (\text{feature}-\text{mean})/\text{standard\_deviation} \quad \text{(Equation 1)}$$

The standardized features were used to train and test seven supervised ML algorithms:

The *sklearn.neighbors.KNeighborsClassifier* function was employed to implement the k-nearest neighbors (kNN) algorithm, utilizing the Minkowski distance and a k-value within the range of 5–10. The optimal k-value, which yielded the highest accuracy, was determined using the *GridSearchCV* function.

The support vector classifier (SVC) utilizes *sklearn.svm.SVC* function with the radial basis function kernel. The gamma and C parameters are set to 1 and 10, respectively.

The *sklearn.linear_model.LogisticRegression* function is utilized for logistic regression (LR), with the parameters "*penalty*" and "*solver*" set to "*l1*" and "*liblinear*," respectively.

The *sklearn.discriminant_analysis.LinearDiscriminantAnalysis* function is utilized for linear discriminant analysis. The parameters "*solver*" and "*store_covariance*" are set to "*svd*" and "*true*," respectively.

The *sklearn.ensemble.RandomForestClassifier* function is utilized in the application of random forest (RF), with the parameters set as follows: "*criterion*" is set to "*gini impurity*," "*n_estimators*" is set to 50, and "*max_depth*" is set to 6.

The decision tree (DT) employs the *sklearn.tree. DecisionTreeClassifier* function, maintaining identical parameter values for "*criterion*," "*n_estimators*," and "*max_depth*," as utilized in the RF algorithm.

Gaussian Naïve Bayes (GNB) using the *sklearn.naive_ bayes.GaussianNB* function.

The accuracy of ML algorithms in correctly classifying the data was evaluated (Equation 2).

$$\text{Accuracy} = (\text{true positives} + \text{true negatives})/\text{total} \quad \text{(Equation 2)}$$

True positives represent the data points correctly classified as male, while true negatives denote those accurately identified as female. The total refers to the overall number of data points.

The *ShuffleSplit* function from the *Scikit-learn* library (version 0.21.3) was utilized to divide the data, allocating 70% for model training and 30% for model testing.

Statistics

We used a *t*-test to compare the thickness of the different datasets obtained from both eyes of male and female subjects and to later carry out an intergroup comparison of retinal layer thickness. We conducted a one-way ANOVA to evaluate the influence of macular field in the retinal thickness as well as two-way ANOVA to evaluate the influence of the classifier type and retinal dataset factors on the accuracies (model training and model testing) of the classifier. For multiple comparisons, we employed the Tukey HSD *post-hoc* test. We compared the accuracies of the model training and model testing using a *t*-test for repeated measures. A confidence level of 5% was applied for the statistical comparisons.

Results

Inter-eye comparison of the retinal thickness for male and female subjects

To ensure that the selection of the eye did not introduce any bias, we conducted a comparison of the thickness of various retinal layers between the right and left eyes of participants of both sexes. Our analysis revealed that no significant differences were observed in any of the retinal layers between the eyes. Based on these findings, we opted to randomly select one eye from each participant for data extraction concerning retinal thickness. Table 1 displays the comparison of retinal thickness in the various datasets obtained from both eyes within the sample.

We randomly select one eye to extract retinal thickness and compared this feature between male and female groups, as depicted in Table 2. Our findings indicated significant differences in the total

TABLE 1 Comparison of the retinal thickness obtained from both eyes of male and female groups.

Thickness (μm)	Male group		*p*-value	Female group		*p*-value
	Right eye	Left eye		Right eye	Left eye	
TR	323.6 ± 10.8	322.3 ± 10.8	0.65	311.1 ± 12.7	309.8 ± 13.4	0.72
RNFL	28 ± 2	27.3 ± 2.2	0.22	25.9 ± 2.3	25.3 ± 2	0.33
GCL	43.4 ± 2.4	43.3 ± 2.4	0.87	40.4 ± 3.6	40.3 ± 3.7	0.89
IPL	36.1 ± 1.6	36.1 ± 1.7	0.86	34 ± 2.7	34.2 ± 2.8	0.88
INL	35.6 ± 2.1	35.7 ± 2.1	0.91	33.5 ± 2.6	33.3 ± 2.3	0.79
OPL	28.4 ± 2.7	29.3 ± 2.8	0.23	28.8 ± 4.1	29.06 ± 4.1	0.81
ONL	69.2 ± 8.1	68.5 ± 8.3	0.76	66.6 ± 6.4	66.4 ± 7.1	0.90
RPE	15 ± 1.1	15 ± 1	0.93	14.9 ± 1.2	14.64 ± 1.4	0.45

TR, total retina; RNFL, retinal nerve fiber layer; GCL, ganglion cell layer; IPL, inner plexiform layer; INL, inner nuclear layer; OPL, outer plexiform layer; ONL, outer nuclear layer; RPE, retinal pigmented epithelium.

TABLE 2 Comparison of retinal layer thickness between male and female groups.

Retinal layers	Retinal thickness (μm)		p-value
	Male group	Female group	
TR	322.9 ± 11.3	310.6 ± 12.9	0.0005
RNFL	27.8 ± 2.1	25.3 ± 1.8	<0.0001
GCL	43.2 ± 2.2	40.4 ± 3.5	0.0012
IPL	36 ± 1.6	34.1 ± 2.8	0.0039
INL	35.6 ± 2.2	33.4 ± 2.5	0.0016
OPL	29.1 ± 2.6	29.3 ± 4.2	0.78
ONL	68.7 ± 8.3	66.4 ± 6.8	0.28
RPE	15.1 ± 1	14.7 ± 1.2	0.22

TR, total retina; RNFL, retinal nerve fiber layer; GCL, ganglion cell layer; IPL, inner plexiform layer; INL, inner nuclear layer; OPL, outer plexiform layer; ONL, outer nuclear layer; RPE, retinal pigmented epithelium.

retina and layers comprising information from the inner retina (RNFL, GCL, IPL, INL), with the male group exhibiting greater thickness compared to the female group ($p < 0.01$). Conversely, no significant differences were discerned in the layers within the outer retina (OPL, ONL, RPE; $p > 0.01$).

In the intergroup comparison, considering the thickness of different macular fields (Table 3), we observed that in datasets representing the total retina and data from the inner retina, the male group had thicker tissues across all fields than the female group ($p < 0.01$). However, in the datasets from the outer retina, we observed a predominance of non-significant differences.

Machine learning accuracies during model training

Table 4 presents the mean accuracies (± standard deviation) derived from model training across various classifiers and retinal datasets. The results of a two-way ANOVA revealed significant effects attributed to both the algorithm factor, the retinal dataset factor, and the interaction between these two factors, as summarized in Table 5. Notably, *post hoc* multiple comparisons demonstrated that the accuracies achieved by all algorithms were markedly superior when utilizing the total retina dataset and datasets originating from the inner retina (RNFL, GCL, IPL, INL), as compared to datasets from the outer retina (OPL, ONL, and RPE).

In evaluating the accuracies of different algorithms across the diverse retinal datasets, multiple comparisons indicated a notable absence of significant differences in algorithm performance within the total retina dataset and the inner retina datasets ($p > 0.05$). Conversely, in the OPL dataset, it was evident that random forest (RF), support vector classifier (SVC), and decision tree (DT) exhibited significantly higher accuracies when contrasted with other algorithms. Similarly, in the ONL dataset, random forest and decision tree outperformed their counterparts. Notably, in the RPE dataset, random forest demonstrated the highest accuracy among all algorithms.

Machine learning accuracies during model testing

Table 6 displays the mean accuracies (± standard deviation) derived from model testing across various classifiers and retinal datasets. Once again, the results of a two-way ANOVA revealed significant effects associated with the algorithm factor, the retinal dataset factor, and their interaction (as summarized in Table 7). *Post hoc* multiple comparisons further substantiated that, much like the training model, all algorithms achieved significantly higher accuracy levels when employing the total retina dataset and datasets from the inner retina, in comparison to the datasets from the outer retina. Consistent with the training model, the results of multiple comparisons within the total retina dataset and datasets from the inner retina indicated an absence of significant differences in algorithm accuracies ($p > 0.05$). In contrast, concerning the outer retina, random forest (RF) exhibited notably higher accuracy compared to other algorithms ($p < 0.05$).

Comparison of the accuracies estimated for the models in the training and testing stages

The comparison of the accuracies calculated for the models in the training and testing showed that 10.8% of the comparisons had significant differences, and all of them showed higher accuracy of the model in the training (Figure 1).

After finding that the random forest classifier outperformed other methods in classifying the datasets, we examined feature importance scores, which indicate the extent to which each feature influences the model's predictions. Random forest employs the Gini impurity, which reveals how frequently a feature is used to split the data in its decision trees. Figure 2 displays the feature importance scores for macular thickness in different fields. We conducted one-way ANOVA to assess the impact of the macular field on the feature importance score for each dataset. We found that in all datasets, there were significant differences ($p < 0.01$), with one or more fields having a greater importance than others in the classification decision.

Discussion

This study's findings reveal significant patterns in the classification accuracy of sex-specific data, utilizing various retinal layers and ML algorithms. The most reliable accuracies for accurately distinguishing between male and female participants were observed when analyzing data from the total retinal structure and the retinal nerve fiber layer. These results suggest that these retinal layers possess unique sex-related characteristics that were effectively identified by the employed ML techniques. Interestingly, the highest classification accuracies were consistently achieved using these retinal layers, yet no statistically significant differences were detected among the accuracies derived from the various ML algorithms used in this study. This suggests that the algorithms consistently performed when tasked with sex classification based

TABLE 3 Comparison of retinal dataset thickness in the different macular fields from measurements obtained from both groups.

Retinal thickness (μm)							
TR	Male	Female	*p*-value	RNFL	Male	Female	*p*-value
C	274.9 ± 15.9	258.6 ± 18.9	<0.01*	C	12 ± 1.5	10.3 ± 2.1	<0.01*
NI	353.1 ± 12.8	338.4 ± 16.9	<0.01*	NI	21.1 ± 2.1	18.8 ± 1.4	<0.01*
NO	328.8 ± 13.3	318 ± 14.0	0.04*	NO	48.6 ± 5.6	44.8 ± 4.5	<0.01*
TI	336.5 ± 10.3	320.6 ± 14.7	<0.01*	TI	16.9 ± 1.4	16 ± 0.9	<0.01*
TO	297.6 ± 13.9	283.3 ± 11.4	<0.01*	TO	18.8 ± 1.2	17.7 ± 1	<0.01*
SI	353 ± 12.8	340 ± 16.2	<0.01*	SI	24.5 ± 2.9	21.9 ± 2.4	<0.01*
SO	313.8 ± 13.3	305.7 ± 13.2	0.02*	SO	39.5 ± 5	36.6 ± 4.1	0.02*
II	351.1 ± 11.7	336.4 ± 16.8	<0.01*	II	26.1 ± 2.6	23.8 ± 2.2	<0.01*
IO	300.8 ± 10.8	291.9 ± 12.5	0.02*	IO	41.8 ± 4.8	39 ± 4.3	0.02*
GCL	Male	Female	*p*-value	IPL	Male	Female	*p*-value
C	15.4 ± 2.8	12.9 ± 4.1	<0.01*	C	21.2 ± 2.6	19.18 ± 3.1	<0.01*
NI	54.7 ± 3.9	50.7 ± 5.9	<0.01*	NI	45.2 ± 3	41.6 ± 4.7	<0.01*
NO	41.7 ± 3.5	40.7 ± 3.3	0.45	NO	31.9 ± 2.5	31.5 ± 3	0.51
TI	51.1 ± 3.4	46.3 ± 5.7	<0.01*	TI	43.7 ± 2.3	41.9 ± 4.3	0.02*
TO	41.2 ± 3.8	36.9 ± 3.5	<0.01*	TO	34.4 ± 2.6	32.3 ± 2.3	<0.01*
SI	55.4 ± 3.2	52.3 ± 5.7	0.01*	SI	44 ± 2.2	41.4 ± 3.4	<0.01*
SO	38.1 ± 2.8	37.3 ± 3.2	0.168	SO	31.1 ± 2.3	30.3 ± 2.5	0.15
II	55.5 ± 2.6	53.3 ± 5.3	0.02*	II	43.6 ± 1.9	41.2 ± 4.1	0.04*
IO	36.2 ± 3.2	35.3 ± 3.5	0.34	IO	29.5 ± 2	28.6 ± 2.5	0.21
INL	Male	Female	*p*-value	OPL	Male	Female	*p*-value
C	17.8 ± 4.1	13.9 ± 4.4	<0.01*	C	21.9 ± 4	22.1 ± 5.8	0.92
NI	41.59 ± 4	38.3 ± 4	<0.01*	NI	33 ± 6.5	32.1 ± 6.5	0.66
NO	37 ± 1.7	36.8 ± 2.8	0.4	NO	29.8 ± 3.1	29 ± 4.4	0.42
TI	37.7 ± 3.3	34.9 ± 3.4	0.01*	TI	29.3 ± 2.4	31.5 ± 7.1	0.20
TO	36.7 ± 2.2	34.8 ± 2.5	<0.01*	TO	27.3 ± 2	27.24 ± 3.8	0.95
SI	40.7 ± 3.2	39.3 ± 3.7	0.07	SI	32.4 ± 5.2	36.4 ± 9.5	0.11
SO	33.8 ± 2	32.9 ± 2.4	0.39	SO	27 ± 1.7	28.3 ± 4.8	0.23
II	42.2 ± 3.5	39.2 ± 4.3	<0.01*	II	32 ± 5.1	31.3 ± 5.4	0.46
IO	33.4 ± 2.3	31.8 ± 2.4	0.09	IO	26.8 ± 2.3	26.3 ± 2.8	0.23
ONL	Male	Female	*p*-value	RPE	Male	Female	*p*-value
C	93.6 ± 9	91 ± 11.63	0.43	C	18.3 ± 1.5	17.3 ± 1.7	0.21
NI	72.3 ± 13	71.1 ± 11.7	0.99	NI	16.2 ± 1.2	16 ± 1.6	0.92
NO	57.4 ± 8.8	58.7 ± 6.7	0.88	NO	14 ± 1.3	13.8 ± 1.4	0.77
TI	75.3 ± 7.8	71.1 ± 8	0.04*	TI	15.1 ± 1.3	14.4 ± 1.3	0.07
TO	60.8 ± 7.2	57.4 ± 6	0.09	TO	13.3 ± 1.2	13.2 ± 1.2	0.27
SI	71.3 ± 10.7	67.1 ± 11	0.07	SI	16 ± 1.5	15.7 ± 1.6	0.50
SO	64.1 ± 8.2	60.5 ± 6.8	0.15	SO	14.1 ± 1.2	13.6 ± 1.5	0.24
II	68.5 ± 10.3	68 ± 8.6	0.88	II	15.4 ± 1	15 ± 1.2	0.24
IO	54 ± 6.3	53 ± 5.5	0.68	IO	13.6 ± 1.2	13.1 ± 1.1	0.21

TR, total retina; RNFL, retinal nerve fiber layer; GCL, ganglion cell layer; IPL, inner plexiform layer; INL, inner nuclear layer; OPL, outer plexiform layer; ONL, outer nuclear layer; RPE, retinal pigmented epithelium. C, central retina; NI, nasal inner; NO, nasal outer; TI, temporal inner; TO, temporal outer; SI, superior inner; SO, superior outer; II, inferior inner; IO, inferior outer.
*$p < 0.05$.

on retinal data, regardless of their inherent methodologies. Moreover, a fascinating trend was observed where classification accuracies showed a decreasing trend as the analysis moved toward the outer retinal layers. Additionally, some algorithms demonstrated statistically significant deviations from others in terms of classification accuracy. Notably, the RF algorithms displayed higher accuracies compared to the others in this context.

While the sex of a patient is typically known during a consultation, it is not always evident whether the retinal thickness of that patient aligns with the sex-based patterns expected. Comparing a patient's retinal thickness to sex-based populational norms can be a valuable tool in evaluating the patient. However, alternative approaches, such as machine learning, can complement conventional statistical methods. For instance, our study revealed

TABLE 4 Comparison of mean accuracies (± standard deviation) obtained from the machine learning algorithms to classify the sex-related differences in the retinal layers (and total retina) for model training.

	Machine learning algorithm accuracies (%)						
Layers	SVC	GNB	RF	KNN	LR	LD	DT
RPE	72.5 ± 9.6	71.8 ± 5.1	83 ± 4.5	64.3 ± 5.5	68.5 ± 6.2	69.3 ± 7.6	71.3 ± 9.9
ONL	69.3 ± 6.5	67.8 ± 7.1	90.5 ± 5.5	68.5 ± 9.4	67.5 ± 8.7	65.3 ± 6.3	82.8 ± 5.2
OPL	79.8 ± 7.5	70.5 ± 4.1	89.5 ± 5.8	71.8 ± 5	65.5 ± 7.5	66.8 ± 7.8	79.8 ± 6.8
INL	84.5 ± 4.5	89 ± 3.4	92.3 ± 3.8	81.5 ± 6.5	85 ± 6.2	85.8 ± 6.7	81.5 ± 6
IPL	85.8 ± 3.3	88 ± 3.3	92 ± 5	83.8 ± 5.4	84.5 ± 6.1	82.3 ± 5.3	82.3 ± 7.2
GCL	89.5 ± 3.7	90 ± 4.3	94.5 ± 2	89.8 ± 4.3	85.5 ± 4.7	87.5 ± 4.3	88 ± 3.9
RNFL	92.3 ± 2.8	91.5 ± 3.8	94.5 ± 2.8	91 ± 4.6	90.5 ± 3.9	91 ± 3.2	90.8 ± 4.7
TR	92.5 ± 2.3	96 ± 2.4	96.5 ± 3.9	91 ± 4.6	93.5 ± 5.3	93.3 ± 3.9	89 ± 4.3

TR, total retina; RNFL, retinal nerve fiber layer; GCL, ganglion cell layer; IPL, inner plexiform layer; INL, inner nuclear layer; OPL, outer plexiform layer; ONL, outer nuclear layer; RPE, retinal pigmented epithelium; SVC, support vector classification; GNB, Gaussian Naïve Bayes; RF, random forest; kNN, k-nearest neighbors; LR, logistic regression; LD, linear discriminant; DT, decision tree.

TABLE 5 Two-way ANOVA results for model training.

	SS	DF	MS	F	p-value
Algorithms	7,937	6	1,322.9	42.87	< 0.001
Retinal datasets	37,140	7	5,305.7	171.93	< 0.001
Algorithms*retinal datasets	6,703	42	159.6	5.17	< 0.001
Residuals	15,554	504	30.9		

SS, sum of squares; DF, degrees of freedom; MS, mean squares.

TABLE 6 Comparison of mean accuracies (± standard deviation) obtained from the machine learning algorithms to classify the sex-related differences in the retinal layers (and total retina) for model testing.

	Machine learning algorithms (%)						
Layers	SVC	GNB	RF	KNN	LR	LD	DT
RPE	68.8 ± 9.5	70.8 ± 5.8	76.8 ± 3.7	59.8 ± 5.2	66 ± 5.6	66.5 ± 7.3	69.5 ± 6
ONL	70.5 ± 8.8	63.5 ± 6.7	89.3 ± 5.4	68 ± 6.5	64.3 ± 5.9	66.8 ± 10	75.5 ± 6
OPL	76.3 ± 4.3	74.5 ± 7.9	88.5 ± 3.8	72 ± 5.2	64.5 ± 9	62.8 ± 7.2	83 ± 6.2
INL	82.8 ± 6.3	85.8 ± 5.5	88.8 ± 4	80.5 ± 6.3	77.5 ± 6.6	80.8 ± 5.3	85.3 ± 7
IPL	85.3 ± 6.6	83.3 ± 5.5	93.8 ± 2.4	80.5 ± 5.1	82.3 ± 5.8	84.3 ± 4.3	85.8 ± 7.1
GCL	89.3 ± 4.4	82 ± 4.1	92.3 ± 4.2	84 ± 7.4	86.3 ± 5.3	88.8 ± 5	89.8 ± 4.4
RNFL	91.5 ± 3.8	91 ± 3.9	94.5 ± 4.7	92.3 ± 4.6	90.3 ± 5.1	91.3 ± 4.6	90 ± 5.3
TR	91.8 ± 2.7	93.3 ± 3.7	94 ± 4.1	89.5 ± 5.1	91.3 ± 3.6	91.5 ± 5.7	91.3 ± 4.3

TR, total retina; RNFL, retinal nerve fiber layer; GCL, ganglion cell layer; IPL, inner plexiform layer; INL, inner nuclear layer; OPL, outer plexiform layer; ONL, outer nuclear layer; RPE, retinal pigmented epithelium; SVC, support vector classification; GNB, Gaussian Naïve Bayes; RF, random forest; kNN, k-nearest neighbors; LR, logistic regression; LD, linear discriminant; DT, decision tree.

that, even in retinal layers where there were no significant differences in thickness between the male and female groups, such as the datasets from the outer retina, we achieved a sex classification accuracy exceeding 75%. What would it signify if a male patient were classified as female based on retinal thickness patterns, or vice versa? It is crucial to emphasize that this classification does not pertain to the patient's actual sex but rather reflects the retinal thickness patterns expected for each sex. The clinical implications of a disparity between a patient's actual sex and a different sex classification based on retinal structure remain unclear, but further investigations may shed light on this question.

An investigation has previously been conducted using a deep learning method to predict sex through macular OCT images (24). It showed that the differences between male and female subjects might not be uniform throughout the macula. The best accuracy in separating data from male and female subjects occurred in the central fovea (around 75%) and lower accuracy was found in the external limit of the fovea (around 70%). They also fed models considering different macular sectors and found non-uniformity in the accuracies (ranging between 52 and 62%). The data they used are comparable to the total retina dataset of the present study. We interpreted that our accuracies were higher because we had fed our models with thickness information of all the macular sectors, and they used information from each sector for their classification.

TABLE 7 Two-way ANOVA results for model testing.

	SS	DF	MS	F	p-value
Algorithms	8,299	6	1,383.1	41.91	<0.001
Retinal datasets	41,178	7	5,882.6	178.25	<0.001
Algorithms*retinal datasets	6,276	42	149.4	4.53	<0.001
Residuals	16,633	504	33		

SS, sum of squares; DF, degrees of freedom; MS, mean squares.

Taking into account the significance of macular field thickness, our results align with the findings achieved using deep learning approaches for the total retinal dataset, wherein the temporal fields were identified as the most crucial for classifying sex. The current study also revealed that in other retinal layers, the field of greatest importance varied.

The difference between the accuracies of the training and testing models is a crucial aspect in the evaluation of machine learning models. This difference can provide insights into how well the model is generalizing to unseen data, which is essential for determining the model's robustness. In the current study, the vast majority of comparisons showed no significant discrepancy between the training and testing accuracies, which is a positive indication. It suggests that the model, which fits the training data well, also exhibits good generalization to new data. This alignment between training and testing accuracies indicates that the model is not overfitting the training data and has the potential for reliable performance on new, unseen data.

The superior performance of random forest in achieving higher accuracies compared to alternative machine learning algorithms in our study can be attributed to several key advantages of this ensemble learning technique. random forest

harnesses the power of multiple decision trees, where each tree is trained on a different subset of the data and with feature randomness (25). This inherent diversity and randomness help mitigate overfitting, a common challenge in machine learning, by reducing the model's sensitivity to noise and outliers (26). Moreover, random forest's ability to handle both classification and regression tasks, its capacity to capture complex non-linear relationships in the data, and its robustness to multicollinearity make it particularly well-suited for a wide range of datasets (27). Additionally, the ensemble nature of random forest allows it to aggregate the predictions from multiple trees, reducing the risk of bias that can be associated with individual models. Consequently, the comprehensive nature of random forest, combining predictive power and robustness, positions it as an attractive choice for achieving high accuracy in diverse machine learning tasks.

Prior research has suggested that male participants typically display a greater retinal thickness compared to female participants (7–12). The impact of sex on retinal layers is still a topic of ongoing debate. Some studies (13–17) have reported thicker retinal layers in male subjects (GCL, IPL, INL, OPL, and ONL), while others have observed minimal or no sex-related differences (18, 19). Some studies have shown that female subjects had a thicker peripapillary RNFL than male subjects (28, 29). The present study uncovers a greater thickness in the inner retinal layers of male subjects compared to female subjects. Sexual hormones interacting with receptors such as estrogen and androgen receptors can affect ocular tissue. However, despite their influence on various ocular structures, the effect of these hormones on retinal layer thickness remains largely uninvestigated (30–35).

Neglecting to account for sex differences in comparisons of retinal thickness between healthy individuals and patients could result in erroneous diagnoses, particularly for inner retinal
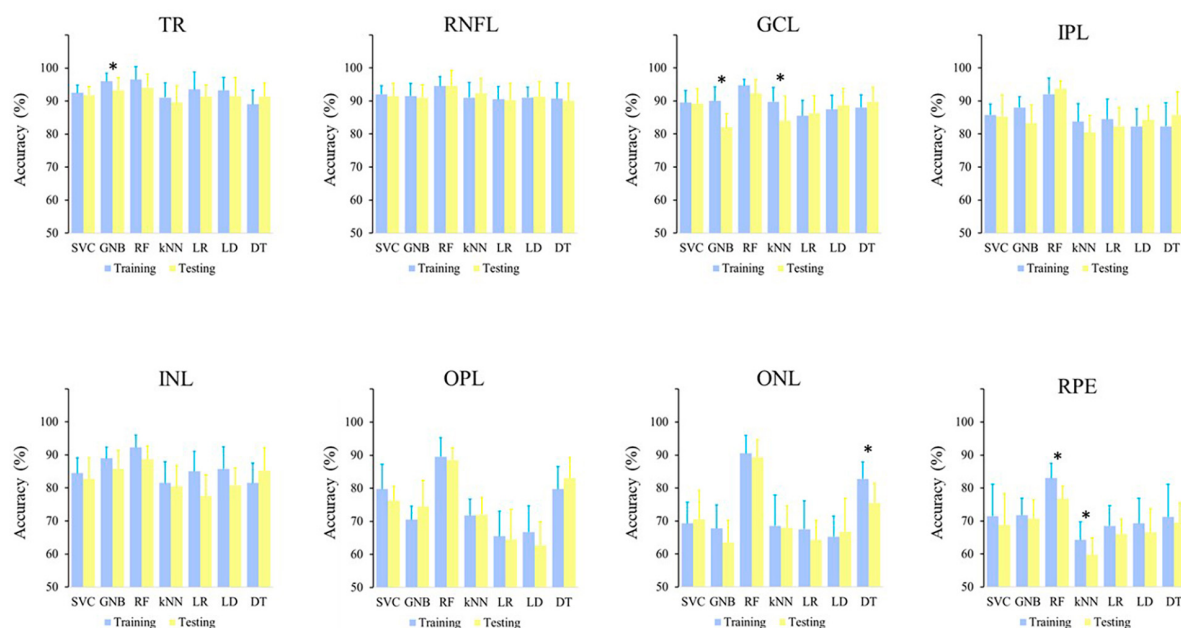
FIGURE 1
Comparison of the algorithm accuracies calculated in the model training and model testing in the different retinal datasets. *p < 0.05.
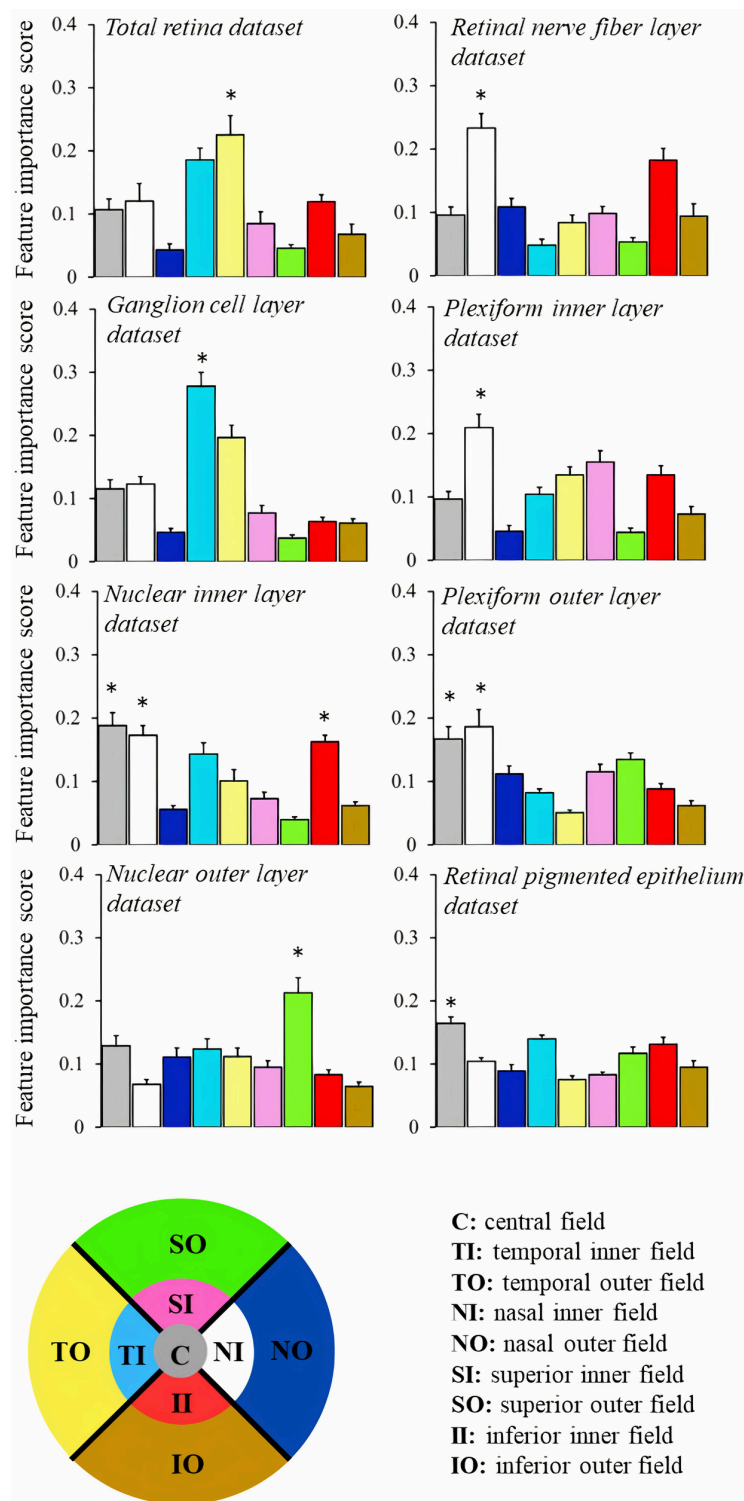
FIGURE 2
Comparison of the feature importance score obtained from random forest algorithm to classify the sex of the participant based on retinal thickness from different datasets. The color code is indicated at the bottom of the figure. *$p < 0.05$.

diseases that display substantial sex-related disparities. Conditions like glaucoma, macular holes, diabetic retinopathy, and age-related macular degeneration demonstrate varying prevalence rates between male and female subjects. This is likely attributable to changes in sex hormone concentrations after the age of 50 (36, 37).

The current investigation focuses on recruiting predominantly young adult participants, and as a result, the applicability of our findings may be limited to this specific age group. This demographic constraint represents a notable limitation of our study. To enhance the generalizability and robustness of our

conclusions, it is imperative for future research endeavors to encompass a broader spectrum of cases, incorporating individuals from various age ranges. In the present study, our primary aim was to demonstrate that various models can learn pertinent sex-related patterns within diverse retinal datasets. While the current sample size has proven adequate for this initial validation, it remains a limitation of the study and should be expanded in future research endeavors.

In conclusion, this research highlights the discriminative capacity of different retinal layers in sex classification, achieving varying levels of accuracy across distinct layers and ML algorithms. The consistently superior performance of the RF algorithm indicates its effectiveness in identifying sex-related characteristics in various retinal layers. Furthermore, the identified patterns of accuracy fluctuations across retinal layers offer invaluable insights for subsequent research and algorithmic advancement in the field of retinal data analysis.

Data availability statement

The original contributions presented in this study are available after inquiries directed to the corresponding author.

Ethics statement

The studies involving humans were approved by the Ethical Committee for Research in Humans of the Universidade Federal do Pará (report number 3.285.557). The studies were conducted in accordance with the local legislation and institutional requirements. The participants provided their written informed consent to participate in this study.

Author contributions

Funding

Conflict of interest

The authors declare that the research was conducted in the absence of any commercial or financial relationships that could be construed as a potential conflict of interest.

The authors declared that they were an editorial board member of Frontiers, at the time of submission. This had no impact on the peer review process and the final decision.

Publisher's note

All claims expressed in this article are solely those of the authors and do not necessarily represent those of their affiliated organizations, or those of the publisher, the editors and the reviewers. Any product that may be evaluated in this article, or claim that may be made by its manufacturer, is not guaranteed or endorsed by the publisher.

References

1. Huang D, Swanson E, Lin C, Schuman J, Stinson W, Chang W, et al. Optical coherence tomography. *Science.* (1991) 254:1178–81. doi: 10.1126/science.1957169

2. Swanson E, Izatt J, Hee M, Huang D, Lin C, Schuman J, et al. In vivo retinal imaging by optical coherence tomography. *Opt Lett.* (1993) 18:1864–6. doi: 10.1364/ol.18.001864

3. Izatt J, Hee M, Swanson E, Lin C, Huang D, Schuman J, et al. Micrometer-scale resolution imaging of the anterior eye in vivo with optical coherence tomography. *Arch Ophthalmol.* (1994) 112:1584–9. doi: 10.1001/archopht.1994.01090240090031

4. Pagon R. Retinitis pigmentosa. *Surv Ophthalmol.* (1988) 33:137–77. doi: 10.1016/0039-6257(88)90085-9

5. Gardner T, Antonetti D, Barber A, LaNoue K, Levison S. Diabetic retinopathy: more than meets the eye. *Surv Ophthalmol.* (2002) 47 Suppl 2:S253–62. doi: 10.1016/s0039-6257(02)00387-9

6. Lim L, Mitchell P, Seddon J, Holz F, Wong T. Age-related macular degeneration. *Lancet.* (2012) 379:1728–38. doi: 10.1016/S0140-6736(12)60282-7

7. Wong A, Chan C, Hui S. Relationship of gender, body mass index, and axial length with central retinal thickness using optical coherence tomography. *Eye.* (2005) 19:292–7. doi: 10.1038/sj.eye.6701466

8. Ooto S, Hangai M, Sakamoto A, Tomidokoro A, Araie M, Otani T, et al. Three-dimensional profile of macular retinal thickness in normal Japanese eyes. *Invest Ophthalmol Vis Sci.* (2010) 51:465–73. doi: 10.1167/iovs.09-4047

9. Adhi M, Aziz S, Muhammad K, Adhi M. Macular thickness by age and gender in healthy eyes using spectral domain optical coherence tomography. *PLoS One.* (2012) 7:e37638. doi: 10.1371/journal.pone.0037638

10. Çubuk M, Kasım B, Koçluk Y, Sukgen E. Effects of age and gender on macular thickness in healthy subjects using spectral optical coherence tomography/scanning laser ophthalmoscopy. *Int Ophthalmol.* (2018) 38:127–31. doi: 10.1007/s10792-016-0432-z

11. Kelty P, Payne J, Trivedi R, Kelty J, Bowie E, Burger B. Macular thickness assessment in healthy eyes based on ethnicity using Stratus OCT optical coherence tomography. *Invest Ophthalmol Vis Sci.* (2008) 49:2668–72. doi: 10.1167/iovs.07-1000

12. Song W, Lee S, Lee E, Kim C, Kim S. Macular thickness variations with sex, age, and axial length in healthy subjects: a spectral domain-optical coherence tomography study. *Invest Ophthalmol Vis Sci.* (2010) 51:3913–8. doi: 10.1167/iovs.09-4189

13. Ooto S, Hangai M, Tomidokoro A, Saito H, Araie M, Otani T, et al. Effects of age, sex, and axial length on the three-dimensional profile of normal macular layer structures. *Invest Ophthalmol Vis Sci.* (2011) 52:8769–79. doi: 10.1167/iovs.11-8388

14. Won J, Kim S, Park Y. Effect of age and sex on retinal layer thickness and volume in normal eyes. *Medicine.* (2016) 95:e5441. doi: 10.1097/MD.0000000000005441

15. Nieves-Moreno M, Martínez-de-la-Casa J, Morales-Fernández L, Sánchez-Jean R, Sáenz-Francés F, García-Feijoó J. Impacts of age and sex on retinal layer thicknesses measured by spectral domain optical coherence tomography with Spectralis. *PLoS One.* (2018) 13:e0194169. doi: 10.1371/journal.pone.0194169

16. Invernizzi A, Pellegrini M, Acquistapace A, Benatti E, Erba S, Cozzi M, et al. Normative data for retinal-layer thickness maps generated by spectral-domain OCT in a white population. *Ophthalmol Retina.* (2018) 2:808.e–15.e. doi: 10.1016/j.oret.2017.12.012

17. Palazon-Cabanes A, Palazon-Cabanes B, Rubio-Velazquez E, Lopez-Bernal M, Garcia-Medina J, Villegas-Perez M. Normative Database for All Retinal Layer Thicknesses Using SD-OCT Posterior Pole Algorithm and the Effects of Age, Gender and Axial Lenght. *J Clin Med.* (2020) 9:3317. doi: 10.3390/jcm9103317

18. Grover S, Murthy R, Brar V, Chalam K. Normative data for macular thickness by high-definition spectral-domain optical coherence tomography (spectralis). *Am J Ophthalmol.* (2009) 148:266–71. doi: 10.1016/j.ajo.2009.03.006

19. Appukuttan B, Giridhar A, Gopalakrishnan M, Sivaprasad S. Normative spectral domain optical coherence tomography data on macular and retinal nerve fiber layer thickness in Indians. *Indian J Ophthalmol.* (2014) 62:316–21. doi: 10.4103/0301-4738.116466

20. Nuzzi R, Scalabrin S, Becco A, Panzica G. Gonadal Hormones and Retinal Disorders: A Review. *Front Endocrinol.* (2018) 9:66. doi: 10.3389/fendo.2018.00066

21. Xu Y, Liu X, Cao X, Huang C, Liu E, Qian S, et al. Artificial intelligence: A powerful paradigm for scientific research. *Innovation.* (2021) 2:100179. doi: 10.1016/j.xinn.2021.100179

22. Ali O, Abdelbaki W, Shrestha A, Elbasi E, Alryalat M, Dwivedi YK. A systematic literature review of artificial intelligence in the healthcare sector: Benefits, challenges, methodologies, and functionalities. *J Innov Knowledge.* (2023) 8:100333.

23. Qin F, Lv Z, Wang D, Hu B, Wu C. Health status prediction for the elderly based on machine learning. *Arch Gerontol Geriatr.* (2020) 90:104121. doi: 10.1016/j.archger.2020.104121

24. Chueh K, Hsieh Y, Chen H, Ma I, Huang S. Identification of sex and age from macular optical coherence tomography and feature analysis using deep learning. *Am J Ophthalmol.* (2022) 235:221–8. doi: 10.1016/j.ajo.2021.09.015

25. Steffens M, Lamina C, Illig T, Bettecken T, Vogler R, Entz P, et al. SNP-based analysis of genetic substructure in the German population. *Hum Hered.* (2006) 62:20–9. doi: 10.1159/000095850

26. Abellán J, Mantas C, Castellano J, Moral-García S. Increasing diversity in random forest algorithm via imprecise probabilities. *Expert Syst Applic.* (2018) 97:228–43.

27. Svetnik V, Liaw A, Tong C, Culberson J, Sheridan R, Feuston B. Random forest: a classification and regression tool for compound classification and QSAR modeling. *J Chem Inf Comput Sci.* (2003) 43:1947–58. doi: 10.1021/ci034160g

28. Li D, Rauscher F, Choi E, Wang M, Baniasadi N, Wirkner K, et al. Sex-specific differences in circumpapillary retinal nerve fiber layer thickness. *Ophthalmology.* (2020) 127:357–68. doi: 10.1016/j.ophtha.2019.09.019

29. Rougier M, Korobelnik J, Malet F, Schweitzer C, Delyfer M, Dartigues J, et al. Retinal nerve fibre layer thickness measured with SD-OCT in a population-based study of French elderly subjects: the Alienor study. *Acta Ophthalmol.* (2015) 93:539–45. doi: 10.1111/aos.12658

30. Ogueta S, Schwartz S, Yamashita C, Farber D. Estrogen receptor in the human eye: influence of gender and age on gene expression. *Invest Ophthalmol Vis Sci.* (1999) 40:1906–11.

31. Rocha E, Wickham L, da Silveira L, Krenzer K, Yu F, Toda I, et al. Identification of androgen receptor protein and 5alpha-reductase mRNA in human ocular tissues. *Br J Ophthalmol.* (2000) 84:76–84. doi: 10.1136/bjo.84.1.76

32. Wickham L, Gao J, Toda I, Rocha E, Ono M, Sullivan D. Identification of androgen, estrogen and progesterone receptor mRNAs in the eye. *Acta Ophthalmol Scand.* (2000) 78:146–53. doi: 10.1034/j.1600-0420.2000.078002146.x

33. Munaut C, Lambert V, Noël A, Frankenne F, Deprez M, Foidart J, et al. Presence of oestrogen receptor type beta in human retina. *Br J Ophthalmol.* (2001) 85:877–82. doi: 10.1136/bjo.85.7.877

34. Gupta P, Johar K, Nagpal K, Vasavada A. Sex hormone receptors in the human eye. *Surv Ophthalmol.* (2005) 50:274–84. doi: 10.1016/j.survophthal.2005.02.005

35. Cascio C, Deidda I, Russo D, Guarneri P. The estrogenic retina: The potential contribution to healthy aging and age-related neurodegenerative diseases of the retina. *Steroids.* (2015) 103:31–41. doi: 10.1016/j.steroids.2015.08.002

36. Evans J, Schwartz S, McHugh J, Thamby-Rajah Y, Hodgson S, Wormald R, et al. Systemic risk factors for idiopathic macular holes: a case-control study. *Eye.* (1998) 12:256–9. doi: 10.1038/eye.1998.60

37. Rudnicka A, Jarrar Z, Wormald R, Cook D, Fletcher A, Owen C. Age and gender variations in age-related macular degeneration prevalence in populations of European ancestry: a meta-analysis. *Ophthalmology.* (2012) 119:571–80. doi: 10.1016/j.ophtha.2011.09.027

Two-photon excitation fluorescence in ophthalmology: safety and improved imaging for functional diagnostics

Vineeta Kaushik[1], Michał Dąbrowski[1,2], Luca Gessa[2], Nelam Kumar[2] and Humberto Fernandes[2]*

[1]Institute of Physical Chemistry, Polish Academy of Sciences, Warsaw, Poland, [2]International Centre for Translational Eye Research, Institute of Physical Chemistry, Polish Academy of Sciences, Warsaw, Poland

Two-photon excitation fluorescence (TPEF) is emerging as a powerful imaging technique with superior penetration power in scattering media, allowing for functional imaging of biological tissues at a subcellular level. TPEF is commonly used in cancer diagnostics, as it enables the direct observation of metabolism within living cells. The technique is now widely used in various medical fields, including ophthalmology. The eye is a complex and delicate organ with multiple layers of different cell types and tissues. Although this structure is ideal for visual perception, it generates aberrations in TPEF eye imaging. However, adaptive optics can now compensate for these aberrations, allowing for improved imaging of the eyes of animal models for human diseases. The eye is naturally built to filter out harmful wavelengths, but these wavelengths can be mimicked and thereby utilized in diagnostics via two-photon (2Ph) excitation. Recent advances in laser-source manufacturing have made it possible to minimize the exposure of *in vivo* measurements within safety, while achieving sufficient signals to detect for functional images, making TPEF a viable option for human application. This review explores recent advances in wavefront-distortion correction in animal models and the safety of use of TPEF on human subjects, both of which make TPEF a potentially powerful tool for ophthalmological diagnostics.

KEYWORDS

two-photon excitation fluorescence, diagnostics, ophthalmology, functional imaging, non-invasive, adaptive optics

1 Introduction

Diagnostics, and early diagnostics in particular, are crucial in ophthalmology. Many eye diseases are progressive and, after a certain point, several are irreversible. Thus, early detection of symptoms can significantly increase the chances of proper treatment, subsequently halting, or at least considerably slowing, the progression of the disease. Basic methods of diagnostics rely on direct visualization and subjective questioning of the patient. Such methods have been complemented with structural imaging, such as optical coherence tomography (OCT) (1, 2), in which technology has advanced to allow for imaging of morphological changes, distinguishing healthy from sick/damaged eye

components. However, there is a need for non-invasive functional imaging that will enable several advanced diagnostic approaches, including measurement of structural changes upon stimulus, for example with optoretinography (ORG) (3–5); direct assessment of biochemical changes, with two-photon (2Ph) imaging (6); and detection of human retinal fluorophores *in situ* in the interphase between the retina and the retinal pigment epithelium (RPE) layer to recognize imbalances in the visual cycle (6). 2Ph imaging is also helpful in examining the collagen arrangements in the human cornea and sclera and the non-collagen limbus ultrastructure of the trabecular meshwork (7).

Advances in 2Ph imaging have alleviated safety concerns and allowed for its potential use in *in vivo* diagnosis of corneal and retinal diseases, at a minimum. Here we briefly introduce the two-photon excitation fluorescence (TPEF) technique and its use in ophthalmology, highlighting some of its most promising applications.

2 2Ph imaging

2Ph imaging is a fluorescence image technique based on the fact that two photons interact with molecules quasi-simultaneously (on the order of femtoseconds), in an incoherent fashion, with the combined energy matching the energy gap between the ground and excited states, and the absorption occurring most strongly near the focal plane, where the photon flux is highest (8) (Figures 1A–D).

This is a very rare event, but can be largely boosted by the use of ultrafast pulsed laser excitation in the range of 10^{20}–10^{30} photons/(cm^2·s) (7), with the number of photons absorbed per fluorophore per pulse (n_a) is given by:

$$ n_a \approx \frac{P_0^2 \delta}{\tau_p f_p^2} \left(\frac{(NA)^2}{2\hbar c\lambda} \right)^2 $$

with τ_p being the pulse duration, δ is the fluorophore's two-photon absorption cross section (~10^{-58} m^3 per photon) at wavelength λ, P_0 being the average laser intensity, f_p being the laser's repetition rate, NA being the numerical aperture of the focusing objective, and $\hbar$ and c being the Planck's constant and the speed of light, respectively (8, 9). With such small cross-section and with a pulse duration of 100 fs and a lens numerical aperture $\approx$ 1.4, Denk and coworkers calculate that an average incident laser power of ~50 mW would saturate the fluorescence output at the limit of one absorbed photon pair per pulse per fluorophore (9).

Currently the 2Ph absorption, after non-radiant energy relaxation, is explored in medical context in three main ways: (i) in the emission of a single photon in the visible range via fluorescence emission (TPEF), (ii) or in case of instantaneous process and no energy lost, in a second-harmonic generation (SHG) scattered UV light (7, 10), and (iii) in fluorescence lifetime imaging microscopy (FLIM) (Figures 1E-I).

TPEF has several unique advantages over conventional fluorescence microscopy, such as reduced phototoxicity, increased penetration depth and improved spatial resolution. The first application of TPEF to biological samples occurred in 1990 (9); since then, it has been used for various medical applications, including ophthalmology (11) (Figures 1J–K).

SHG is a coherent process, thus the phase and polarization of the generated photon are related to those of the incident photons, bringing advantages over other imaging techniques such as high contrast, minimal photobleaching, deep penetration depth, and allowing label-free imaging. SHG was first demonstrated in 1961 (12) and can be used for high-resolution optical microscopy in biology and the medical sciences (Figure 1L) (see Supplementary Material).

FLIM extracts the lifetime from the fluorescence emission (10), allowing the separation of fluorophores that just by the intensity at a particular wavelength would not be distinguishable (10, 13–17) (see Supplementary Material).

Such unique characteristics grant TPEF an amazing potential for use in both structural and functional imaging. In ophthalmology, progress has been made in evaluating the applicability of 2Ph in the clinic for corneal and retinal analysis. Moreover, TPEF, as a non-invasive and label-free optical imaging technique, allows the characterization of specimens without interference from the biochemical composition and/or physiological state of the samples (18).

3 Safety

Safety has been a critical element in developing 2Ph imaging for application in ophthalmology, especially when imaging the retina where melanin-mediated interference can preclude detection of the signal of interest. Thus, advances in manufacturing the laser source (with spatial, temporal and spectral properties finely modulated) were key in maximizing the signal and minimizing the exposure to laser light (6, 19); i.e., very intense but short pulses (which, if continued, would vaporize the biological samples), at a high repetition rate, that produce high instantaneous energy but low average (20). The probability of TPEF events increases with photon flux, thus requiring powerful lasers (or less powerful if the laser produces short fs pulses, making the instantaneous intensity very high). Despite the use of these high-intensity short pulses, eye tissue interrogations remain within safe limits because of the minimal cross-section of material illuminated, and the very limited time period over which the pulses are delivered (Figure 1M). Technology tested in mice revealed the possibility of extracting biochemical information using TPEF imaging, within safe limits and without any perceived damage judged by several criteria, including *in vivo* imaging using SLO and OCT; retinal function assay by ERG; and *ex vivo* quantification of rhodopsin and 11-cis retinal by immune histology and TPEF imaging (6, 21). To ensure a more significant safety margin for use in human retinas, Palczewska et al. (21) further diminished the potential sources of photodamage by decreasing the pulse repetition frequency (PRF) (17), and by adding other design features in the setup (22, 23). In more detail, Palczewska and colleagues' setting is now capable of recording retinoids derivative in human retinas using average light power of only 0.3 mW for an exposure time of 40 s per measurement (that is sufficient to collect 30 frames), when considering a NA of 0.22, is well below the safety limits prescribed by the American National Standard for Safe Use of Lasers, ANSI Z136.1–2014. Using a laser of λ = 780 nm, a pulse duration of 76 fs, and imaging a squared retinal area of 17.6° and using the equation:
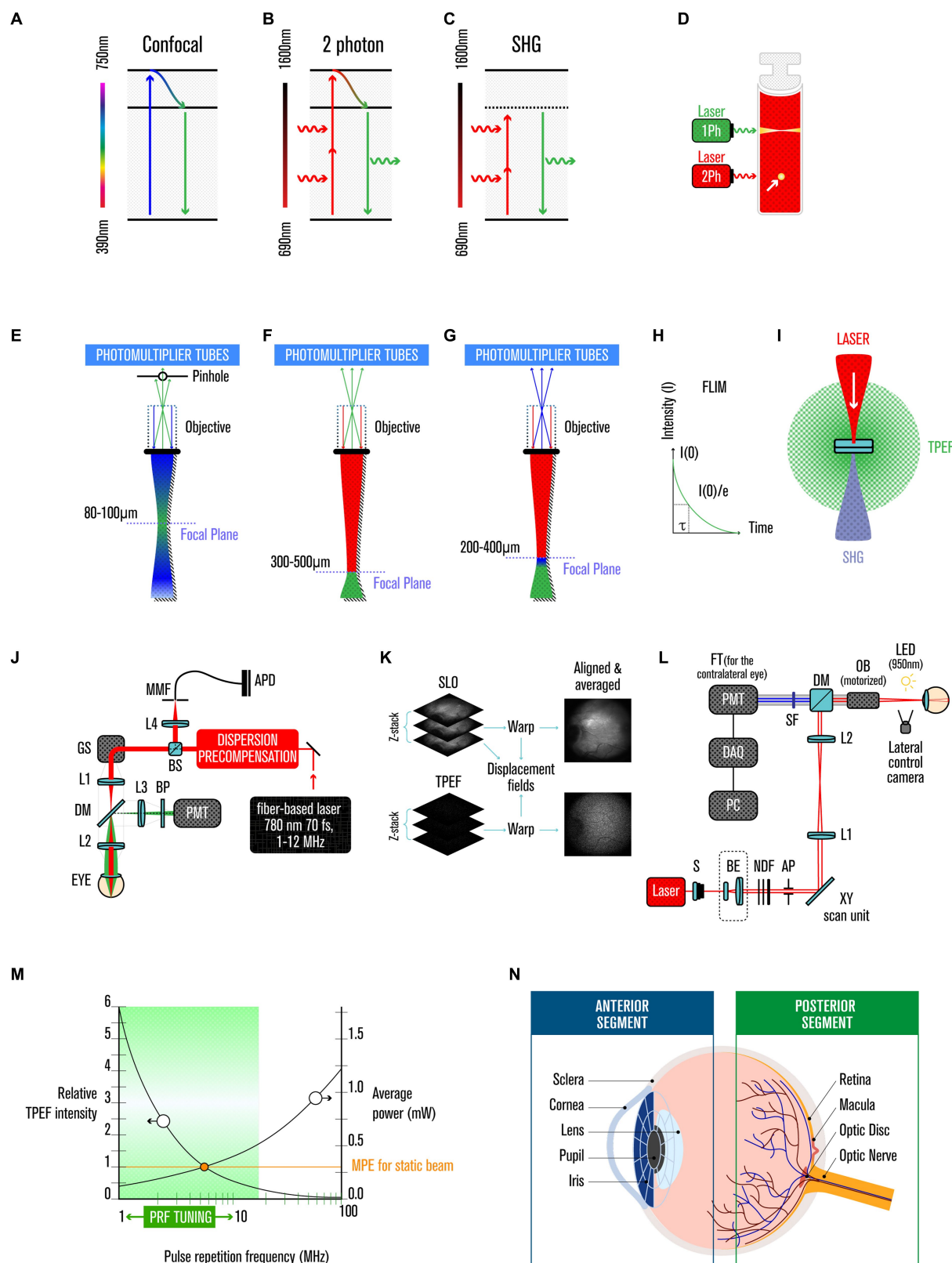
FIGURE 1
Two-photon imaging. **(A)** Jablonski diagram of fluorophore excitation by single, **(B)** two-photon, and **(C)** secondary-harmonic generation (SHG).
(D) comparison of one and two-photon (*yellow arrow*) excitation profiles. **(E)** focal plane range by single, **(F)** two-photon, and **(G)** SHG. **(H)** FLIM
histogram of photon counts versus arrival time after the laser pulse. **(I)** two-photon excited fluorescence and SHG are isotopically emitted.
(J) experimental TPEF-SLO setup, and its **(K)** imaging processing. **(L)** experimental SHG setup. **(M)** relative TPEF intensity as a function of pulse
repetition frequency. **(N)** anatomy of the human eye.

$$RE = \frac{P \cdot T_{\exp}}{A_{retina}}$$

For the retinal exposures (RE), where P is average excitation power, T_{exp} is exposure time and A_{retina} is the area of the exposed retina (see Supplementary Material).

In another study, Avila et al. (7) used a high-repetition infrared laser and, keeping the maximum laser power (MP) within safety limits, obtained 2Ph images while protecting both the cornea and the retina (7). For their setting, and considering both the International Commission on Non-Ionizing Radiation Protection (ICNRP) (24), and the ANSI Z136.1–2000 (19), Avila and co-workers an MPE of 3.49 W/cm^2 was determined, and they collect their images with exposure times of 0.42 s (7).

4 Image improvement

Adaptive optics (AO) is a technique that at its core uses a wavefront sensor to measure the distortion in an optical wavefront, and corrects them using a deformable mirror, thus in ophthalmology AO corrects for eye aberrations (25). Additionally, one impact of reducing the pulse duration in TPEF imaging is the increased phase distortion, caused not only by the tissues but also by the optical component due to the increase in the pulse spectral bandwidth, which needs to be compensated for (6, 26). Another impact to some extent is wavefront distortion, due to intermediate tissue layers; this problem may be overcome using AO (6, 27–29). Several innovative approaches to solve such problems include Differential Aberration Imaging (DAI), which computes out tissue-induced aberrations (30); real time Iterative Aberrations Correction, which involves iterative algorithms to adjust the optical elements and thus the quality of the images (31); and Offline Aberration Corrections that involve post-processing corrections to improve image quality (32). However, adaptive optics needs to correct the wavefront aberrations without inducing much photobleaching or increasing the exposure of the sample. This refinement was achieved for 2Ph microscopy in 2009 (33), and it was used for other imaging modalities in ophthalmology practice in 1997 (34) and in a clinical setting in 2000 (35). More information on adaptive optics, including its use on different cells and tissues, clinical applications, and current limitations and perspectives, can be found in a review by Akyol and colleagues (36).

5 TPEF use in ophthalmology

The eyes are a very sensitive organ that in parallel to detect a large spectrum of radiation and over a large range of intensities, needs to protect its delicate fabric of different tissues and cells from radiation damage. UV light is particularly detrimental (it can lead to irreversible changes in the transparency of the human cornea and lens (37)), but is filtered before it reaches the sensitive photoreceptors by the cornea and lens, and it is also quenched by the presence of melanin, that works not only as a photo-screen but also as an antioxidant (38).

In TPEF, two less-energetic (i.e., near IR range) photons are used to excite molecules instead of a single high-energy photon (i.e., in the UV range), thus bypassing the usage of UV illumination limitations.

This approach provides multiple advantages for using TPEF as a diagnostic tool, including: (i) it causes less damage (8–10), as it has a quadratic dependence on the excitation intensity (instead of the linear dependency of one-photon excitation); (ii) it has a more profound penetration power in tissues because the excitation is limited to the focal volume with high photon density (8–10, 20) (Figures 1E–F), and there is decreased scattering (8–10, 32); and (iii) in ophthalmology, it avoids the sequestration of UV light by the anterior segment of the human eye (39, 40) (Figure 1N).

The eye is composed of anterior and posterior segments (Figure 1N). The anterior segment contains the cornea, iris, ciliary body, and lens; and the posterior segment comprises the retina, choroid and optic nerve. Between the cornea and the optical nerve, the eye is coated by a white fibrous tissue called the sclera, which is the supporting structure that shapes and protects the eyeball. The posterior segment is responsible for detecting a light stimulus and its converting it into an electrical stimulus that the brain can process to generate images. In contrast, the anterior segment focuses the light beam onto the retina and blocks damaging UV light.

The cornea is the outermost anterior part of the eye, and it is transparent and avascular to allow light transmission and refraction (10). Its thickness varies from 500 μm in the center to 700 μm toward the periphery. The cornea is comprised of five main layers (epithelium, Browman's layer, stroma, Descemet's membrane, and endothelium). The stroma accounts for ~90% of the corneal thickness, and is composed of stacked collagen lamellae (7, 10). SHG allows the visualization of non-centrosymmetric molecules, such as collagen (7, 41, 42). It was first performed *ex vivo* (41, 43–47) and later performed *in vivo* in rabbits and humans (7, 41, 48). *Ex vivo* work indicates that TPEF can distinguish between pathological and non-pathological cornea for diseases such as keratoconus (KC), Acanthamoeba keratitis (AK), and stromal corneal scars (SCS), based on collagen fiber organization and stromal autofluorescence (AF) lifetime, as well as cell morphology and metabolism (41). Moreover, TPEF can detect changes in the ratio of free and protein-bound NAD(P)H to infer a decrease in cell metabolism (20, 41); and other clinical applications have been investigated over the years, as reviewed in 2022 (10). Recently, human eyes were evaluated *in vivo*, and information on the collagen arrangements and morphological features was obtained for the cornea, sclera, and trabecular meshwork (7). The latter revealed small features that may play a role in intraocular pressure regulation and glaucoma diagnostics, and mirrored the observations of *ex vivo* studies (7, 49–51).

As indicated, the posterior part of the eye includes the retina, where light stimuli are converted into electric stimuli that are further processed by the brain to generate images. One key piece of the process is the visual cycle, which contains many natural fluorophores that can be detected (6). However, their short excitation wavelengths do not permit the use of traditional one-photon imaging, as UV light will cause eye damage (22). As the anterior segment filters the light, 2Ph delivered in femtosecond pulses can interrogate such molecules in the retina (6, 17, 52, 53). TPEF imaging can detect several disease-specific biomarkers (52, 54, 55), as well as light- and age-induced retinal defects since they cause changes in retinoid metabolism (6, 56). More specifically, this imaging technique was employed to identify lipid droplets with a high concentration of retinyl esters (57), which over-accumulate in Rpe65−/− mice and are absent in Lrat−/− mice (58, 59). The ablated genes in these mouse models code for two key

enzymes in the visual cycle, RPE65 and LRAT, respectively. Rpe65−/− mice are a model for Leber congenital amaurosis, and Lrat−/− mice are a model for retinitis pigmentosa (6, 60). In animal models, TPEF imaging can distinguish aberrant bisretinoid patterns caused by Stargardt disease (61). In addition to the disease setting, during ageing some retinoids form bisretinoids that are fluorescent and thus can be analyzed with 2Ph ophthalmoscopy (62). From a therapeutic point of view, TPEF imaging is also potentially relevant, as it can help to track restoration of visual function. Examples include monitoring gene therapy of pathogenic mutations in the Rpe65 gene (63), tracking the drug-induced diminution of bisretinoids in a mouse model of Stargardt disease (61), and probing the protective effects of pharmacological agents on photoreceptor-induced light damage (64).

6 Other medical applications and comparison to other ocular techniques

TPEF is effective in exciting aromatic amino acids and other fluorophores present in the cells such as NAD and FAD allowing the analysis of living tissues (65, 66), thus getting used in different fields other than ophthalmology including neurobiology for studying neuronal signaling processes (67), oncology for investigating metabolism in cancer cells (68), and in the field of embryology for studies on living embryos (69). 2PEF has proved to be useful also in the field of immunology, thanks to the ability to give information about living cells revealing several mechanisms of the adaptive immune response (70).

Diagnostics of the cornea have historically relied on imaging techniques such as a slit-lamp microscope and specular and confocal microscopy, further supported by anterior segment OCT and corneal topography (41). These techniques can detect alterations of cell morphology, but they cannot monitor changes in the metabolism of cells or the structural organization of the stroma (41).

In terms of structural imaging of cornea, TPEF is superior to OCT and specular microscopy (or reflectance confocal microscopy) allowing the visualization of collagen fibers, and overall giving better contrast/resolution of the different corneal layers (7). Also, functional imaging is impossible with standard OCT.

Like the cornea, the retina has been examined with various imaging techniques, such as color photography, narrow-band reflectance photography, scanning-laser ophthalmoscopy (SLO) and fundus autofluorescence (6). Despite offering 2D-structural information, or 3D information when OCT is used, and allowing scrutiny of the retinal layers (6), these techniques do not offer insights into metabolic status or other functional information, and the information they provide does not correspond unfailingly to visual acuity (71). 2Ph imaging permits the measurement of the retinoids *in vivo* and thus facilitates an evaluation of the health of the visual cycle.

Fundus Autofluorescence (FAF) captures the natural fluorescence emitted by retinal pigments, thus providing insights into retinal health and metabolic changes, and applicable in conditions like macular degeneration and inherited retinal diseases (72). FAF and TPEF, applied to the posterior segment of the eye, share many similarities, but there are key differences. The more sticking is the fact that TPEF can pinpoint fluorophores active in the visual cycle, and not only passive ones such as melanin (73), and components of lipofuscins (22), and using lower Res, 1.76 J/cm^2 for a multiple-day exposure (22) versus 15 J/cm^2 (74), and 20.4 J/cm^2 (75), using near-infra-red

autofluorescence (NIR-FAF), thus also avoiding photochemical degradation of retinoids (76, 77).

7 Future perspectives

Two current limitations of TPEF are the slow acquisition times and low signal-to-noise ratio. Current developments with the use of multiple detectors offer the promise that faster and more efficient imaging collection (78). Using lasers that are frequency encoded (FE), Heuke and colleagues, offer now the possibility of excitation discrimination (in addition to the already available emission discrimination) and thus enable an unprecedented number of fluorophores to be imaged simultaneously (78).

There are a few areas where we think 2Ph imaging will have a significant impact in ophthalmology. Namely advances in the imaging of other retinal layers such as retinal ganglion cells with fiber-based two-photon fluorescence lifetime imaging ophthalmoscopy (FLIO) (79), or SHG to image the density and distribution of rhodopsin in rod photoreceptors (80). Moreover, 2Ph imaging can be used to assess corneas viability for transplantation (43), detect changes in the corneal shape and/or its mechanical properties and identify the initiation of loss of transparency, and thus future sight impaired or vision loss (7). Even when such a process occurs, since NIR excitation light penetrates cataractous lenses in a nondestructively way (22), 2Ph can nonetheless be used to access retinal function in elderly people, coincidentally more prone to suffer from illness on both eye segments. One final front where 2Ph will be used in the future is on drug impact and mechanism of action of drug action in retinal tissue (6).

8 Conclusion

In recent decades, and during recent years in particular, advances in TPEF technology, including adaptive optics and safety improvements, have raised its status and highlighted it as a potentially powerful tool with ophthalmological clinical applications, especially due to its functional imaging capacity. There are several challenges, however, to its widespread use, including the cost and the complexity of the current instrumentation, the need for self-assembly of the equipment, the costs and slow-speed of running adaptive optics, and the limited data from human *in vivo* tests (due to safety concerns that now seem to have been addressed). Nevertheless, enough of the limitations on the technology have been overcome, so that TPEF may now be considered a valuable potential tool for clinical diagnostics, to distinguish healthy from pathological eyes in a non-invasive and label-free manner (Table 1). TPEF can be used for structural and functional imaging of both the anterior and posterior segments of the eye, and it may be relevant for diagnosing and tracking treatment efficacy for ocular diseases including keratoconus, keratitis, bulbous keratopathy, fibrosis, Stargardt disease, and retinitis pigmentosa, among others.

Author contributions

VK: Writing – review & editing. MD: Writing – review & editing. LG: Writing – review & editing. NK: Writing – review & editing. HF: Writing – original draft, Writing – review & editing.

TABLE 1 Advantages and disadvantages of TPEF in ophthalmology.

TPEF in ophthalmology	
Advantages	Disadvantages
Non-invasive	Price
Functional imaging	Safety concerns for animal/human usage
Decreased photodamage	Not available "off the shelf"
High penetration depth	Adaptive Optics, slow speed
High contrast	Image acquisition time
in vivo/in situ	Lower signal to noise (SNR) ratio
Dye-free	Complexity of interpretation

Conflict of interest

The authors declare that the research was conducted in the absence of any commercial or financial relationships that could be construed as a potential conflict of interest.

Publisher's note

All claims expressed in this article are solely those of the authors and do not necessarily represent those of their affiliated organizations, or those of the publisher, the editors and the reviewers. Any product that may be evaluated in this article, or claim that may be made by its manufacturer, is not guaranteed or endorsed by the publisher.

Supplementary material

The Supplementary material for this article can be found online at: https://www.frontiersin.org/articles/10.3389/fmed.2023.1293640/full#supplementary-material

References

1. Huang D, Swanson EA, Lin CP, Schuman JS, Stinson WG, Chang W, et al. Optical coherence tomography. *Science*. (1991) 254:1178–81. doi: 10.1126/science.1957169

2. Fujimoto J, Huang D. Foreword: 25 years of optical coherence tomography. *Invest Ophthalmol Vis Sci*. (2016) 57:OCTi-OCTii. doi: 10.1167/iovs.16-20269

3. Meleppat RK, Valente D, Pijewska E, Lee S, Jonnal RS, Doble NP, et al. Progress on the development of FF-SS-OCT system for functional retinal imaging. *Ophthal Technol*. (2023) XXXIII. doi: 10.1117/12.2650676

4. Roorda A. Optoretinography is coming of age. *Proc Natl Acad Sci U S A*. (2021) 118. doi: 10.1073/pnas.2119737118

5. Kim TH, Ma G, Son T, Yao X. Functional optical coherence tomography for intrinsic signal Optoretinography: recent developments and deployment challenges. *Front Med*. (2022) 9:864824. doi: 10.3389/fmed.2022.864824

6. Palczewska G, Wojtkowski M, Palczewski K. From mouse to human: accessing the biochemistry of vision in vivo by two-photon excitation. *Prog Retin Eye Res*. (2023) 93:101170. doi: 10.1016/j.preteyeres.2023.101170

7. Avila FJ, Gambin A, Artal P, Bueno JM. In vivo two-photon microscopy of the human eye. *Sci Rep*. (2019) 9:10121. doi: 10.1038/s41598-019-46568-z

8. So PTC, Dong CY, Masters BR, Berland KM. Two-photon excitation fluorescence microscopy. *Annu Rev Biomed Eng*. (2000) 2:399–429. doi: 10.1146/annurev.bioeng.2.1.399

9. Denk W, Strickler JH, Webb WW. Two-photon laser scanning fluorescence microscopy. *Science*. (1990) 248:73–6. doi: 10.1126/science.2321027

10. Batista A, Guimaraes P, Domingues JP, Quadrado MJ, Morgado AM. Two-photon imaging for non-invasive corneal examination. *Sensors*. (2022) 22. doi: 10.3390/s22249699

11. Kaushik V, Gessa L, Kumar N, Fernandes H. Towards a new biomarker for diabetic retinopathy: exploring RBP3 structure and retinoids binding for functional imaging of eyes in vivo. *Int J Mol Sci*. (2023) 24. doi: 10.3390/ijms24054408

12. Franken PA, Hill AE, Peters CW, Weinreich G. Generation of optical harmonics. *Phys Rev Lett*. (1961) 7:118–9. doi: 10.1103/PhysRevLett.7.118

13. Datta R, Heaster TM, Sharick JT, Gillette AA, Skala MC. Fluorescence lifetime imaging microscopy: fundamentals and advances in instrumentation, analysis, and applications. *J Biomed Opt*. (2020) 25:1–43. doi: 10.1117/1.JBO.25.7.071203

14. Li H, Yu J, Zhang R, Li X, Zheng W. Two-photon excitation fluorescence lifetime imaging microscopy: a promising diagnostic tool for digestive tract tumors. *J Innov Opt Health Sci*. (2019) 12. doi: 10.1142/S179354581930009X

15. Lakowicz JR, Szmacinski H, Nowaczyk K, Johnson ML. Fluorescence lifetime imaging of free and protein-bound NADH. *Proc Natl Acad Sci U S A*. (1992) 89:1271–5. doi: 10.1073/pnas.89.4.1271

16. Rahim MK, Zhao J, Patel HV, Lagouros HA, Kota R, Fernandez I, et al. Phasor analysis of fluorescence lifetime enables quantitative multiplexed molecular imaging of three probes. *Anal Chem*. (2022) 94:14185–94. doi: 10.1021/acs.analchem.2c02149

17. Palczewska G, Boguslawski J, Stremplewski P, Kornaszewski L, Zhang J, Dong Z, et al. Noninvasive two-photon optical biopsy of retinal fluorophores. *Proc Natl Acad Sci U S A*. (2020) 117:22532–43. doi: 10.1073/pnas.2007527117

18. Georgakoudi I, Quinn KP. Optical imaging using endogenous contrast to assess metabolic state. *Annu Rev Biomed Eng*. (2012) 14:351–67. doi: 10.1146/annurev-bioeng-071811-150108

19. Delori FC, Webb RH, Sliney DHAmerican National Standards Institute. Maximum permissible exposures for ocular safety (ANSI 2000), with emphasis on ophthalmic devices. *J Opt Soc Am A Opt Image Sci Vis*. (2007) 24:1250–65. doi: 10.1364/JOSAA.24.001250

20. Wang BG, Konig K, Halbhuber KJ. Two-photon microscopy of deep intravital tissues and its merits in clinical research. *J Microsc*. (2010) 238:1–20. doi: 10.1111/j.1365-2818.2009.03330.x

21. Palczewska G, Stremplewski P, Suh S, Alexander N, Salom D, Dong Z, et al. Two-photon imaging of the mammalian retina with ultrafast pulsing laser. *JCI Insight*. (2018) 3. doi: 10.1172/jci.insight.121555

22. Boguslawski J, Palczewska G, Tomczewski S, Milkiewicz J, Kasprzycki P, Stachowiak D, et al. In vivo imaging of the human eye using a 2-photon-excited fluorescence scanning laser ophthalmoscope. *J Clin Invest*. (2022) 132. doi: 10.1172/JCI154218

23. Boguslawski J, Tomczewski S, Dabrowski M, Komar K, Milkiewicz J, Palczewska G, et al. In vivo imaging of the human retina using a two-photon excited fluorescence ophthalmoscope. *STAR Protoc*. (2023) 4:102225. doi: 10.1016/j.xpro.2023.102225

24. Sliney D, Aron-Rosa D, DeLori F, Fankhauser F, Landry R, Mainster M, et al. Adjustment of guidelines for exposure of the eye to optical radiation from ocular instruments:

statement from a task group of the international commission on non-ionizing radiation protection (ICNIRP). *Appl Opt*. (2005) 44:2162–76. doi: 10.1364/ao.44.002162

25. Williams DR, Burns SA, Miller DT, Roorda A. Evolution of adaptive optics retinal imaging [invited]. *Biomed Opt Express*. (2023) 14:1307–38. doi: 10.1364/BOE.485371

26. Entenberg D, Wyckoff J, Gligorijevic B, Roussos ET, Verkhusha VV, Pollard JW, et al. Setup and use of a two-laser multiphoton microscope for multichannel intravital fluorescence imaging. *Nat Protoc*. (2011) 6:1500–20. doi: 10.1038/nprot.2011.376

27. Biss DP, Sumorok D, Burns SA, Webb RH, Zhou Y, Bifano TG, et al. In vivo fluorescent imaging of the mouse retina using adaptive optics. *Opt Lett*. (2007) 32:659–61. doi: 10.1364/OL.32.000659

28. Cua M, Wahl DJ, Zhao Y, Lee S, Bonora S, Zawadzki RJ, et al. Coherence-gated Sensorless adaptive optics multiphoton retinal imaging. *Sci Rep*. (2016) 6:32223. doi: 10.1038/srep32223

29. Hunter JJ, Masella B, Dubra A, Sharma R, Yin L, Merigan WH, et al. Images of photoreceptors in living primate eyes using adaptive optics two-photon ophthalmoscopy. *Biomed Opt Express*. (2010) 2:139–48. doi: 10.1364/BOE.2.000139

30. Xiao S, Mertz J. Contrast improvement in two-photon microscopy with instantaneous differential aberration imaging. *Biomed Opt Express*. (2019) 10:2467–77. doi: 10.1364/BOE.10.002467

31. Champelovier D, Teixeira J, Conan JM, Balla N, Mugnier LM, Tressard T, et al. Image-based adaptive optics for in vivo imaging in the hippocampus. *Sci Rep*. (2017) 7:42924. doi: 10.1038/srep42924

32. Helmchen F, Denk W. Deep tissue two-photon microscopy. *Nat Methods*. (2005) 2:932–40. doi: 10.1038/nmeth818

33. Debarre D, Botcherby EJ, Watanabe T, Srinivas S, Booth MJ, Wilson T. Image-based adaptive optics for two-photon microscopy. *Opt Lett*. (2009) 34:2495–7. doi: 10.1364/OL.34.002495

34. Liang J, Williams DR, Miller DT. Supernormal vision and high-resolution retinal imaging through adaptive optics. *J Opt Soc Am A Opt Image Sci Vis*. (1997) 14:2884–92. doi: 10.1364/JOSAA.14.002884

35. Roorda A. Adaptive optics ophthalmoscopy. *J Refract Surg*. (2000) 16:S602–7. doi: 10.3928/1081-597X-20000901-23

36. Akyol E, Hagag AM, Sivaprasad S, Lotery AJ. Adaptive optics: principles and applications in ophthalmology. *Eye (Lond)*. (2021) 35:244–64. doi: 10.1038/s41433-020-01286-z

37. Soderberg PG, Talebizadeh N, Yu Z, Galichanin K. Does infrared or ultraviolet light damage the lens? *Eye (Lond)*. (2016) 30:241–6. doi: 10.1038/eye.2015.266

38. Hu DN, Simon JD, Sarna T. Role of ocular melanin in ophthalmic physiology and pathology. *Photochem Photobiol*. (2008) 84:639–44. doi: 10.1111/j.1751-1097.2008.00316.x

39. Glickman RD. Ultraviolet phototoxicity to the retina. *Eye Contact Lens*. (2011) 37:196–205. doi: 10.1097/ICL.0b013e31821e45a9

40. Jayabalan GS, Bille JF, Mao XW, Gimbel HV, Rauser ME, Wenz F, et al. Retinal safety evaluation of two-photon laser scanning in rats. *Biomed Opt Express*. (2019) 10:3217–31. doi: 10.1364/BOE.10.003217

41. Batista A, Breunig HG, Konig A, Schindele A, Hager T, Seitz B, et al. High-resolution, label-free two-photon imaging of diseased human corneas. *J Biomed Opt*. (2018) 23:1–8. doi: 10.1117/1.JBO.23.3.036002

42. Tian L, Qu J, Guo Z, Jin Y, Meng Y, Deng X. Microscopic second-harmonic generation emission direction in fibrillous collagen type I by quasi-phase-matching theory. *J Appl Phys*. (2010) 108. doi: 10.1063/1.3474667

43. Batista A, Breunig HG, Konig A, Schindele A, Hager T, Seitz B, et al. Assessment of human corneas prior to transplantation using high-resolution two-photon imaging. *Invest Ophthalmol Vis Sci*. (2018) 59:176–84. doi: 10.1167/iovs.17-22002

44. Piston DW, Masters BR, Webb WW. Three-dimensionally resolved NAD(P)H cellular metabolic redox imaging of the in situ cornea with two-photon excitation laser scanning microscopy. *J Microsc*. (1995) 178:20–7. doi: 10.1111/j.1365-2818.1995.tb03576.x

45. Teng SW, Tan HY, Peng JL, Lin HH, Kim KH, Lo W, et al. Multiphoton autofluorescence and second-harmonic generation imaging of the ex vivo porcine eye. *Invest Ophthalmol Vis Sci*. (2006) 47:1216–24. doi: 10.1167/iovs.04-1520

46. Batista A, Breunig HG, Uchugonova A, Morgado AM, Konig K. Two-photon spectral fluorescence lifetime and second-harmonic generation imaging of the porcine cornea with a 12-femtosecond laser microscope. *J Biomed Opt*. (2016) 21:36002. doi: 10.1117/1.JBO.21.3.036002

47. Aptel F, Olivier N, Deniset-Besseau A, Legeais JM, Plamann K, Schanne-Klein MC, et al. Multimodal nonlinear imaging of the human cornea. *Invest Ophthalmol Vis Sci*. (2010) 51:2459–65. doi: 10.1167/iovs.09-4586

48. Manns F, Konig K, Soderberg PG, Wang B, Krauss O, Ho A, et al. First in vivo animal studies on intraocular nanosurgery and multiphoton tomography with low-energy 80-MHz near-infrared femtosecond laser pulses. *Ophthal Technol*. (2004) XIV. doi: 10.1117/12.528287

49. Ammar DA, Lei TC, Gibson EA, Kahook MY. Two-photon imaging of the trabecular meshwork. *Mol Vis*. (2010) 16:935–44.

50. Gonzalez JM, Ko MK, Pouw A, Tan JC. Tissue-based multiphoton analysis of actomyosin and structural responses in human trabecular meshwork. *Sci Rep*. (2016) 6:21315. doi: 10.1038/srep21315

51. Gonzalez JM Jr, Heur M, Tan JC. Two-photon immunofluorescence characterization of the trabecular meshwork in situ. *Invest Ophthalmol Vis Sci*. (2012) 53:3395–404. doi: 10.1167/iovs.11-8570

52. Palczewska G, Maeda T, Imanishi Y, Sun W, Chen Y, Williams DR, et al. Noninvasive multiphoton fluorescence microscopy resolves retinol and retinal condensation products in mouse eyes. *Nat Med*. (2010) 16:1444–9. doi: 10.1038/nm.2260

53. Stremplewski P, Komar K, Palczewski K, Wojtkowski M, Palczewska G. Periscope for noninvasive two-photon imaging of murine retina in vivo. *Biomed Opt Express*. (2015) 6:3352–61. doi: 10.1364/BOE.6.003352

54. Palczewska G, Golczak M, Williams DR, Hunter JJ, Palczewski K. Endogenous fluorophores enable two-photon imaging of the primate eye. *Invest Ophthalmol Vis Sci*. (2014) 55:4438–47. doi: 10.1167/iovs.14-14395

55. Imanishi Y, Palczewski K. Visualization of retinoid storage and trafficking by two-photon microscopy. *Methods Mol Biol*. (2010) 652:247–61. doi: 10.1007/978-1-60327-325-1_14

56. Maeda A, Palczewska G, Golczak M, Kohno H, Dong Z, Maeda T, et al. Two-photon microscopy reveals early rod photoreceptor cell damage in light-exposed mutant mice. *Proc Natl Acad Sci U S A*. (2014) 111:E1428–37. doi: 10.1073/pnas.1317986111

57. Imanishi Y, Batten ML, Piston DW, Baehr W, Palczewski K. Noninvasive two-photon imaging reveals retinyl ester storage structures in the eye. *J Cell Biol*. (2004) 164:373–83. doi: 10.1083/jcb.200311079

58. Batten ML, Imanishi Y, Tu DC, Doan T, Zhu L, Pang J, et al. Pharmacological and rAAV gene therapy rescue of visual functions in a blind mouse model of Leber congenital amaurosis. *PLoS Med*. (2005) 2:e333. doi: 10.1371/journal.pmed.0020333

59. Batten ML, Imanishi Y, Maeda T, Tu DC, Moise AR, Bronson D, et al. Lecithin-retinol acyltransferase is essential for accumulation of all-trans-retinyl esters in the eye and in the liver. *J Biol Chem*. (2004) 279:10422–32. doi: 10.1074/jbc.M312410200

60. Kiser PD, Palczewski K. Retinoids and retinal diseases. *Annu Rev Vis Sci*. (2016) 2:197–234. doi: 10.1146/annurev-vision-111815-114407

61. Palczewska G, Maeda A, Golczak M, Arai E, Dong Z, Perusek L, et al. Receptor MER tyrosine kinase proto-oncogene (MERTK) is not required for transfer of bis-retinoids to the retinal pigmented epithelium. *J Biol Chem*. (2016) 291:26937–49. doi: 10.1074/jbc.M116.764563

62. Sparrow JR, Wu Y, Kim CY, Zhou J. Phospholipid meets all-trans-retinal: the making of RPE bisretinoids. *J Lipid Res*. (2010) 51:247–61. doi: 10.1194/jlr.R000687

63. Suh S, Choi EH, Leinonen H, Foik AT, Newby GA, Yeh WH, et al. Restoration of visual function in adult mice with an inherited retinal disease via adenine base editing. *Nat Biomed Eng*. (2021) 5:169–78. doi: 10.1038/s41551-020-00632-6

64. Maeda A, Golczak M, Chen Y, Okano K, Kohno H, Shiose S, et al. Primary amines protect against retinal degeneration in mouse models of retinopathies. *Nat Chem Biol*. (2011) 8:170–8. doi: 10.1038/nchembio.759

65. Richards-Kortum R, Sevick-Muraca E. Quantitative optical spectroscopy for tissue diagnosis. *Annu Rev Phys Chem*. (1996) 47:555–606. doi: 10.1146/annurev.physchem.47.1.555

66. Lakowicz JR. *Principles of fluorescence spectroscopy*. Boston, MA: Springer (2006).

67. Mostany R, Miquelajauregui A, Shtrahman M, Portera-Cailliau C. Two-photon excitation microscopy and its applications in neuroscience. *Methods Mol Biol*. (2015) 1251:25–42. doi: 10.1007/978-1-4939-2080-8_2

68. Sawyer TW, Koevary JW, Howard CC, Austin OJ, Rice PFS, Hutchens GV, et al. Fluorescence and multiphoton imaging for tissue characterization of a model of postmenopausal ovarian cancer. *Lasers Surg Med*. (2020) 52:993–1009. doi: 10.1002/lsm.23251

69. Supatto W, Truong TV, Debarre D, Beaurepaire E. Advances in multiphoton microscopy for imaging embryos. *Curr Opin Genet Dev*. (2011) 21:538–48. doi: 10.1016/j.gde.2011.08.003

70. Cahalan MD, Parker I. Choreography of cell motility and interaction dynamics imaged by two-photon microscopy in lymphoid organs. *Annu Rev Immunol*. (2008) 26:585–626. doi: 10.1146/annurev.immunol.24.021605.090620

71. Blumenkranz MS, Haller JA, Kuppermann BD, Williams GA, Ip M, Davis M, et al. Correlation of visual acuity and macular thickness measured by optical coherence tomography in patients with persistent macular edema. *Retina*. (2010) 30:1090–4. doi: 10.1097/IAE.0b013e3181dcfaf3

72. Schmitz-Valckenberg S, Pfau M, Fleckenstein M, Staurenghi G, Sparrow JR, Bindewald-Wittich A, et al. Fundus autofluorescence imaging. *Prog Retin Eye Res*. (2021) 81:100893. doi: 10.1016/j.preteyeres.2020.100893

73. Keilhauer CN, Delori FC. Near-infrared autofluorescence imaging of the fundus: visualization of ocular melanin. *Invest Ophthalmol Vis Sci*. (2006) 47:3556–64. doi: 10.1167/iovs.06-0122

74. Masella BD, Williams DR, Fischer WS, Rossi EA, Hunter JJ. Long-term reduction in infrared autofluorescence caused by infrared light below the maximum permissible exposure. *Invest Ophthalmol Vis Sci*. (2014) 55:3929–38. doi: 10.1167/iovs.13-12562

75. Schwarz C, Sharma R, Fischer WS, Chung M, Palczewska G, Palczewski K, et al. Safety assessment in macaques of light exposures for functional two-photon ophthalmoscopy in humans. *Biomed Opt Express*. (2016) 7:5148–69. doi: 10.1364/BOE.7.005148

76. Tolleson WH, Cherng SH, Xia Q, Boudreau M, Yin JJ, Wamer WG, et al. Photodecomposition and phototoxicity of natural retinoids. *Int J Environ Res Public Health*. (2005) 2:147–55. doi: 10.3390/ijerph2005010147

77. Ueda K, Zhao J, Kim HJ, Sparrow JR. Photodegradation of retinal bisretinoids in mouse models and implications for macular degeneration. *Proc Natl Acad Sci U S A*. (2016) 113:6904–9. doi: 10.1073/pnas.1524774113

78. Heuke S, Silva Martins C, Andre R, LeGoff L, Rigneault H. Frequency-encoded two-photon excited fluorescence microscopy. *Opt Lett*. (2023) 48:4113–6. doi: 10.1364/OL.496071

79. Della Volpe-Waizel M, Traber GL, Maloca P, Zinkernagel M, Schmidt-Erfurth U, Rubin G, et al. New Technologies for Outcome Measures in retinal disease: review from the European vision institute special interest focus group. *Ophthalmic Res*. (2020) 63:77–87. doi: 10.1159/000501887

80. Nemet BA, Nikolenko V, Yuste R. Second harmonic imaging of membrane potential of neurons with retinal. *J Biomed Opt*. (2004) 9:873–81. doi: 10.1117/1.1783353

Check for updates

Enhanced depth imaging optical coherence tomography features of two types of Vogt–Koyanagi–Harada disease: fuzzy or lost pattern of the choroidal vasculature is of diagnostic value

Xinshu Liu[1], Shuling Wang[2], Yan An[1] and Hao Zhang[1]*

[1]Department of Ophthalmology, The Fourth People's Hospital of Shenyang, China Medical University, Shenyang, Liaoning, China, [2]School of Business Administration, Shenyang Pharmaceutical University, Shenyang, Liaoning, China

Objective: This study aimed to compare enhanced depth imaging optical coherence tomography (EDI-OCT) features of exudative retinal detachment (ERD) type and optic disc (OD) swelling type Vogt–Koyanagi–Harada (VKH) disease.

Methods: Hospitalized VKH patients were retrospectively reviewed and classified into the ERD type and the OD swelling type. The EDI-OCT features were then analyzed.

Results: The study included 32 ERD type and 15 OD swelling type VKH patients at the acute uveitis stage. The interval between the onset of ocular symptoms and the start of treatment in OD swelling type VKH disease was significantly longer compared to the ERD type ($p < 0.001$). A fuzzy or lost pattern of the choroidal vasculature was observed in 100% of VKH patients of both types. Moreover, high frequencies (greater than or equal to 50%) of fluctuations in the internal limiting membrane, interdigitation zone disruption, ERD, retinal pigment epithelium (RPE) folds, and ellipsoid zone disruption were observed in both types. Patients with OD swelling type VKH disease exhibited higher frequencies of OD swelling and hyperreflective substances above the RPE ($p < 0.001$ and $p = 0.003$, respectively), with lower frequencies of ERD and bacillary layer detachment ($p = 0.012$ and $p < 0.001$, respectively). At the convalescence stage, changes in the EDI-OCT images of 10 ERD type and 5 OD swelling type VKH patients were analyzed. The frequencies of the OCT features decreased with similar trends in both types of VKH disease.

Conclusion: Although ERD type and OD swelling type VKH disease have their own unique characteristics, they share common EDI-OCT features. The Fuzzy or lost pattern of the choroidal vasculature that indicates choroidal inflammation may serve as a diagnostic aid for VKH disease, especially for the OD swelling type and the early-stage ERD type.

KEYWORDS

exudative retinal detachment, fuzzy or lost pattern of the choroidal vasculature, optical coherence tomography, optic disc swelling, Vogt-Koyanagi-Harada disease

1 Introduction

Vogt–Koyanagi–Harada (VKH) disease is a multisystemic autoimmune disorder that mediated by T cells acting against antigens found on melanocytes. It is characterized by bilateral granulomatous panuveitis and associated with central nervous system, auditory, and integumentary involvement (1). The most characteristic manifestation of panuveitis is exudative retinal detachment (ERD) (2). However, in some patients, ERD is not remarkable, and optic disc (OD) swelling is the more prominent fundus finding (3). Okunuki et al. (3) reported the clinical features of two types of VKH disease, ERD and OD swelling, and highlighted the differences in disease course and treatment response. Nevertheless, OD swelling type VKH disease, which needs to be differentiated from other conditions, such as optic neuritis, elevated intracranial pressure, and other autoimmune inflammatory conditions and infections, still tends to be misdiagnosed (4–6).

Optical coherence tomography (OCT) provides *in vivo* images of the retina and the choroid and is widely used in evaluating and diagnosing fundus diseases. OCT studies primarily focused on the topographic features of the retina and the choroid in VKH disease. Gupta et al. (7) reported the presence of retinal pigment epithelium (RPE) striations in OCT images of acute VKH patients. Furthermore, Agarwal et al. (8) found that bacillary layer detachment (BLD) is a common finding in OCT images of patients with acute VKH disease. Enhanced depth imaging OCT (EDI-OCT) provides more information about the choroid. In Agarwal et al.'s (9) study, the EDI-OCT-derived choroidal vascularity index had a statistically significant reduction over time in VKH patients. Using the newly invented optical coherence tomography angiography (OCTA), Liang et al. (10) found that the choriocapillary vascular density decreased in VKH patients compared with normal controls. Despite prior researches, no research comparing the OCT features of ERD type and OD swelling type VKH disease has been reported. In the current study, EDI-OCT images of two types of VKH disease at acute uveitis and convalescence stages were analyzed to offer additional clues to the diagnosis and evaluation of these two types of VKH disease, especially the OD swelling type.

2 Subjects and methods

2.1 Subjects

We retrospectively reviewed the medical records of consecutively hospitalized VKH patients in the Fourth People's Hospital of Shenyang between June 2017 and August 2020. This study was approved by the Institutional Review Board of the Fourth People's Hospital of Shenyang and adhered to the tenets of the Declaration of Helsinki. Patients with acute VKH disease, who had not received prior treatment, were included. VKH disease was diagnosed in accordance with the revised criteria of the International Committee on Nomenclature (11). The follow-up information was collected from patients who received regular follow-ups for at least 2 months. Patients with a history of other retinal and/or choroidal diseases, myopia >6 diopters, and opaque

optical media were excluded. All patients received oral prednisone at an initial dose of 0.8–1.0 mg/kg of body weight daily, followed by a gradual tampering of the dose thereafter (1, 12). Additional oral immunomodulatory agents, topical steroids, and mydriatics were administered when necessary. VKH patients were divided into two groups based on whether they had clinically prominent ERD at presentation by Dr. Zhang. Patients with clinically evident ERD with or without OD swelling detected by indirect ophthalmoscopy were defined as having ERD type VKH disease, and patients with clinically evident OD hyperemia and swelling with no ERD detected by indirect ophthalmoscopy were defined as having OD swelling type VKH disease (3).

2.2 OCT examination

OCT was performed using the Spectralis HRA+OCT system (Heidelberg Engineering, Heidelberg, Germany) fellow function at each visit. Raster scans with EDI were acquired at the macular region, with a minimum of 25 B-scans per volume scan of 30°∗20°. Each B-scan was averaged over 9 frames, with a distance of 240 mm between consecutive scans. The OCT images at presentation and then at 1 week, 4 weeks, and 8 weeks after treatment initiation were independently reviewed by Dr. Liu and Dr. An. In cases of disagreement, Dr. Zhang made the final decision after a panel discussion. The following 10 OCT features of VKH patients were recorded in the current study: ERD, OD swelling, fluctuations in the internal limiting membrane (ILM), BLD, RPE folds, fuzzy or lost pattern of the choroidal vasculature, hyperreflective substances above RPE, ellipsoid zone (EZ) disruption, interdigitation zone (IZ) disruption, and RPE detachment (PED) (Figure 1). In cases of OD swelling type VKH disease, very mild ERD that was not observable during fundus examination was detectable by OCT. Fluctuations in the ILM refer to the loss of its smooth surface, resulting in fluctuating changes with at least 2 peaks or troughs (13). BLD was the break within myoids that isolates ellipsoids and outer segments from the remaining photoreceptor cell bodies (8, 14). RPE folds were the loss of the smooth surface of the RPE layer, resulting in various forms of protrusion. One peak or trough in the RPE layer was defined as an RPE fold (13).

2.3 Main outcome measures

The primary outcome of this study was EDI-OCT features of ERD type and OD swelling type VKH disease at the acute uveitis stage. We further observed the changes in these features at the convalescence stage.

2.4 Statistical analysis

Comparisons between the two types of VKH disease were conducted using SPSS 23.0 software for Windows (SPSS Inc., Chicago, IL, USA). Regarding demographic characteristics, the independent samples t-test was used for normal distribution continuous variables, the Mann–Whitney test was used for non-normal distribution continuous variables, and the chi-squared test

FIGURE 1
Enhanced depth imaging optical coherence tomography images of two types of Vogt–Koyanagi–Harada (VKH) disease at the acute uveitis stage. **(A)** The left eye of a patient with exudative retinal detachment (ERD) type VKH disease without optic disc (OD) swelling. ERD, bacillary layer detachment (BLD) and retinal pigment epithelium detachment (PED) were obvious. The pattern of the choroidal vasculature was fuzzy. **(B)** The left eye of a patient with ERD type VKH disease with OD swelling. The pattern of the choroidal vasculature was fuzzier than that in **(A)**. **(C)** The right eye of a patient with OD swelling type VKH disease with no ERD. OD swelling was obvious. Fluctuations in the internal limiting membrane (FILM), retinal pigment epithelium folds (RPEF), ellipsoid zone disruption (EZD) and interdigitation zone disruption (IZD) were displayed. The pattern of the choroidal vasculature was completely lost. **(D)** The left eye of a patient with OD swelling type VKH disease with shallow ERD. Hyperreflective substances above the RPE (HSRPE) was observed. The pattern of the choroidal vasculature was completely lost. **(E)** The left eye of a patient with OD swelling type VKH disease. Fuzzy of the choroidal vasculature was the only feature observed in addition to OD swelling.

was used for categorical variables. Generalized estimating equation was applied to accommodate the correlation between two eyes of the same person when comparing OCT features at the acute uveitis stage. $P < 0.05$ was considered statistically significant.

3 Results

This study included 47 VKH patients (94 eyes) presented at the acute uveitis stage, with 15 (30 eyes) of them receiving regular follow-ups for 2 months. Of the patients included, 32 patients (64 eyes) were classified as having ERD type VKH disease, while 15 patients (30 eyes) were classified as having OD swelling type VKH disease. The male percentages of the ERD type and the OD swelling type were 50.0% and 53.3%, respectively ($P = 0.831$). The average age at the onset of ocular symptoms in patients with the OD swelling type (49.2 ± 12.6 years) was higher than that in patients with the ERD type (42.5 ± 13.5 years); however, the difference was not statistically significant ($P = 0.112$). The interval between the onset of ocular symptoms and the start of treatment in the OD swelling type [12(9, 20) days] was significantly longer than that in the ERD type [7(4, 13) days] ($P < 0.001$). The demographic characteristics are presented in Table 1.

Detailed information of EDI-OCT features of the two types of VKH disease at the acute uveitis stage is presented and compared in Table 2. OCT features with a frequency of 50% or higher were first evaluated. For ERD type VKH patients, the following frequencies of OCT features were observed: ERD (100%), fluctuations in the ILM (100%), fuzzy or lost pattern of the choroidal vasculature

TABLE 1 Demographic characteristics of two types of Vogt-Koyanagi-Harada disease.

	ERD type	OD swelling type	*P*
Number of patients	32	15	NA
Number of eyes	64	30	NA
Male percentage	50.0%	53.3%	0.831[a]
Average age (years)	42.5 ± 13.5	49.2 ± 12.6	0.112[b]
Interval between the onset of ocular symptoms and the start of treatment (days)	7(4, 13)	12(9, 20)	**<0.001[c]**

ERD, exudative retinal detachment; OD, optic disc; [a]chi square test, [b]independent-samples t-test, [c]Mann–Whitney test. Bold value was statistically significant.

(100%), IZ disruption (100%), RPE folds (87.5%), EZ disruption (70.3%), and BLD (65.6%). For OD swelling type VKH patients, the following frequencies of OCT features were observed: OD swelling (100%), fuzzy or lost pattern of the choroidal vasculature (100%), fluctuations in the ILM (93.3%), IZ disruption (93.3%), RPE folds (86.7%), ERD (76.7%), EZ disruption (53.3%), and hyperreflective substances above RPE (50%). Moreover, we observed a low frequency of PED (10.9% in the ERD type and 10% in the OD swelling type) in both types. Notably, up to 60% of the OCT features showed a high level of consistency between the two types of VKH disease, except for the following statistically significant differences:

TABLE 2 Enhanced depth imaging optical coherence tomography features of two types of Vogt-Koyanagi-Harada disease at the acute uveitis stage.

Features	ERD type (n = 64)	OD swelling type (n = 30)	P
ERD	64 (100.0%)	23 (76.7%)	**0.012**
OD swelling	15 (23.4%)	30 (100.0%)	**<0.001**
Fluctuations in the ILM	64 (100.0%)	28 (93.3%)	0.301
Bacillary layer detachment	42 (65.6%)	0 (0)	**<0.001**
RPE folds	56 (87.5%)	26 (86.7%)	0.937
Fuzzy or lost pattern of the choroidal vasculature	64 (100.0%)	30 (100.0%)	NA
Hyperreflective substances above RPE	7 (10.9%)	15 (50.0%)	**0.003**
EZ disruption	45 (70.3%)	16 (53.3%)	0.251
IZ disruption	64 (100.0%)	28 (93.3%)	0.301
PED	7 (10.9%)	3 (10.0%)	0.894

ERD, exudative retinal detachment; OD, optic disc; ILM, internal limiting membrane; RPE, retinal pigment epithelium; EZ, ellipsoid zone; IZ, interdigitation zone; PED, RPE detachment. Bold values were statistically significant.

In cases of the OD swelling type, the frequencies of OD swelling and hyperreflective substances above the RPE were higher than that in the ERD type (100% vs. 23.4% and 50% vs. 10.9%; $p < 0.001$ and $p = 0.003$); while the frequencies of ERD and BLD were lower than that in the ERD type (76.7% vs. 100% and 0 vs. 65.6%; $p = 0.012$ and $p < 0.001$).

The frequencies of all EDI-OCT features presented downward trends on different levels after treatment initiation in both types. More specifically, ERD and RPE folds resolved within 8 weeks and 4 weeks, respectively, in both types. In the ERD type, OD swelling subsided within 8 weeks, and fluctuations in the ILM and BLD subsided within 4 weeks; In the OD swelling type, fuzzy or lost pattern of the choroidal vasculature and EZ disruption regressed within 8 weeks. The frequencies of the fuzzy or lost pattern of the choroidal vasculature, hyperreflective substances above RPE, and EZ disruption in the ERD type and the OD swelling type, fluctuations in the ILM and hyperreflective substances above RPE in the OD swelling type were all below 40% within 8 weeks. IZ disruption and PED only improved within 8 weeks in a few cases of both types.

4 Discussion

In the present study, the OD swelling type VKH patients got longer interval between the onset of ocular symptoms and the start of treatment. OD swelling type VKH disease shares some common EDI-OCT features with ERD type VKH disease at the acute uveitis stage. The fuzzy or lost pattern of the choroidal vasculature was observed in 100% of the patients of both types of VKH, and

fluctuations in the ILM, IZ disruption, ERD, RPE folds and EZ disruption were observed in at least 50% of the patients. Meanwhile, patients with OD swelling type VKH disease had higher frequencies of OD swelling and hyperreflective substances above the RPE, with lower frequencies of ERD and BLD. A good response to systematic anti-inflammatory treatment was observed in all OCT features of both types.

In our study and Okunuki et al.'s (3) study, the interval between the onset of ocular symptoms and the start of treatment in OD swelling type VKH disease was significantly longer than that in ERD type VKH disease. Two possible reasons may explain the treatment delay. On the one hand, compared to the dramatic decreased visual acuity due to abrupt progression of ERD in the ERD type, visual impairment in OD swelling type VKH disease was less severe due to no or subclinical ERD (detectable by OCT) at disease onset. Patients sought health care after a delay. On the other hand, the diagnosis of OD swelling type VKH may delay. In Le et al.'s (5) report, an OD swelling type VKH patient received her diagnosis after excluding other autoimmune, malignant, or infective etiologies following extensive investigations and a nearly 1 year period of observation. The treatment delay may be associated with chronic recurrent disease course and poor visual prognosis.

The fuzzy or lost pattern of the choroidal vasculature, the only choroidal OCT feature recorded and analyzed in the present study, was originally described as an indocyanine green angiography (ICGA) sign of VKH disease (15). Miyanaga et al. (15) observed a fuzzy or lost pattern of the choroidal vasculature in the intermediate-to-late phase of ICGA in all the initial acute VKH patients studied and presumed it to be an indication of diffuse inflammatory vasculopathy of choroidal vessels. We also observed this phenomenon in EDI-OCT images, and it was the only OCT feature observed in 100% of VKH patients of both types at the acute uveitis stage. During severe inflammation, the pattern of the choroidal vasculature was completely lost. With the remission of inflammation, the outline of the individual choroidal vessels gradually became clear. Lee et al. (16) observed a darkened type choroid morphology in EDI-OCT images of acute VKH patients. The darkened morphology was characterized as diffuse, homogenous, and hypo-reflective pattern with markedly decreased visibility of the large choroidal vessel layer (16), which is similar to our study's fuzzy or lost pattern of the choroidal vasculature. Although the fuzzy or lost pattern of the choroidal vasculature was observed in both ICGA and EDI-OCT images of acute VKH patients, we presumed different imaging principles. We suppose that, at the acute uveitis stage, edematous choroidal stroma and RPE cells caused by choroidal inflammation may block and scatter the near-infrared light reflected from the choroidal vasculature during OCT imaging, leading to a fuzzy or lost pattern of the choroidal vasculature. The fuzzy or lost pattern of the choroidal vasculature in EDI-OCT images, an indication of choroidal inflammation, is useful for the diagnosis of OD swelling type VKH disease, which tends to be misdiagnosed as optic neuritis or elevated intracranial pressure because of prominent OD swelling. It is also valuable for diagnosing very early-stage ERD type VKH disease, when the choroidal inflammation has not yet involved adjacent structures.

Fluctuations in the ILM, ERD, RPE folds, and OD swelling occur when choroidal inflammation progresses. Lin et al. (17) first

observed and defined fluctuations in the ILM in OCT images of 34 out of 65 VKH eyes (52.3%). They also proposed local constriction caused by inflammatory cells infiltrating in the vitreous and diffuse, but uneven, edema of the retina and the choroid due to inflammation may be the cause (17). We also observed fluctuations in the ILM in more than 50% of the eyes of both types of VKH disease patients, and the frequencies of fluctuations in the ILM of two types of VKH showed no significant difference. In our study, the subclinical ERD detected by OCT at the acute uveitis stage of OD swelling type VKH disease was shallow and localized compared to the high and extensive ERD of the ERD type. Moreover, the frequency of ERD was observed to be lower in the OD swelling type. Gupta et al. described RPE folds, also known as RPE undulations, as peaks and troughs of the RPE layer in all 4 VKH patients (eight eyes) studied with 3-dimensional OCT (7). Hosoda et al. (18) hypothesized that the thick and deformed inflammatory choroid of VKH patients contributes to the formation of RPE folds. RPE folds were also common in our study, seen in more than 80% of eyes of both types of VKH disease patients, with the frequencies between the two types showing no significant difference. Fluctuations in the ILM, ERD, and RPE folds were common OCT features in both types of VKH disease, which may help in the diagnosis. The frequency of OD swelling at the acute uveitis stage of OD swelling type VKH disease was significantly higher than that of the ERD type. A previous study speculated that older age and crowded discs correlate with the occurrence of OD swelling (19). The average age of OD swelling type VKH disease was higher than that of the ERD type; however, it is not significant in the present study, and a larger sample size is needed to show statistical significance. Further studies on the choroidal circulation and disc morphology of OD swelling type VKH disease are warranted. These OCT features responded rapidly to systemic corticosteroid treatment in both types of VKH disease in our study. All of these features regressed within 8 weeks, except OD swelling and fluctuations in the ILM in the OD swelling type which may be due to severe OD hyperemia and swelling. Close monitoring of these OCT features would help in the evaluation of therapeutic efficacy.

OCT features related to tissue disorganization (BLD, EZ disruption, and IZ disruption) of VKH disease are discussed below. BLD, a common OCT feature of ERD type VKH disease, described as the cystoid space and membranous structure previously (20), was termed and defined by Mehta et al. (14) as the break within inner segment myoids that isolate ellipsoids and outer segments from the remaining photoreceptor cell bodies. Hydrostatic forces originating from choroidal inflammation and strengthening adherence at the IZ by the subretinal fibrin may both contribute to the split in the structural weakness myoid layer of VKH patients (8, 21). From Agarwal et al.'s (8) report, BLD was found in 112 of the 118 (94.9%) VKH eyes with serous retinal detachment at presentation, all of which resolved within 3.4 ± 1.3 days after intravenous methylprednisolone therapy (8). The percentage of BLD was 65.6% in ERD type VKH eyes at the acute uveitis stage in our study, and all regressed within 4 weeks after oral prednisone therapy. The percentage of BLD in the ERD type in the present study is lower than that in the former report (8), which may be due to different inclusion criteria. In the former report, only patients with multifocal serous retinal detachment were included (8), which may exclude less severe ERD type VKH patients. Based on the consensus of the International Nomenclature for Optical

Coherence Tomography Panel, the outer three hyperreflective bands that were identified included the EZ, IZ, and RPE/Bruch's complex (22). Zhao et al. (13) observed the disappearance of the three-layer structure on OCT images of acute uveitis stage VKH patients. In our study, disruption of the EZ occurred in 70.3% of the eyes in the ERD type and 53.3% of the eyes in the OD swelling type, while disruption of the IZ occurred in 100% of the eyes in the ERD type and 93.3% of the eyes in the OD swelling type at the acute uveitis stage. We propose two explanations to help illustrate the occurrence of EZ and IZ disruption: outer segments and ellipsoids of photoreceptor cells injured in sequence by inflammation from the choroid and ellipsoids and outer segment degeneration after isolating from the remaining photoreceptor cell bodies in the BLD region. The EZ was gradually restored after systematic anti-inflammatory treatment. IZ restoration was slow (10% in the ERD type and 40% in the OD swelling type within 8 weeks), and the hyperreflective band of IZ may not be observed in some VKH patients until years after presentation based on our clinical experience.

Hyperreflective substances above the RPE may be constituted by degenerated photoreceptor outer segments, inflammatory exudation, and hyperplasia of RPE cells (23) after a period of disease onset. The frequency of hyperreflective substances above the RPE was higher in OD swelling type VKH disease than that in the ERD type at the acute uveitis stage. The longer interval between the onset of ocular symptoms and the start of treatment in OD swelling type than that in ERD type may be responsible. Degenerated photoreceptor outer segments and inflammatory exudation increase over time, and hyperplasia of RPE cells occurred at a certain time. Degenerated photoreceptor outer segments and inflammatory exudation are gradually resolved; however, hyperplasia of RPE cells remains (24), which may help explain why a small number of hyperreflective substances above the RPE still existed until the 8-week follow-up.

PED on OCT images is less common in VKH disease. In our study, it was observed in 7 out of 64 eyes (10.9%) and 3 out of 30 eyes (10%) at the acute uveitis stage of ERD type and OD swelling type VKH disease, respectively. Khochtali et al. (25) reported two acute VKH disease patients with bilateral PED. Although resolution of PED after systemic corticosteroids would suggest an underlying inflammatory mechanism, the exact process of PED is still unclear.

5 Conclusion

The current study compared EDI-OCT features of ERD type and OD swelling type VKH disease at acute uveitis and convalescence stages and explored the underlying physiopathological mechanisms. Although ERD type and OD swelling type VKH disease bear their own unique characteristics, they share common OCT features. Fuzzy or lost pattern of the choroidal vasculature indicates choroidal inflammation and was observed in all VKH patients at the acute uveitis stage. This may serve as a diagnostic aid for VKH disease, especially for the OD swelling type and the early-stage ERD type. All OCT features responded well to systematic anti-inflammatory treatment. Close monitoring of these OCT features would help in the evaluation of therapeutic efficacy.

Data availability statement

The raw data supporting the conclusions of this article will be made available by the authors, without undue reservation.

Ethics statement

The studies involving humans were approved by the Institutional Review Board of the Fourth People's Hospital of Shenyang. The studies were conducted in accordance with the local legislation and institutional requirements. Written informed consent for participation was not required from the participants or the participants' legal guardians/next of kin in accordance with the national legislation and institutional requirements.

Author contributions

XL: Conceptualization, Data curation, Formal analysis, Funding acquisition, Investigation, Methodology, Resources, Software, Validation, Visualization, Writing – original draft, Writing – review & editing. SW: Supervision, Visualization, Writing – review & editing. YA: Data curation, Formal analysis, Investigation, Writing – original draft. HZ: Conceptualization, Investigation, Project administration, Supervision, Writing – review & editing.

Funding

Acknowledgments

Conflict of interest

The authors declare that the research was conducted in the absence of any commercial or financial relationships that could be construed as a potential conflict of interest.

Publisher's note

All claims expressed in this article are solely those of the authors and do not necessarily represent those of their affiliated organizations, or those of the publisher, the editors and the reviewers. Any product that may be evaluated in this article, or claim that may be made by its manufacturer, is not guaranteed or endorsed by the publisher.

References

1. Du L, Kijlstra A, Yang P. Vogt-Koyanagi-Harada disease: Novel insights into pathophysiology, diagnosis and treatment. *Prog Retin Eye Res.* (2016) 52:84–111. doi: 10.1016/j.preteyeres.2016.02.002

2. Herbort CP, Tugal-Tutkun I, Abu-El-Asrar A, Gupta A, Takeuchi M, Fardeau C, et al. Precise, simplified diagnostic criteria and optimised management of initial-onset Vogt-Koyanagi-Harada disease: an updated review. *Eye.* (2022) 36:29–43. doi: 10.1038/s41433-021-01573-3

3. Okunuki Y, Tsubota K, Kezuka T, Goto H. Differences in the clinical features of two types of Vogt-Koyanagi-Harada disease: serous retinal detachment and optic disc swelling. *Jpn J Ophthalmol.* (2015) 59:103–8. doi: 10.1007/s10384-014-0367-8

4. Nichani P, Christakis PG, Micieli JA. Headache and bilateral optic disc edema as the initial manifestation of Vogt-Koyanagi-Harada disease. *J Neuroophthalmol.* (2021) 41:e128–30. doi: 10.1097/WNO.0000000000000917

5. Le TA, Simon S, Gilhotra J, Hissaria P. Vogt-Koyanagi-Harada syndrome presenting with bilateral optic disc swelling and leptomeningeal enhancement. *BMJ Case Rep.* (2019) 12:e229719. doi: 10.1136/bcr-2019-229719

6. Yang HK, Park KH, Kim JS, Hwang JM. Bilateral disc edema in a patient with Vogt-Koyanagi-Harada disease. *Can J Ophthalmol.* (2014) 49:e54–6. doi: 10.1016/j.jcjo.2014.01.002

7. Gupta V, Gupta A, Gupta P, Sharma A. Spectral-domain cirrus optical coherence tomography of choroidal striations seen in the acute stage of Vogt-Koyanagi-Harada disease. *Am J Ophthalmol.* (2009) 147:148–53. doi: 10.1016/j.ajo.2008.07.028

8. Agarwal A, Freund KB, Kumar A, Aggarwal K, Sharma D, Katoch D, et al. Bacillary layer detachment in acute Vogt-Koyanagi-Harada disease: A novel swept-source optical coherence tomography analysis. *Retina.* (2021) 41:774–83. doi: 10.1097/IAE.0000000000002914

9. Agrawal R, Li LK, Nakhate V, Khandelwal N, Mahendradas P. Choroidal vascularity index in Vogt-Koyanagi-Harada disease: an EDI-OCT derived tool for monitoring disease progression. *Transl Vis Sci Technol.* (2016) 5:7. doi: 10.1167/tvst.5.4.7

10. Liang A, Jia S, Gao F, Han X, Pei M, Qu Y, et al. Decrease of choriocapillary vascular density measured by optical coherence tomography angiography in Vogt-Koyanagi-Harada disease. *Graefe's Arch Clin Exp Ophthalmol.* (2021) 259:3395–404. doi: 10.1007/s00417-021-05238-5

11. Read RW, Holland GN, Rao NA, Tabbara KF, Ohno S, Arellanes-Garcia L, et al. Revised diagnostic criteria for Vogt-Koyanagi-Harada disease: report of an international committee on nomenclature. *Am J Ophthalmol.* (2001) 131:647–52. doi: 10.1016/s0002-9394(01)00925-4

12. Yang P, Ye Z, Du L, Zhou Q, Qi J, Liang L, et al. Novel treatment regimen of Vogt-Koyanagi-Harada disease with a reduced dose of corticosteroids combined with immunosuppressive agents. *Curr Eye Res.* (2018) 43:254–61. doi: 10.1080/02713683.2017.1383444

13. Zhao GL Li RZ, Pang YH, Wang XQ, Peng HJ, Wei JF, et al. Diagnostic function of 3D optical coherence tomography images in diagnosis of Vogt-Koyanagi-Harada Disease at acute uveitis stage. *Med Sci Monit.* (2018) 24:687–97. doi: 10.12659/msm.905931

14. Mehta N, Chong J, Tsui E, Duncan JL, Curcio CA, Freund KB, et al. Presumed foveal bacillary layer detachment in a patient with toxoplasmosis chorioretinitis and pachychoroid disease. *Retin Cases Brief Rep.* (2021) 15:391–8. doi: 10.1097/ICB.0000000000000817

15. Miyanaga M, Kawaguchi T, Miyata K, Horie S, Mochizuki M, Herbort CP. Indocyanine green angiography findings in initial acute pretreatment Vogt-Koyanagi-Harada disease in Japanese patients. *Jpn J Ophthalmol.* (2010) 54:377–82. doi: 10.1007/s10384-010-0853-6

16. Lee H, Bae K, Kang SW, Woo SJ, Ryoo NK, Kim SJ, et al. Morphologic characteristics of choroid in the major choroidal thickening diseases, studied by optical coherence tomography. *PLoS ONE.* (2016) 11:e147139. doi: 10.1371/journal.pone.0147139

17. Lin D, Chen W, Zhang G, Huang H, Zhou Z, Cen L, et al. Comparison of the optical coherence tomographic characters between acute Vogt-Koyanagi-Harada disease and acute central serous chorioretinopathy. *BMC Ophthalmol.* (2014) 14:87.

18. Hosoda Y, Uji A, Hangai M, Morooka S, Nishijima K, Yoshimura N. Relationship between retinal lesions and inward choroidal bulging in Vogt-Koyanagi-Harada disease. *Am J Ophthalmol.* (2014) 157:1056–63. doi: 10.1016/j.ajo.2014.01.015

19. Nakao K, Abematsu N, Mizushima Y, Sakamoto T. Optic disc swelling in Vogt-Koyanagi-Harada disease. *Invest Ophth Vis Sci.* (2012) 53:1917–22. doi: 10.1167/iovs.11-8984

20. Ishihara K, Hangai M, Kita M, Yoshimura N. Acute Vogt–Koyanagi–Harada disease in enhanced spectral-domain optical coherence tomography. *Ophthalmology.* (2009) 116:1799–807. doi: 10.1016/j.ophtha.2009.04.002

21. Liakopoulos S, Keane PA, Ristau T, Kirchhof B, Walsh AC, Sadda SR. Atypical outer retinal fluid accumulation in choroidal neovascularization: a novel OCT finding. *Ophthal Surg Lasers Imag Retina*. (2013) 44:S11–8. doi: 10.3928/23258160-2013 1101-03

22. Staurenghi G, Sadda S, Chakravarthy U, Spaide RF. Proposed lexicon for anatomic landmarks in normal posterior segment spectral-domain optical coherence tomography. *Ophthalmology.* (2014) 121:1572–8. doi: 10.1016/j.ophtha.2014.02.023

23. Miura M, Makita S, Azuma S, Yasuno Y, Sugiyama S, Mino T, et al. Evaluation of retinal pigment epithelium layer change in Vogt-Koyanagi-Harada disease with multicontrast optical coherence tomography. *Invest Ophth Vis Sci.* (2019) 60:3352–62. doi: 10.1167/iovs.19-27378

24. Nakamura T, Hayashi A, Oiwake T. Long-term changes of retinal pigment epithelium in the eyes with Vogt-Koyanagi-Harada disease observed by adaptive optics imaging. *Clin Ophthalmol.* (2019) 13:927–33. doi: 10.2147/OPTH.S199886

25. Khochtali S, Ksiaa I, Megzari K, Khairallah M. Retinal pigment epithelium detachment in acute Vogt-Koyanagi-Harada disease: an unusual finding at presentation. *Ocul Immunol Inflamm.* (2019) 27:591–4. doi: 10.1080/09273948.2018.1433304

Check for updates

Frontiers in Medicine

Case report: Intraretinal hyperflow microinfiltration lesions on swept-source optical coherence tomography angiography as a potential biomarker of primary vitreoretinal lymphoma

Zhangxing Xu[1,2†], Haixia Bai[1†], Xin Liu[1], Junhui Shen[1], Yongchao Su[1,3] and Yao Wang[1*]

[1]Eye Center, The Second Affiliated Hospital, School of Medicine, Zhejiang University, Zhejiang Provincial Key Laboratory of Ophthalmology, Zhejiang Provincial Clinical Research Center for Eye Diseases, Zhejiang Provincial Engineering Institute on Eye Diseases, Hangzhou, Zhejiang, China, [2]Department of Ophthalmology, Ningbo Medical Center LiHuiLi Hospital, Ningbo, Zhejiang Province, China, [3]Department of Ophthalmology, Haiyan People's Hospital, Jiaxing, Zhejiang Province, China

Primary vitreoretinal lymphoma (PVRL) is often associated with central nervous system involvement, contributing to a heightened mortality rate, thus imaging features that are characteristic enough to be potential biomarkers of PVRL are important, either in diagnosis or in assessment of disease activity. This report details the case of a 68-year-old male who presented with blurred vision in both eyes persisting for 2 months. Fundus examination demonstrated vitreous opacity and multiple subretinal yellow nodular lesions of varying sizes in the peripheral fundus of both eyes. Multiple vertical hyperreflective lesions in the neural retina of posterior pole, indistinct outer retina borders in the fovea, and hyperreflective lesions in the sub-retinal pigment epithelium (RPE) space of the peripheral retina were demonstrated on swept-source optical coherence tomography (SS-OCT) of the left eye. Hyperflow signals corresponding to the vertical hyperreflective lesions were detected on swept-source optical coherence tomography angiography (SS-OCTA) images of retinal deep capillary plexus (DCP) layer. Notably, the hyperflow signals, precisely located around retinal vessels from the nerve fiber layer to the outer plexiform layer, were postulated to stem from the dilation of infiltrated retinal vessels. Vitreous pathological results of the left eye confirmed the diagnosis of PVRL. Treatments with intravitreal methotrexate injections led to a marked improvement of best-corrected visual acuity (BCVA) and regression of the hyperflow microinfiltration lesions demonstrated on SS-OCTA. In conclusion, SS-OCTA effectively delineated the vertical hyperreflective lesions and corresponding hyperflow signals in the posterior pole macular region of a patient with PVRL. These lesions significantly diminished following intravitreal methotrexate injections. We speculated that the specific hyperflow signals on SS-OCTA could act as a potential biomarker of PVRL, and SS-OCTA holds promise in facilitating early diagnosis and monitoring therapeutic responses in PVRL cases.

Introduction

Primary vitreoretinal lymphoma (PVRL) is a rare malignancy occurring in the retina or vitreous of the eye, comprising less than 0.01% of all ocular diseases (1–4). The average onset age of PVRL is 50–60 years, with a male-to-female ratio of 1: 2. It is a high-grade typical B-cell malignancy. Central nervous system involvement will appear in 50–80% of patients with PVRL several years after ocular symptoms, which causes a poor prognosis (2, 5). The etiopathogenesis of primary intraocular lymphoma is still not well understood (6). Both the infectious theory and hematological spread theory have been implicated in the etiology of PVRL (7). Patients typically present with nonspecific complaints of painless blurred vision, floaters or both. Examination of the posterior segment reveals vitritis and development of creamy lymphoma choroidal infiltration with orange-yellow infiltrates deep to the RPE (4, 8). These creamy lesions can also develop in the posterior pole of retina. Optical coherence tomography (OCT) offers an obvious advantage in assessing disease activity and monitoring response to treatment in PVRL. OCT demonstrates vitreous cells, RPE nodularity, and outer retinal hyperreflectivity, pigment epithelial detachment, epiretinal membrane and retinal disorganization (9). Vertical hyperreflective lesions are also a common finding on OCT in PVRL (10). As one of the few reports on optical coherence tomography angiography (OCTA) presentations of PVRL, the research of Chen et al. discovered perivascular flower-bud-like lesions (PFBLs) visualized on *enface* OCTA as novel features of PVRL, which may represent the perivascular infiltration or migration of lymphoma cells (11). This report elucidates the characteristics of vertical hyperreflective lesions on swept-source OCT/OCTA (SS-OCT/OCTA), analyzing the association between vertical hyperreflective lesions on SS-OCT and corresponding hyperflow signals on SS-OCTA images of deep capillary plexus (DCP) layer. Therefore, we try to delve into the possible origin of the hyperflow signals, and consolidate the role of SS-OCTA findings in diagnosing PVRL and monitoring the activity of PVRL involving the posterior pole of fundus.

Case presentation

A 68-year-old Chinese male presented to our hospital for worsening blurry vision in both eyes for 2 months. He reported no significant past ocular or medical history. The best-corrected visual acuity (BCVA) was 20/30 in the right and 20/60 in the left eye. The anterior segment examination revealed mild cataract of both eyes. There were no keratic precipitates or anterior chamber cells. Mild vitreous opacity with asteroid hyalosis, and several subretinal yellow lesions in the nasal peripheral fundus was observed in the right eye (Figure 1A). Moderate vitreous opacity, multiple subretinal yellow nodular lesions with varying sizes, streaky pigmentation and white exudation on the surface of several yellow subretinal nodules were

detected in the left eye (Figure 1B). B-scan ultrasonography showed clusters of moderately or highly condensed punctate echoes in vitreous cavity and irregular hypoechoic lesions under the retina of the left eye (Figure 1C). SS-OCT (Ultrawide SS-OCT/OCTA, BM-400K BMizar, TowardPi Medical Technology, Beijing, China) revealed outer retina with fuzzy borders and one vertical hyperreflective lesion in the posterior pole of fundus of the left eye (Figure 2G1). SS-OCTA image of superficial capillary plexus (SCP) layer with scanning areas of 6 mm × 6 mm showed no abnormal blood flow signals of the left eye (Figure 2A1). Multiple hyperflow signals corresponding to the vertical hyperreflective lesions on SS-OCT were unexpectedly demonstrated on the *enface* SS-OCTA images of DCP layer (Figure 2B1), which were more pronounced on the *enface* structural image of DCP layer (Figure 2D1). The *enface* structural image of SCP layer showed no abnormal reflectance correlated with lymphoma (Figure 2C1). SS-OCT B-scan with flow overlay of SCP layer and DCP layer showed inhomogenous flow signals of the vertical intraretinal hyperreflective lesion (Figures 2E1,F1). Vessel density map of SCP layer demonstrated several warm hues dots corresponding to these hyperflow spots, and they were distributed along the retinal vessels (Supplementary Figure S1). Notably, neither similar vertical hyperreflective lesions in SS-OCT nor hyperflow spots in SS-OCTA were detected in the posterior pole of the right eye (Figure 3). Homogenous hyperreflective lesions sub-RPE space in the peripheral retina could also be detected by 24 mm OCT scan (Figures 1D,E). Additionally, the aqueous humor examination of the left eye showed an elevated level of interleukin-10 (IL-10) at 21.8 pg./mL and a decreased level of IL-6 at 0.3 pg./mL, resulting in a high IL-10/IL-6 ratio of 70.4.

We strongly suspected the possibility of PVRL and performed diagnostic 23 gauge-vitrectomy for his left eye (Figure 4A). Moderate vitreous opacity was observed in the surgery, and multiple yellow nodular lesions and white exudation in the inferior retina were proved to be subretinal. Vitreous fluid was collected for cytology, immunohistochemistry and molecular analysis. Cytology unveiled atypical lymphocytes with an elevated nucleus/cytoplasm ratio and multiple prominent nucleoli (Figure 4B). Lymphoma cells in the vitreous presented positive B-cell marker of CD20, CD79a, Bcl-2 and Bcl-6, with a high Ki-67 positive rate of 30–40% (Figure 4C). There was only weak positivity of CD3, the T-cell marker. The results of IgH gene rearrangement were positive, and TCR gene rearrangement was negative in monoclonality analysis.

There were no positive findings in cranial-enhanced magnetic resonance imaging (MRI) and whole-body positron emission tomography-computed tomography (PET-CT). Thereby, a diagnosis of PVRL of both eyes was definitively confirmed.

The treatment regimen for both eyes was as follows: an induction phase of weekly intravitreal methotrexate injections for 4 weeks at a dose of 400 μg in 0.05 mL; after induction, biweekly consolidation methotrexate injections were given for 1 month at a dose of 400 μg in 0.05 mL; and a maintenance phase involves monthly methotrexate
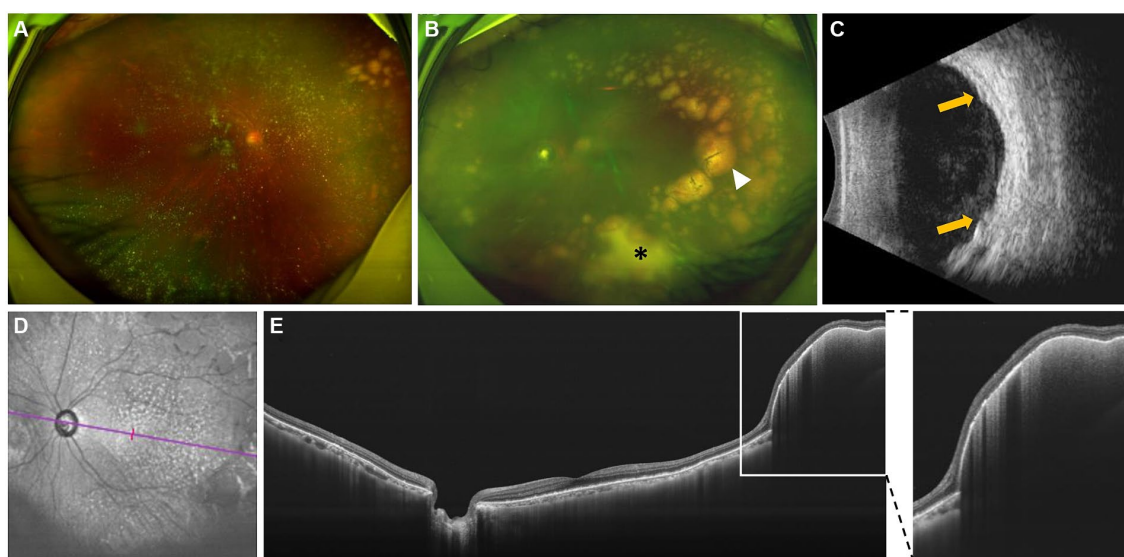
FIGURE 1
Fundus photographs, B-scan ultrasonography and swept-source Optical Coherence Tomography (SS-OCT) examinations at initial presentation.
(A) Asteroid hyalosis and several subretinal yellow deposits were detected in the nasal retina of the right eye. **(B)** Moderate vitreous opacity, multiple subretinal yellow nodular lesions with varying sizes, streaky pigmentation (white arrowhead) and white exudation (asterisk) on the surface of several yellow subretinal nodules were detected in the left eye. **(C)** B-scan ultrasonography showed clusters of moderately or highly condensed punctate echoes in vitreous cavity, and irregular hypoechoic lesions (yellow arrows) under the retina of the left eye. **(D,E)** Infrared image and SS-OCT images with scanning length of 24 mm of the left eye. Homogenous hyperreflective lesions in the sub-RPE space were detected in the peripheral retina. An enlarged inset is provided on the right.

injections for 10 months. A neuro-oncological consultation was recommended to assess the necessity of prophylactic systemic chemotherapy. Following the induction phase, the patient's BCVA improved to 20/22 of the right eye and 20/30 of the left eye. SS-OCT showed that the corresponding vertical hyperreflective lesions almost vanished. Furthermore, outer retina fuzzy borders were in remission in the left eye, and ellipsoid zone and external limiting membrane could be recognized on SS-OCT (Figures 2E2–G2). The preexisting hyperflow spots on SS-OCTA images of DCP layer almost disappeared (Figure 2B2). *Enface* SS-OCTA structural images of DCP layer also showed the preexisting hyperreflective lesions almost disappeared (Figure 2D2). SS-OCTA image of SCP layer and *enface* SS-OCTA structural images of SCP layer showed no great difference from pre-treatment images (Figures 2A2,C2). No significant changes were detected on SS-OCT in the macular area of the right eye. Fundus examination demonstrated a clear vitreous cavity postoperatively. The number and size of the peripheral white-yellow lesions were reduced obviously in both eyes, especially in the infratemporal peripheral fundus of the left eye. Moreover, the white exudation on the surface of yellow subretinal nodules in the inferior peripheral fundus of the left eye also diminished (Figures 4D,E).

The study protocol adhered to the tenets of the Declaration of Helsinki and was approved by the Medical Ethics Committee of the Second Affiliated Hospital of Zhejiang University School of Medicine, Hangzhou, China. All the clinical data were obtained from the electronic medical record system, with the patients' consent.

Discussion

OCT is widely used in assessing disease activity and monitoring therapeutic response in PVRL. OCT findings of PVRL include outer

retina fuzzy borders, pigment epithelium detachments (PED), subretinal hyperreflective infiltration, intraretinal infiltration, subretinal fluid (SRF) and subretinal fibrosis (12). Even though pathological examination remains the gold standard for diagnosing PVRL, the specific characterizations on OCT are of great significance for the early diagnosis of PVRL. However, there are only few reported data available with SS-OCTA. SS-OCT/OCTA, distinguished by its higher resolution and broader scanning range, enhances lesion visualization in greater detail compared to traditional Spectral Domain OCT/OCTA (13). Notably, SS-OCTA can especially provide layered blood flow images with unprecedented resolution in a rapid and non-invasive way.

In our case, SS-OCT showed outer retina fuzzy borders, PED and intraretinal infiltrations, which help to establish the diagnosis of PVRL. Intraretinal infiltrations manifested as several vertical hyperreflective lesions with various width and length on SS-OCT. Most of these hyperreflective lesions extended from ganglion cell layer or inner plexiform layer to the outer layer of the neuroretina such as external limiting membrane or ellipsoid zone. Some lesions were challenging to discern due to the blurring of outer retinal boundaries. The biggest intraretinal infiltration extended from retinal nerve fiber layer to RPE, suggesting the potential for the lesion to infiltrate the entire retinal layer. Some small intraretinal infiltrations extended from inner nuclear layer to outer nuclear layer, with the majority around the outer plexiform layer. Deák et al. described the lesions as vertical hyperreflective lesions (VHRLs), which were often localized around second-order and third-order retinal vessels, varied in width but extended from the inner retina to the outermost part of the neuroretina or the RPE. Additionally, Deák et al. highlighted that VHRL could be indicative of a diagnosis of vitreoretinal lymphoma (10). In our case, some intraretinal infiltrations differed from the reported VHRLs by being shorter, thicker, and pointed like ears of wheat. Saito et al.
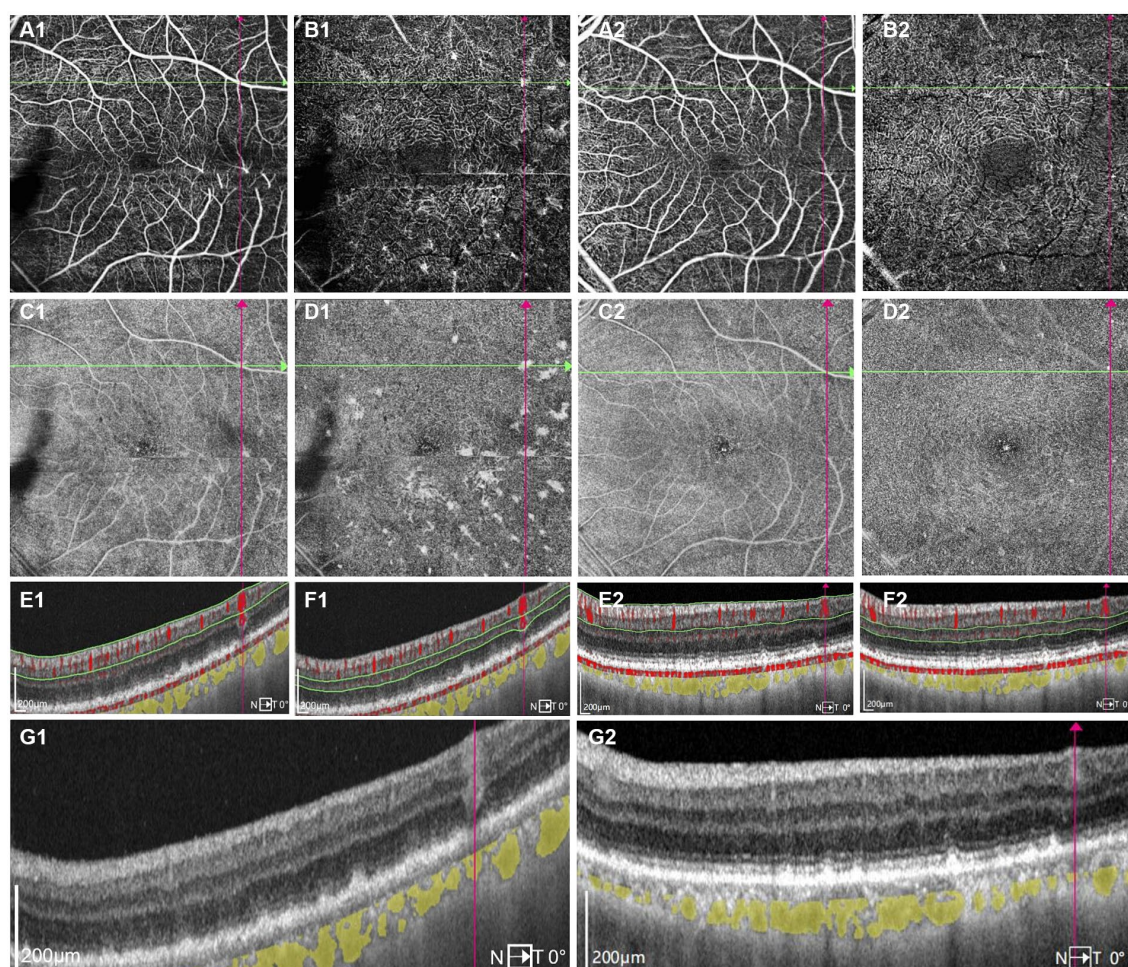
FIGURE 2

One typical intraretinal hyperflow microinfiltration lesions located beneath superficial retinal vessel on Swept-Source Optical Coherence Tomography Angiography (SS-OCTA) with scanning areas of 6 mm × 6 mm of the left eye **(A1–G1)** before and **(A2–G2)** after induction phase of intravitreal methotrexate injections. **(A1)** SS-OCTA image of (superficial capillary plexus) SCP layer showed no abnormal blood flow signals correlated with lymphoma. **(B1)** SS-OCTA image of retinal deep capillary plexus (DCP) layer showed several hyperflow spots. **(C1)** *Enface* SS-OCTA structural images of SCP layer showed no abnormal reflectance correlated with lymphoma. **(D1)** *Enface* SS-OCTA structural images of DCP layer showed multiple hyperreflective lesions. **(E1,F1)** SS-OCT B-scan with flow overlay of **(E1)** SCP layer and **(F1)** DCP layer showed inhomogenous flow signals of the vertical intraretinal hyperreflective lesion. The boundary of flow signals overlaid on the vertical intraretinal hyperreflective lesions was difficult to clearly distinguish from the flow signals of retinal vessels above them. **(G1)** SS-OCT showed outer retina with fuzzy borders and the vertical hyperreflective lesion extended from retinal nerve fiber layer to RPE. The hyporeflective vascular wall boundary of vessels above intraretinal infiltrations was absent. **(A2)** SS-OCTA image of SCP layer showed no great difference from **A1**. **(B2)** SS-OCTA image of DCP layer showed the preexisting hyperflow spots almost disappeared. **(C2)** *Enface* SS-OCTA structural images of SCP layer showed no great difference from **C1**. **(D2)** *Enface* SS-OCTA structural images of DCP layer showed the preexisting hyperreflective lesions almost disappeared. **(E2,F2)** SS-OCT B-scan with flow overlay of **(E2)** SCP layer and **(F2)** DCP layer showed the preexisting hyperflow signals of the vertical intraretinal hyperreflective lesion almost disappear. **(G2)** SS-OCT showed the corresponding vertical hyperreflective lesions almost vanished, outer retina fuzzy borders were in remission.

described intraretinal infiltrations as "focal round lesions in the neural retinal layer," some of which were larger than VHRLs and the lesions of our findings (14). Meanwhile, observations of Zhao et al. revealed that the diffuse and homogeneous hyperreflective lesions with blurred boundaries of neuroretina were also intraretinal infiltrations of PVRL (12). These diverse OCT features of intraretinal infiltrations may be able to provide clues to general infiltration patterns of malignant lymphocytes. We supposed that these microinfiltrations in our case might develop into larger lesions like VHRLs or diffuse intraretinal infiltrations along with the disease progression. Since the pathophysiology of PVRL is still not completely clear, histologic examinations of retinal tissues are imperative to elucidate the origin and infiltration mechanisms of PVRL.

No abnormal blood flow signals correlated with lymphoma were observed on the SS-OCTA image of SCP layer with scanning areas of 6 mm × 6 mm of the left eye. However, the SS-OCTA image of DCP layer showed several hyperflow spots of the left eye, which were corresponding to the vertical intraretinal microinfiltrations. The average size of these hyperflow spots were $19,606 \pm 14,412$ um^2 (range: 2100–60,000 um^2) on the SS-OCTA image of DCP layer. All the hyperflow spots located in the perifoveal area. Remarkably, the study revealed that a majority of the intraretinal microinfiltrations (15, 65.2%) were situated directly beneath superficial retinal vessels within the retinal nerve fiber layer. Conversely, there were no discernible vessels overlaying the remaining intraretinal microinfiltrations (8, 34.8%). However, there were apparent smaller blood flow signals originating
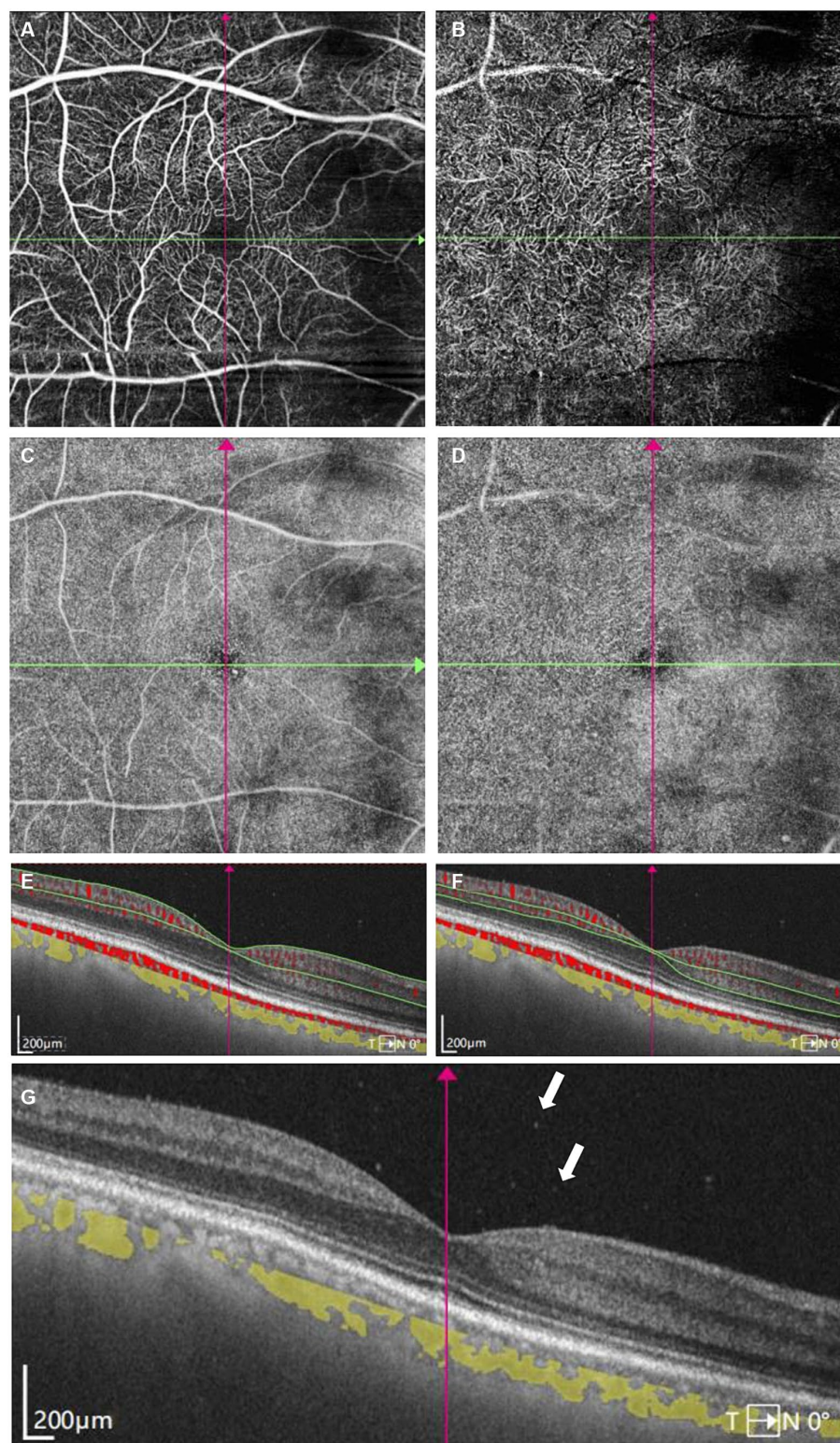
FIGURE 3
Swept-Source Optical Coherence Tomography Angiography (SS-OCTA) examinations of the right eye at initial presentation. **(A)** SS-OCTA image of superficial capillary plexus (SCP) layer. **(B)** SS-OCTA image of retinal deep capillary plexus (DCP) layer. **(C)** *Enface* SS-OCTA structural images of SCP layer. **(D)** *Enface* SS-OCTA structural images of DCP layer. **(A–D)** showed no obvious abnormality correlated with lymphoma. **(E,F)** SS-OCT B-scan centered on the fovea with flow overlay of **(E)** SCP layer and **(F)** DCP layer showed no obvious abnormal blood flow signals correlated with lymphoma. **(G)** SS-OCT showed several vitreous cells (white arrows).
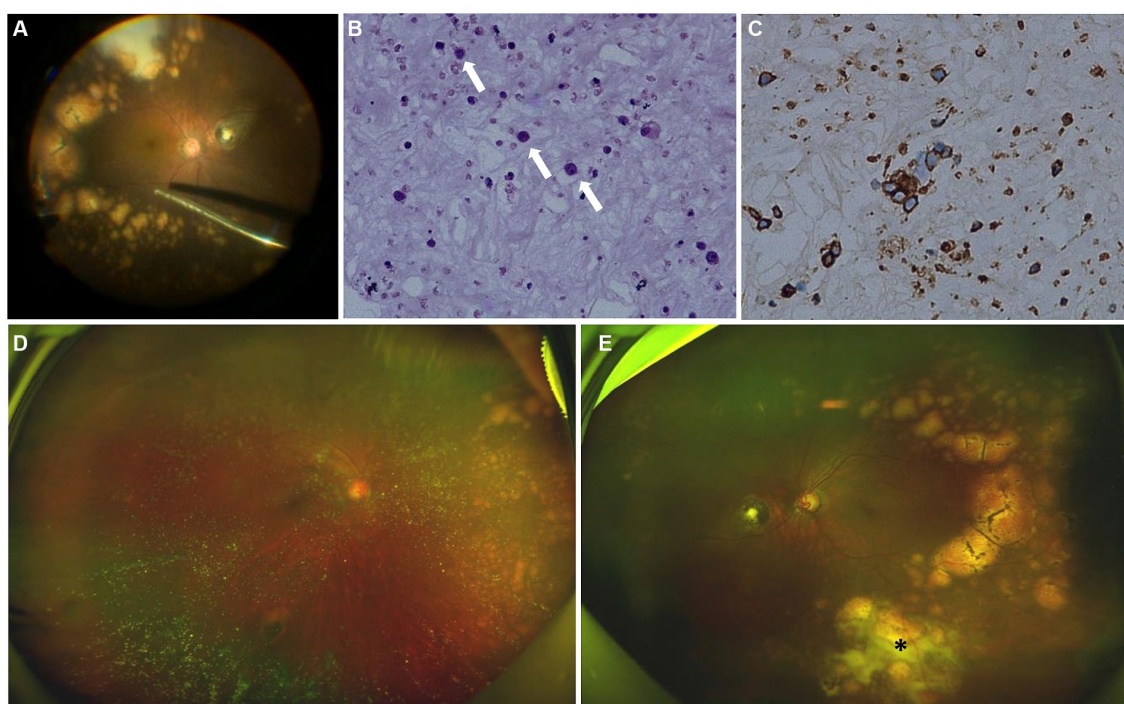
FIGURE 4
Intraoperative fundus image, cytology and immunohistochemical test of the vitreous after surgery, fundus photographs examinations after induction phase of intravitreal methotrexate injections. **(A)** Intraoperative fundus image showed multiple subretinal yellow nodular lesions with varying sizes, streaky pigmentation and white exudation (surgeo's view). **(B)** The vitreous was infiltrated with numerous lymphocytes (white arrows) (hematoxylin and eosin ×400). **(C)** Immunohistochemical stains are positive for CD20 in the lymphocytes (peroxidase anti-peroxidase ×400). **(D)** The number and size of white-yellow subretinal lesions in the nasal retina of the right eye were reduced. **(E)** The opacity of vitreous disappeared. The number and size of white-yellow subretinal lesions were reduced obviously. White exudation (asterisk) on the surface of yellow subretinal nodules in the inferior peripheral fundus also diminished.

from the outer plexiform layer around them (Supplementary Figure S2). Moreover, the size of intraretinal microinfiltrations was unrelated to their positioning beneath retinal vessels.

SS-OCT with flow overlay also demonstrated inhomogenous flow signals of the vertical intraretinal hyperreflective lesions. It was challenging to distinguish the boundary of flow signals overlaying the vertical intraretinal hyperreflective lesions from the flow signals of retinal vessels above them. Among these lesions, 2 (8.7%) exhibited blood flow signals above the lesion, 3 (13.0%) presented scattered blood flow signals, 6 (26.1%) showed blood flow signals centrally, and 11 (47.8%) displayed blood flow signals laterally. Additionally, one lesion (4.3%) exhibited no significant blood flow distribution.

It is well documented that the migration of lymphocytes within the nervous tissues relies on a selective interaction between adhesion molecules on lymphocytes and the vascular endothelium of the central nervous system (15). Chen et al. described hyperreflective lesions along the vessels on the mid-retinal slabs of *enface* OCTA as perivascular flower-bud-like lesions (PFBLs) in 34.3% of PVRL cases. They also found that vessels with PFBLs showed higher reflectance than the surrounding retina, with the clear hyporeflective vascular wall boundary absent. They posited that PFBLs could potentially represent lymphoma deposits originating from retinal vascular microinfiltrations, given their proximity to retinal vessels (11). Intraretina hyperreflective infiltrations with hyperflow signals reported in our case manifested a similar hyperreflective appearance to PFBLs on *enface* SS-OCTA structural images of DCP layers. Additionally, we also noticed that the hyporeflective vascular wall

boundary of vessels above intraretinal infiltrations was absent on SS-OCT before treatment (Figure 2G1), implying the infiltration of vascular wall. However, there were still some notable differences between the two lesions. Primarily, all PFBLs were situated along the vessels on *enface* SS-OCTA. While we observed that certain intraretinal microinfiltrations were not located along retinal vessels in the retinal nerve fiber layer. In addition, no hyperflow signals were detected in PFBLs by SS-OCTA, while hyperflow signals were obvious in the intraretinal microinfiltration lesions on DCP layer in our case. Moreover, these intraretinal infiltrations located close to retinal vessels from retinal nerve fiber layer to the outer plexiform layer, thus we suppose that these intraretinal microinfiltrations could potentially result from hematological spread from surrounding infiltrated vessels. The microenvironment with sufficient blood supply from retinal vessels may play a pivotal role in the growth, invasion and metastasis of malignant lymphocytes. That may also explain why intraretinal microinfiltrations mostly located around retinal vessels. Pierro et al. reported a case of a patient affected by PVRL with multiple subretinal hyperreflective infiltrates on OCT, and reported that several hyperreflective lesions were also detected on OCTA structural images (16). To our knowledge, few articles have previously observed hyperflow signals on SS-OCTA images of DCP layers in patients with PVRL. The current pathological results are still not sufficient to elucidate the relationship between PVRL and retinal vascular infiltration. Passarin et al. reported a case of brain intravascular lymphomatosis presenting hemorrhage of brain vessels. They postulated that the mechanism of hemorrhage might be chronic

degenerative or inflammatory changes of the vessel wall with lymphomatosis (17). we excluded images with artifacts that might affect the evaluations in our case. Moreover, we calculated the diameter of the retinal vessels above the microinfiltration lesions on SCP layer. The average diameter of these retinal vessels decreased from 54.27 ± 13.08 um (range: 33–72 um) to 48.73 ± 8.51 um (range: 28–59 um) after methotrexate intravitreal injections. Hence, we hypothesize that the interaction between lymphocytes and vascular endothelial cells could potentially induce chronic damage to the vascular wall, resulting in the dilation of retinal vessels. The abnormal hyperflow signals could stem from the dilation of infiltrated retinal vessels. Histologic examinations of retinal tissues may be essential in elucidating the pathological mechanism associated with the hyperflow signals.

In the left eye, multiple hyperreflective lesions on *enface* SS-OCTA structural images of DCP layers were also detected to be co-localized with the vertical hyperreflective lesions (Figure 2D1). These lesions presented as punctations of varying sizes. Larger lesions displayed as irregular masses with spiculated sign, which were morphologically different from the roundish PFBLs. The spiculated sign on SS-OCTA seemed to demonstrate the metastasis characteristic of infiltrating tumor cells into surrounding normal tissues more vividly. The average size of hyperreflective lesions on *enface* SS-OCTA structural images was $55,561 \pm 86,184$ um^2 (range: 5900–93,000 um^2), which was significantly larger than those observed on SS-OCTA images of DCP layer. This could be attributed to the fact that *enface* SS-OCTA structural images displayed the actual size of intraretinal microinfiltrations, whereas SS-OCTA images only depicted the blood flow signals within these lesions. Moreover, these lesions were reduced and the spiculated sign was in remission after intravitreal methotrexate injections. This suggests that observation of intraretinal microinfiltration lesions on SS-OCTA might also play a crucial role in monitoring the therapeutic efficacy of PVRL. Since there was no interference of retinal vessel signals, microinfiltration lesions seemed to be much more intuitional on *enface* SS-OCTA structural images than that on angiographic images (Figures 2B1,D1).

Interestingly, none of the intraretinal microinfiltration lesions were detectable on the wide-angle fundus photography, infrared or fluorescein angiography fundus images. We supposed that these lesions might be an ultra-early prediction of PVRL infiltration, implying that the intraretinal microinfiltration lesions might evolve into visible lesions on fundus along with the disease progression. SS-OCTA was sensitive and noninvasive to detect the occurrence and development of the intraretinal microinfiltration lesions, thus we believe that it would be a feasible approach for early diagnosis and monitoring the therapeutic efficacy of PVRL. Intraretinal hyperflow microinfiltration lesions exhibited by SS-OCTA could also act as significant biomarkers to evaluate the activity of PVRL. Further investigations are needed to reveal the natural development process of intraretinal infiltrations.

There were several limitations. First, the vessel diameter was manually measured using the built-in measurement tool in OCTA device. Due to the indistinct vessel boundary, measurement error should be considered when vessel diameter was compared before and after treatment. Histological examination is essential for elucidating the morphology of infiltrated retinal vessels. Second, hyperreflective intraretinal lesion was previously detected in SS-OCT in uveitis cases such as sarcoidosis (18), whose OCTA manifestation has seldom been reported. It is uncertain whether the hyperflow signals in the microinfiltration lesion was typical character of PVRL. Hence, More PVRL cases were required to verify the dilation of infiltrated retinal vessels over the microinfiltration lesion, and further clarify the value of hyperflow signals in differential diagnosis and activity assessment.

Conclusion

SS-OCTA has been increasingly used in assessing the fundus disease due to its superiority in resolution, depth and width. This report characterized intraretinal microinfiltrations of PVRL using wide-field SS-OCTA. Those distinctive lesions presented as vertical hyperreflective lesions in SS-OCT, locating close to retinal vessels from the retinal nerve fiber layer to the outer plexiform layer, exhibiting a concentrated distribution in the macular region. Notably, traditional fundus photography or fluorescein angiography failed to detect these lesions. Intriguingly, SS-OCTA images of DCP layer demonstrated a number of punctate hyperflow lesions corresponding to those intraretinal microinfiltrations lesions, which were supposed to be the dilation of the infiltrated retinal vessels. The microinfiltrations exhibited sensitivity to intraocular chemotherapy of methotrexate, rapidly disappearing after the fourth injection. The Intraretinal hyperflow microinfiltration lesions detected by SS-OCTA would act as significant biomarkers to evaluate activity of PVRL. Furthermore, SS-OCTA can clearly demonstrate the location, size and variation of microinfiltration lesions. This underscores the potential of SS-OCTA in the early diagnosis of PVRL microinfiltrations and the monitoring of therapeutic responses.

Data availability statement

The original contributions presented in the study are included in the article/Supplementary material, further inquiries can be directed to the corresponding author.

Ethics statement

The studies involving humans were approved by Medical Ethics Committee of the Second Affiliated Hospital of Zhejiang University School of Medicine, Hangzhou, China. The studies were conducted in accordance with the local legislation and institutional requirements. The participants provided their written informed consent to participate in this study. Written informed consent was obtained from the individual(s) for the publication of any potentially identifiable images or data included in this article.

Author contributions

administration, Resources, Writing – review & editing, Conceptualization, Investigation, Methodology.

Conflict of interest

The authors declare that the research was conducted in the absence of any commercial or financial relationships that could be construed as a potential conflict of interest.

Publisher's note

All claims expressed in this article are solely those of the authors and do not necessarily represent those of their affiliated organizations, or those of the publisher, the editors and the reviewers. Any product that may be evaluated in this article, or claim that may be made by its manufacturer, is not guaranteed or endorsed by the publisher.

Supplementary material

The Supplementary material for this article can be found online at: https://www.frontiersin.org/articles/10.3389/fmed.2024.1386979/full#supplementary-material

SUPPLEMENTARY FIGURE S1
Vessel density map of superficial capillary plexus layer of the left eye before induction phase of intravitreal methotrexate injections. Several warm hues dots were distributed along the retinal vessels.

SUPPLEMENTARY FIGURE S2
Another typical intraretinal hyperflow microinfiltration lesions on Swept-Source Optical Coherence Tomography Angiography (SS-OCTA) with scanning areas of 6mm × 6mm of the left eye **(A1–G1)** before and **(A2–G2)** after induction phase of intravitreal methotrexate injections. **(A1)** SS-OCTA image of superficial capillary plexus (SCP) layer showed no abnormal blood flow signals correlated with lymphoma. **(B1)** SS-OCTA image of retinal deep capillary plexus (DCP) layer showed several hyperflow spots. **(C1)** *Enface* SS-OCTA structural images of SCP layer showed no abnormal reflectance correlated with lymphoma. **(D1)** *Enface* SS-OCTA structural images of DCP layer showed multiple hyperreflective lesions. **(E1,F1)** SS-OCT B-scan with flow overlay of **(E1)** SCP layer and **(F1)** DCP layer showed flow signals of the small vertical intraretinal hyperreflective lesion. There were apparent smaller blood flow signals originating from the outer plexiform layer around it. **(G1)** SS-OCT showed outer retina with fuzzy borders and the vertical hyperreflective lesion extended from inner nuclear layer to outer nuclear layer. **(A2)** SS-OCTA image of SCP layer showed no great difference from A1. **(B2)** SS-OCTA image of DCP layer showed the preexisting hyperflow spots almost disappeared. **(C2)** *Enface* SS-OCTA structural images of SCP layer showed no great difference from **C1**. **(D2)** *Enface* SS-OCTA structural images of DCP layer showed the preexisting hyperreflective lesions almost disappeared. **(E2,F2)** SS-OCT B-scan with flow overlay of **(E2)** SCP layer and **(F2)** DCP layer showed the preexisting hyperflow signals of the vertical intraretinal hyperreflective lesion almost disappear. **(G2)** SS-OCT showed the corresponding vertical hyperreflective lesions almost vanished, outer retina fuzzy borders were in remission.

References

1. Chan C-C, Rubenstein JL, Coupland SE, Davis JL, Harbour JW, Johnston PB, et al. Primary vitreoretinal lymphoma: a report from an international primary central nervous system lymphoma collaborative group symposium. *Oncologist*. (2011) 16:1589–99. doi: 10.1634/theoncologist.2011-0210

2. Mochizuki M, Singh AD. Epidemiology and clinical features of intraocular lymphoma. *Ocul Immunol Inflamm*. (2009) 17:69–72. doi: 10.1080/09273940902957305

3. Iguaracyra A, Sarah EC. Primary vitreoretinal lymphoma—a review. *Asia-Pac J Ophthalmol*. (2017) 6:283–9. doi: 10.22608/APO.2017150

4. Sobolewska B, Chee S-P, Zaguia F, Goldstein DA, Smith JR, Fend F, et al. Vitreoretinal lymphoma. *Cancer*. (2021) 13:3921. doi: 10.3390/cancers13163921

5. Davis JL. Intraocular lymphoma: a clinical perspective. *Eye*. (2013) 27:153–62. doi: 10.1038/eye.2012.250

6. Coupland SE, Chan CC, Smith J. Pathophysiology of retinal lymphoma. *Ocul Immunol Inflamm*. (2009) 17:227–37. doi: 10.1080/09273940903168696

7. Venkatesh R, Bavaharan B, Mahendradas P, Yadav NK. Primary vitreoretinal lymphoma: prevalence, impact, and management challenges. *Clin Ophthalmol*. (2019) 13:353–64. doi: 10.2147/OPTH.S159014

8. Toledo JJ, Asencio M, García JR, Morales LA, Tomkinson C, Cajigal C. OCT angiography: imaging of choroidal and retinal tumors. *Ophthalmol Retina*. (2018) 2:613–22. doi: 10.1016/j.oret.2017.10.006

9. Xu LT, Huang Y, Liao A, Anthony CL, Voloschin A, Yeh S. Multimodal diagnostic imaging in primary vitreoretinal lymphoma. *Int J Retina Vitr*. (2022) 8:58. doi: 10.1186/s40942-022-00405-0

10. Deák GG, Goldstein DA, Zhou M, Fawzi AA, Jampol LM. Vertical Hyperreflective lesions on optical coherence tomography in vitreoretinal lymphoma. *JAMA Ophthalmol*. (2019) 137:194–8. doi: 10.1001/jamaophthalmol.2018.5835

11. Chen W, Gu J, Liu S, Zhao Z, Jiang T, Xu G, et al. Perivascular flower-bud-like lesions on en face optical coherence tomography angiography in patients with vitreoretinal lymphoma. *Retina*. (2022) 42:2169–75. doi: 10.1097/IAE.0000000000003579

12. Zhao H, Wang X, Mao Y, Peng X. Longitudinal observation of OCT imaging is a valuable tool to monitor primary vitreoretinal lymphoma treated with intravitreal injections of methotrexate. *BMC Ophthalmol*. (2020) 20:10. doi: 10.1186/s12886-019-1300-1

13. Zheng F, Deng X, Zhang Q, He J, Ye P, Liu S, et al. Advances in swept-source optical coherence tomography and optical coherence tomography angiography. *Adv Ophthalmol Pract Res*. (2023) 3:67–79. doi: 10.1016/j.aopr.2022.10.005

14. Saito T, Ohguro N, Iwahashi C, Hashida N. Optical coherence tomography manifestations of primary vitreoretinal lymphoma. *Graefes Arch Clin Exp Ophthalmol*. (2016) 254:2319–26. doi: 10.1007/s00417-016-3395-x

15. Citterio G, Reni M, Gatta G, Ferreri AJM. Primary central nervous system lymphoma. *Crit Rev Oncol Hematol*. (2017) 113:97–110. doi: 10.1016/j.critrevonc.2017.03.019

16. Pierro L, Arrigo A, Casalino G, Miserocchi E, Aragona E, Bandello F. En face optical coherence tomography angiography of primary vitreoretinal lymphoma. Ophthalmic Surg lasers imaging. *Retina*. (2018) 49:49. doi: 10.3928/23258160-20181002-26

17. Passarin MG, Wen PY, Vattemi E, Buffone E, Ghimenton C, Bontempini L, et al. Intravascular lymphomatosis and intracerebral haemorrhage. *Neurol Sci*. (2010) 31:793–7. doi: 10.1007/s10072-010-0284-7

18. De Saint SG, Gratiot C, Debieb AC, Monnet D, Brézin AP. Retinal and pre-retinal nodules: a rare manifestation of probable ocular sarcoidosis. *Am J Ophthalmol Case Rep*. (2022) 26:101525. doi: 10.1016/j.ajoc.2022.101525

Swept-source optical coherence tomography in ocular surface diseases: anterior segment analysis repeatability and its limits

Alberto Recchioni[1,2,3], Abinaya Priya Venkataraman[4], Saaeha Rauz[1,2†] and Alberto Domínguez-Vicent[4*†]

[1]Academic Unit of Ophthalmology, Institute of Inflammation and Aging, University of Birmingham, Birmingham, United Kingdom, [2]Birmingham and Midland Eye Center, Sandwell and West Birmingham NHS Trust, Birmingham, United Kingdom, [3]Optometry and Vision Sciences Group, School of Life and Health Sciences, Aston University, Birmingham, United Kingdom, [4]Division of Eye and Vision, Department of Clinical Neuroscience, Karolinska Institutet, Solna, Sweden

Purpose: This study aims to evaluate the repeatability of anterior segment optical coherence tomography (AS-OCT) in diverse ocular surface disorder (OSD) cohorts, exploring various anterior segment parameters and their accuracy in different disease groups.

Methods: A total of 239 participants across six distinct OSD groups and healthy controls underwent nonmydriatic AS-OCT imaging using the Tomey CASIA 2 device. Anterior segment parameters including anterior chamber depth, width, angle metrics, corneal thickness, keratometry, lens vault, and others were meticulously assessed. Statistical analyses determined repeatability limits and coefficients of variation for each parameter within the different OSD cohorts.

Results: Repeatability for anterior chamber and corneal parameters remained consistent across all OSD groups, indicating minimal impact of ocular surface disease on accuracy. The coefficient of variation (CoV) for the trabecular iris-space area was about 20% for all cohorts. Ocular surface inflammation emerged as a key factor in dry eye, affecting immune-mediated and non-immune conditions alongside age-related ocular surface changes. While anterior chamber depth measurements showed variations, particularly in immune (CoV = 2.5%) and non-immune (CoV = 3.8%) OSD groups, parameters like anterior chamber width and angle to angle showed similar values among the cohorts. Keratometry measures remained stable despite OSD (CoV lower than 1%).

Conclusion: The Tomey CASIA 2 demonstrated reliable repeatability for measuring anterior segment parameters in diverse OSD cohorts. Despite challenges posed by dry eye conditions, this technology holds promise in assessing OSD, suggesting potential clinical protocols similar to those in healthy controls.

KEYWORDS

ocular surface disorders, repeatability, anterior segment OCT, Corneal topography, anterior segment parameters

Introduction

The ocular surface plays a pivotal role in maintaining ocular health by providing a barrier to the external environment. As previously defined by Gipson (1), the ocular surface is seen a system composed of "*the surface and glandular epithelia of the cornea, conjunctiva, lacrimal gland, accessory lacrimal glands, and meibomian gland, and their apical (tears) and basal (connective tissue) matrices, the eyelashes with their associated glands of Moll and Zeis, those components of the eyelids responsible for the blink, and the nasolacrimal duct.*"

The failure of mechanisms responsible for maintaining a healthy ocular surface is underpinned by a group of disorders of diverse pathogenesis leading to ocular surface disease (OSD) (2). A feature of complex OSD is dry eye disease driven by inflammation in many autoimmune-driven conditions including Sjögren's Syndrome, Ocular Mucous Membrane Pemphigoid, Stevens-Johnson Syndrome (3). Additionally, non-immune conditions such as meibomian glands disease, corneal transplantation, chemical injury or trauma can also lead to ocular surface disease. Dry eye symptoms and therapy have major impact on patients' quality of life leading to anxiety and depression (4–6).

Ocular surface disorders can be described within five clinical domains (tear film; eyelids, lid margins and meibomian glands (MG); conjunctiva and fornices; cornea; anterior chamber and sclera) across defining descriptors of activity, damage and a relevant clinical assessment /investigation toolkit (3). The latter includes tear film osmolarity, MG secretion quality, fluorescein and lissamine green staining, and a number of visual function tests (in-vivo confocal microscopy (IVCM), anterior segment optical coherence tomography (AS-OCT), ocular surface analyser (OSA), ultrasound biomicroscopy (UBM), Spectroscopy, topography, photography, angiography).

Despite being commonly used in clinic, the impact of objective metrics that consider ocular vital dyes, flashing lights (white and blue cobalt illumination) and tear break-up time tests (e.g., tear evaporation stress) are still posed into debate (7). Instilling vegetable-based dye (e.g., fluorescein) into an altered ocular surface in OSD might lead the clinician to false conclusions because it might induce discomfort and reflex tearing; in fact, an uncontrolled amount of instilled fluorescein can be potentially seen as patches of corneal dryness instead of oversaturation of the stained epithelial cells (8).

Recently, a plethora of new anterior segment visual function medical devices have entered the clinical arena that are non-contact and do not require the use of vital dyes to enhance visualization of pathology or delivering objective metrics that quantify disease outcomes. These include interferometry, infra-red meibography, corneal epithelial thickness, non-invasive ocular surface analysis and devices such as AST-OCT. The evaluation of the anterior segment parameters, such as corneal thickness and curvature, anterior chamber depth (ACD), width, and drainage angle are performed during new and follow-up visits in a range of subspecialty clinics (corneal, cataract, glaucoma) (9–11). It is important to assess how reliable these anterior segment measurements are in the presence of OSD, as the altered ocular surface epithelium, goblet cell loss, anormal tear film and keratinization may influence the accuracy of these

measurements. Previous studies have shown that the repeatability of the corneal and anterior chamber parameters is related to the qualitative and quantitative tear film metrics (12, 13). Repeatability of the newer devices in the context of ocular surface dryness is unclear. Scan resolution, acquisition time and the internal algorithm are not fully validated for patients with an ocular surface condition. In this study, we have evaluated the repeatability of a newer swept-source AS-OCT (ss-AS-OCT) Casia2 (Tomey, Japan) able to obtain non-invasive high-resolution cross-section of biological structures using low-coherence light. By considering ss-AS-OCT technology in a range of OSD versus healthy cohorts, we wanted to determine the impact of the ocular surface condition on the accuracy of measurements of the anterior segment structures.

Materials and methods

Participants

This study was conducted following the tenants Declaration of Helsinki and approval from the Sandwell and West Birmingham NHS Trust Clinical Effectiveness and Safeguarding Group (Project Registration number #1843, and Project Registration date 08/10/2021). A data-sharing agreement was signed between Sandwell and West Birmingham NHS Trust and Karolinska Institutet. Informed consent was obtained from each patient. A total of 239 participants presenting to the inflammatory eye diseases clinic at the Birmingham and Midland Eye Centre (UK) underwent anterior segment imaging. Patients were categorized into six aetiological clinical groups. G1 = Sjögren's syndrome, G2 = Immune-mediated OSD (Ocular Mucous Membrane Pemphigoid, Stevens-Johnson Syndrome / Toxic Epidermal Necrolysis, Graft-versus-Host Disease); G3 = Non-Immune-mediated OSD (Meibomian Glands Disease, Ocular Rosacea, Atopic Blepharo-keratoconjunctivitis); G4 = High Risk Corneal Transplantation Surgery; G5 = Miscellaneous (Neurotrophic, Injury/Trauma, Preservative Toxicity, Exposure keratopathy, Inherited); and G6 = Healthy controls (participants with no known ocular or systemic disorders and no previous ocular surgery). Only one eye per participant was included with at least 2 readable scans.

Instrumentation and OCT measurements

The participants underwent nonmydriatic OCT imaging with the swept-source anterior segment Casia2 (Tomey, Japan). The Casia2 has a swept laser source of 1310 nm wavelength and performs up to 50,000 A-scans/second. The axial and transverse resolution are 10 μm and 30 μm, respectively. The maximum scan depth and width are approximately 13 mm and 16 mm, respectively. This instrument allows the possibility to image all the anterior segment of the eye including cornea, conjunctiva, anterior chamber, iris and both surfaces of the crystalline lens. In this study, the standard *anterior segment screening* mode was used which is composed of 16 radial scans delivered in approximately 0.3 s avoiding long and stressful ocular surface exposure. The
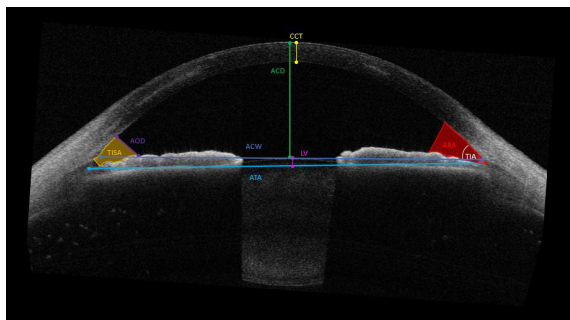
FIGURE 1
Parameters measured by the CASIA2 anterior chamber depth (ACD); the anterior chamber width (ACW), the angle opening distance (AOD) and angle recess area (ARA) 250 µm, 500 µm, and 750 µm, respectively; angle to angle (ATA); apical corneal thickness (CTApex) and thinnest corneal thickness (CTThin); Flat keratometry (Kf) and Steep keratometry (Ks); lens vault (LV); trabecular iris angle (TIA) and trabecular iris-space area (TISA) at 250 µm, 500 µm, and 750 µm, respectively.

repeated measurements were taken under repeatability conditions obtained with the same method, on identical test items, in the same laboratory, by the same operator, using the same equipment, and within short intervals of time (14, 15) by an experienced examiner (AR), with sufficient breaks in between to ensure good patient cooperation. Scans were repeated in there was poor fixation, lid blink during image capture, or if the scan was of unacceptable according to the instrument's analysis software.

Parameters analysed

A number of anterior segment measurements were analysed: (1) the ACD measured from the corneal endothelium level to the anterior lens surface, (2) the anterior chamber width (ACW) measured between the two scleral spurs, (3) the angle opening distance (AOD) between the posterior corneoscleral surface and the anterior iris surface perpendicular to the trabecular meshwork at 250 µm, 500 µm, and 750 µm from the scleral spur, respectively, (4) the angle recess area (ARA) formed by AOD, iris surface and the inner corneo-scleral wall traversed at the angle recess at 250 µm, 500 µm, and 750 µm, respectively, (5) angle to angle (ATA) measured between the angle recesses on the nasal and temporal sides, (6) apical corneal thickness (CTApex), (7) the thinnest corneal thickness (CTThin) measured between the anterior and posterior surfaces of the cornea on the apical point, (8) Anterior Flat keratometry (Kf) measured considering the flattest corneal radius in millimeters (mm), (9) Anterior Steep keratometry (Ks) measured considering the steepest corneal radius in millimeters (mm), (10) lens vault (LV) measured between the anterior crystalline lens surface and the horizontal line joining the two scleral spurs, (11) trabecular iris angle (TIA), and (12) trabecular iris-space area (TISA) measured between the apex in the iris recess and the scleral spur and the point on the iris perpendicularly at 250 µm, 500 µm, and 750 µm, respectively (Figure 1).

In addition, ocular surface metrics such as Ocular Surface Disease Index (OSDI® questionnaire (OSDI) to assess the symptoms of dry eye disease and their impact on vision-related quality of life), fluorescein break-up time (FBUT) measured with 1% preservative-free fluorescein, tear meniscus height (TMH) at the lower eyelid margin, conjunctival inflammation (INFLCONJ) (16) and SICCA ocular staining score (OSS) (17) were measured, and the responses were also included in the analysis.

Statistical analysis

The statistical analyses were performed using SPSS for Windows version 23.0 (SPSS Inc., Chicago, USA), and MATLAB (Mathworks inc., USA). The within-subject standard deviation (Sw), repeatability limits (Rlim) and coefficients of variation (CoVs) were used to describe the repeatability of each measurement parameter in each cohort. The Sw, which represents the repeatability of the measurements, was calculated with a one-way analysis of variance. The repeatability limit was calculated as $[1.96 \cdot \sqrt{2} \cdot S_w]$, and it represents the expected limits that 95 % of the measurements should be within (18). The CoVs were calculated by dividing the Sw by the mean and then expressed in percentage. Data normality was tested using the Shapiro–Wilk test. The bivariate correlation analysis for non-normally distributed data was analyzed using the Spearman test. A guide to interpreting the correlation strength was derived from the recommendations of Navarro (19). A p-value of 0.05 was taken to be statistically significant.

Results

The participants characteristics are summarised in Table 1. The descriptive statistics of the analysed parameters and ocular surface metrics for each group are given in Table 2. Figure 2 shows example AS-OCT images from each group.

Anterior chamber parameters

Figure 3 shows the Rlim values for ACD (upper left panel), ACW (upper central panel) and ATA (upper right panel). The respective values for ACD in immune and non-immune OSD cohorts were higher compared to other cohorts whereas the trend was opposite for the ACW and ATA measurements. The coefficients of variations were similar amongst all three metrics (Table 3). Most of the AOD (bottom right) and ARA (bottom left) RLim measured at 250 µm, 500 µm, and 750 µm were higher in the corneal transplant group (G4) (Figure 3). However, most of the AOD and ARA CoVs were slightly higher in the Neurotrophic, Injury/Trauma, Preservative Toxicity, Exposure keratopathy and Inherited (G5) compared to other groups except for most of the ARA values that were similar to the SS group (G1) Table 3. There were no significant differences in the Sw among the groups for any of these parameters ($p > 0.05$).

Corneal parameters

RLim for CTApex and Kf were higher in non-immune OSD cohort while CTThin and Ks showed higher RLim and CoVs in the

TABLE 1 Participants characteristics.

	All OSD Patients	Group 1 (Sjögren's Syndrome)	Group 2 (Immune)	Group 3 (Non-Immune)	Group 4 (Corneal Transplantation)	Group 5 (Other)	Group 6 (Healthy)	P-Value
Biological sex (Male/Female)	239	4 / 46	28 / 32	31 / 29	13 / 4	4 / 8	13 / 27	< 0.001
Ethnicity*								
White	124	25	31	25	8	8	27	< 0.001
Mixed or multiple ethnic groups	5	2	1	1	0	0	1	0.639
Asian or Asian British	52	12	7	14	6	2	11	0.043
Black, Black British, Caribbean or African	12	5	1	4	1	0	1	< 0.001
Other ethnic group	5	0	0	5	0	0	0	< 0.001
Unknown group	41	6	20	11	2	2	0	< 0.001
	[median (range)]	[median (range)]	[median (range)]	[median (range)]	[median (range)]	[median (range)]	[median (range)]	P-Value
Age (years)	[60 (17–96)]	[59 (27–88)]	[69 (17–89)]	[60 (20–96)]	[56 (30–91)]	[58 (42–96)]	[55 (35–96)]	0.123
OSDI TOTAL (score)	[35.40 (0.00–100.00)]	[52.50 (8.30–100)]	[18.80 (0.00–100)]	[33.30 (0.00–100)]	[55.20 (0–87.50)]	[44.40 (8.30–77.30)]	[18.53 (0.00–75)]	0.731
FBUT (s)	[5.00 (5.00–15.00)]	[4.00 (0.00–8.00)]	[5.00 (0.00–10.50)]	[4.50 (0.00–15.00)]	[5.00 (0.00–12.00)]	[4.50 (2.00–12.00)]	[8.03 (2.61–12.52)]	0.289
TMH (mm)	[0.10 (0.00–0.43)]	[0.10 (0.00–0.30)]	[0.10 (0.00–0.30)]	[0.15 (0.00–0.40)]	[0.10 (0.00–0.30)]	[0.10 (0.10–0.30)]	[0.24 (0.06–0.43)]	0.541
INFLCONJ (score)	[0.00 (0.00–8.50)]	[0.00 (0.00–5.50)]	[0.00 (0.00–8.00)]	[0.00 (0.00–8.50)]	[0.00 (0.00–8.50)]	[0.00 (0.00–4.00)]	[1.35 (0.01–4.18)]	0.111
OSS (score)	[2.00 (0.00–10.50)]	[4.00 (0.50–10–50)]	[2.00 (0.00–7.00)]	[2.25 (0.00–7.50)]	[2.75 (0.00–6.00)]	[2.50 (0.00–3.50)]	[1.52 (0.46–2.67)]	0.391

G1, Sjögren's syndrome; G2, Immune; G3, Non-Immune; G4, Corneal Transplantation, G5 Other, Ocular Surface Disease [Neurotrophic ($n = 4$), Injury/Trauma ($n = 3$), Preservative Toxicity ($n = 1$), Exposure keratopathy ($n = 3$) and Inherited ($n = 1$)]; G6, Healthy controls; Clinical Features: OSDI, Ocular Surface Disease Index (patient symptomatology score); FBUT, Fluoresceine Break-up Time (patient tear film evaporation time in seconds); TMH, Tear Meniscus Height (patient tear film volume estimation in mm); INFLCONJ, Inflammation Conjunctival Score (patient conjunctival eye redness score); OSS, SICCA Ocular Staining Score; Data: reported as median and range (MIN-MAX, with p-values from Mann-Whitney U tests [$p < 0.05$; $p < 0.01$; $p < 0.001$; NS, Not Significant]. *As a matter of ease, groups were classified as follows: 1, White British | 2, White Irish | 3, White Gypsy or Irish Traveler | 4, Any other White background all under White; 5, Mix White and Black Caribbean | 6, Mix White and Black African | 7, Mix White and Asian | 8, Any Other Mixed/multiple ethnic background all under Mixed or multiple ethnic groups; 9, Indian | 10, Pakistani | 11, Bangladeshi | 12, Chinese | 13, Any other Asian background all under Asian or Asian British; 14, Black African | 15, Black Caribbean | 16, Any other Black/African/Caribbean background all under Black, Black British, Caribbean or African; 17, Arab | 18, Any other ethnic group all under Other ethnic group; rest of them as 19, Not known/not provided are all under unknown group.

TABLE 2 Summary of the anterior chamber parameters.

Groups Variables	Group 1 (Sjögren's Syndrome)	Group 2 (Immune)	Group 3 (Non-Immune)	Group 4 (Corneal Transplant)	Group 5 (Other)	Group 6 (Healthy)
	Mean ± STD	Mean ± STD	Mean ± STD	Mean ± STD	Mean ± STD	Mean ± STD
Anterior Chamber parameters						
ACD	2.93 ± 0.46	3.02 ± 0.57	2.94 ± 0.45	3.54 ± 0.62	2.92 ± 0.43	3.08 ± 0.54
ACW	12.01 ± 0.51	11.97 ± 0.50	12.00 ± 0.45	12.03 ± 0.58	12.18 ± 0.67	11.96 ± 0.52
AOD250N	0.29 ± 0.13	0.29 ± 0.15	0.27 ± 0.11	0.39 ± 0.15	0.24 ± 0.09	0.27 ± 0.12
AOD250T	0.31 ± 0.16	0.31 ± 0.21	0.28 ± 0.14	0.36 ± 0.11	0.25 ± 0.13	0.32 ± 0.17
AOD500N	0.40 ± 0.20	0.40 ± 0.22	0.39 ± 0.17	0.63 ± 0.28	0.35 ± 0.13	0.41 ± 0.20
AOD500T	0.42 ± 0.22	0.44 ± 0.28	0.39 ± 0.20	0.55 ± 0.18	0.36 ± 0.21	0.47 ± 0.23
AOD750N	0.54 ± 0.27	0.57 ± 0.31	0.53 ± 0.25	0.91 ± 0.39	0.49 ± 0.22	0.59 ± 0.30
AOD750T	0.56 ± 0.28	0.62 ± 0.37	0.54 ± 0.28	0.78 ± 0.27	0.48 ± 0.25	0.64 ± 0.33
ARA250N	0.07 ± 0.04	0.06 ± 0.05	0.06 ± 0.03	0.09 ± 0.05	0.05 ± 0.02	0.06 ± 0.03
ARA250T	0.07 ± 0.04	0.08 ± 0.08	0.06 ± 0.04	0.08 ± 0.03	0.05 ± 0.03	0.07 ± 0.05
ARA500N	0.15 ± 0.08	0.15 ± 0.09	0.14 ± 0.06	0.22 ± 0.10	0.12 ± 0.05	0.14 ± 0.07
ARA500T	0.16 ± 0.09	0.17 ± 0.13	0.15 ± 0.08	0.19 ± 0.06	0.13 ± 0.07	0.17 ± 0.10
ARA750N	0.27 ± 0.14	0.27 ± 0.15	0.26 ± 0.11	0.41 ± 0.18	0.23 ± 0.09	0.27 ± 0.13
ARA750T	0.28 ± 0.15	0.31 ± 0.21	0.27 ± 0.13	0.36 ± 0.12	0.24 ± 0.12	0.31 ± 0.16
ATA	11.74 ± 0.54	11.66 ± 0.59	11.73 ± 0.43	11.78 ± 0.57	11.89 ± 0.64	11.72 ± 0.56
TIA250N	52.87 ± 17.08	53.81 ± 20.21	52.88 ± 15.59	63.75 ± 14.91	53.79 ± 17.41	50.68 ± 19.78
TIA250T	53.31 ± 18.84	53.99 ± 19.11	53.17 ± 18.92	60.69 ± 12.89	51.90 ± 21.86	53.74 ± 19.52
TIA500N	40.54 ± 14.22	41.30 ± 16.04	40.52 ± 12.54	53.92 ± 16.02	40.08 ± 13.31	40.86 ± 16.99
TIA500T	40.74 ± 15.78	42.71 ± 16.78	40.28 ± 16.05	50.29 ± 10.70	38.34 ± 16.23	44.01 ± 17.25
TIA750N	36.11 ± 13.67	37.83 ± 14.77	36.63 ± 12.49	51.04 ± 15.18	36.70 ± 13.21	38.31 ± 16.31
TIA750T	37.75 ± 13.86	39.78 ± 16.26	36.33 ± 14.70	47.87 ± 10.29	34.68 ± 13.66	40.55 ± 18.05
TISA250N	0.06 ± 0.03	0.06 ± 0.03	0.05 ± 0.02	0.08 ± 0.03	0.05 ± 0.02	0.05 ± 0.03
TISA250T	0.06 ± 0.03	0.07 ± 0.05	0.06 ± 0.03	0.07 ± 0.02	0.05 ± 0.02	0.06 ± 0.04
TISA500N	0.15 ± 0.07	0.14 ± 0.08	0.14 ± 0.06	0.21 ± 0.09	0.12 ± 0.05	0.14 ± 0.06
TISA500T	0.15 ± 0.08	0.16 ± 0.11	0.14 ± 0.07	0.19 ± 0.06	0.13 ± 0.06	0.16 ± 0.08
TISA750N	0.26 ± 0.13	0.27 ± 0.14	0.25 ± 0.11	0.40 ± 0.17	0.23 ± 0.09	0.27 ± 0.13
TISA750T	0.28 ± 0.14	0.29 ± 0.19	0.26 ± 0.12	0.35 ± 0.11	0.23 ± 0.12	0.30 ± 0.15
Corneal parameters						
CTApex	525.41 ± 41.73	529.70 ± 33.97	525.51 ± 48.69	520.62 ± 67.34	520.29 ± 52.15	522.46 ± 38.84
CTThin	513.60 ± 52.10	516.86 ± 39.26	504.04 ± 56.71	471.59 ± 83.17	498.08 ± 92.09	514.31 ± 37.43
Kf	48.24 ± 2.08	48.96 ± 2.59	48.88 ± 3.81	49.54 ± 5.21	47.29 ± 3.05	47.91 ± 1.93
Ks	49.79 ± 2.70	50.26 ± 3.31	50.22 ± 4.14	52.69 ± 6.27	48.46 ± 2.51	49.06 ± 2.01
LV	0.26 ± 0.41	0.15 ± 0.51	0.24 ± 0.38	−0.22 ± 0.48	0.32 ± 0.32	0.12 ± 0.51

Parameters included as mean ± STD: anterior chamber depth (ACD), anterior chamber width (ACW), angle opening distance (AOD), angle recess area (ARA) 250 μm, 500 μm, and 750 μm, angle to angle (ATA), trabecular iris angle (TIA), trabecular iris-space area (TISA) at 250 μm, 500 μm, and 750 μm, apical corneal thickness (CTApex), thinnest corneal thickness (CTThin); Flat keratometry (Kf) and Steep keratometry (Ks) and lens vault (LV).

corneal transplant group (G4) (Figure 4 and Table 4). There were no significant differences in the Sw among the groups for any of these parameters ($p > 0.05$).

Other anterior segment parameters

All TIA RLim measured at 250 μm, 500 μm, and 750 μm were higher in the G5 cohort, with a similar trend observed for the CoVs values. Most of the TISA RLim were higher in the G4 cohort while

for the CoVs highest values were seen in G5 (Figure 5). CoVs value for LV was majorly higher in the G2 cohort (Table 5). There were no significant differences in the Sw among the groups for any of these parameters ($p > 0.05$).

Discussion

This is the first study assessing the repeatability of an anterior segment OCT in different ocular surface disorder groups for
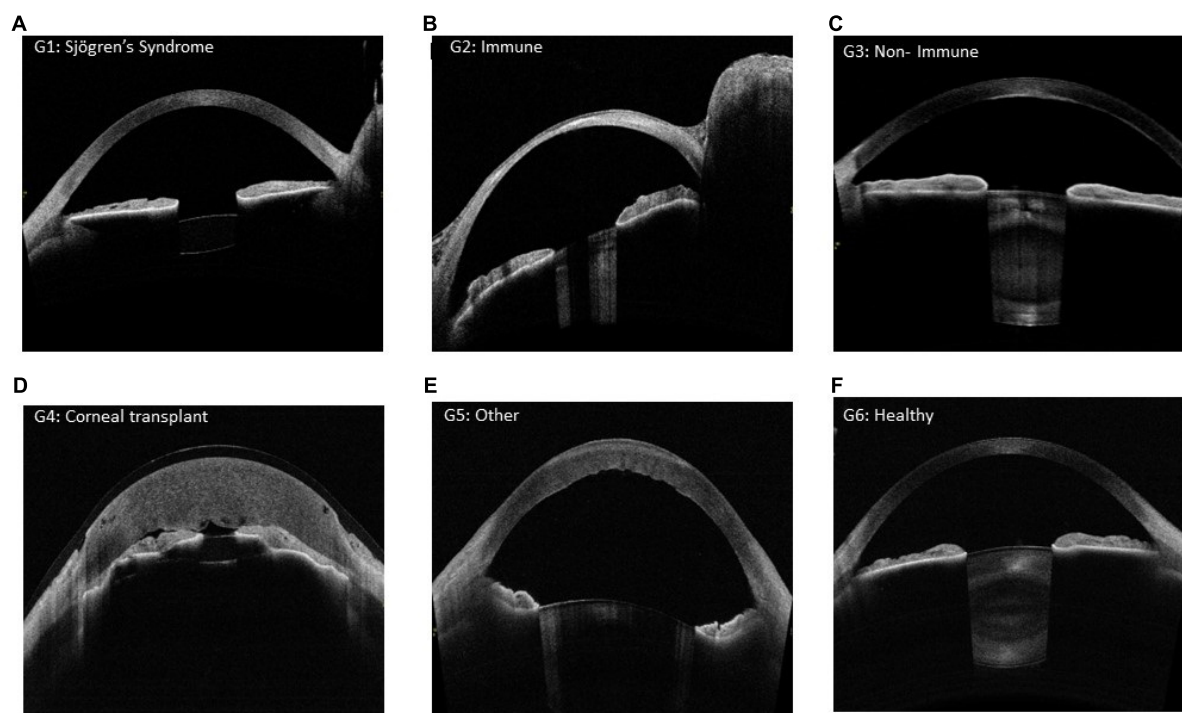
FIGURE 2
(A) Sjögren's syndrome, **(B)** Immune, **(C)** Non- Immune, **(D)** Corneal Transplantation, **(E)** Other and **(F)** Healthy.

measuring various anterior segment parameters. Our results show that the repeatability for the anterior chamber and corneal parameters were similar among all groups and the presence of ocular surface disease did not impact the accuracy. Similarly, the RLim for the LV and TISA were also similar among all groups.

Ocular surface inflammation is a pivotal driver of dry eye for patients with underlying immune-mediated and conditions and those without (20). Additionally, aging can negatively impact on ocular surface health both in the 'healthy' population and those known to ocular surface disorders.

There is a wide range of new techniques that are able to provide quantitative parameters of different anterior segment structures. Although, the damaging effect of ocular surface disorders might have an impact on the performance of these innovative tools. In fact, the ocular surface is the first media that these devices encounter during the measurements, and hence its homeostasis plays a crucial role in the precision of the quantitative metrics (21). Nevertheless, in this study we have not considered ocular surface metrics such as corneal scarring, vascularisation and the presence of conjunctival scarring that appear in severe ocular surface disease (22). The availability of anterior segment imaging devices in public hospitals is still limited due to their cost, maintenance and measurement efficacy (need of repeated measurements/time allocated for each consultation) (23). The use of OCT in the anterior segment is constantly increasing with newer devices able to provide faster scanning modes and images with higher resolution (~15 μm). More recently, ss-AS-OCT has proven to be the foremost technique in detailing the front structures of the eye. Newer AS-OCTs can provide better scanning with deeper tissue penetration and enhanced scanning modes to depict anterior

segment pathologies (24). Also, they appeared to be reasonably repeatable showing excellent intradevice measurement in healthy cohorts (25). However, as shown in a previous study considering posterior segment OCT, it appears that dry eye can be responsible for the reduction in scan quality compromising repeatability (26).

In the present study, the RLim values for the ACD measurements were larger in both ocular surface disease cohorts (G2: Immune and G3: Non-immune) compared to the other groups, but the differences were not significantly different ($p > 0.05$). It is shown that severe and chronic ocular surface disease patients have altered endothelial cell layer caused by the reduced corneal nerves density (27). Also, Belmonte et al. (28) suggested that prolonged inflammation stress and reduced tear film availability over the ocular surface might lead to abnormal corneal nerves ending developing further symptomatology and affecting the deeper corneal structure. This could result in decreased precision of the endothelial layer segmentation. The RLim for ACW measurements were on a similar magnitude among the groups, and the CoVs never exceeded 1.6%. The ACW is a measure of the distance between the scleral spurs, hence altercations of the ocular surface may not affect the precision of this parameter. Although, chronic dryness might affect the scleral thickness due to the tissue's perpetual inflammation (29), it might not influence the precision of the ACW measurement. Similar to the ACW, the RLim for ATA was similar among the groups and the CoVs never exceeded 2%. Repeatability of AOD and ARA, there is no clear trend among the groups. However, the RLim for G5 showed larger values at many points but this could also be attributed to smaller sample size in that group. As Pentacam devices are still one of the most considered instruments in public hospital settings in the UK, we decided to
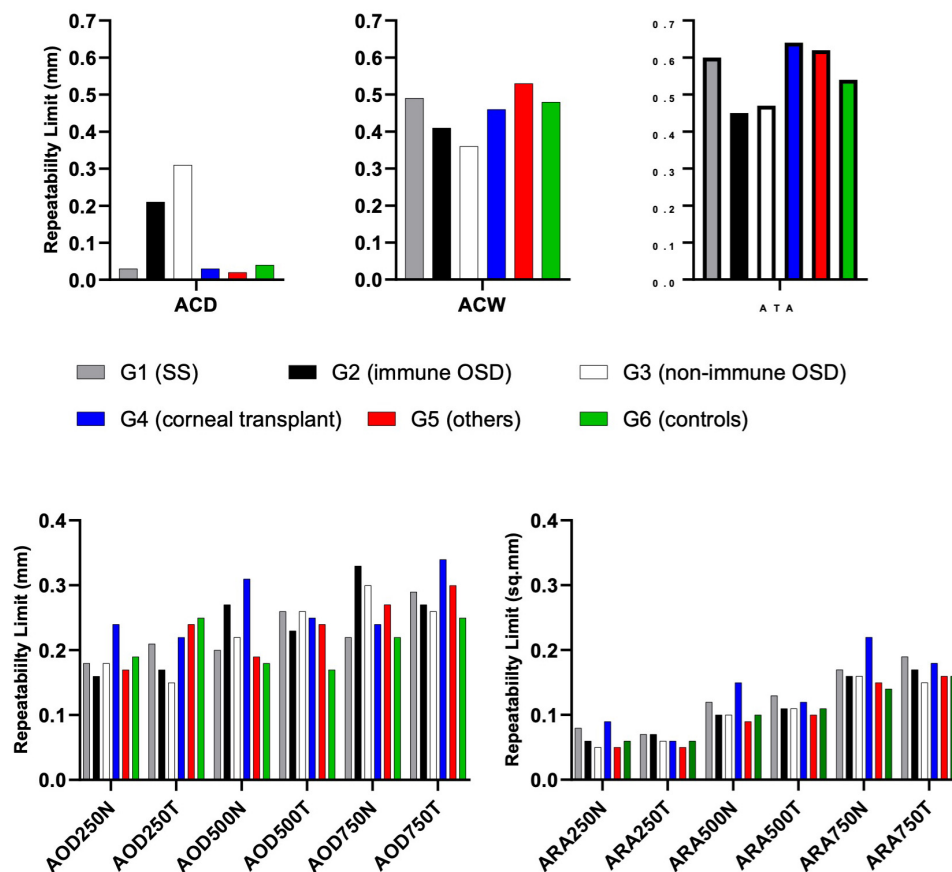
FIGURE 3
Repeatability limits for ACD, ACW, ATA, AOD and ARA at 250, 500 and 750 μm, respectively. Refer to Table 2 for abbreviations.

TABLE 3 Coefficient of variation (%) for ACD, ACW, ATA, AOD and ARA at 250, 500 and 750 μm, respectively.

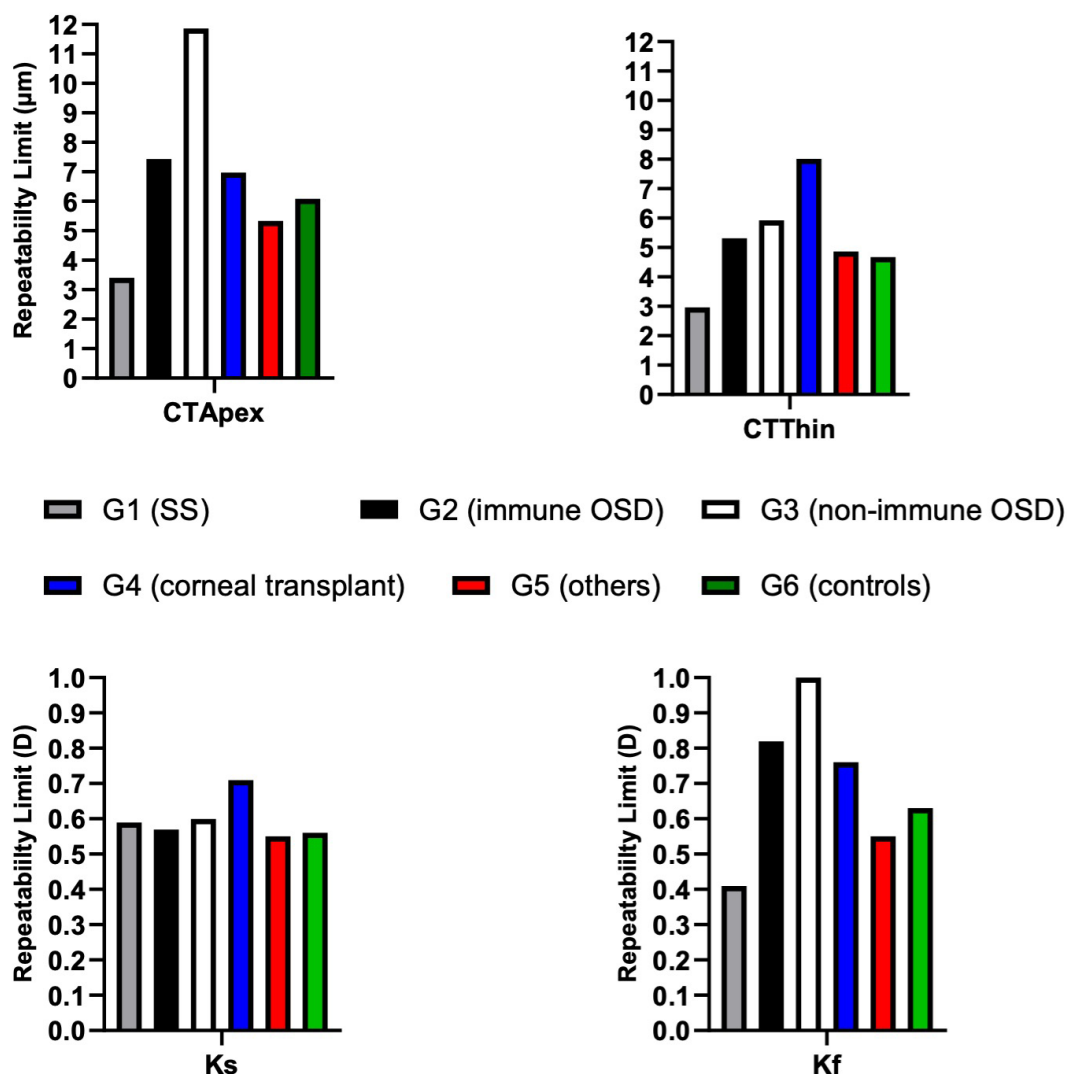| Groups Variables	G1 (Sjögren's Syndrome)	G2 (Immune)	G3 (Non-Immune)	G4 (Corneal Transplant)	G5 (Other)	G6 (Healthy)
Coefficients of Variation (%)						
ACD	0.4	2.5	3.8	0.3	0.2	0.5
ACW	1.5	1.2	1.1	1.4	1.6	1.4
AOD250N	22.4	20.1	24.3	22.5	26.2	24.6
AOD250T	25.0	19.9	19.5	22.0	34.2	27.9
AOD500N	17.7	23.6	20.4	17.8	20.3	16.1
AOD500T	22.7	18.5	23.5	16.8	24.2	13.5
AOD750N	14.9	20.9	20.4	9.5	20.0	13.4
AOD750T	18.4	15.7	17.2	15.8	22.0	14.1
ARA250N	41.9	31.6	33.5	36.8	37.9	37.4
ARA250T	36.3	31.0	32.4	28.1	34.2	30.4
ARA500N	28.1	23.9	25.7	25.7	26.4	24.7
ARA500T	28.4	23.4	26.3	21.9	28.5	22.8
ARA750N	22.4	21.6	22.5	18.9	23.2	18.7
ARA750T	24.4	20.0	20.1	17.6	25.1	18.9
ATA	1.9	1.4	1.5	2.0	1.9	1.7

Refer to Table 2 for abbreviations.

FIGURE 4
Repeatability limits for CTApex, CTThin, Kf and Ks. Refer to Table 2 for abbreviations.

TABLE 4 Coefficients of variation (%) for corneal thickness and curvature.

Groups Variables	G1 (Sjögren's Syndrome)	G2 (Immune)	G3 (Non-Immune)	G4 (Corneal Transplant)	G5 (Other)	G6 (Healthy)
Coefficients of Variation (%)						
CTApex	0.2	0.5	0.8	0.5	0.4	0.4
CTThin	0.2	0.4	0.4	0.6	0.4	0.3
Kf	0.3	0.6	0.7	0.6	0.4	0.5
Ks	0.4	0.4	0.4	0.5	0.4	0.4

Refer to Table 2 for abbreviations.

compare the corneal thickness measurements in our cohorts with similar studies done with them but acknowledging these might be not the gold standard for pachymetry measurements.

Corneal thickness measurements variation was seen among the RLim values for the different clinical groups. However, the CoVs were less than 1%. Previous studies using Pentacam show contradicting results. Lee et al. reported that the repeatability with Pentacam for the central corneal thickness measurement was worse for the dry eye group (34 subjects) that predominantly had aqueous-deficient dry eye compared to controls (30). However, another study that included dry eyes subjects with causes similar to that included in the present study showed that the repeatability was similar between dry eye (138 subjects) and control groups (13). Not surprisingly, the anterior corneal power (the RLim for the Kf) was different amongst groups. Whereas when evaluating Ks, the RLim was more similar amongst the groups. However, the CoV
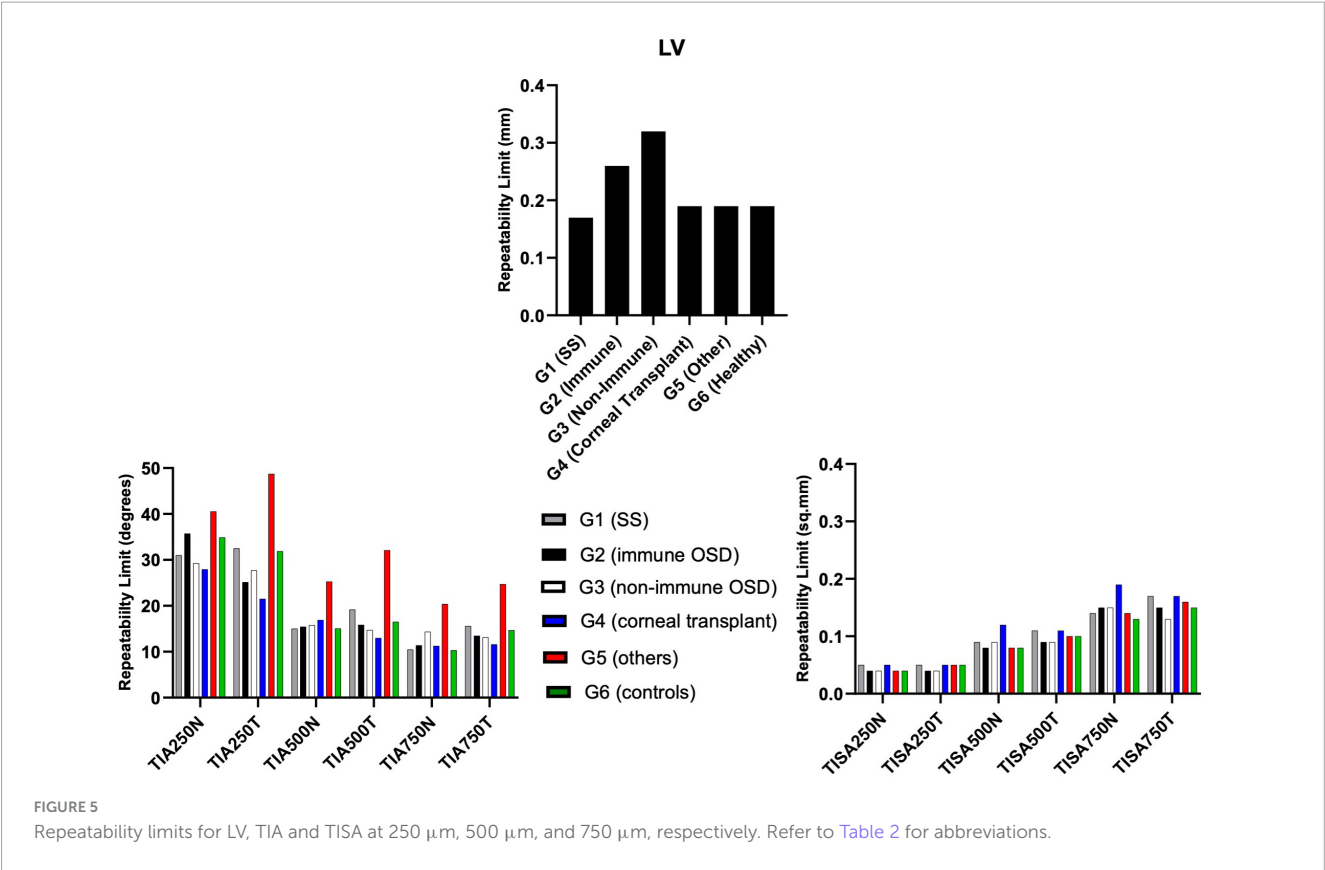
FIGURE 5
Repeatability limits for LV, TIA and TISA at 250 μm, 500 μm, and 750 μm, respectively. Refer to Table 2 for abbreviations.

TABLE 5 Coefficients of variation (%) for LV, TIA and TISA at 250 μm, 500 μm, and 750 μm, respectively.

Groups Variables	G1 (Sjögren's Syndrome)	G2 (Immune)	G3 (Non-Immune)	G4 (Corneal Transplant)	G5 (Other)	G6 (Healthy)
Coefficients of Variation (%)						
LV	23.3	63.5	48.1	31.4	21.2	58.2
TIA250N	21.2	23.9	20.0	15.8	27.2	24.8
TIA250T	22.0	16.8	18.8	12.8	33.9	21.4
TIA500N	13.4	13.5	14.1	11.3	22.8	13.3
TIA500T	17.0	13.4	13.2	9.3	30.2	13.5
TIA750N	10.5	10.9	14.1	8.0	20.0	9.7
TIA750T	14.9	12.2	13.1	8.8	25.7	13.1
TISA250N	28.5	25.7	29.3	26.3	31.9	29.6
TISA250T	28.2	24.1	24.2	23.8	33.9	28.7
TISA500N	22.3	21.5	24.0	21.6	24.0	21.8
TISA500T	25.3	20.4	23.6	20.6	28.4	21.7
TISA750N	19.1	20.3	21.6	16.8	21.8	17.0
TISA750T	22.7	18.4	18.2	17.0	25.0	18.2

Refer to Table 2 for abbreviations.

values of Kf and Ks were lower than 1 % for all groups confirming that these measurements were not affected by the conditions of the ocular surface. Corneal topographic measurements were shown to be highly repeatable in severe dry eye disease using Pentacam (13). Another study using the IOLMaster 500 evaluated the influence of artificial tears on the keratometric measurements in cataract patients. The repeatability was found to be similar between the control and dry eye groups before instillation of artificial tears. However, the variation in the measurements was larger in the dry eye group after instillation of artificial tears (13, 31). Both previous studies mentioned, and our present results suggest that the repeatability of the keratometer does not vary largely among the dry eye groups. This could be related to the fast acquisition time.

The RLim for LV showed similar trend to that of ACD, with G2 and G3 showing larger values. Regarding TIA and TISA, G5 showed the largest CoV values, which could be related to the low sample size in this group.

Previous swept-source AS-OCT studies have also reported that the repeatability of anterior chamber angle parameters is lower compared to other anterior segment parameters in healthy eyes (32, 33). In recent years, TIA and TISA values have been widely accepted as objective metrics in determining angle opening in normal and disease populations (34, 35). If these metrics are meant to be used in the clinic, the measurement variability should be taken into consideration. The repeatability values presented in this study are based on measurements using the anterior segment screening protocol, which contains 16 radial B-scans and takes 0.3 s. A previously studied by Liu et al. (36) using the same instrument, the authors reported better repeatability values for the anterior chamber angle parameters compared to the present study but without considering ocular surface disease cohorts. However, in that study the measurements were performed with the anterior chamber angle scan protocol, which contains 128 radial B-scans and takes 2.3 seconds. It should be considered that dry eye subjects might have trouble keeping their eyes open and fixate if the acquisition time is longer.

Correlations results between dry eye metrics and AS-OCT measurements have been shown to be controversial too: in a research published by Diana and Ana (37) none of the dry eye metrics such as tear film thickness, tear meniscus area and tear meniscus height assessed via AS-OCT were discriminative between healthy and disease cohorts. However, findings from Schmidl et al. (38) showed that tear film thickness values measured with AS-OCT with dry eye correlated with patient's symptomatology. this discrepancy could be due to the fact that dry eye disease is a multifactorial disease: (3) and many other variables can also play a role in the diagnosis and severity of the condition across different patients.

This is the first study where ss-AS-OCT was used in OSD cohorts that included severe immune-mediated conditions such as Sjögren's Syndrome, Ocular Mucous Membrane Pemphigoid, Stevens Johnson-Syndrome, etc. Our results show that Tomey CASIA 2 demonstrates good repeatability when dealing with OSD patients.

The results of the present study show good repeatability for measuring anterior segment parameters measured with Tomey CASIA 2 in OSD cohorts. These results demonstrate that the clinical measurement protocol used in healthy controls could be also used in OSD subjects.

Data availability statement

The raw data supporting the conclusions of this article will be made available by the authors, without undue reservation.

Ethics statement

This study was conducted following the tenants Declaration of Helsinki and approval from the Sandwell and West Birmingham NHS Trust Clinical Effectiveness and Safeguarding Group (Project Registration #1843). The studies were conducted in accordance with the local legislation and institutional requirements. The participants provided their written informed consent to participate in this study.

Author contributions

AR: Conceptualization, Data curation, Investigation, Methodology, Validation, Writing—original draft, Writing—review and editing, Funding acquisition. AV: Conceptualization, Formal analysis, Investigation, Methodology, Validation, Writing—original draft, Writing—review and editing. SR: Conceptualization, Data curation, Funding acquisition, Investigation, Project administration, Validation, Writing—review and editing. AD-V: Conceptualization, Formal analysis, Investigation, Supervision, Writing—original draft, Writing—review and editing, Methodology, Validation.

Funding

Conflict of interest

The authors declare that the research was conducted in the absence of any commercial or financial relationships that could be construed as a potential conflict of interest.

The author(s) declared that they were an editorial board member of Frontiers, at the time of submission. This had no impact on the peer review process and the final decision.

Publisher's note

References

1. Gipson I. The ocular surface: The challenge to enable and protect vision: The Friedenwald lecture. *Invest Ophthalmol Vis Sci.* (2007) 48:4390. doi: 10.1167/iovs.07-0770

2. Mathewson P, Williams G, Watson S, Hodson J, Bron A, Rauz S. Defining ocular surface disease activity and damage indices by an international delphi consultation. *Ocul Surf.* (2017) 15:97–111. doi: 10.1016/j.jtos.2016.08.005

3. Craig J, Nichols K, Akpek E, Caffery B, Dua H, Joo C, et al. TFOS DEWS II definition and classification report. *Ocul Surf.* (2017) 15:276–83.

4. Bron A, De Paiva C, Chauhan S, Bonini S, Gabison E, Jain S, et al. TFOS DEWS II pathophysiology report. *Ocul Surf.* (2017) 15:438–510.

5. Slade A, Recchioni A, Aiyegbusi O, Retzer A, Nice L, Dancey E, et al. Identifying patient-valued outcomes for use in early phase trials of ocular surface disease interventions. *Ocul Surf.* (2023) 29:550–6. doi: 10.1016/j.jtos.2023.07.005

6. Vakros G, Scollo P, Hodson J, Murray P, Rauz S. Anxiety and depression in inflammatory eye disease: Exploring the potential impact of topical treatment frequency as a putative psychometric item. *BMJ Open Ophthalmol.* (2021) 6:e000649. doi: 10.1136/bmjophth-2020-000649

7. Savini G, Prabhawasat P, Kojima T, Grueterich M, Espana E, Goto E. The challenge of dry eye diagnosis. *Clin Ophthalmol.* (2008) 2:31–55.

8. Foulks G. Challenges and pitfalls in clinical trials of treatments for dry eye. *Ocul Surf.* (2003) 1:20–30.

9. Ramos J, Li Y, Huang D. Clinical and research applications of anterior segment optical coherence tomography - a review. *Clin Exp Ophthalmol.* (2009) 37:81–9.

10. Mohammed I, Tran S, Toledo-Espiett L, Munir W. The detection of keratoconus using novel metrics derived by anterior segment optical coherence tomography. *Int Ophthalmol.* (2022) 42:2117–26. doi: 10.1007/s10792-021-02210-4

11. Sharma R, Sharma A, Arora T, Sharma S, Sobti A, Jha B, et al. Application of anterior segment optical coherence tomography in glaucoma. *Surv Ophthalmol.* (2014) 59:311–27.

12. Kundu G, Shetty R, Khamar P, Gupta S, Mullick R, Ganesan V, et al. Impact of tear optics on the repeatability of Pentacam AXL wave and iTrace in measuring anterior segment parameters and aberrations. *Indian J Ophthalmol.* (2022) 70:1150–7. doi: 10.4103/ijo.IJO_2153_21

13. Guven S. The repeatability of corneal topography measurements in severe dry eye disease. *BMC Ophthalmol.* (2022) 22:306. doi: 10.1186/s12886-022-02534-4

14. ISO. *Accuracy (trueness and precision) of measurement methods and results-Part 1: General principles and definitions.* International Organization for Standardization (1994).

15. TCIT: ISO 3534-1:2006. *Statistics — Vocabulary and symbols — Part 1: General statistical terms and terms used in probability.* (2006). 102006.

16. Williams G, Saw V, Saeed T, Evans S, Cottrell P, Curnow S, et al. Validation of a fornix depth measurer: A putative tool for the assessment of progressive cicatrising conjunctivitis. *Br J Ophthalmol.* (2011) 95:842–7. doi: 10.1136/bjo.2010.188011

17. Whitcher J, Shiboski C, Shiboski S, Heidenreich A, Kitagawa K, Zhang S, et al. A simplified quantitative method for assessing keratoconjunctivitis sicca from the Sjögren's syndrome international registry. *Am J Ophthalmol.* (2010) 149:405–15. doi: 10.1016/j.ajo.2009.09.013

18. McAlinden C, Khadka J, Pesudovs K. Statistical methods for conducting agreement (comparison of clinical tests) and precision (repeatability or reproducibility) studies in optometry and ophthalmology. *Ophthalmic Physiol Opt.* (2011) 31:330–8.

19. Navarro D. *Learning statistics with R: A tutorial for psychology students and other beginners* (Version 0.6). R package version 0.5.1. Sydney: University of New South Wales (2015). Available online at: https://learningstatisticswithr.com

20. Pflugfelder S, Beuerman R, Stern M. *Dry eye and ocular surface disorders.* Boca Raton, FL: CRC Press (2004).

21. Hiraoka T, Asano H, Ogami T, Nakano S, Okamoto Y, Yamada Y, et al. Influence of dry eye disease on the measurement repeatability of corneal curvature radius and axial length in patients with cataract. *J Clin Med.* (2022) 11:710. doi: 10.3390/jcm11030710

22. Ong H, Minassian D, Rauz S, Mehta J, Dart J. Validation of a clinical assessment tool for cicatrising conjunctivitis. *Ocul Surf.* (2020) 18:121–9.

23. Szczesna-Iskander D. Measurement variability of the TearLab Osmolarity system. *Cont Lens Anterior Eye.* (2016) 39:353–8.

24. Mirzayev I, Gündüz A, Ellialtıoğlu P, Gündüz ÖÖ. Clinical utility of anterior segment swept-source optical coherence tomography: A systematic review. *Photodiagn Photodyn Ther.* (2023) 42:103334. doi: 10.1016/j.pdpdt.2023.103334

25. Pardeshi A, Song A, Lazkani N, Xie X, Huang A, Xu B. Intradevice repeatability and interdevice agreement of ocular biometric measurements: A comparison of two swept-source anterior segment OCT devices. *Transl Vis Sci Technol.* (2020) 9:14. doi: 10.1167/tvst.9.9.14

26. Lee W, Lim H, Kim J, Ryu C, Shin Y, Kim J. Repeatability of macular microvasculature measurements using optical coherence tomography angiography according to tear breakup time in dry eye disease. *Retina.* (2021) 41:2301–9. doi: 10.1097/IAE.0000000000003177

27. Kheirkhah A, Saboo U, Abud T, Dohlman T, Arnoldner M, Hamrah P, et al. Reduced corneal endothelial cell density in patients with dry eye disease. *Am J Ophthalmol.* (2015) 159:1022–6.e2.

28. Belmonte C, Nichols J, Cox S, Brock J, Begley C, Bereiter D, et al. TFOS DEWS II pain and sensation report. *Ocul Surf.* (2017) 15:404–37.

29. Kaya H, Karasu U, Martin Ç, Taşçi M, Pekel G. Measurements of scleral thickness and corneal optic densitometry in patients with systemic lupus erythematosus. *Medicine.* (2020) 99:e21467. doi: 10.1097/MD.0000000000021467

30. Lee J, Kim J, Kim S. Repeatability of central corneal thickness measurement using rotating scheimpflug camera in dry and normal eyes. *Eye Contact Lens.* (2018) 44:S29–32. doi: 10.1097/ICL.0000000000000373

31. Röggla V, Leydolt C, Schartmüller D, Schwarzenbacher L, Meyer E, Abela-Formanek C, et al. Influence of artificial tears on keratometric measurements in cataract patients. *Am J Ophthalmol.* (2021) 221:1–8. doi: 10.1016/j.ajo.2020.08.024

32. Cheng S, Zhang J, Li T, Wu Z, Wang P, Yu A. Repeatability and agreement of two swept-source optical coherence tomographers for anterior segment parameter measurements. *J Glaucoma.* (2022) 31:602–8.

33. Chan PM, Lai G, Chiu V, Chong A, Yu M, Leung CK. Anterior chamber angle imaging with swept-source optical coherence tomography: Comparison between CASIAII and ANTERION. *Sci Rep.* (2020) 10:18771. doi: 10.1038/s41598-020-74813-3

34. Kudsieh B, Fernández-Vigo J, Vila-Arteaga J, Aritz Urcola J, Martínez-de-la-Casa J, García-Feijóo J, et al. Update on the usefulness of optical coherence tomography in assessing the iridocorneal angle. *Arch SocEsp Oftalmol.* (2019) 94:478–90. doi: 10.1016/j.oftal.2019.06.007

35. Fernández-Vigo J, García-Feijóo J, Martínez-de-la-Casa J, García-Bella J, Arriola-Villalobos P, Fernández-Pérez C, et al. Fourier domain optical coherence tomography to assess the iridocorneal angle and correlation study in a large Caucasian population. *BMC Ophthalmol.* (2016) 16:42. doi: 10.1186/s12886-016-0219-z

36. Liu S, Yu M, Ye C, Lam D, Leung C. Anterior chamber angle imaging with swept-source optical coherence tomography: An investigation on variability of angle measurement. *Invest Ophthalmol Vis Sci.* (2011) 52:8598–603.

37. Diana M, Ana B. Tear evaluation by anterior segment OCT in dry eye disease. *Rom J Ophthalmol.* (2021) 65:25–30.

38. Schmidl D, Witkowska K, Kaya S, Baar C, Faatz H, Nepp J, et al. The association between subjective and objective parameters for the assessment of dry-eye syndrome. *Invest Ophthalmol Vis Sci.* (2015) 56:1467–72.

Check for updates

Case report: Characterizing of free-floating pigmented vitreous cyst using swept-source optical coherence tomography

Kexin Shi[1,2], Qichuan Yin[1,2], Yuxin Huang[1,2], Sifan Zheng[3], Yao Wang[1,2]* and Xingchao Shentu[1,2]*

[1]The Eye Center, Second Affiliated Hospital of School of Medicine, Zhejiang University, Hangzhou, Zhejiang, China, [2]Zhejiang Provincial Key Lab of Ophthalmology, Hangzhou, Zhejiang, China, [3]GKT School of Medical Education, King's College London, London, United Kingdom

Aim: A free-floating vitreous cyst is a rare eye disease. This study aimed to find diagnostic imaging methods and imaging features for vitreous cysts.

Methods: This article presents a case report along with a literature review of published cases of vitreous cysts. The case report describes a highly myopic 60-year-old woman with a pigmented, free-floating vitreous cyst in her right eye. A search of the PubMed database using the keywords "vitreous cyst" was performed to identify other cases reported in the literature and to summarize the imaging methods used to diagnose and visualize vitreous cysts and the imaging features of vitreous cysts.

Results: A thorough ophthalmic examination was performed in the present case, including slit-lamp photography, B-scan ultrasound, broad line fundus imaging, spectral-domain optical coherence tomography (SD-OCT), and ultra-wide field SS-OCT. The literature review revealed the imaging methods used in previously reported cases of vitreous cysts in which ultra-wide field SS-OCT has the advantages of wide scanning depth and high imaging clarity.

Conclusion: SS-OCT has an advantage over SD-OCT in providing intuitive morphological characteristic images for the diagnosis of posterior vitreous cysts. The comprehensive assessment of multimodal imaging examinations, including SS-OCT, is of significant value for the diagnosis and differential diagnosis of vitreous cysts.

KEYWORDS

vitreous cyst, optical coherence tomography, B-scan ultrasound, slit lamp, fundus photography

1 Introduction

Vitreous cysts are rare ocular malformations. It can be either congenital or acquired. A vitreous cyst is usually detected during a routine ophthalmological examination or when it migrates to the visual axis and causes visual disturbances (1). Patients are often asymptomatic or may complain of intermittent blurred vision (2). In recent years, there have been only a few clinical case reports of vitreous cysts (3–10). The imaging studies in these reports are not uniform and lack systematic review.

Optical coherence tomography (OCT) is a non-invasive three-dimensional tomography technique that has been in use since 1991 (11). After continuous technological development, OCT has evolved from early time-domain OCT (TD-OCT) to spectral-domain OCT (SD-OCT) and finally to the latest swept-source OCT (SS-OCT) (12). OCT has evolved to enable detailed imaging of many intraocular structures (13). Wide field OCT (based on SS-OCT) has been used to detect non-perfused areas and retinal neovascularization in retinal vascular disorders (14); however, its application in vitreous cysts is rarely mentioned.

Here, we report a case of a vitreous cyst that has been observed and objectively assessed using multiple imaging methods, including a clear scan of the cyst contents using ultra-widefield SS-OCT. We also reviewed the relevant published literature on vitreous cysts and summarized the imaging methods that can objectively and qualitatively evaluate vitreous cysts. We concluded that SS-OCT can be used for the diagnosis of posterior vitreous cysts and has unique advantages.

2 Case presentation

A 60-year-old woman presented to the Eye Center, Second Affiliated Hospital of School of Medicine, Zhejiang University, complaining of blurred vision in both eyes for more than 3 years. She had a history of high myopia in both eyes for more than 30 years and had no previous history of ocular trauma, infectious eye disease, or abnormal tracing. Ophthalmological examination revealed an uncorrected visual acuity of 20/200 in the right eye and 20/100 in the left eye. The anterior chamber, iris, pupil, intraocular pressure, and eye movement were normal. The lenses of both eyes were opacified, and the fundus showed typical changes of high myopia. A pigmented cyst can be faintly seen in the right eye in the vitreous cavity, with a clear view obfuscated by cataract formation. The patient was followed up after microincision phacoemulsification combined with intraocular lens implantation in the right eye.

We performed a series of imaging tests on the patient's right eye after cataract surgery. Under the slit lamp, a free-floating cyst of approximately two optic disk diameters was observed in the vitreous body. The cyst was semi-transparent with a smooth surface and covered with brown pigment. When the patient rolled her right eye, the cyst moved with it (Supplementary Video 1). The broad line fundus imaging (CLARUS 500™; Carl Zeiss Meditec AG, Jena, Germany) showed a more clearly pigmented free-floating vitreous cyst with a defined boundary, spherical with small protrusions, located close to the mid-periphery retina (Figure 1A). We used an ultrasound B-scan to examine the cyst's internal structure, which showed a cystic echo in the inferior vitreous cavity near the eyeball wall of the right eye, with an anechoic dark area inside. However, it was difficult to determine whether the cyst adhered to the eyeball wall (Figure 1B). SD-OCT (Figure 1C, Heidelberg Spectrails, Heidelberg, Germany) showed a hyper-reflective shell with hypo-reflective contents. Due to the depth limitation of SD-OCT scanning, some lesions were anterior to the upper limit of OCT and appeared as reflection images. The ultra-wide field SS-OCT (Figure 1D, VG200D; SVision Imaging, Henan, China), with a maximum scanning depth of up to 12 mm, demonstrated a complete oval-shaped, hyper-reflective thin shell filled with a homogeneous hypo-reflective liquid that did not adhere to the retina and shadowing of the underlying retina. The diagnosis was a

pigmented vitreous cyst. As the patient had no visual impairment due to the cyst, she opted for conservative management. The cyst remained stable at the 3-month follow-up.

3 Discussion

Free-floating vitreous cysts were first described in 1899 (15), and only a few cases have been previously reported. Based on the limited reports, no gender difference was observed in patient profiles. Patients were primarily aged between 5 and 68, with most occurrences between 10 and 20 years (16). Vitreous cysts are primarily described as spherical or oval, rarely leaf-splitting, and in the 0.15 to 12 mm size range (17). Non-pigmented cysts have a yellowish appearance, while pigmented cysts are covered with sepia pigment particles. These vitreous cysts are usually asymptomatic and are often detected because of other ocular symptoms. However, when they involve the visual axis, they may cause blurred vision, shadows in the field of vision, or floating objects when moving (18). The embryonic origin of primary vitreous cysts remains controversial. Some researchers suggest that cysts may have originated from the primary hyaloid system, while others believe cysts originate in the iris, ciliary body, or retinal pigment epithelium (19, 20). Acquired vitreous cysts have been reported secondary to a variety of intraocular lesions. The most common reason is eye trauma (21), with other described causes including lattice degeneration, retinitis pigmentosa, retinal detachment, retinitis, choroidal disease, ciliary adenoma, ciliary ectopia, and intraocular infection (22–25).

Multimodal imaging studies are crucial for the diagnosis and differential diagnosis of vitreous cysts. Vitreous cysts in particular need to be differentiated from cysts caused by parasites, such as cysticercoid cysts (26). A slit-lamp examination can be used to observe the cyst's shape, size, color, transparency, and activity (1). The cyst's mobility can also be checked by having the patient turn her eye slightly. Fundus photography, especially broad line fundus photography, can qualitatively assess vitreous cysts. Adjacent fundus lesions can also be recorded (27), which may infer the etiology of vitreous cysts. However, the limitations of slit-lamp examination and fundus photography are that the internal components of the cyst cannot be detected, and the relationship between the cyst and the adjacent retina cannot be completely determined.

In addition, ultrasonography is also important for the diagnosis and measurement of the cyst. The typical B-ultrasound features of vitreous cysts describe the cysts as round or quasi-round, with moderate echo, thin wall, smooth echo wall, an anechoic dark area inside the cyst, and a positive posterior movement (28). These ultrasonographic features are distinguished from the dense circular echoes seen in the central portion of cysticercosis lesions in the vitreous cavity (29). However, the images of ultrasound are relatively rough and have low resolution, which cannot perfectly meet the needs of clinicians to explore the details of cysts.

In recent years, optical coherence tomography (OCT), as a non-invasive imaging technology, has been used in the diagnosis and treatment of vitreous cysts (30). OCT is a three-dimensional tomography technology that utilizes the biological tissue scattered light coherence principle for imaging and observation of living tissue. OCT has the advantages of non-contact, high resolution, and high speed (31). At present, the most commonly used is frequency-domain OCT. According
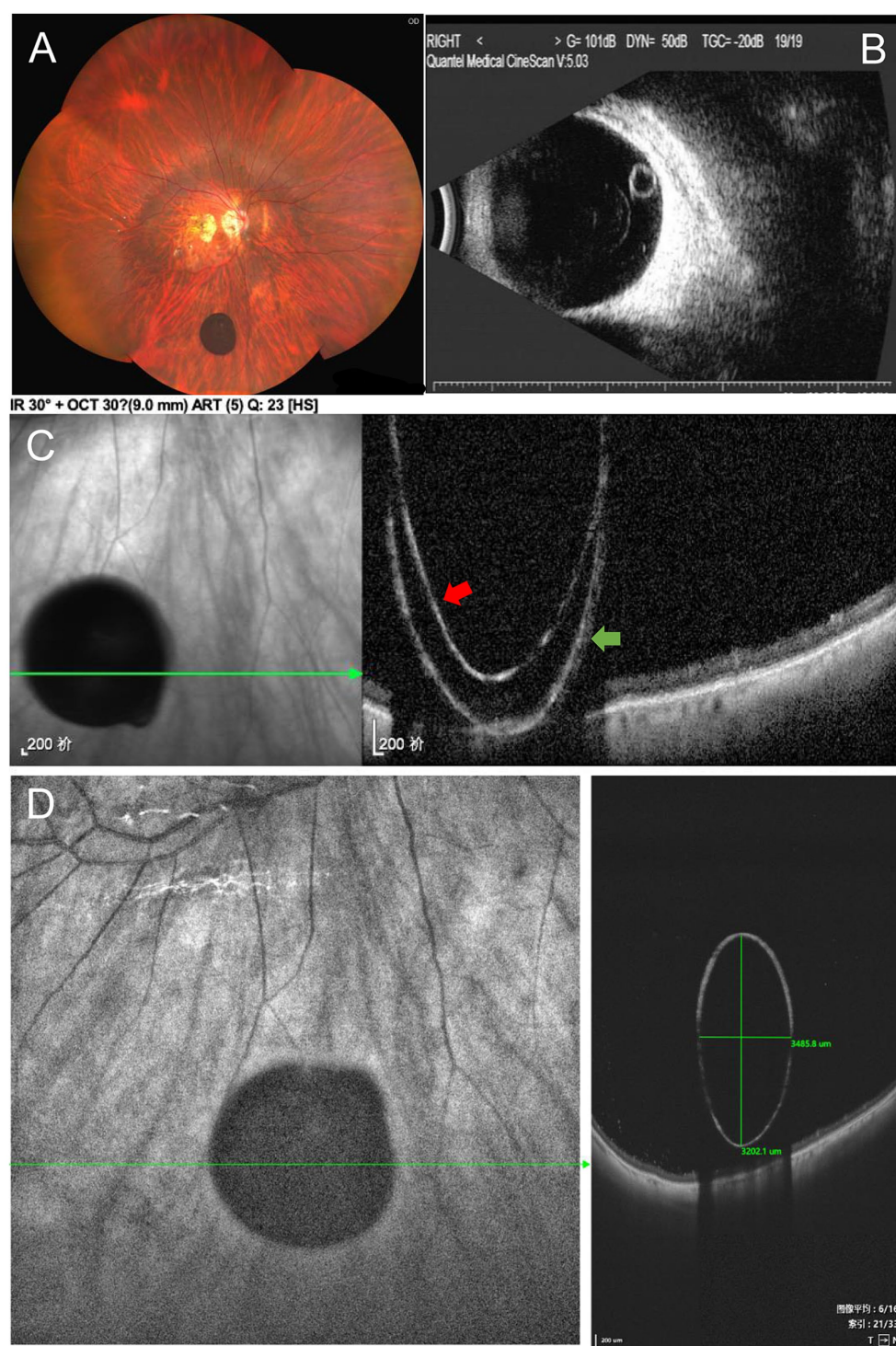
FIGURE 1
(A) Broad line fundus imaging showed a round, pigmented cyst. **(B)** Ultrasound B-scan showed the posterior-located vitreous cyst. **(C)** Spectral-domain OCT (SD-OCT) showed an image of a cyst with an inverse line. Red arrow: High-reflectivity band corresponds to the posterior edge of the vitreous cyst. Green arrow: The reflection image formed by exceeding the SD-OCT upper limit. **(D)** Ultra-wide field swept-source optical coherence tomography (SS-OCT), with 9 mm scan depth and 12 mm scan length, demonstrated a complete cyst image (3.5 mm × 3.2 mm in size) with a hyper-reflective enclosure, hypo-reflective content, and shadowing of the underlying retina.

to different methods of obtaining interference spectra, it is divided into spectral-domain OCT (SD-OCT), based on the spectrometer, and swept-frequency OCT (SS-OCT), based on a swept-frequency light source. OCT can display the internal structure of the vitreous cyst and the relationship between the cyst and the retina. Kevin et al. used SD-OCT for objective, qualitative assessment of large vitreous cysts. The OCT showed that the cysts cast shadows on both sides of the fovea, which was consistent with the annular scotoma symptoms described by the patient (32). Kevin et al.

also suggested that OCT could be used to assess the risk–benefit ratio of vitrectomy in patients with symptomatic large vitreous floaters. Using SD-OCT, Dragnev et al. found that the cysts were multi-lobular and contained highly reflective material in addition to fluid on OCT scans (33). They speculated that these hyper-reflective spots correspond to premelonosomes, suggesting that the cysts originate from the primary hyaloid system.

Although SD-OCT is more frequently used in the evaluation of vitreous cysts, the shape of the cyst cannot be fully displayed due to the limited depth of SD-OCT scanning. The relationship between the cyst and surrounding tissues cannot be displayed simultaneously. Yonekawa et al. reported the use of SD-OCT to evaluate vitreous cysts, and the image showed that the anterior surface of the lesion was beyond the upper limit of SD-OCT, which appeared as a reflection image (34). However, SS-OCT uses a longer wavelength for imaging than SD-OCT, which has deeper penetration of biological tissue, and the swept-frequency light source has high instantaneous coherence, which can achieve a deeper longitudinal imaging range (35). Based on low sensitivity attenuation and larger longitudinal imaging range, SS-OCT can obtain a larger imaging depth than SD-OCT (36), which can facilitate imaging of the anterior segment, large-scale fundus imaging, and axial length imaging and feasibility. Using SS-OCT, Guo et al. reported a case of a vitreous cyst in a 48-year-old woman (37). The high-resolution images showed that the cyst was surrounded by a thin hyper-reflective wall and a posterior cortical anterior vitreous pocket. Unlike the typical liquid cyst interior morphology in our reported case, the cyst in their case was composed of a hyper-reflective septum with a slightly central agglutination. The hyper-reflective septum may be associated with premelonosomes. In addition, the ultra-wide field SS-OCT instrument used in our case offers super-depth imaging of up to 12 mm, which allows for a clearer display of the entire cyst, including its internal fluid structure and positional relationship with the retina, compared to the conventional SS-OCT instrument, thus enhancing clinical evaluation. Ultra-wide field SS-OCT can also obtain clear scan images at different levels, similar to pathological slices. Overall, SS-OCT meets the ever-increasing demands for detection speed, sensitivity, and functionality.

Some less commonly reported imaging methods can also be used in the diagnosis and differential diagnosis of vitreous cysts. Ocular ultrasound biomicroscopy (UBM) can be used to detect cysts arising from the iris/ciliary body (38) but is limited to the anterior segment. Infrared imaging has also been reported, which can show multiple areas of hyper-reflection on the cyst surface (39), but the image clarity is poor. Fluorescein angiography (FA) can be used to rule out overlying vascularization of the cyst (40), but only for cysts connected to the retina. Compared to other imaging methods, SS-OCT can display the external and internal structures of cysts across multiple layers, such as pathological slices, and provides a better differential diagnosis for the nature of cysts.

The treatment of vitreous cysts depends on the patient's wishes, symptoms, degree of visual impairment, cyst characteristics, and location (41). Most vitreous cysts are asymptomatic or have a minimal visual impact, which only requires observation and regular follow-up. A minority with significant visual impairment or rapidly growing were considered for intervention. Treatment options include argon laser photocoagulation and neodymium:YAG (Nd:YAG) laser photocoagulation to remove the cyst (42, 43). Alternatively, vitrectomy surgery and pathological examination may also be performed to determine the benign or malignant nature of the cyst (44). However, these invasive treatments may be accompanied by serious complications, even with the relatively safe Nd:YAG laser, which has been reported to have

caused iatrogenic cataract formation (45). Therefore, the treatment of vitreous cysts needs to be carried out with caution, and imaging plays a crucial role in guiding treatment decisions.

4 Conclusion

In conclusion, vitreous cysts are a rare condition that needs to be qualitatively examined and observed using the correct imaging methods, which are crucial for the diagnosis and treatment of the disease. We reported a case of a free-floating pigmented vitreous cyst, summarized the current clinical reports of imaging examination methods for vitreous cysts, and proposed the value of SS-OCT in the diagnosis of a posterior vitreous cyst.

Data availability statement

The original contributions presented in the study are included in the article/Supplementary material, further inquiries can be directed to the corresponding authors.

Ethics statement

The studies involving humans were approved by Ethics Committee of the Second Affiliated Hospital of Zhejiang University. The studies were conducted in accordance with the local legislation and institutional requirements. The participants provided their written informed consent to participate in this study. Written informed consent was obtained from the individual(s) for the publication of any potentially identifiable images or data included in this article.

Author contributions

KS: Data curation, Formal analysis, Writing – original draft. QY: Data curation, Writing – original draft. YH: Data curation, Formal analysis, Writing – original draft. SZ: Writing – review & editing. YW: Funding acquisition, Writing – review & editing. XS: Conceptualization, Funding acquisition, Supervision, Writing – review & editing.

Funding

Conflict of interest

The authors declare that the research was conducted in the absence of any commercial or financial relationships that could be construed as a potential conflict of interest.

The author(s) declared that they were an editorial board member of Frontiers, at the time of submission. This had no impact on the peer review process and the final decision.

Publisher's note

All claims expressed in this article are solely those of the authors and do not necessarily represent those of their affiliated organizations, or those of the publisher, the editors and the reviewers. Any product that may be evaluated in this article, or claim that may be made by its manufacturer, is not guaranteed or endorsed by the publisher.

Supplementary material

The Supplementary material for this article can be found online at: https://www.frontiersin.org/articles/10.3389/fmed.2024.1428353/full#supplementary-material

References

1. Sun CB. Free-floating cyst in the vitreous. *N Engl J Med.* (2022) 386:e1. doi: 10.1056/NEJMicm2112627

2. Aydin E, Demir HD, Tasliyurt T. Idiopathic pigmented free-floating posterior vitreous cyst. *Int Ophthalmol.* (2009) 29:299–301. doi: 10.1007/s10792-008-9230-6

3. Dhull C, Rani D, Azad S. Free-floating pigmented intravitreal cyst-where did it come from? *Ophthalmol Retina.* (2020) 4:1208. doi: 10.1016/j.oret.2020.06.001

4. Robben P, Van Ginderdeuren R, Thoma D, Deghislage C, Van Calster J, Blanckaert J, et al. Primary vitreous cysts. *GMS Ophthalmol Cases.* (2020) 10:2020. doi: 10.3205/oc000145

5. Garcia-Saenz MC, Lloreda Martin L, De La Puente AV, Arias-Puente A. Free-floating vitreous cyst. *J Fr Ophthalmol.* (2019) 42:662–5. doi: 10.1016/j.jfo.2018.12.020

6. Moreno-Arrones JP, Jiménez-Parras R. Vitreous cyst: a case presentation. *Arch Soc Esp Oftalmol.* (2012) 87:20–2. doi: 10.1016/j.oftal.2011.06.019

7. Salman IA. Free-floating pigmented vitreous cyst. *Eurasian J Med.* (2017) 49:155. doi: 10.5152/eurasianjmed.2016.265

8. Hassan AS, Hoffman J, Kirthi V. Pigmented spherical body floating within the globe. *BMJ Case Rep.* (2016) 2016:bcr2015212050. doi: 10.1136/bcr-2015-212050

9. Caminal-Mitjana JM, Padrón-Pérez N, Arias-Barquet L, Rubio Caso MJ. Pigmented free-floating vitreous cyst. ophthalmic Surg lasers imaging. *Retina.* (2014) 45:e23–5. doi: 10.3928/23258160-20140509-01

10. Léonard A, De Potter P. Partially pigmented vitreous cyst. *J Fr Ophthalmol.* (2013) 36:e105–7. doi: 10.1016/j.jfo.2012.08.013

11. Huang D, Swanson EA, Lin CP. Optical coherence tomography. *Science.* (1991) 254:1178–81. doi: 10.1126/science.1957169

12. Leitgeb R, Hitzenberger CK, Fercher AF. Performance of fourier domain vs. time domain optical coherence tomography. *Opt Express.* (2003) 11:889–94. doi: 10.1364/oe.11.000889

13. Adhi M, Duker JS. Optical coherence tomography–current and future applications. *Curr Opin Ophthalmol.* (2013) 24:213–21. doi: 10.1097/ICU.0b013e32835f8bf8

14. Russell JF, Flynn HW Jr, Sridhar J, Townsend JH, Shi Y, Fan KC, et al. Distribution of diabetic neovascularization on ultra-widefield fluorescein angiography and on simulated widefield OCT angiography. *Am J Ophthalmol.* (2019) 207:110–20. doi: 10.1016/j.ajo.2019.05.031

15. Tansley JO. Cyst of the vitreous. *Trans Am Ophthalmol Soc.* (1899) 8:507–9.

16. Cruciani F, Santino G, Salandri AG. Monolateral idiopathic cyst of the vitreous. *Acta Ophthalmol Scand.* (1999) 77:601–3. doi: 10.1034/j.1600-0420.1999.770527.x

17. Jones WL. Free-floating vitreous cyst. *Optom Vis Sci.* (1998) 75:171–3. doi: 10.1097/00006324-199803000-00021

18. Sherif M, Moulin A, Wolfensberger TJ. Surgical therapy for idiopathic pigmented intravitreal cyst. *Klin Monatsbl Augenheilkd.* (2018) 235:485–6. doi: 10.1055/s-0043-121571

19. Orellana J, O'Malley R, McPherson A, Font RL. Pigmented free-floating vitreous cysts in two young adults. Electron microscopic observations. *Ophthalmology.* (1985) 92:297–302. doi: 10.1016/S0161-6420(85)34042-3

20. Nork T, Millecchia L. Treatment and histopathology of a congenital vitreous cyst. *Ophthalmology.* (1998) 105:825–30. doi: 10.1016/S0161-6420(98)95020-5

21. Ludwig CA, Leng T. Idiopathic pigmented vitreous cyst. *Acta Ophthalmol.* (2016) 94:e83–4. doi: 10.1111/aos.12785

22. Lu J, Mai G, Liu R, Luo Y, Lu L. Acquired nonpigmented vitreous cyst associated with lattice degeneration. *Ophthalmic Surg Lasers Imaging Retina.* (2017) 48:856–8. doi: 10.3928/23258160-20170928-13

23. Frasson M, de Queiroz AC, Lino BT, Nehemy MB. Vitreous cyst and retinitis pigmentosa: case report. *Arq Bras Oftalmol.* (2010) 73:179–81. doi: 10.1590/s0004-27492010000200016

24. Tranos PG, Ferrante P, Pavesio C. Posterior vitreous cyst and intermediate uveitis. *Eye (Lond).* (2010) 24:1115–6. doi: 10.1038/eye.2009.274

25. Tuncer S, Bayramoglu S. Pigmented free-floating vitreous cyst in a patient with high myopia and uveal coloboma simulating choroidal melanoma. *Ophthalmic Surg Lasers Imaging.* (2011) 42:49–52. doi: 10.3928/15428877-20110407-02

26. Ganger A, Agarwal R, Kumar V. Asymptomatic free-floating vitreous cyst masquerading as cysticercosis. *BMJ Case Rep.* (2016) 2016:bcr2016217690. doi: 10.1136/bcr-2016-217690

27. Grewal DS, Fekrat S. Dynamic imaging of a pigmented free-floating vitreous cyst. *Ophthalmic Surg Lasers Imaging Retina.* (2016) 47:975–7. doi: 10.3928/23258160-20161004-15

28. Asiyo-Vogel MN, el-Hifnawi e-S, Laqua H. Ultrastructural features of a solitary vitreous cyst. *Retina.* (1996) 16:250–4. doi: 10.1097/00006982-199616030-00012

29. Liu GA, Ye RZ, Lai JQ, Wang YH. Clinical and ultrasonographic features of 11 cases of vitreous cysts. *J Clin Ophthalmol.* (2018) 26:496–9. doi: 10.3969/j.issn.1006-8422.2018.06.005

30. Lavric A, Urbancic M. Floating vitreous cyst: two clinical cases. *Case Rep Ophthalmol.* (2013) 4:243–7. doi: 10.1159/000356569

31. Fu J, Tan S, Peng C, Zhou H, Wei S. A comparative study of alteration in retinal layer segmentation alteration by SD-OCT in neuromyelitis optica spectrum disorders: a systematic review and meta-analysis. *Adv Ophthalmol Pract Res.* (2021) 1:100007. doi: 10.1016/j.aopr.2021.100007

32. Kevin PK, James PM, David JK, Connell PP. Objective assessment of symptomatic vitreous floaters using optical coherence tomography: a case report. *BMC Ophthalmol.* (2015) 15:22. doi: 10.1186/s12886-015-0003-5

33. Dragnev D, Shanmugalingam S. Optical coherence tomography in a patient with cogenital vitreous cyst. *BMJ Case Rep.* (2014) 2014:bcr2014204474. doi: 10.1136/bcr-2014-204474

34. Yonekawa Y, Todorich B, Randhawa S. Free-floating pigmented vitreous cyst: optical coherence tomography findings. *Ophthalmology.* (2016) 123:2041. doi: 10.1016/j.ophtha.2016.05.032

35. Pinilla I, Sanchez-Cano A, Insa G, Bartolomé I, Perdices L, Orduna-Hospital E. Choroidal differences between spectral and swept-source domain technologies. *Curr Eye Res.* (2021) 46:239–47. doi: 10.1080/02713683.2020.1795883

36. Liu G, Yang J, Wang J, Li Y, Zang P, Jia Y, et al. Extended axial imaging range, widefield swept source optical coherence tomography angiography. *J Biophotonics.* (2017) 10:1464–72. doi: 10.1002/jbio.201600325

37. Guo X, Lei B, Gao Y. A pigmented vitreous cyst within the posterior Precortical vitreous pocket. *JAMA Ophthalmol.* (2022) 140:e214681. doi: 10.1001/jamaophthalmol.2021.4681

38. Majumder PD, Ganesh NG, Tomar VPS, Kharel R, Sen P. Pigmented free floating vitreous cyst in a 10 years old child. *Nepal J Ophthalmol.* (2017) 9:190–3. doi: 10.3126/nepjoph.v9i2.19268

39. Kumar V, Jain S, Bhayana AA, Singh BS. Free floating pigmented vitreous cyst. *Indian J Ophthalmol.* (2019) 67:140–1. doi: 10.4103/ijo.IJO_855_18

40. Toklu Y, Raza S, Cakmak HB, Cagil N. Free-floating vitreous cyst in an adult male. *Korean J Ophthalmol.* (2013) 27:463–5. doi: 10.3341/kjo.2013.27.6.463

41. Gulkilik G, Odabasi M, Erdur SK, Ozsutcu M, Eliacik M, Demirci G, et al. A case of pigmented, free-floating vitreous cyst treated with micropulse diode laser. *Clin Exp Optom.* (2016) 99:90–2. doi: 10.1111/cxo.12308

42. Desai RU, Saffra NA. Argon laser photocystotomy of a vitreous cyst. *Ophthalmic Surg Lasers Imaging.* (2010) 9:1–4. doi: 10.3928/15428877-20100215-79

43. Gupta R, Pannu BKS, Bhargav S, Narang S, Sood S. Nd:YAG laser photocystotomy of a free-floating pigmented anterior vitreous cyst. *Ophthalmic Surg Lasers Imaging.* (2003) 34:203–5. doi: 10.3928/1542-8877-20030501-07

44. Lira RP, Jungmann P, Moraes LF, Silveira AP. Clinical features, histopathological analysis and surgical treatment of a free floating vitreous cyst: a case report. *Arq Bras Oftalmol.* (2006) 69:753–5. doi: 10.1590/s0004-27492006000500026

45. Lin JC, Katz LJ, Spaeth GL, Klancnik JM Jr. An "exploding cataract" following Nd:YAG laser iridectomy. *Ophthalmic Surg Lasers Imaging.* (2003) 34:310–1. doi: 10.3928/1542-8877-20030701-08

Check for updates

Dry age-related macular degeneration classification from optical coherence tomography images based on ensemble deep learning architecture

Jikun Yang[1,2], Bin Wu[2], Jing Wang[2], Yuanyuan Lu[2], Zhenbo Zhao[1,2], Yuxi Ding[2], Kaili Tang[1,2], Feng Lu[3] and Liwei Ma[1,2]*

[1]Aier Eye Medical Center of Anhui Medical University, Anhui, China, [2]Shenyang Aier Excellence Eye Hospital, Shenyang, Liaoning, China, [3]School of automation, Shenyang Aerospace University, Shenyang, Liaoning, China

Background: Dry age-related macular degeneration (AMD) is a retinal disease, which has been the third leading cause of vision loss. But current AMD classification technologies did not focus on the classification of early stage. This study aimed to develop a deep learning architecture to improve the classification accuracy of dry AMD, through the analysis of optical coherence tomography (OCT) images.

Methods: We put forward an ensemble deep learning architecture which integrated four different convolution neural networks including ResNet50, EfficientNetB4, MobileNetV3 and Xception. All networks were pre-trained and fine-tuned. Then diverse convolution neural networks were combined. To classify OCT images, the proposed architecture was trained on the dataset from Shenyang Aier Excellence Hospital. The number of original images was 4,096 from 1,310 patients. After rotation and flipping operations, the dataset consisting of 16,384 retinal OCT images could be established.

Results: Evaluation and comparison obtained from three-fold cross-validation were used to show the advantage of the proposed architecture. Four metrics were applied to compare the performance of each base model. Moreover, different combination strategies were also compared to validate the merit of the proposed architecture. The results demonstrated that the proposed architecture could categorize various stages of AMD. Moreover, the proposed network could improve the classification performance of nascent geographic atrophy (nGA).

Conclusion: In this article, an ensemble deep learning was proposed to classify dry AMD progression stages. The performance of the proposed architecture produced promising classification results which showed its advantage to provide global diagnosis for early AMD screening. The classification performance demonstrated its potential for individualized treatment plans for patients with AMD.

KEYWORDS

dry age-related macular degeneration, optical coherence tomography, ensemble deep learning, NGA, early AMD detection

1 Introduction

AMD is a retinal disease that is a major cause of blindness around the world (1). According to the World Health Organization, it was estimated that 288 million people globally suffered from intermediate or late-stage AMD (2). As the global population aged, AMD was expected to affect more people. Therefore, it was important to detect and screen AMD, especially for early stage of AMD. Based on the clinical appearance of AMD, it could be classified into early stage, intermediate stage and late stage (3). Early and intermediate AMD, also known as non-advanced dry AMD, were described by a slow progressive dysfunction of the retinal pigment epithelium (RPE) and presence of drusen. The late stage was defined by presence of geographic atrophy (GA) (4).

A recent approval released by the U.S. Food and Drug Administration highlights the importance of early detection of GA, which demonstrated that nGA was a pivotal marker for the prediction of the development of GA (5). It could help clinicians to better detect and screen AMD in the early stage. However, nGA has drusen with a diameter larger than 63 μm without atrophy or neovascular disease. This condition made it difficult to detect nGA accurately. Moreover, complex interference factors of nGA in shape, size and location exacerbated the difficulty to differentiate it from other retinal lesions (6).

In traditional retinal images, OCT images enabled visualization of thickness, structure and detail of various layers of the retina (7). In addition, when the retina developed a disease, OCT enabled the visualization of abnormal features and damaged retinal structures (8). Therefore, retinal OCT images were used in this article to detect nGA. In OCT images, spectral-domain OCT features unique in these areas included: subsidence of the outer plexiform layer (OPL) and inner nuclear layer (INL), and development of a hyporeflective wedge-shaped band within the limits of the OPL. These characteristics were defined as nGA, describing features that portended the development of drusen-associated atrophy. Cross-sectional examination of participants with bilateral intermediate AMD revealed that independent risk fact (9). The hypo-reflective wedge in nGA represented the presence of a hyporeflective wedge-shaped band within the limits of the OPL that subsequently developed as the characteristic feature of this stage. There was also typically drusen regression that was accompanied by a vortexlike subsidence of the INL and OPL at this stage. Different stages of dry AMD in OCT images were shown in Figure 1.

Although OCT images were widely applied into the treatment and diagnosis of AMD (10–13), the process was time-consuming due to manual operation and analysis. Ophthalmologists may provide incorrect results even if they had great expertise. With the development of artificial intelligence, machine learning and deep learning algorithms had been used in the diagnosis and treatment tasks, such as classification, detection and segmentation of AMD (14). Deep Learning (DL) had been widely used in the medical field to monitor information in medical images for the diagnosis of various diseases (7, 15–18). Recently, DL integrated with OCT imaging analysis, had been utilized for intelligent and accurate classification of AMD (19). However, most of previous

---

Abbreviations: AMD, Age-related macular degeneration; OCT, Optical coherence tomography; nGA, Nascent geographic atrophy; INL, Inner nuclear layer; OPL, Outer plexiform layer; DL, Deep Learning; CNN, Convolutional neural network; ROC, Receiver operating characteristics curve; Acc, Accuracy; Sen, Sensitivity; Spc, Specificity; F1, F1-score.

DL-based retinal OCT detection technologies focused primarily on the advanced stage. The main limitation came from the datasets which were mainly comprised of intermediate and late stages of AMD. Additionally, the challenge from the OCT image noise, the accuracy of diagnosis and the division among diverse stages increased the difficulty of early detection (20). A detection architecture based on a two-stage convolution neural network (CNN) with OCT images was proposed by He (21). In the first stage, ResNet50 CNN model was employed to categorize OCT images. Then image feature vector set was accepted by the local outlier factor algorithm in the second stage. This model was tested on the external Duke dataset which consisted of 723 AMD and 1,407 healthy control volumes. This architecture was able to achieve the performance of sensitivity of 95.0% and specificity of 95.0%. Similarly, a two-stage DL architecture was proposed by Motozawa (22). The first stage was capable of distinguishing healthy controls from OCT images. Then AMD with and without exudative changes could be detected in the second stage. This architecture was able to achieve a performance of 98.4% sensitivity, 88.3% specificity and 93.9% accuracy.

Similarly, a visual geometry group CNN architecture was developed by Lee for the categories of retinal diseases (23). This CNN model was trained and tested on 80,839 OCT images to evaluate the performance. The performance of AUC of 92.7% with an accuracy of 87.6% could be obtained. CNN models with fully automated technology were proposed by Derradji to segment retinal atrophy lesions in dry AMD (24). Due to segmentation technologies, this architecture was able to achieve a performance of 85% accuracy and 91% sensitivity.

To better differentiate AMD from healthy controls, Holland developed a pre-trained self-supervised deep learning architecture (25). The performance of 92% AUC was able to be achieved on the test images. However, it was difficult to distinguish between early stage and intermediate stage. To overcome this challenge, Bulut applied Xception models to the detection of AMD based on color fundus images (26). Through analysis of 50 different parameters, this architecture could obtain the highest performance of accuracy of 82.5%. Moreover, Chakravorti proposed an efficient CNN for AMD classification (27). This network trained on fundus images could categorize them in four types of AMD, reducing computational complexity with high performance. Instead of training networks on fundus images, Tomas developed an algorithm for the diagnosis of AMD in retinal OCT images. This algorithms was able to perform the detection of AMD based on the estimate of statistical approaches and randomization (28). Additionally, Zheng extended a five-category intelligent auxiliary diagnosis architecture for common retinal diseases. For the 4 common diseases, the best results of sensitivity, specificity, and F1-scores were 97.12, 99.52 and 98.21%, respectively (29). Vaiyapuri presented a new multi-retinal disease diagnosis model to determine diverse types of retinal diseases. Experimental results demonstrated that this architecture outperformed the exiting technologies for advanced AMD with the performance of accuracy 0.963 (30). Inspired by nature language processing, Lee presented CNN-LSTM and CNN-Transformer. Both deep learning architectures used a Long-Short Term Memory and a Transformer module, respectively with CNN, to capture the sequential information in OCT images for classification tasks. The proposed architecture was superior to the baseline architectures that utilized only single-visit CNN model to predict the risk of late AMD (31). Combining a multi-scale residual convolutional neural network and a vision transformer, Kar featured a generative adversarial network for the detection of AMD (32). Rigorous evaluations on multiple databases validated the architecture's robustness and efficacy.
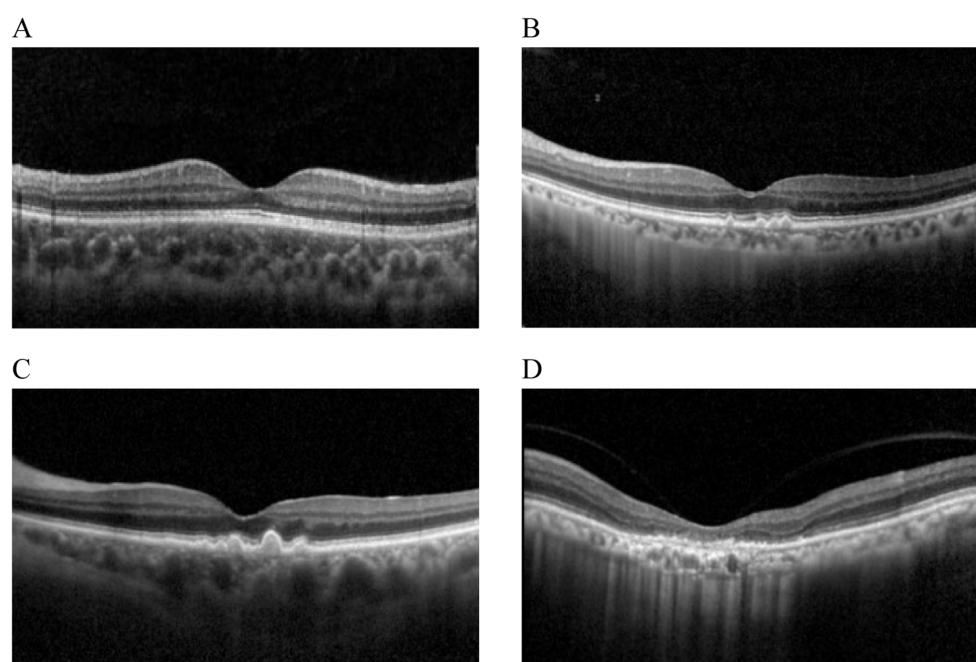
FIGURE 1
Different stages of dry AMD in OCT imaging. **(A)** Normal. **(B)** Drusen. **(C)** nGA. **(D)** GA.

In summary, many of the mentioned studies had focused on the application of deep learning and OCT for classifcation of AMD, achieving impressive accuracy rates. However, these studies lacked a comprehensive prediction for nGA. In this paper, we aimed to diagnose early stage of AMD with strong predictor nGA. We provided an ensemble deep learning architecture consisting of four components (ResNet50, EfficientNetB4, MobileNetV3 and Xception) to analyze OCT images. In order to accurately detect the early stage of AMD, an OCT-based ensemble DL architecture was proposed in which the images would be classified into four categories: normal, Drusen, nGA and GA. The main contributions of this work were as follows:

1. To the best of our knowledge, this was the first investigation to use ensemble DL technologies to detect and classify nGA.
2. The proposed architecture showed its advantage and provided detection results which could be utilized as a useful computer-aided diagnostic tool for clinical OCT-based early AMD diagnosis.
3. This paper proposed an ensemble technique by combining the predictions of four base CNNs—ResNet50, EfficientNetB4, MobileNetV3 and Xception. Based on the knowledge gained from ImageNet dataset, each base CNN was fine-tuned for the specific OCT image classification task.

2 Methods

2.1 Datasets

Although there were some public OCT datasets, they were not suitable for the detection of early stage of AMD. This study was retrospective. We used OCT images collected in 2019–2023 which

were gathered from 1,310 patients (male and female) of diverse age groups and ethnicity from Shenyang Aier Excellence Eye Hospital. The images in this dataset had been divided into four different classes: normal, drusen, nGA and GA. The training set and the test set were about 80 and 20% of the patients, respectively. All OCT images were captured from Heidelberg Spectralis HRA which was able to provide 6 mm × 6 mm B-scan length. The quality of OCT images were analyzed by ophthalmologists. All OCT images were clear and free of artifacts. Every OCT image was either normal or AMD without other retinal diseases. According to the judgment of ophthalmologists, OCT images that met the selection criteria were stored in the database. Any participant with any other ocular, systemic or neurological disease that could have an impact on the assessment of the retina, was excluded.
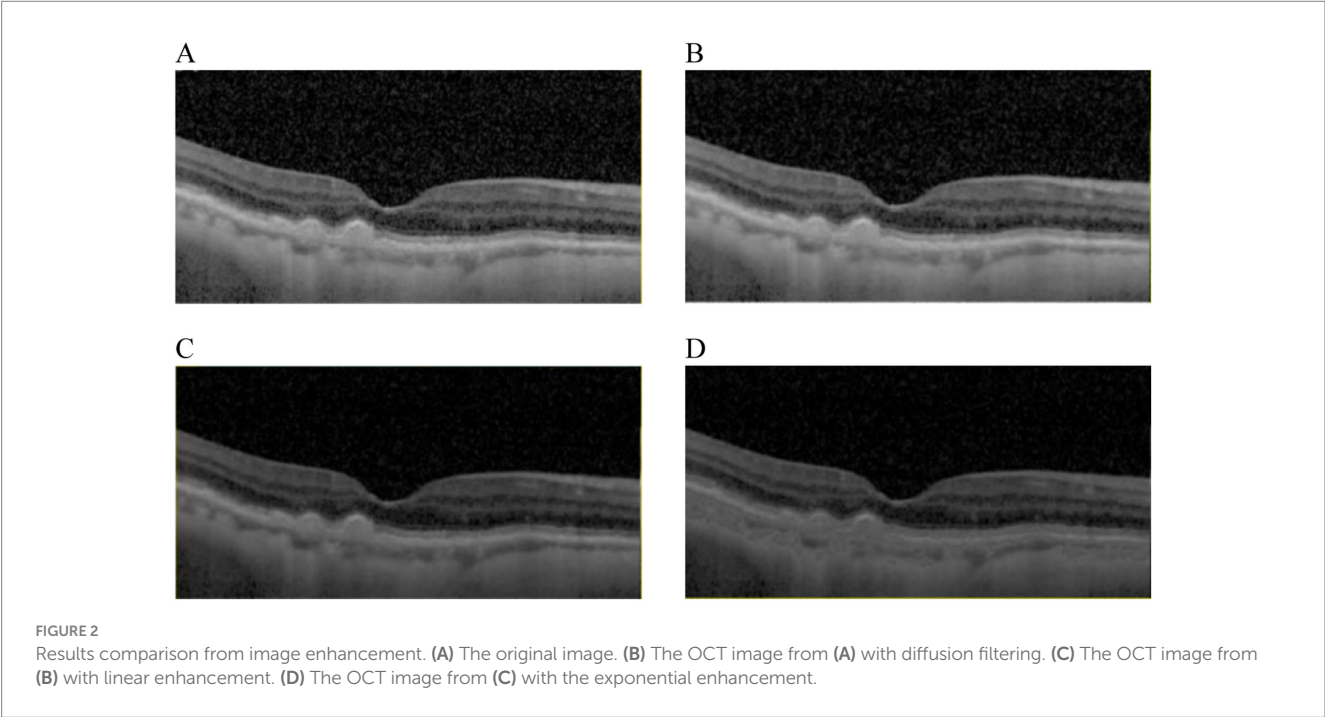
To improve the generalizability and reduce the risk of overfitting of the proposed architecture, this paper employed three-fold cross-validation to evaluate the performance. In one epoch of cross-validation, two-fold OCT images were used for training while the rest of OCT images were used for test. The training and test process would be performed three times and the average of results could be utilized to assess the performance of the proposed architecture. The number of training and test images were detailed in Table 1.

2.2 Image enhancement

The aim of OCT images enhancement was to provide high quality images which would improve the performance of the proposed architecture. The visibility of significant features would be enhanced by image enhancement algorithms, such as diffusion filtering, linear enhancement and exponential enhancement. Results of different image enhancement algorithms were displayed in Figure 2, where the original OCT image was shown in Figure 2A. To start with, a

TABLE 1 The detail of three cross-fold training and test datasets.

OCT Datasets	Fold 1		Fold 2		Fold 3	
	Train	Test	Train	Test	Train	Test
Patients (%)	1,040 (80%)	270 (20%)	1,040 (79%)	270 (21%)	1,040 (80%)	270 (20%)
Images (16384)	13,107	3,277	12,943	3,441	13,107	3,277
Normal (3072)	2,455	617	2,427	645	2,455	617
Drusen (5120)	4,094	1,024	4,045	1,075	4,094	1,024
nGA (4096)	3,277	819	3,236	860	3,277	819
GA (4096)	3,277	819	3,236	860	3,277	819

FIGURE 2
Results comparison from image enhancement. **(A)** The original image. **(B)** The OCT image from **(A)** with diffusion filtering. **(C)** The OCT image from **(B)** with linear enhancement. **(D)** The OCT image from **(C)** with the exponential enhancement.

diffusion filtering algorithm (33) was applied to reduce noise from the original OCT image, as presented in Figure 2B. Then linear enhancement (34) was employed to highlight the contrast between background and retinal layers, as shown in Figure 2C. At last, the OCT image was processed based on exponential enhancement (35) to further accentuate contrast between different layers. With the enhancement procedure, the final result could be obtained, as shown in Figure 2D.

2.3 Ensemble deep learning architecture

In this article, we built an ensemble deep learning architecture which consisted of four base models (ResNet50, EfficientNetB4, MobileNetV3 and Xception). After image enhancement, OCT images were further processed via image preprocessing, such as reshaping, normalization and augmentation. Then the OCT images were fed to every base model which was pre-trained on ImageNet and connected to full-connection layers. The prediction scores Y_i ($i = 1,2,3,4$) were obtained from four models. The weights would also be calculated based on these scores. As distributing weights to base models, we could obtain the final prediction through adding and normalizing

these prediction scores. The global ensemble architecture was presented in Figure 3.

In the OCT image pre-processing step, all OCT images were converted into gray values which ranged from 0 to 1. In order to obtain optimal classification performance, we tested OCT images with different shapes. We found that input images with 320×320 could provide the best performance. The visibility of AMD features were emphasized to accentuate contrast between different retinal layers. Moreover, data augmentation could improve the generality of the proposed method. The size of training data could be augmented. The number of original images was 4,096. Every original image was rotated $90°$, $180°$, and $270°$ respectively. Besides all original images could be flipped. After augmentation, the total number of images was 16,384. 80% of the total images were used for training and the unseen images were employed for test purpose. The whole dataset was labeled by two ophthalmologists. Then the proposed architecture was comprised of four fine-tuning models. To reduce training time, transfer learning technology was used. The base models were pre-trained on ImageNet dataset. The weights before 'FC' were kept frozen. Then the training process would fine-tune weights between 'FC' layers with a learning rate 0.001. To further avoid overfitting and reduce computation, 'dropout layer' with a dropout rate of 0.4 had also

FIGURE 3
The global ensemble architecture.

FIGURE 4
The training process of transfer learning.
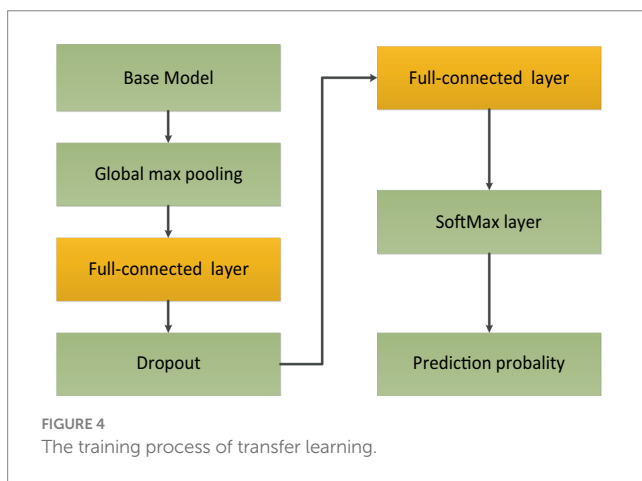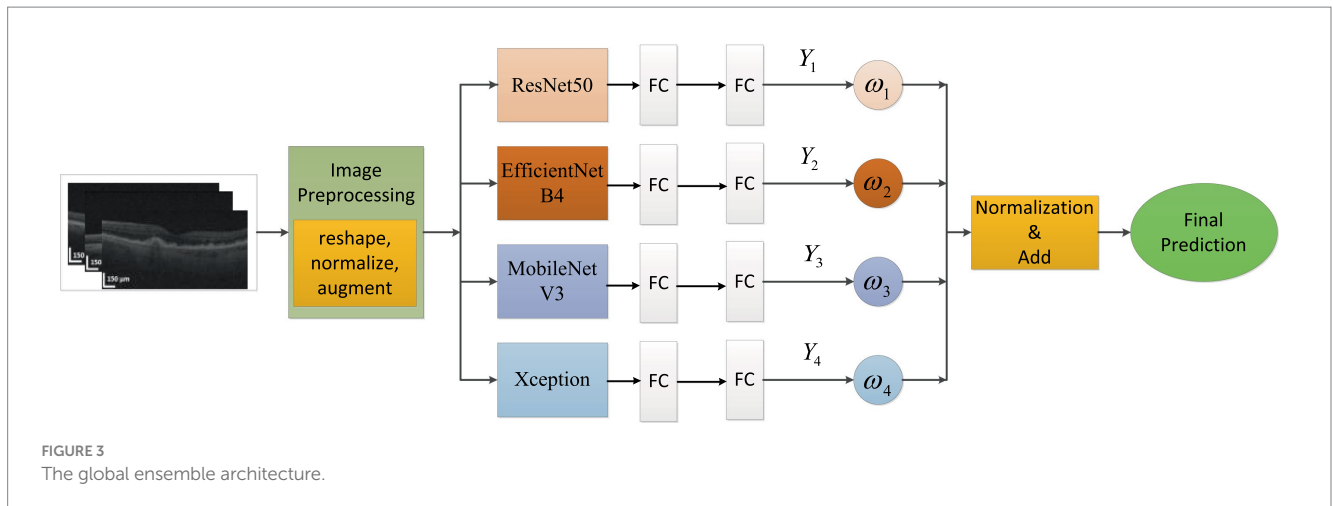
been added between 'FC' layers. Because classification of AMD was performed with four categories, soft-max activation with four categories had been added after 'FC' layer for classification task of AMD. The training process of transfer learning was shown in Figure 4.

The proposed architecture could be formed with the following steps: First, different base models, also known as CNNs, were analyzed after fine-tuning. Based on the performance of different base models, it could be found that the ResNet50, EfficientNetB4, MobileNetV3 and Xception had better performance compared to other CNN models on the test dataset. Then a comparative analysis of the weights combination strategies among different base models were performed. These strategies contained simple averaging, weighting function, majority voting and stacking methods. The weighting function was proportional to the performance of base models on test dataset. From these comparison results, the weighting function strategy could obtain the best performance for the classification of early AMD. The combination strategy of the proposed ensemble-based architecture was shown in Figure 5.

It could be found that four base models produced four prediction scores Y_i ($i=1,2,3,4$). The final prediction score could be calculated based on weights which were proportional to the performance of base models. At last, the accuracy of diagnosis was compared with the ground truth to evaluate the performance of the ensemble deep learning architecture. The weights could be calculated based on the following mathematical formulation, as shown in Equation 1:

$$\omega = F_{com}\left(Y_1(x), Y_2(x), Y_3(x), Y_4(x)\right) \tag{1}$$

Where F_{com} was the combination function which represented an aggregation strategy with various weights ω. If the the prediction probabilities from ith model was Y_i, then the weight ω_i could be expressed as Equation 2:

$$\omega_i = \frac{Y_i}{\sum\limits_{n=1}^{4} Y_n} \tag{2}$$

The weights which denoted the significance of every base model. The final prediction probability P on the test dataset could be obtained based on the weights combination strategy, as shown in Equation 3:

$$P = \sum_{i=1}^{4} \omega_i Y_i \tag{3}$$

The experimental results would be obtained and analyzed based on the proposed architecture in the next section.

3 Results

All experiments were conducted in Pytorch and the hardware was composed of 64 hyper-thread processors, $8 \times$ RTX 2080 Ti, and windows10. All OCT images were set to the shape 320×320.

Base CNN models were evaluated on the test dataset. The classification task was performed for four categories of dry AMD (normal, drusen, nGA, and GA). Diverse metrics were used to evaluate the efficacy of base models, including accuracy (Acc), sensitivity (Sen), specificity (Spc) and F$_1$-score (F$_1$) for overall classification performance. Sen described how well the test caught all of positive cases and Spc described how well the test classified negative cases as negatives. F$_1$ was a metric that offered an overall measure of the model's accuracy. These metrics could be expressed from Equations 4–7:
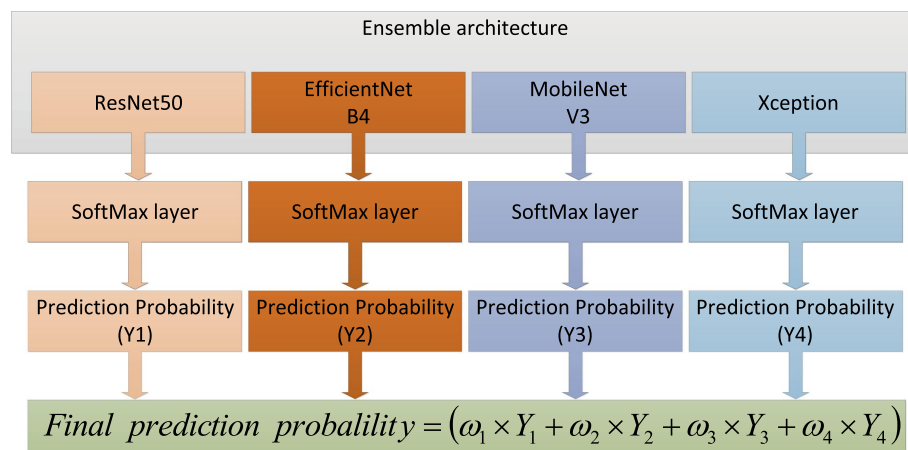
FIGURE 5
The combination strategy of the proposed ensemble-based architecture.

TABLE 2 The performance comparison among different methods.

Methods	Sen (%)			Spc (%)			F₁ (%)			F₁ (average)
	Fold1	Fold2	Fold3	Fold1	Fold2	Fold3	Fold1	Fold2	Fold3	
ResNet50	92.67	92.16	91.45	93.52	93.33	92.95	92.82	93.29	92.17	92.76
EfficientNetB4	90.23	90.15	91.06	92.44	91.22	92.15	92.63	91.29	91.18	91.71
MobileNetV3	92.54	90.33	93.08	93.11	87.15	91.22	92.25	89.93	92.54	91.57
Xception	92.71	89.66	92.13	91.08	90.53	84.57	91.12	91.56	90.81	91.16
VGG19	90.33	92.58	90.87	91.54	91.25	91.53	91.85	89.92	87.75	89.84
InceptionResNetV2	92.31	87.88	90.21	89.66	90.18	89.55	89.48	89.76	89.73	89.66
EfficientNetB0	90.55	90.28	88.93	84.57	91.16	90.15	88.61	89.28	87.63	88.51
NASNetMobile	91.56	89.15	90.23	86.43	90.22	87.38	87.33	88.07	89.06	88.15

$$Accuracy\left(Acc\right)=\frac{TP+TN}{TP+FP+TN+FN} \quad (4)$$

$$Sensitivity\left(Sen\right)=\frac{TP}{TP+FN} \quad (5)$$

$$Specificity\left(Spc\right)=\frac{TN}{TN+FP} \quad (6)$$

$$F_1-score\left(F_1\right)=\frac{2TP}{2TP+FP+FN} \quad (7)$$

Where *TP*, *TN*, *FP*, and *FN* represented true positives, true negatives, false positives, false negatives, respectively. The performance of each base model and the proposed architecture would be compared and evaluated using above performance metrics. 80% of the sample images were employed for training and the rest of images were used for testing. Different base models were assessed on the test dataset. The performance results were presented in Table 2.

Different ensemble strategies were also compared, such as majority voting, stacking, simple averaging, and weighting function (the proposed method). Majority voting meant that the prediction result from every base model was defined as a "vote." The most votes were used as the final prediction result. Stacking could be conducted by training classifiers on the combined classification scores in an ensemble architecture. Then the ensemble architecture would classify test images based on the trained classifiers. Simple averaging overlooked the effect from weights. It used an average weight to process every prediction scores. Instead of obtaining an average weight, the weighting function would allocate weights to various base models. The weights were proportional to the performance of base models on the train dataset. The prediction scores would be further processed to get the final prediction result. The comparison results were detailed in Table 3.

Based on the F₁ score in Table 3, the confusion matrix was also utilized to further show overall classification results with different architectures, as shown in Figure 6.

The performance between the proposed ensemble architecture and base models were also analyzed. The training epoch was set to 400. In every epoch, the corresponding results were recorded. The comparison results were shown in Figure 7. Four categories of dry AMD were used to analyze the performance of classification. The

classification Acc from base models and ensemble architecture were presented in Table 4.

To give a comprehensive analysis from true positive rate and false positive rate, receiver operating characteristics curve (ROC) was also plotted for four categories: normal, drusen, nGA and GA, as shown in Figure 8.

The visualization of heatmaps could also be generated to improve the interpretability in OCT images based on Grad-CAM. To show the classification basis, heatmaps of drusen, nGA, GA were generated respectively, as shown in Figure 9.

TABLE 3 The performance comparison from different ensembling strategies.

Strategy	Acc (%)	Sen (%)	Spc (%)	F1 (%)
majority voting	93.15	88.56	92.54	92.37
stacking	94.32	95.49	86.25	92.22
simple averaging	90.11	88.23	89.25	84.33
weighting function	96.51	93.31	94.56	97.45

4 Discussion

In this study, an ensemble deep learning architecture was proposed. To choose base models, different base models were tested and the performance results were shown in Table 2. The results were sorted in descending order based on F_1 score since it offered a

FIGURE 6
The confusion matrix of overall classification results. **(A)** Majority voting. **(B)** Stacking. **(C)** Simple averaging. **(D)** Weighting function.

FIGURE 7
The performance of accuracy in 400 epochs. **(A)** ResNet 50. **(B)** EfficientNetB4. **(C)** MobileNetV3. **(D)** Xception. **(E)** Proposed.
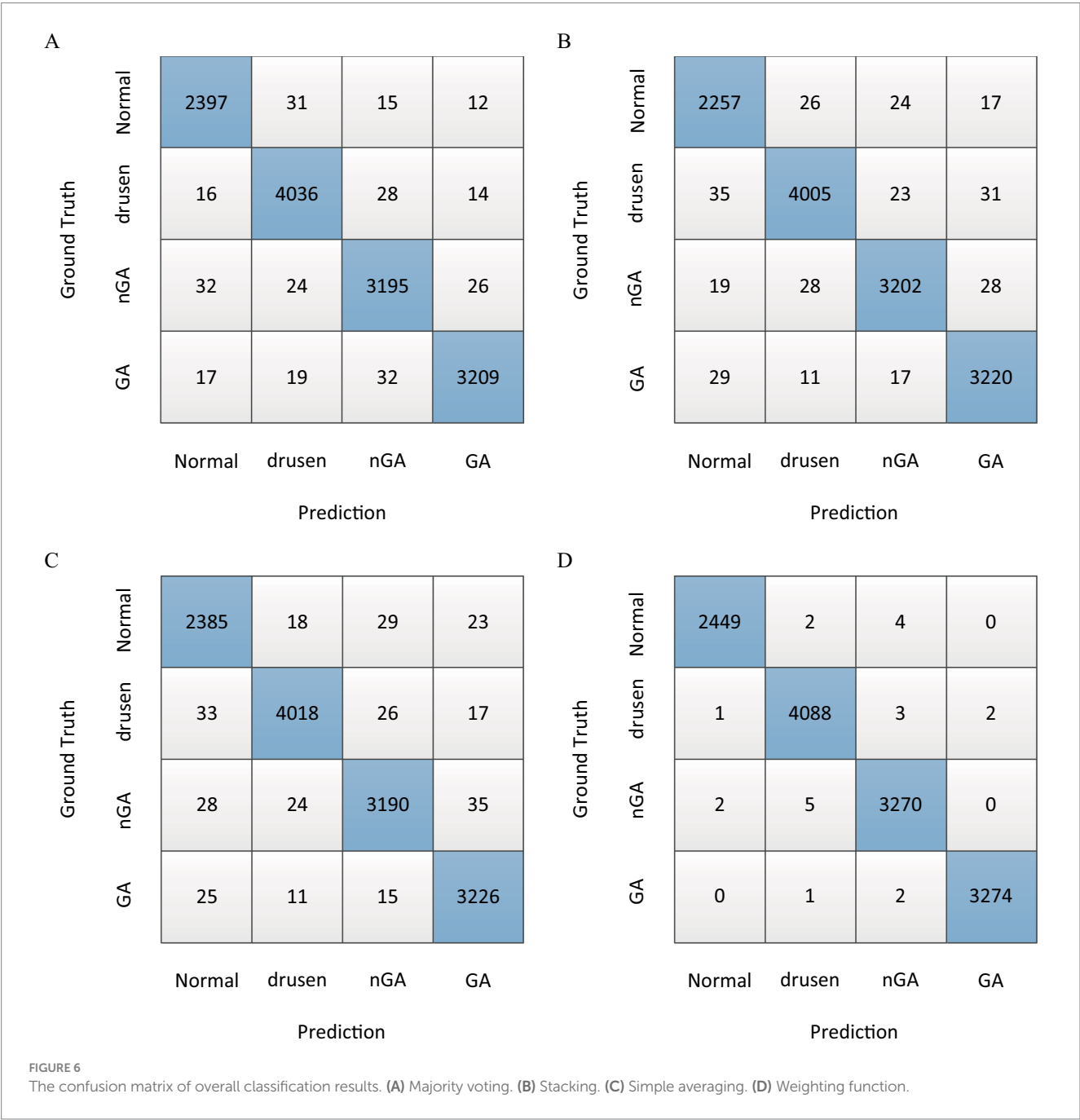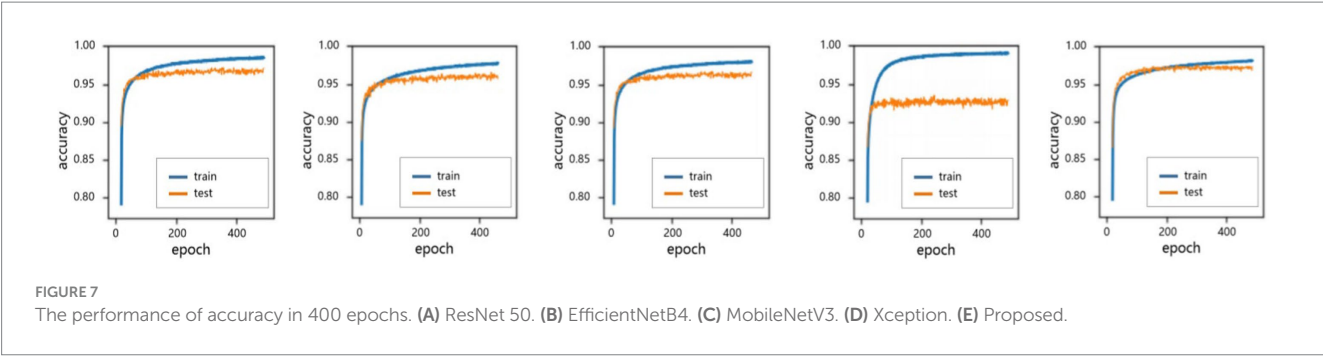
TABLE 4 The Acc (%) comparison among different classification results.

	ResNet50	EfficientNetB4	MobileNetV3	Xception	Proposed
Normal	92.66	93.25	88.64	91.65	96.66
Drusen	92.71	91.64	92.57	87.30	94.85
nGA	91.56	89.66	89.43	85.22	98.21
GA	92.55	93.85	89.64	92.74	96.31
F_1 (average)	92.82	91.71	91.57	91.16	97.45

comprehensive evaluation of different models. Therefore F_1 score could provide a basis for base models selection. Notably, four CNN models (ResNet50, EfficientNetB4, MobileNetV3 and Xception) could produce better results due to the consideration of local detail features and global semantic features. These base models would be served as base components in the ensemble architecture.

For the same base models, there were different combination strategies. In this study, majority voting, stacking, simple averaging and weighting function (the proposed method) were compared. The comparison results in Table 3 showed that both stacking and weighting function had better accuracy with 94.32% Acc and 96.51% Acc, respectively. Stacking strategy had the similar performance of sensitivity to the weighting function strategy which had better performance with 94.56% Spc. As presented in the column of F_1 score, it could be found that weighting function had the best performance of classification with 97.45% F_1 score. Moreover, the confusion matrices in Figure 6 demonstrated the advantage of the proposed architecture which could provide the best overall classification with less errors.

All base models could be fused based on tasks. Therefore, four categories of dry AMD were used to analyze the performance of different models. Comparison results were shown in Figure 7. It could be found that the proposed architecture and base models had similar performance. There were no over-fitting. Besides, the proposed architecture had better performance than base models with training epochs increasing. From comparison results in Table 4, it could also be found that the proposed architecture could generate commendable results. Compared with base models, the ensemble architecture could significantly improve the classification performance with the highest accuracy for all classes, especially for nGA. In terms of sensitivity and specificity, the proposed architecture outperformed all base models. It demonstrated that the proposed architecture could detect true positives and true negatives much better. For base models, F_1-score were 92.82, 91.71, 91.57, and 91.16%, respectively, while the proposed method could archive the highest F_1-score (97.45%). The comparison

results demonstrated that the proposed architecture had better robustness and better performance of accuracy due to the combination of base models. ROC was provided to analyze overall performance of classification. Comparison results in Figure 8 showed that the maximum area could be obtained from the proposed architecture. It meant that the proposed architecture could provide more accurate classification results, especially for nGA.

The heat maps generated through Gram-CAM validated that typical features from dry AMD could be successfully detected. Three categories of pathological features (drusen, nGA and GA) could be correctly accentuated. In particular, the early stage of AMD with nGA could be correctly highlighted and observed, as shown in Figure 9. The heat maps demonstrated that the proposed architecture could successfully identify distinctive features and relevant lesions.

5 Conclusion

The intention of this article was to provide an architecture for an automated diagnosis and classification of AMD using OCT images, including the detection of early-stage dry AMD with nGA. The proposed architecture did not need to segment biomarkers. By combining image enhancement and base CNN models, the performance of detection of dry AMD could be improved. Experimental results showed that three categories of pathological features could be correctly detected and observed, particularly for the nGA feature. The proposed ensemble architecture and base models had similar performance. There were no over-fitting. Moreover, the proposed ensemble architecture had the best classification performance for the present OCT images classification task. It suggested that the proposed ensemble architecture was superior in classification task for early stage of AMD. In the future, multi-modal images such as fundus photography and angiography can be used to
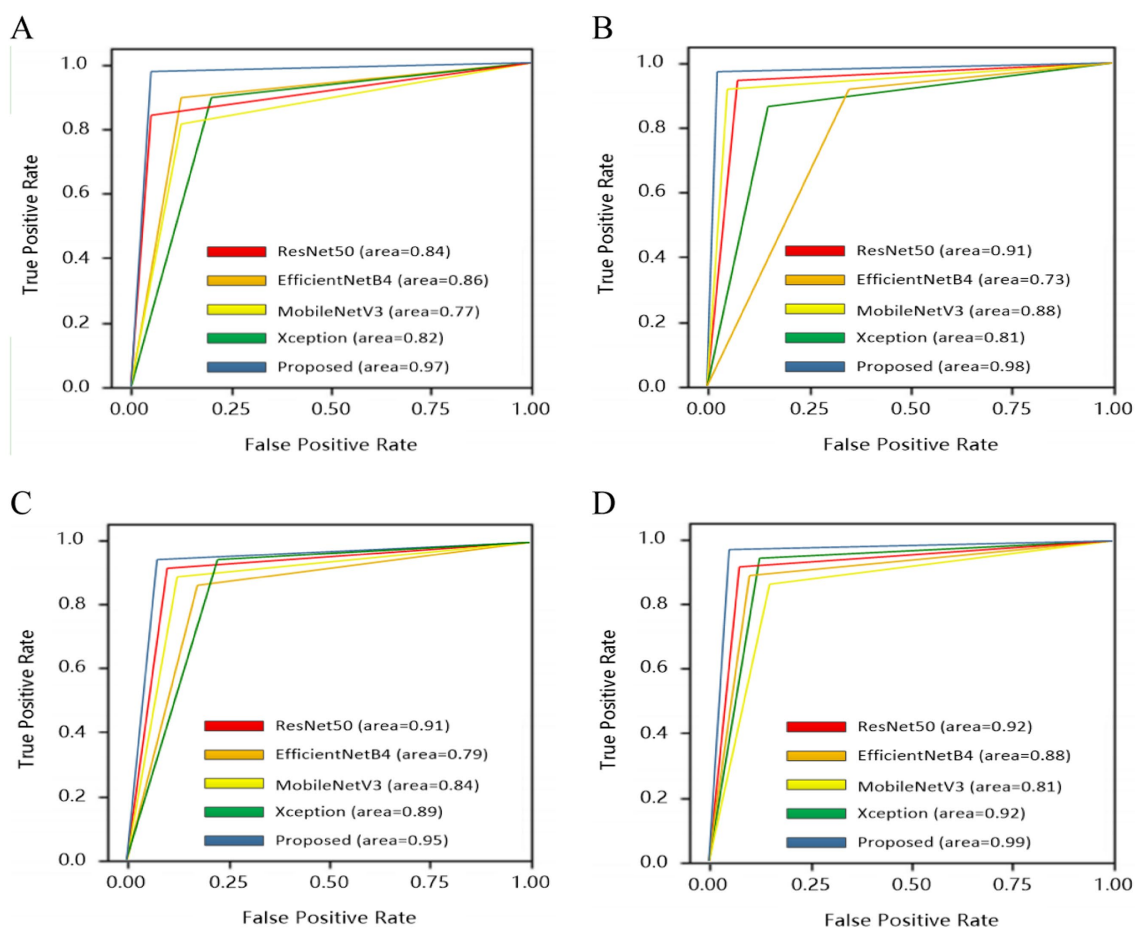
FIGURE 8
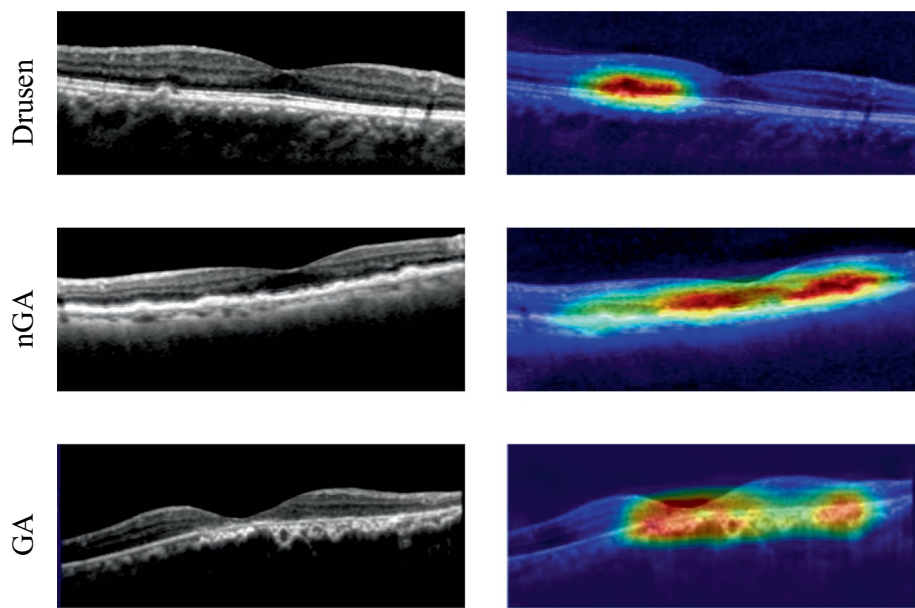ROC comparison among different methods. **(A)** Normal. **(B)** Drusen. **(C)** nGA. **(D)** GA.

FIGURE 9
Heatmaps from dry AMD with pathological features.

supplement OCT images. Besides the diagnostic performance can be improved by integrating other artificial intelligence technologies such as segmentation and attention mechanism.

Data availability statement

The raw data supporting the conclusions of this article will be made available by the authors, without undue reservation.

Ethics statement

Written informed consent was obtained from the individual(s) for the publication of any potentially identifiable images or data included in this article.

Author contributions

JY: Writing – original draft. BW: Investigation, Writing – original draft. JW: Software, Writing – original draft. YL: Data curation, Writing – review & editing. ZZ: Methodology, Writing – review & editing. YD: Formal analysis, Writing – review & editing. KT: Formal analysis, Writing – review & editing. FL: Project administration, Writing – review & editing. LM: Supervision, Writing – original draft, Writing – review & editing.

Conflict of interest

The authors declare that the research was conducted in the absence of any commercial or financial relationships that could be construed as a potential conflict of interest.

Publisher's note

All claims expressed in this article are solely those of the authors and do not necessarily represent those of their affiliated organizations, or those of the publisher, the editors and the reviewers. Any product that may be evaluated in this article, or claim that may be made by its manufacturer, is not guaranteed or endorsed by the publisher.

References

1. Wu Z, Fletcher EL, Kumar H, Greferath U, Guymer RH. Reticular pseudodrusen: a critical phenotype in age-related macular degeneration. *Prog Retin Eye Res*. (2022) 88:101017. doi: 10.1016/j.preteyeres.2021.101017

2. Yang S, Zhao J, Sun X. Resistance to anti-VEGF therapy in neovascular age-related macular degeneration: a comprehensive review. *Drug Des Devel Ther*. (2016):1857–67. doi: 10.2147/DDDT.S97653

3. Mitchell P, Liew G, Gopinath B, Wong TY. Age-related macular degeneration. *Lancet*. (2018) 392:1147–59. doi: 10.1016/S0140-6736(18)31550-2

4. Mrowicka M, Mrowicki J, Kucharska E, Majsterek I. Lutein and zeaxanthin and their roles in age-related macular degeneration—neurodegenerative disease. *Nutrients*. (2022) 14:827. doi: 10.3390/nu14040827

5. Schmidt-Erfurth U, Waldstein SM. A paradigm shift in imaging biomarkers in neovascular age-related macular degeneration. *Prog Retin Eye Res*. (2016) 50:1–24. doi: 10.1016/j.preteyeres.2015.07.007

6. Wong CW, Yanagi Y, Lee WK, Ogura Y, Yeo I, Wong TY, et al. Age-related macular degeneration and polypoidal choroidal vasculopathy in Asians. *Prog Retin Eye Res*. (2016) 53:107–39. doi: 10.1016/j.preteyeres.2016.04.002

7. Sadda SR, Guymer R, Holz FG, Schmitz-Valckenberg S, Curcio CA, Bird AC, et al. Consensus definition for atrophy associated with age-related macular degeneration on OCT: classification of atrophy report 3. *Ophthalmology*. (2018) 125:537–48. doi: 10.1016/j.ophtha.2017.09.028

8. Grunwald JE, Pistilli M, Ying G, Maguire MG, Daniel E, Martin DF, et al. Growth of geographic atrophy in the comparison of age-related macular degeneration treatments trials. *Ophthalmology*. (2015) 122:809–16. doi: 10.1016/j.ophtha.2014.11.007

9. Wu Z, Luu CD, Ayton LN, Goh JK, Lucci LM, Hubbard WC, et al. Optical coherence tomography–defined changes preceding the development of drusen-associated atrophy in age-related macular degeneration. *Ophthalmology*. (2014) 121:2415–22. doi: 10.1016/j.ophtha.2014.06.034

10. Burlina PM, Joshi N, Pekala M, Pacheco KD, Freund DE, Bressler NM. Automated grading of age-related macular degeneration from color fundus images using deep convolutional neural networks. *JAMA Ophthalmol*. (2017) 135:1170–6. doi: 10.1001/jamaophthalmol.2017.3782

11. Ting DSW, Pasquale LR, Peng L, Campbell JP, Lee AY, Raman R, et al. Artificial intelligence and deep learning in ophthalmology. *Br J Ophthalmol*. (2019) 103:167–75. doi: 10.1136/bjophthalmol-2018-313173

12. Ting DSJ, Foo VHX, Yang LWY, Sia JT, Ang M, Lin H, et al. Artificial intelligence for anterior segment diseases: emerging applications in ophthalmology. *Br J Ophthalmol*. (2021) 105:158–68. doi: 10.1136/bjophthalmol-2019-315651

13. Aggarwal R, Sounderajah V, Martin G, Ting DSW, Karthikesalingam A, King D, et al. Diagnostic accuracy of deep learning in medical imaging: a systematic review and meta-analysis. *NPJ Dig Med*. (2021) 4:65. doi: 10.1038/s41746-021-00438-z

14. Chen R, Zhang W, Song F, Yu H, Cao D, Zheng Y, et al. Translating color fundus photography to indocyanine green angiography using deep-learning for age-related macular degeneration screening. *NPJ Dig Med*. (2024) 7:34. doi: 10.1038/s41746-024-01018-7

15. Gholami S, Scheppke L, Kshirsagar M, Wu Y, Dodhia R, Bonelli R, et al. Self-supervised learning for improved optical coherence tomography detection of macular telangiectasia type 2. *JAMA Ophthalmol*. (2024) 142:226–33. doi: 10.1001/jamaophthalmol.2023.6454

16. Jin K, Yan Y, Chen M, Wang J, Pan X, Liu X, et al. Multimodal deep learning with feature level fusion for identification of choroidal neovascularization activity in age-related macular degeneration. *Acta Ophthalmol*. (2022) 100:e512–20. doi: 10.1111/aos.14928

17. Iafe NA, Phasukkijwatana N, Sarraf D. Optical coherence tomography angiography of type 1 neovascularization in age-related macular degeneration. *OCT Angiography Retinal Macular Dis*. (2016) 56:45–51. doi: 10.1159/000442776

18. Jia Y, Bailey ST, Wilson DJ, Tan O, Klein ML, Flaxel CJ, et al. Quantitative optical coherence tomography angiography of choroidal neovascularization in age-related macular degeneration. *Ophthalmology*. (2014) 121:1435–44. doi: 10.1016/j.ophtha.2014.01.034

19. Tombolini B, Crincoli E, Sacconi R, Battista M, Fantaguzzi F, Servillo A, et al. Optical coherence tomography angiography: a 2023 focused update on age-related macular degeneration. *Ophthalmol Therapy*. (2024) 13:449–67. doi: 10.1007/s40123-023-00870-2

20. El-Ateif S, Idri A. Eye diseases diagnosis using deep learning and multimodal medical eye imaging. *Multimed Tools Appl*. (2023) 83:30773–818. doi: 10.1007/s11042-023-16835-3

21. He T, Zhou Q, Zou Y. Automatic detection of age-related macular degeneration based on deep learning and local outlier factor algorithm. *Diagnostics*. (2022) 12:532. doi: 10.3390/diagnostics12020532

22. Motozawa N, An G, Takagi S, Kitahata S, Mandai M, Hirami Y, et al. Optical coherence tomography-based deep-learning models for classifying normal and age-related macular degeneration and exudative and non-exudative age-related macular degeneration changes. *Ophthalmol Therapy*. (2019) 8:527–39. doi: 10.1007/s40123-019-00207-y

23. Lee CS, Baughman DM, Lee AY. Deep learning is effective for the classification of OCT images of Normal versus age-related macular degeneration. Ophthalmology. *Retina*. (2017) 1:322–7. doi: 10.1016/j.oret.2016.12.009

24. Derradji Y, Mosinska A, Apostolopoulos S, Ciller C, de Zanet S, Mantel I. Fully-automated atrophy segmentation in dry age-related macular degeneration in optical coherence tomography. *Sci Rep*. (2021) 11:21893. doi: 10.1038/s41598-021-01227-0

25. Holland R, Menten MJ, Leingang O, Bogunovic H, Hagag AM, Kaye R, et al. Self-supervised pretraining enables deep learning-based classification of AMD with fewer annotations. *Invest Ophthalmol Vis Sci*. (2022) 63:3004.

26. Bulut B, Kalın V, Güneş B B, Khazhin Rim. Deep learning approach for detection of retinal abnormalities based on color fundus images. 2020 innovations in intelligent systems and applications conference (ASYU), (2020): 1–6.

27. Chen YM, Huang WT, Ho WH, Tsai JT. Classification of age-related macular degeneration using convolutional-neural-network-based transfer learning. *BMC Bioinformat*. (2021) 22:1–16. doi: 10.1186/s12859-021-04001-1

28. Thomas A, Sunija AP, Manoj R, Ramachandran R, Ramachandran S, Varun PG, et al. RPE layer detection and baseline estimation using statistical methods and

29. Zheng B, Jiang Q, Lu B, He K, Wu MN, Hao XL, et al. Five-category intelligent auxiliary diagnosis model of common fundus diseases based on fundus images. *Transl Vis Sci Technol*. (2021) 10:20–0. doi: 10.1167/tvst.10.7.20

30. Vaiyapuri T, Srinivasan S, Yacin Sikkandar M, Balaji TS, Kadry S, Meqdad MN, et al. Intelligent deep learning based multi-retinal disease diagnosis and classification framework. *Comput Materials Continua*. (2022) 73:5543–57. doi: 10.32604/cmc.2022.023919

31. Lee J, Wanyan T, Chen Q, Keenan Tiarnan D. L., Glicksberg Benjamin S., Chew Emily Y., et al. (2022). Predicting age-related macular degeneration progression with longitudinal fundus images using deep learning[C]//international workshop on machine learning in medical imaging. Cham: Springer Nature Switzerland: 11–20.

32. Kar MK, Neog DR, Nath MK. Retinal vessel segmentation using multi-scale residual convolutional neural network (MSR-net) combined with generative adversarial networks. *Circuits Syst Signal Process*. (2023) 42:1206–35. doi: 10.1007/s00034-022-02190-5

33. Deng L, Zhu H, Yang Z, Li Y. Hessian matrix-based fourth-order anisotropic diffusion filter for image denoising. *Opt Laser Technol*. (2019) 110:184–90. doi: 10.1016/j.optlastec.2018.08.043

34. Wang W, Wu X, Yuan X, Gao Z. An experiment-based review of low-light image enhancement methods. *IEEE Access*. (2020) 8:87884–917. doi: 10.1109/ACCESS.2020.2992749

35. McDonald A, Clerk AA. Exponentially-enhanced quantum sensing with non-Hermitian lattice dynamics. *Nat Commun*. (2020) 11:5382. doi: 10.1038/s41467-020-19090-4

Check for updates

Changes in retinal nerve fiber layer and vessel densities after scleral buckling in patients with rhegmatogenous retinal detachment observed by OCTA

Cuiwen Zhang[1†], Linlin Liu[2] and Yiping Jiang[2]*

[1]The First Clinical Medical College of Gannan Medical University, Ganzhou, China, [2]First Affiliated Hospital of Gannan Medical University, Ganzhou, China

Purpose: To observe the changes in peripapillary retinal nerve fiber layer (RNFL) thickness and peripapillary vessel densities (VD) in patients with rhegmatogenous retinal detachment (RRD) after scleral buckling (SB) by OCTA.

Methods: A total of 40 patients (40 eyes) with monocular RRD who underwent SB were included in the study, with the operated eyes (40 eyes) as the study group and the contralateral healthy eyes (40 eyes) as the control to analyse the changes in peripapillary RNFL thickness and VD before and after surgery. Data were analysed by paired samples t-test or Wilcoxon signed rank sum test.

Results: Comparison of the peripapillary RNFL thickness in the 8 areas between the two groups during the 6-month follow-up period: All 8 peripapillary areas of the optic disc were statistically different before surgery, except for the tempo superior and tempo inferior, which were statistically different at each postoperative follow-up point, and the remaining 6 areas in the operated eyes group were progressively closer to those in the healthy eyes group, and there was no significant difference between the two groups. Comparison of peripapillary VD in the 8 areas between the two groups during the 6-month follow-up: Peripapillary VD in the 8 areas in the two groups were all statistically different before surgery, and except for superior tempo, which was statistically different at each postoperative follow-up time point, the remaining seven areas in the operated eyes group became progressively closer to that in the healthy eyes group and there was no significant difference.

Conclusion: RRD negatively affects the peripapillary RNFL, but both peripapillary RNFL thickness and VD gradually improved in the operated eyes close to the contralateral eyes after SB.

1 Introduction

Rhegmatogenous retinal detachment (RRD) is a separation of the retinal nerve fiber layer from the pigment epithelial layer caused by the retinal hole. It is the most common type of retinal detachment in clinical practice, with an incidence of approximately 1 in 10,000 per year; and a blindness rate of nearly 100% if left untreated (1, 2). Scleral buckling (SB) and vitrectomy are the mainstay of treatment for RRD (3). Vitrectomy for RRD requires the injection of silicone oil or gas into the vitreous cavity (3, 4). Silicone oil is a commonly used intraocular filler because of its proximity to the vitreous. Silicone oil has been shown to hurt the optic nerve and retinal microcirculation (5). In contrast, SB for RRD consists of placing silicone strips or silicone sponges on the sclera corresponding to the fissure to create a depression in the sclera and choroid, reduce vitreous traction around the fissure, and seal the fissure. The effect on the optic nerve and retinal microcirculation around the optic disc has not been studied in detail.

Although visual acuity has been a commonly used clinical method to assess postoperative visual function, it is somewhat subjective, often macular dependent and does not provide a comprehensive, objective and accurate assessment of visual function (6). The ganglion cell body is located in the ganglion cell layer and its axons travel inward and parallel to the inner surface of the retina before entering the optic nerve to form the retinal nerve fibre layer (RNFL). RNFL thickness, which depends primarily on the number of ganglion cell axons, is an important indicator of quantitative response to changes in optic nerve and visual conduction function (7), which is directly related to visual acuity, contrast sensitivity, colour vision, visual field and other visual functions (8). The peripapillary vessel densities (VD) form a unique vascular network within the RNFL around the optic nerve head and are the innermost capillaries of the RNFL. They provide nutrients to the RNFL, which is relatively thicker in normal eyes in areas with higher VD and less spaced capillaries, and therefore thickest around the optic disc (9). In cotton-wool spots, intraretinal haemorrhages and ischaemic optic neuropathy, RNFL defects have an important correlation with the peripapillary VD, which has not been given enough attention in the past due to the difficulty of imaging it with certainty, but monitoring the peripapillary RNFL and VD is important for assessing visual function.

Evaluation of the tissues surrounding the optic disc provides information necessary for the diagnosis and evaluation of a wide range of ocular and neurological disorders (10). Optical coherence tomography angiography (OCTA) is a rapid and non-invasive ophthalmic imaging technique with the advantages of high resolution and reproducibility (11, 12); that can automatically measure retinal RNFL thickness and VD parameters in 8 regions around the optic disc. In this study, we investigated the changes in RNFL and VD after SB in patients with RRD using OCTA.

2 Materials and methods

2.1 General information

Patients who underwent SB for monocular RRD in our hospital between November 2021 and March 2023 were included in the study. The operated eyes was the study group and the contralateral healthy eyes was the control. Inclusion criteria: (1) Patients with a clinical diagnosis of monocular RRD whose contralateral eyes were normal (normal eyes had normal visual acuity, intraocular pressure, slit lamp,

fundus and other examinations and had not received any treatment); (2) Refractive error between the RRD eye and the contralateral healthy eye of <3.00D; (3) Patients with RRD according to the American Retina Society's 1983 PVR grading criteria (13): PVR grades A, B, and C; (4) no previous ocular surgical treatment; and (5) at least 6 months of follow-up. Exclusion criteria: (1) Patients with ocular and systemic diseases other than RRD, such as glaucoma, diabetes mellitus, hypertension, etc., (2) Patients with failed SB or recurrence of retinal detachment during the follow-up period; (3) Patients with macular lentigines; (4) Patients with pathology in the contralateral eye during the follow-up period; (5) Patients who cannot be clearly imaged on OCTA due to refractive interchromatic opacities, or whose 8 divisions of the peripapillary area cannot be measured on OCTA for various reasons; (6) Patients who cannot cooperate with the examination for various reasons; (7) Patients whose OCTA cannot be clearly imaged due to refractive interstitial opacities or whose data in all 8 peripapillary disc locations cannot be measured for various reasons; (8) Patients who cannot cooperate with the examination for various reasons. All patients underwent a comprehensive ophthalmic examination of both eyes at enrolment, including best corrected visual acuity, intraocular pressure, slit-lamp examination, fundus photography, indirect ophthalmoscopy, and OCTA. The study adhered to the tenets of the Declaration of Helsinki and was approved by the Ethics Committee of First Affiliated Hospital of Gannan Medical University. Informed consent was obtained prior to the inclusion of subjects.

2.2 Surgical techniques

Patients were fully informed of the possible risks and complications of SB before surgery, and patients or their relatives signed the informed consent form and then underwent surgery. Patients were placed in the recumbent position, anaesthetised under retrobulbar anaesthesia, the eyelids were opened with a lid opener, the bulbar conjunctiva was incised in a circular pattern according to the location of the retinal hole, the rectus muscle traction suture was fixed, and a 360-degree peripheral funduscopy was performed, and a 360-degree peripheral fundus examination was performed with a bimanual indirect ophthalmoscope under the upper pressure of the cryoprobe to find the retinal hole and the area of degeneration, and the retina around the hole and the area of degeneration was frozen, and condensation was stopped when the retinal pigment epithelium or the retina became whitish, and the sclera was located outside the hole and pre-positioned under the suture. The pre-positioned sutures were placed under the sutures with a silicone sponge and the pre-positioned sutures were tightened so that the fissure was well closed at the pressure ridge.

2.3 OCTA imaging

All patients were examined by trained and experienced clinical technologists. RNFL and VD images around the optic disc were obtained in both eyes using OCTA (Optovue RTVue XR Avanti, Optovue Inc., United States) and OCTA data were measured multiple times at each follow-up visit and the better quality images were selected for analysis. The Angio-Disc scan mode was selected for a 4.5 × 4.5 mm rectangular scan centred on the optic disc, the image was automatically segmented into a 2.0 mm diameter circle centred

on the optic disc, and a circle 2.0 mm around this circle was defined as the peripapillary region, and the instrument delineated the peripapillary region as nasal superior, superior nasal, superior tempo, tempo superior, tempo inferior, inferior tempo, inferior nasal, nasal inferior. The instrument automatically detects RNFL and VD parameters in the above eight regions around the optic disc. The instrument automatically divides the optic disc periphery globally into 8 zones to generate RNFL and VD parameters (Figure 1) and automatically displays the signal strength index (SSI). In patients with RRD who underwent SB, intraocular pressure in both eyes, interocular ophthalmoscopy after pupil dilation, and OCTA were performed preoperatively and at 1 day, 2 weeks, 1 month, 3 months, and 6 months postoperatively to record RNFL thickness, VD in each quadrant around the optic disc and SSI in the operated and healthy eyes at different times.

2.4 Statistical methods

SPSS23.0 software was used for statistical analysis, and the measurement data conforming to normal distribution were expressed as the mean ± standard deviation (SD), and the comparison between the operated eyes group and the healthy eyes group was performed by the paired samples t-test; the non-normally distributed data were expressed as median [interquartile range], and the comparison between the operated eyes group and the healthy eyes group was performed by the *Wilcoxon* signed rank-sum test. Differences were considered statistically significant at $p < 0.05$.

3 Results

3.1 Basic data

Sixty-five patients were initially identified as subjects, of which 18 patients were lost to follow-up, 3 patients had recurrent RRD during follow-up, 4 patients also had RRD in the contralateral eyes during the 6-month follow-up period, and 40 patients (40 eyes) were finally included in the analysis, including 21 male and 19 female patients, with a mean age of (49.26 ± 15.25) years and a mean duration of RRD of (1.01 ± 1.31) months. The RRD-affected eyes (40 eyes) that underwent SB were the study group (operated eyes group) and the contralateral healthy eyes of the patients (40 eyes) were the control group (Table 1). The intraocular pressure of these 40 patients was within the normal range during the follow-up period.

3.2 Comparison of SSI between the operated and healthy eye groups at different time points

The SSI was smaller in the operated eye group than in the healthy eye group at 1 day (6.600 ± 0.87 vs. 8.325 ± 0.92; $p < 0.001$) and 2 weeks (8.125 ± 0.82 vs. 8.550 ± 0.75; $p = 0.022$) after surgery, and the SSI was lower in the operated eye group than in the healthy eye group at 1 day preoperatively (8.025 ± 0.73 vs. 8.250 ± 1.17; $p = 0.246$), 1 month postoperatively (8.150 ± 0.86 vs. 8.300 ± 0.99; $p = 0.430$), 3 months postoperatively (8.175 ± 1.04 vs. 8.250 ± 1.06 $p = 0.701$), and 6 months postoperatively (8.125 ± 1.02 vs. 8.150 ± 1.05; $p = 0.905$) the operated eye group was not significantly different from the healthy eye group (Table 2).

3.2.1 Comparison of peripapillary RNFL between the operated eye and the healthy eye groups at different preoperative and postoperative time points of the SB

At 6-month follow-up, the results of the corresponding comparison of peripapillary RNFL thickness between the operated eye group and the healthy eye group, respectively, showed that, preoperatively, the operated eye group had nasal superior (111 [96–134] vs. 105 [94–116]; $p = 0.014$), superior nasal (156 [120–191] vs. 138 [114–155]; $p = 0.009$), superior tempo (149 [126–200] vs. 133 [122–149]; $p = 0.003$), tempo superior (99 [81–211] vs. 86 [78–95]; $p < 0.001$), tempo inferior (85 [74–135] vs. 76 [64–86]; $p < 0.001$), inferior tempo (165 [131–188] vs.
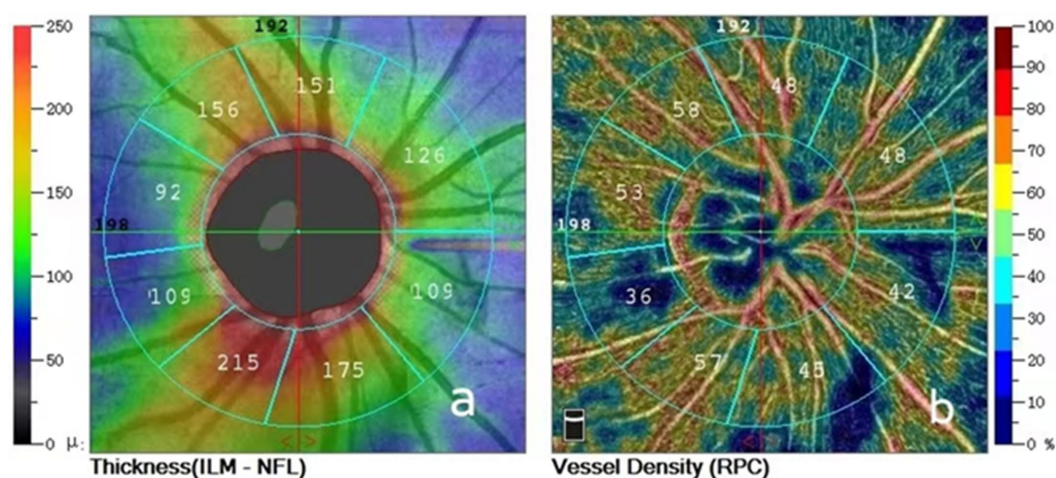

FIGURE 1
(A) Peripapillary retinal nerve fiber layer thickness divided into eight areas; **(B)** Peripapillary vessel densities divided into eight areas.

152 [135–165]; $p = 0.046$), inferior nasal (156 [137–182)] vs. 143 [129–155]; $p = 0.003$), nasal inferior (104 [89–128] vs. 86 [76–99]; $p < 0.001$), and global (126.75 [115.13–133.13] vs. 115.75 [108.88–122.88]; $p < 0.001$) had a greater RNFL than the healthy eye group prior to surgery; beginning at 1 month postoperatively, the superior tempo in both groups (143.00 [122.00–155.00] vs. 134.00 [123.00–146.00]; $p = 0.05$) and inferior nasal (148.00 [129.00–161.00] vs. 143.00 [127.00–154.00]; $p = 0.491$) were not significantly different; starting at 3 months postoperatively, the two groups had a higher superior nasal (145.00 [128.00–162.00] vs. 136.00 [115.00–155.00]; $p = 0.069$), superior tempo (141.00 [119.00–155.00] vs. 135.00 [120.00–148.00]; $p = 0.118$), inferior tempo (165.00 [139.00–179.00] vs. 156.00 [134.00–167.00]; $p < 0.074$), inferior nasal (143.00 [129.00–157.00] vs. 142.00 [129.00–154.00]; $p = 0.711$), nasal inferior (90.00 [82.00–107.00] vs. 86.00 [78.00–102.00]), $p < 0.053$) were not significantly different; at 6 months postoperatively, only tempo inferior (88.00 [75.00–99.00] vs. 79.00 [68.00–86.00]; $p < 0.001$ and global (124.29 [113.00–129.71] vs. 116.63 [109.75–124.25]; $p < 0.001$, the operated eye group was still larger than the healthy side group (Table 3).

3.2.2 Comparison of global peripapillary RNFL in the operated eye group and the healthy eye group at different preoperative and postoperative time points of the SB

Preoperatively, the global RNFL around the optic disc in the operated eye group was significantly larger than that in the healthy eye group, the RNFL around the optic disc in the operated eye group

TABLE 1 Patient information.

Parameter	Value
Age	49.26 ± 15.25
Time of retinal detachment	1.01 ± 1.31
Gender	
Male	21 (52.5%)
Female	19 (47.5%)
Range of retinal detachment	
1 quadrant	12 (30.0%)
2 quadrant	18 (45.0%)
3 quadrant	10 (25.0%)
Surgical pressure range	
1 quadrant	18 (45.0%)
2 quadrant	22 (55.0%)

decreased significantly on the first day of surgery, increased at 2 weeks postoperatively, and then gradually became smaller and closer to that of the healthy eye, with less fluctuation of the RNFL in the healthy eye group (Figure 2).

3.2.3 Global RNFL and SSI over time around the optic disc in the operated eye group

The global RNFL around the optic disc in the operated eye group decreased significantly at 1 day postoperatively and increased slightly at 2 weeks postoperatively, and the trend of SSI changes in the operated eye group was the same as that of RNFL before 2 weeks postoperatively, and the SSI increased significantly at 2 weeks postoperatively, and was more fluctuating and less fluctuating at 2 weeks, and the trend of RNFL changes was different (Figure 3).

3.2.4 Comparison of peripapillary VD between the operated eye and the healthy eye group at different preoperative and postoperative time points of the SB

Comparison of peripapillary VD between the operated and fellow eyes at 6-month follow-up showed that: preoperatively, the operated group had nasal superior (47.00 [43.00–48.00] vs. 49.00 [47.00–51.00]; $p = 0.001$), nasal superior (48.00 [43.00–52.00] vs. 52.00 [49.00–55.00]; $p < 0.001$), temporal superior (50.00 [44.00–55.00] vs. 56.00 [52.00–59.00]; $p < 0.001$), temporal superior (53.00 [47.00–57.00] vs. 56.00 [53.00–58.00], $p = 0.016$), inferior tempo (49.00 [44.00–52.00] vs. 53.00 [48.00–56.00]; $p = 0.001$), inferior tempo (55.00 [47.00–58.00] vs. 58.00 [53.00–60.00]; $p = 0.004$), inferior nasal (49.00 [45.00–53.00] vs. 53.00 [51.00–55.00]; $p < 0.001$), inferior nasal (46.00 [42.00–49.00] vs. 48.00 [45.00–50.00]; $p = 0.027$) and global (48.88 [38.88–45.88] vs. 53.00 [50.88–54.88]; $p < 0.001$) had smaller VD preoperatively than the healthy eye group; starting 1 month postoperatively, both nasal superior (48.00 [45.00–50.00] vs. 49.00 [47.00–50.00]; $p = 0.063$), tempo superior (55.00 [53.00–58.00] vs. 57.00 [54.00–59.00]; $p = 0.516$), tempo inferior (51.00 [48.00–54.00] vs. 53.00 [49.00–56.00]; $p = 0.126$) did not show significant differences; from 3 months postoperatively, the two groups nasal superior (50.00 [46.00–51.00] vs. 49.00 [46.00–51.00]; $p = 0.907$), superior nasal (51.00 [47.00–54.00] vs. 51.00 [48.00–57.00]; $p = 0.504$), tempo superior (57.00 [55.00–59.00] vs. 56.00 [54.00–59.00]; $p = 0.346$), tempo inferior (53.00 [49.00–56.00] vs. 54.00 [50.00–55.00]; $p = 0.504$), nasal inferior (48.00 [44.00–51.00] vs. 47.00 [44.00–50.00]; $p = 0.434$) were not significantly different; at 6 months only the superior temporal side (54.00 [51.00–56.00]

TABLE 2 Comparison of preoperative and postoperative SSI at different time points between the operated eye group and the healthy eye group.

SSI	Operated eye group	Healthy eye group	t	p
Preoperative	8.070 ± 0.74	8.279 ± 1.14	−1.177	0.246
1 day postoperatively	6.767 ± 1.04	8.372 ± 0.90	−8.376	<0.001
2 weeks postoperatively	8.186 ± 0.82	8.581 ± 0.73	−2.369	0.022
1 month postoperatively	8.209 ± 0.86	8.348 ± 0.97	−0.798	0.429
3 month postoperatively	8.233 ± 1.02	8.302 ± 1.04	−0.387	0.701
6 month postoperatively	8.186 ± 1.01	8.209 ± 1.04	−0.121	0.904

TABLE 3 Comparison of peripapillary RNFL between the operated eye and the healthy eye at different preoperative and postoperative time points of the SB (μm).

	Preoperative		Z	p	1 day postoperatively		Z	p
	Operated eye group	Healthy eye group			Operated eye group	Healthy eye group		
NS	111.00 [96.00–134.00]	105.00 [94.00–116.00]	−2.47	0.014	113.00 [101.00–129.00]	104.00 [93.00–114.00]	−2.808	0.005
SN	156.00 [120.00–191.00]	138.00 [114.00–155.00]	−2.609	0.009	142.00 [133.00–171.00]	130.00 [110.00–150.00]	−3.089	0.002
ST	149.00 [126.00–200.00]	133.00 [122.00–149.00]	−3.008	0.003	132.00 [114.00–151.00]	135.00 [120.00–148.00]	−0.755	0.450
TS	99.00 [81.00–211.00]	86.00 [78.00–95.00]	−4.058	<0.001	88.00 [77.00–95.00]	89.00 [79.00–98.00]	−2.368	0.018
TI	85.00 [74.00–135.00]	76.00 [64.00–86.00]	−4.246	<0.001	86.00 [79.00–103.00]	78.00 [66.00–85.00]	−4.342	<0.001
IT	165.00 [131.00–188.00]	152.00 [135.00–165.00]	−1.999	0.046	162.00 [141.00–184.00]	155.00 [135.00–165.00]	−2.096	0.036
IN	156.00 [137.00–182.00]	143.00 [129.00–155.00]	−3.007	0.003	148.00 [126.00–163.00]	145.00 [126.00–155.00]	−0.163	0.870
NI	104.00 [89.00–128.00]	86.00 [76.00–99.00]	−4.052	<0.001	90.00 [80.00–102.00]	84.00 [75.00–95.00]	−2.048	0.041
Global	138.25 [125.25–151.63]	115.75 [108.38–124.25]	−5.687	<0.001	121.50 [112.50–136.25]	114.50 [108.00–123.00]	−3.792	<0.001

	2 weeks postoperatively		Z	p	1 month postoperatively		Z	p
	Operated eye group	Healthy eye group			Operated eye group	Healthy eye group		
NS	113.00 [103.00–124.00]	106.00 [97.00–117.00]	−3.246	0.001	113.00 [102.00–123.00]	106.00 [98.00–116.00]	−2.639	0.008
SN	113.00 [103.00–124.00]	106.00 [97.00–117.00]	−3.246	0.001	149.00 [130.00–164.00]	136.00 [114.00–155.00]	−2.178	0.029
ST	146.00 [123.00–161.00]	135.00 [124.00–149.00]	−1.951	0.051	143.00 [122.00–155.00]	134.00 [123.00–146.00]	−1.903	0.057
TS	93.00 [80.00–100.00]	85.00 [77.00–95.00]	−2.651	0.008	92.00 [80.00–100.00]	86.00 [77.00–95.00]	−2.815	0.005
TI	85.00 [81.00–100.00]	76.00 [65.00–83.00]	−4.789	<0.001	87.00 [78.00–100.00]	75.00 [65.00–85.00]	−4.428	<0.001
IT	173.00 [142.00–185.00]	155.00 [136.00–165.00]	−3.225	0.001	160.00 [138.00–180.00]	155.00 [135.00–165.00]	−2.279	0.023
IN	155.00 [131.00–168.00]	126.00 [126.00–156.00]	−1.999	0.046	148.00 [129.00–161.00]	143.00 [127.00–154.00]	−0.689	0.491
NI	90.00 [83.00–111.00]	85.00 [77.00–98.00]	−2.627	0.009	94.00 [82.00–109.00]	88.00 [78.00–100.00]	−2.537	0.011
Global	126.75 [115.13–133.13]	115.75 [108.88–122.88]	−4.927	<0.001	124.38 [113.63–130.38]	116.63 [108.25–123.75]	−4.352	<0.001

	3 month postoperatively		Z	p	6 month postoperatively		Z	p
	Operated eye group	Healthy eye group			Operated eye group	Healthy eye group		
NS	110.00 [102.00–119.00]	105.00 [98.00–113.00]	−2.038	0.042	108.00 [100.00–119.00]	106.00 [98.00–114.00]	−1.459	0.145
SN	145.00 [128.00–162.00]	136.00 [115.00–155.00]	−1.821	0.069	135.00 [116.00–160.00]	138.00 [115.00–154.00]	−0.984	0.325
ST	141.00 [119.00–155.00]	135.00 [120.00–148.00]	−1.563	0.118	143.00 [122.00–155.00]	134.00 [123.00–146.00]	−1.903	0.057
TS	93.00 [81.00–101.00]	85.00 [76.00–93.00]	−3.128	0.002	92.00-[80.00–100.00]	86.00 [77.00–95.00]	−2.815	0.005
TI	88.00 [79.00–100.00]	79.00 [66.00–85.00]	−4.772	<0.001	88.00 [75.00–99.00]	79.00 [68.00–86.00]	−4.321	<0.001
IT	165.00 [139.00–179.00]	156.00 [134.00–167.00]	−1.787	0.074	160.00 [134.00–175.00]	156.00 [132.00–168.00]	0.196	0.196
IN	143.00 [129.00–157.00]	142.00 [129.00–154.00]	−0.37	0.711	147.00 [129.00–157.00]	143.00 [130.00–156.00]	−0.25	0.803
NI	90.00 [82.00–107.00]	86.00 [78.00–102.00]	−1.938	0.053	89.00 [80.00–103.00]	86.00 [78.00–102.00]	−1.314	0.189
Global	120.63 [114.13–130.50]	116.00 [110.50–124.50]	−4.009	<0.001	124.29 [113.00–129.71]	116.63 [109.75–124.25]	−4.021	<0.001

vs. 55.00 [51.00–58.00]; $p = 0.013$) remained smaller in the operated eye group than in the healthy eye group (Table 4).

3.2.5 Changes in peripapillary global VD of the optic disc over time in the operated and healthy eye groups

Preoperatively, the total VD around the optic disc in the operated eye group was significantly smaller than that in the healthy eye group, and postoperatively, the VD gradually increased

closer to that in the healthy eye group, which had less fluctuation in VD (Figure 4).

3.2.6 Global VD and SSI over time around the optic disc in the operated eye group

The SSI in the operated eye group decreased significantly at 1 day postoperatively and increased significantly at 2 weeks postoperatively, and the overall VD around the optic disc increased. The trends of the two changes were different (Figure 5).
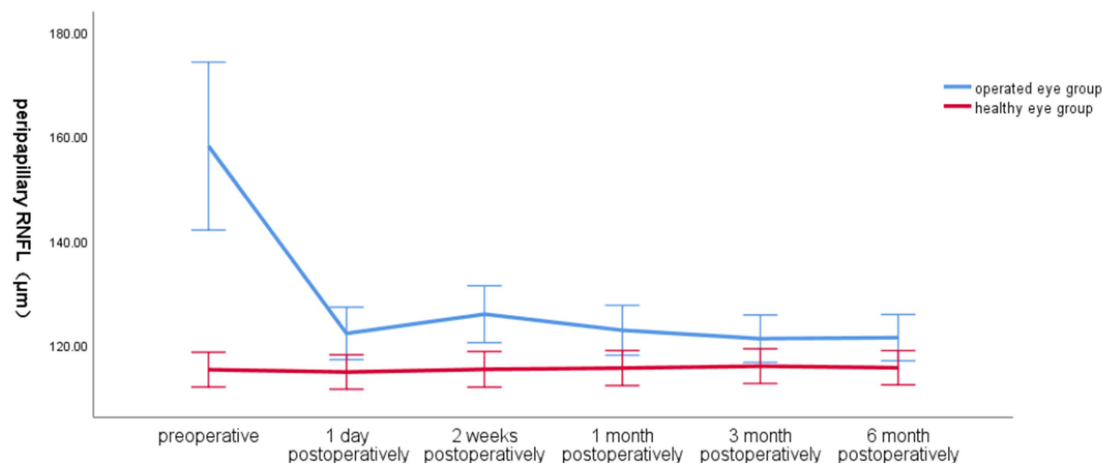
FIGURE 2
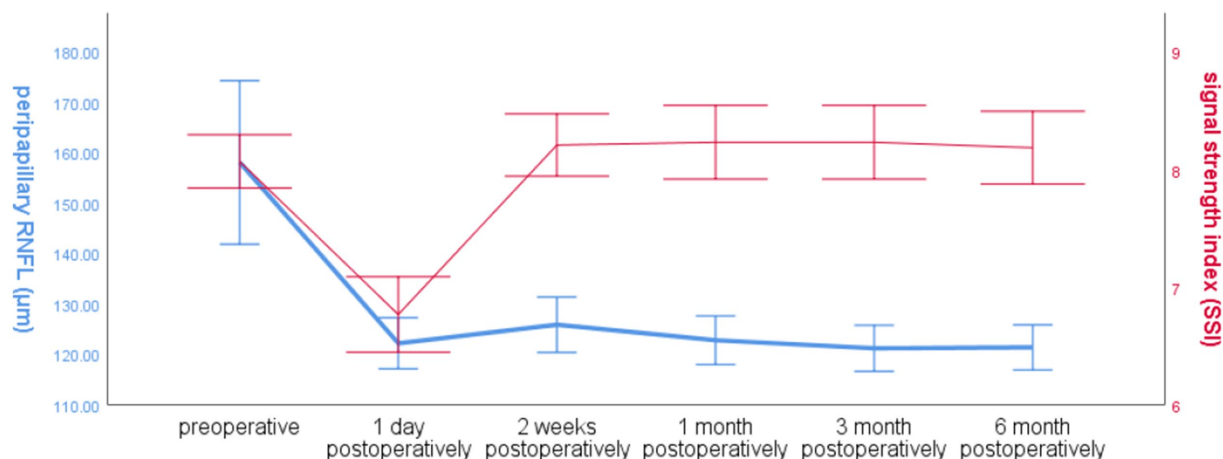Line graph of global RNFL around the optic disc over time in the operated and healthy eye groups.

FIGURE 3
Line graph of global RNFL mean and SSI over time around the optic disc in the operated eye group.

4 Discussion

In the early stages of RRD, patients have floating objects, flashing sensations or curtain-like occlusions in front of the eyes that gradually expand and severely affect vision, or even have only light sensation or no light sensation, and early diagnosis and treatment are crucial to save vision (14). SB and vitrectomy are currently accepted as the main treatment for RRD (3). Among them, vitrectomy for RRD requires the injection of fillers into the vitreous cavity, and silicone oil is one of the main fillers used for vitrectomy, which has been shown to have toxic effects on the retina (5, 15), resulting in significantly lower peripapillary VD than that of normal eyes (9), and a gradual decrease in RNFL thickness after surgery, especially in the retinal area over the optic disc. After silicone oil removal, peripapillary VD increased slightly but was still smaller than that of the contralateral normal eyes, while RNFL recovery was not evident (16–18). RNFL thickness and VD are closely related to visual acuity (19, 20). RNFL thickness is mainly

determined by the number of ganglion cell axons and is an important index to quantitatively respond to changes in optic nerve cell function and visual conduction (7); VD indicates the supply of nutrients to the retina (9). Insufficient blood supply affects retinal cell function (21). This is why it is important to monitor the RNFL and the VD.

As mentioned above, there are many studies on the changes in RNFL and VD after silicone oil-filled vitrectomy for RRD, and most of the findings suggest that there is a negative effect on RNFL and VD after surgery, SB has a lower incidence of postoperative cataract and glaucoma than silicone oil-filled vitrectomy (22, 23), does not require vitrectomy, causes less damage, has a lower cost of surgery, and does not require prone position after surgery (24, 25). However, there is less research information on the effects of SB on peripapillary RNFL and VD production, so we objectively analysed the effects of SB on the retina by observing the changes in peripapillary RNFL thickness and VD in the preoperative and postoperative periods of RRD using OCTA. As there is still no objective criterion for the selection of

TABLE 4 Comparison of peripapillary VD between the operated eye and the healthy eye group at different preoperative and postoperative time points of the SB (%).

	Preoperative		Z	p	1 day postoperatively		Z	p
	Operated eye group	Healthy eye group			Operated eye group	Healthy eye group		
NS	47.00 [43.00–48.00]	49.00 [47.00–51.00]	−3.384	0.001	45.00 [40.00–49.00]	50.00 [47.00–52.00]	−4.051	<0.001
SN	48.00 [43.00–52.00]	52.00 [49.00–55.00]	−4.314	<0.001	48.00 [42.00–51.00]	52.00 [49.00–56.00]	−3.659	<0.001
ST	50.00 [44.00–55.00]	56.00 [52.00–59.00]	−4.23	<0.001	52.00 [47.00–54.00]	54.00 [51.00–59.00]	−3.429	0.001
TS	53.00 [47.00–57.00]	56.00 [53.00–58.00]	−2.408	0.016	52.00 [48.00–57.00]	57.00 [54.00–59.00]	−3.648	<0.001
TI	49.00 [44.00–52.00]	53.00 [48.00–56.00]	−3.289	0.001	50.00 [46.00–55.00]	52.00 [48.00–55.00]	−2.344	0.019
IT	55.00 [47.00–58.00]	58.00 [53.00–60.00]	−2.853	0.004	54.00 [48.00–57.00]	56.00 [55.00–60.00]	−4.64	<0.001
IN	49.00 [45.00–53.00]	53.00 [51.00–55.00]	−4.345	<0.001	48.00 [43.00–52.00]	52.00 [50.00–54.00]	−4.08	<0.001
NI	46.00 [42.00–49.00]	48.00 [45.00–50.00]	−2.214	0.027	42.00 [36.00–47.00]	48.00 [45.00–49.00]	−4.508	<0.001
Global	48.88 [38.88–45.88]	53.00 [50.88–54.88]	−5.712	<0.001	49.00 [46.00–50.38]	53.00 [50.75–54.75]	−5.12	<0.01

	2 weeks postoperatively		Z	p	1 month postoperatively		Z	p
	Operated eye group	Healthy eye group			Operated eye group	Healthy eye group		
NS	46.00 [43.00–49.00]	49.00 [46.00–51.00]	−3.648	<0.001	48.00 [45.00–50.00]	49.00 [47.00–50.00]	−1.856	0.063
SN	48.00 [45.00–53.00]	50.00 [47.00–55.00]	−2,712	0.007	49.00 [45.00–53.00]	51.00 [48.00–55.00]	−2.464	0.014
ST	52.00 [50.00–56.00]	55.00 [51.00–58.00]	−2.625	0.012	52.00 [50.00–56.00]	55.00 [51.00–58.00]	−2.292	0.022
TS	54.00 [52.00–57.00]	56.00 [54.00–59.00]	−3.01	0.003	55.00 [53.00–58.00]	57.00 [54.00–59.00]	−0.649	0.516
TI	50.00 [46.00–55.00]	52.00 [49.00–56.00]	−2.064	0.039	51.00 [48.00–54.00]	53.00 [49.00–56.00]	−1.529	0.126
IT	56.00 [50.00–59.00]	57.00 [54.00–60.00]	−2.439	0.015	55.00 [52.00–59.00]	56.00 [54.00–60.00]	−2.714	0.007
IN	48.00 [45.00–53.00]	53.00 [51.00–54.00]	−3.965	<0.001	50.00 [47.00–54.00]	52.00 [51.00–54.00]	−2.526	0.012
NI	44.00 [40.00–47.00]	46.00 [44.00–49.00]	−3.312	0.001	47.00 [42.00–48.00]	47.00 [44.00–49.00]	−2.319	0.020
Global	50.38 [48.13–51.75]	52.38 [51.13–54.38]	−4.704	<0.001	51.25 [48.00–52.88]	52.38 [51.00–53.88]	−3.163	0.002

	3 month postoperatively		Z	p	6 month postoperatively		Z	p
	Operated eye group	Healthy eye group			Operated eye group	Healthy eye group		
NS	50.00 [46.00–51.00]	49.00 [46.00–51.00]	−0.117	0.907	50.00 [47.00–52.00]	50.00 [46.00–51.00]	−1.337	0.181
SN	51.00 [47.00–54.00]	51.00 [48.00–57.00]	−0.668	0.504	51.00 [48.00–55.00]	51.00 [48.00–56.00]	−0.816	0.389
ST	53.00 [50.00–55.00]	55.00 [52.00–58.00]	−3.093	0.002	54.00 [51.00–56.00]	55.00 [51.00–58.00]	−2.491	0.013
TS	57.00 [55.00–59.00]	56.00 [54.00–59.00]	−0.942	0.346	56.00 [54.00–59.00]	56.00 [54.00–58.00]	−0.666	0.506
TI	53.00 [49.00–56.00]	54.00 [50.00–55.00]	−0.669	0.504	53.00 [48.00–56.00]	53.00 [49.00–56.00]	−1.5	0.134
IT	55.00 [53.00–58.00]	58.00 [55.00–60.00]	−2.428	0.015	57.00 [53.00–60.00]	58.00 [53.00–59.00]	−1.27	0.204
IN	50.00 [48.00–54.00]	52.00 [51.00–54.00]	−2.567	0.010	52.00 [49.00–55.00]	53.00 [51.00–55.00]	−1.351	0.177
NI	48.00 [44.00–51.00]	47.00 [44.00–50.00]	−0.783	0.434	48.00 [45.00–51.00]	46.00 [43.00–49.00]	−1.663	0.096
Global	52.38 [48.75–53.63]	53.25 [51.00–54.38]	−1.997	0.046	52.75 [49.88–54.38]	52.50 [51.00–54.25]	−0.075	0.940

surgical modalities for the treatment of RRD (26–28), it is also hoped that this study can provide an objective reference for better selection of surgical modalities.

Given the heterogeneity of RNFL thickness and VD distribution in different areas of the optic disc, pre-and post-operative changes may vary, in this study we divided the patients' peripapillary retina into eight areas by OCTA and recorded and analysed the peripapillary RNFL and VD in detail at preoperative and different postoperative time points.

Considering that the scan quality affects the scan data and that the distribution of RNFL thickness and VD in different regions of the optic disc is inhomogeneous and may vary preoperatively and postoperatively, we recorded and analysed in detail the scanning SSI, the peripapillary global and the RNFL and VD of the peripapillary global division of the optic disc into eight regions by the OCTA instrument in each OCTA.

Ozdek et al. (29) used a scanning laser polarimeter to assess the changes in RNFL thickness around the optic disc after successful
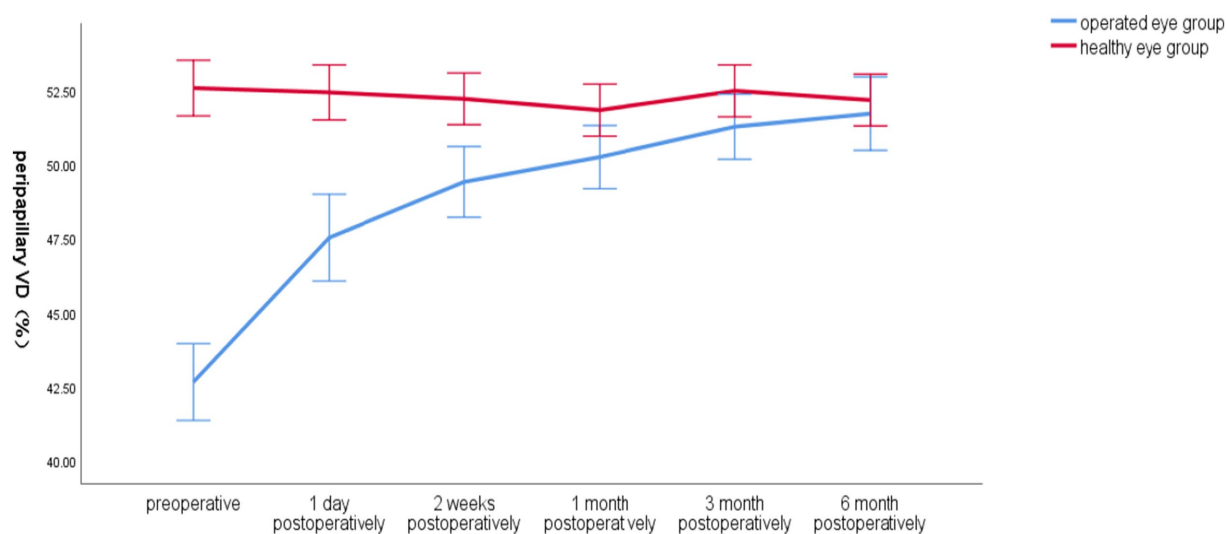
FIGURE 4
Line graph of mean global VD around the optic disc over time in the operated and healthy eye groups.
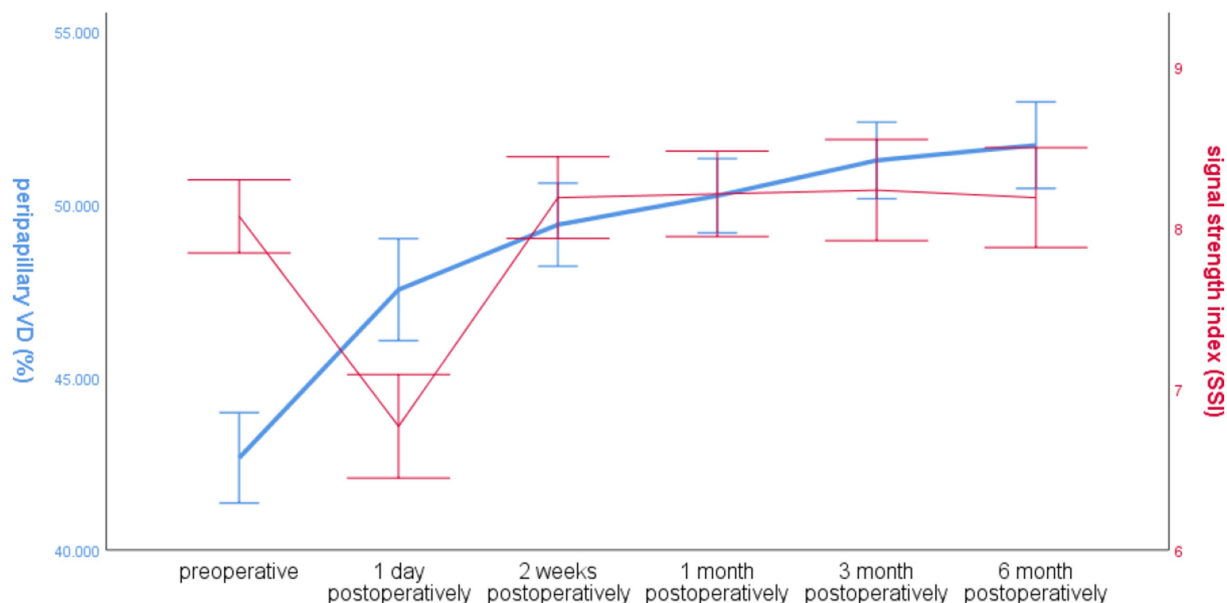

FIGURE 5
Line graph of global RNFL mean and SSI over time around the optic disc in the operated eye group.

SB. They did not perform a statistical study of preoperative RNFL and scan quality. We found that there was no significant difference between the statistical results of SSI between the two groups, and the RNFL of the operated eye group was larger than that of the healthy eye group, suggesting that retinal detachment makes the periphery of the disc RNFL to increase. It has been suggested that the thickening of the RNFL in patients with RRD may be related to oedema or Müller cell hypertrophy and proliferation (7, 30). There was a significant decrease in SSI in the operated eye group within 2 weeks postoperatively, which could be due to a decrease in tear film quality or an increase in the postoperative inflammatory response, and as we could not exclude the

effect of SSI on the RNFL scan at 2 weeks postoperatively, we could not differentiate whether the difference in peripapillary RNFL and VD between the two disc groups at 2 weeks postoperatively was due to the quality of the scans or due to the surgery, which could not be accurately assessed at this time. There was no significant difference in SSI between the two groups at 1 month postoperatively, and the areas that progressed further into the operated eye group over time were not significantly different from the healthy eye group. At 6 months post-operatively, there were no significant differences between the operated eye groups, except for two regions, tempo superior and tempo inferior, which remained different in the operated eye group compared to the

healthy eye group. Which may indicate that most of the regions around the optic disc of the operated eye gradually approached and converged to the healthy eye after SB. Therefore, we believe that SB can improve the thickness of the RNFL, which is conducive to the recovery of visual function, and the recovery of the tempo superior and tempo inferior regions is slower, and it will take more than 6 months to fully recover to the level of the healthy eye.

It has been shown that RRD have higher retinal blood flow and better postoperative visual acuity (31). To investigate the effect of SB on retinal blood flow, an early study by Yoshida et al. (32) found that SB leads to a decrease in ocular blood flow perfusion, probably due to an increase in vascular resistance caused by pressurised objects, However, they mainly studied choroidal blood flow and only compared the postoperative period with the contralateral healthy eye, and did not monitor preoperative blood flow for comparison, which cannot exclude the effect of RRD itself on blood flow. Fineman et al. (33)reported a case of transient vision loss in a patient with scleral ring ligation and concluded that there is a significant reduction in ocular perfusion after ring ligation, leading to vision loss, but that this phenomenon is reversible. As SB surgery continues to evolve, clinicians tend to select segmental external compression and incise only the compressed quadrant of the conjunctiva to minimise damage, and the incidence of postoperative transient vision loss is relatively low.

There are a large number of findings on the changes in macular VD before and after SB in RRD: Bartolomé-Sesé et al. (34) investigated the changes in macular VD after vitrectomy combined with or without SB and SF6 as tamponade for the treatment of RRD, and the results of the study showed no significant changes in macular VD. Fallico et al. (35) investigated the changes in macular VD after SB in patients with RRD and showed that RRD causes a decrease in macular VD, but a trend towards an increase in VD was found at the 6-month postoperative follow-up. Barca et al. (36) found that regardless of whether RRD involved the macular region or not, the preoperative VD in the macular region of the operated eyes was lower than that of the healthy eyes, and after treatment with SB, there was a gradual recovery of the postoperative VD in the macular region. There was no significant difference from the healthy eyes at 6 months.

Results of studies on peripapillary VD are still scarce. Zabel et al. (6) analysed the retinal condition of 20 patients with retinal detachment. They performed fundus OCTA 6–14 months postoperatively and found that the VD of the operated eye was smaller than that of the contralateral healthy eye, but they did not perform preoperative OCTA on the patients and were unable to distinguish whether the reduction in blood flow was due to RRD disease effects or to surgery. In contrast, Nagahara et al. (37) observed fundus blood flow in 12 patients with RRD at 1 week, 1 month and 3 months after surgery and concluded that SB had a negative effect on retinal blood flow only in the pressure area and had no effect on retinal blood flow in other pressure areas, including the fundus of the optic disc. We found that the trend of peripapillary VD was similar to the changes in macular VD studied by Barca et al. Comparative analysis of peripapillary VD in the operated eyes group and the healthy eyes group showed that preoperative VD in all areas of the peripapillary disc was small compared to that of the healthy eyes. Still, postoperative VD in the operated eyes gradually recovered and there was no significant difference from that of the healthy eyes at 6 months, except for the superior temporal. However, the global value of the two groups are not significantly different. This suggests that, similar to the RNFL described

above, we thought that SSI might adversely affect the scanning results of VD, but there was no significant difference in SSI between the two groups preoperatively, while the blood flow density in the operated eye group was significantly smaller than that in the healthy eye group, suggesting that RRD also adversely affects VD, and SSI was one of the factors for the lower blood flow in the operated eye group compared to that in the healthy eye group at 1 day and 2 weeks after surgery, with no significant difference between the operated and healthy eye groups in SSI at 1 month after surgery, and VD was higher than that in the healthy eye group. At 1 month after surgery, the SSI of the operated eye group was not significantly different from that of the healthy eye group. The VD had a tendency to gradually increase compared to that of the preoperative eye and gradually recovered to near that of the healthy eye, while the changes in each region were different, which needed to be studied separately, and it would take more than 6 months for their regions to fully recover to the level of the healthy eye.

Our study has the following limitations: Refractive error affects measurement results, and although we included patients with refractive error less than 3.00D, we did not include data on specific refractive error and axial length in the analysis, which may have introduced some error into the results, and because of the decrease in scan quality within 2 weeks postoperatively due to surgery, we did not exclude errors in the results due to SSI at this time, so the accuracy of deriving postoperative RNFL and VD values within 2 weeks is not high. All the patients we included had intraocular pressure within the normal range during the follow-up period, so we neglected the effect of intraocular pressure on RNFL and VD. All patients included in the analysis had no lesions in the contralateral eyes during the follow-up period, so we used a comparison of the healthy eyes contralateral to the operated eyes to study the effect of SB on RNFL and VD and did not include the normal population for comparison. Because the sample size was not large enough, we did not perform a more detailed subgroup analysis of whether different locations of the cingulate would have different effects on RNFL and VD in different areas of the peripapillary disc, but we divided the peripapillary disc region into 8 areas for separate analyses and there was a tendency for each area to be progressively closer to the healthy eyes, which may show that RNFL and VD recovered progressively after SB surgery. We will continue to increase the sample size, extend the follow-up time, and perform more detailed grouping for further investigation in the future.

In conclusion, SB does not negatively affect the peripapillary RNFL and VD after treatment of RRD, and both RNFL and VD progressively approach those of the healthy eyes after surgery. And it takes more than 6 months to fully recover to the level of healthy eyes.

Data availability statement

The original contributions presented in the study are included in the article/supplementary material, further inquiries can be directed to the corresponding author.

Ethics statement

The studies involving humans were approved by the First Affiliated Hospital of Gannan Medical University. The studies were conducted in accordance with the local legislation and institutional requirements.

The participants provided their written informed consent to participate in this study.

Author contributions

CZ: Writing – original draft, Writing – review & editing. LL: Writing – review & editing, Writing – original draft. YJ: Writing – review & editing, Writing – original draft.

Funding

Conflict of interest

Publisher's note

References

1. Moledina M, Charteris DG, Chandra A. The genetic architecture of non-syndromic Rhegmatogenous retinal detachment. *Genes (Basel)*. (2022) 13:1675. doi: 10.3390/genes13091675

2. Feltgen N, Walter P. Rhegmatogenous retinal detachment--an ophthalmologic emergency. *Dtsch Arztebl Int*. (2014) 111:12–21. doi: 10.3238/arztebl.2014.0012

3. Znaor L, Medic A, Binder S, Vucinovic A, Marin Lovric J, Puljak L. Pars plana vitrectomy versus scleral buckling for repairing simple rhegmatogenous retinal detachments. *Cochrane Database Syst Rev*. (2019) 2019:Cd009562. doi: 10.1002/14651858.CD009562.pub2

4. Mason RH, Minaker SA, Marafon SB, Figueiredo N, Hillier RJ, Muni RH. Retinal displacement following rhegmatogenous retinal detachment: a systematic review and meta-analysis. *Surv Ophthalmol*. (2022) 67:950–64. doi: 10.1016/j.survophthal.2022.01.002

5. Pichi F, Hay S, Abboud EB. Inner retinal toxicity due to silicone oil: a case series and review of the literature. *Int Ophthalmol*. (2020) 40:2413–22. doi: 10.1007/s10792-020-01418-0

6. Zabel P, Zabel K, Kazmierczak K, Stankiewicz M, Jaworski D, Suwala K, et al. Vascular density and macular sensitivity in eyes after scleral buckling surgery for macula-on rhegmatogenous retinal detachment. *PLoS One*. (2023) 18:e0279683. doi: 10.1371/journal.pone.0279683

7. Sodhi PK, Yadav A, Shaw E, Kumar S, Sharma N, Sharma S. Predictors of retinal nerve Fiber layer parameters following scleral buckling surgery in primary Rhegmatogenous retinal detachment. *Cureus*. (2022) 14:e21754. doi: 10.7759/cureus.21754

8. Ocansey S, Abu EK, Owusu-Ansah A, Mensah S, Oduro-Boateng J, Kojo RA, et al. Normative values of retinal nerve fibre layer thickness and optic nerve head parameters and their association with visual function in an African population. *J Ophthalmol*. (2020) 2020:7150673. doi: 10.1155/2020/7150673

9. Lu B, Zhang P, Liu H, Jia H, Yu Y, Wang F, et al. Peripapillary vessel density in eyes with Rhegmatogenous retinal detachment after pars Plana vitrectomy. *J Ophthalmol*. (2021) 2021:1–7. doi: 10.1155/2021/6621820

10. Fang DQ, Yang DW, Mai XT, Cheung CY, Chen HY. Repeatability, interocular correlation and agreement of optic nerve head vessel density in healthy eyes: a swept-source optical coherence tomographic angiography study. *Int J Ophthalmol*. (2024) 17:896–903. doi: 10.18240/ijo.2024.05.14

11. Spaide RF, Fujimoto JG, Waheed NK, Sadda SR, Staurenghi G. Optical coherence tomography angiography. *Prog Retin Eye Res*. (2018) 64:1–55. doi: 10.1016/j.preteyeres.2017.11.003

12. Vu AF, Alber SA, Chang MY, Park SS. Prospective cross-sectional study of repeatability of Peripapillary capillary density measurement using optical coherence tomography angiography in eyes with optic nerve and retinal vascular pathology. *J Neuroophthalmol*. (2022) 42:73–8. doi: 10.1097/WNO.0000000000001216

13. The Retina Society Terminology Committee. The classification of retinal detachment with proliferative vitreoretinopathy. *Ophthalmology*. (1983) 90:121–5. doi: 10.1016/S0161-6420(83)34588-7

14. Kunikata H, Abe T, Nakazawa T. Historical, current and future approaches to surgery for Rhegmatogenous retinal detachment. *Tohoku J Exp Med*. (2019) 248:159–68. doi: 10.1620/tjem.248.159

15. Raczyńska D, Mitrosz K, Raczyńska K, Glasner L. The influence of silicone oil on the ganglion cell complex after pars Plana vitrectomy for Rhegmatogenous retinal detachment. *Curr Pharm Des*. (2018) 24:3476–93. doi: 10.2174/1381612824666180813115438

16. Jiang J, Li R, Zhou JX, Li RM, Wang RH, Wang XP, et al. Peripapillary changes after vitrectomy and silicone oil tamponade for rhegmatogenous retinal detachment. *Indian J Ophthalmol*. (2021) 69:3579–83. doi: 10.4103/ijo.IJO_508_21

17. Wang E, Chen Y, Li N, Min H. Effect of silicone oil on peripapillary capillary density in patients with rhegmatogenous retinal detachment. *BMC Ophthalmol*. (2020) 20:268. doi: 10.1186/s12886-020-01533-7

18. Inan S, Polat O, Ozcan S, Inan UU. Comparison of long-term automated retinal layer segmentation analysis of the macula between silicone oil and gas tamponade after vitrectomy for Rhegmatogenous retinal detachment. *Ophthalmic Res*. (2020) 63:524–32. doi: 10.1159/000506382

19. Hwang YH, Byun ZY, Hwang DD. Changes in circumpapillary retinal nerve fiber layer thickness after vitrectomy for rhegmatogenous retinal detachment. *Sci Rep*. (2022) 12:9630. doi: 10.1038/s41598-022-13070-y

20. Çetinkaya Yaprak A, Küçük MF, Yaprak L, Erol MK. Change in retinal and choroidal microvascular structures after rhegmatogenous retinal detachment surgery and effects on visual recovery. *J Fr Ophtalmol*. (2021) 44:804–12. doi: 10.1016/j.jfo.2020.11.027

21. Wu YX, Yin S, Song SS, Liu X, Deng YX, Lu XJ. Retinal ischemia-reperfusion injury and pretreatment with *Lycium barbarum* glycopeptide. *Int J Ophthalmol*. (2024) 17:1599–605. doi: 10.18240/ijo.2024.09.04

22. Coman Cernat CC, Munteanu M, Malita D, Stanca S, Patoni Popescu SI, Musat O, et al. Corneal endothelial changes induced by pars plana vitrectomy with silicone oil tamponade for retinal detachment. *Exp Ther Med*. (2021) 22:961. doi: 10.3892/etm.2021.10393

23. Park SW, Lee JJ, Lee JE. Scleral buckling in the management of rhegmatogenous retinal detachment: patient selection and perspectives. *Clin Ophthalmol*. (2018) 12:1605–15. doi: 10.2147/OPTH.S153717

24. Fallico M, Alosi P, Reibaldi M, Longo A, Bonfiglio V, Avitabile T, et al. Scleral buckling: a review of clinical aspects and current concepts. *J Clin Med*. (2022) 11:314. doi: 10.3390/jcm11020314

25. Gao Y, Ruan T, Chen N, Yu B, Xing X, Du Q, et al. A comparison of face-down positioning and adjustable positioning after pars Plana vitrectomy for macular hole retinal detachment in high myopia. *Front Med (Lausanne)*. (2022) 9:780475. doi: 10.3389/fmed.2022.780475

26. Gutierrez M, Rodriguez JL, Zamora-de La Cruz D, Flores Pimentel MA, Jimenez-Corona A, Novak LC, et al. Pars plana vitrectomy combined with scleral buckle versus pars plana vitrectomy for giant retinal tear. *Cochrane Database Syst Rev*. (2019) 12:Cd012646. doi: 10.1002/14651858.CD012646.pub2

27. Hillier RJ, Felfeli T, Berger AR, Wong DT, Altomare F, Dai D, et al. The pneumatic Retinopexy versus vitrectomy for the Management of Primary Rhegmatogenous Retinal Detachment Outcomes Randomized Trial (PIVOT). *Ophthalmology*. (2019) 126:531–9. doi: 10.1016/j.ophtha.2018.11.014

28. Popovic MM, Muni RH, Nichani P, Kertes PJ. Pars plana vitrectomy, scleral buckle, and pneumatic retinopexy for the management of rhegmatogenous retinal detachment: a meta-analysis. *Surv Ophthalmol*. (2022) 67:184–96. doi: 10.1016/j.survophthal.2021.05.008

29. Ozdek S, Lonneville Y, Onol M, Gurelik G, Hasanreisoglu B. Assessment of retinal nerve fiber layer thickness with NFA-GDx following successful scleral buckling surgery. *Eur J Ophthalmol*. (2003) 13:697–701. doi: 10.1177/112067210301300806

30. Lee YH, Lee JE, Shin YI, Lee KM, Jo YJ, Kim JY. Longitudinal changes in retinal nerve fiber layer thickness after vitrectomy for rhegmatogenous retinal detachment. *Invest Ophthalmol Vis Sci*. (2012) 53:5471–4. doi: 10.1167/iovs.12-9782

31. Kaderli ST, Karalezli A, Sul S. Microvascular retinal alterations in rhegmatogenous retinal detachment after pneumatic retinopexy. *Acta Ophthalmol*. (2021) 99:383–9. doi: 10.1111/aos.14624

32. Yoshida A, Hirokawa H, Ishiko S, Ogasawara H. Ocular circulatory changes following scleral buckling procedures. *Br J Ophthalmol*. (1992) 76:529–31. doi: 10.1136/bjo.76.9.529

33. Fineman MS, Regillo CD, Sergott RC, Spaeth G, Vander J. Transient visual loss and decreased ocular blood flow velocities following a scleral buckling procedure. *Arch Ophthalmol*. (1999) 117:1647–8.

34. Bartolomé-Sesé I, Díaz-Barreda MD, Orduna-Hospital E, Boned-Murillo A, Ascaso FJ, Pinilla I. Long-term follow-up of macular perfusion evaluated by optical coherence tomography angiography after Rhegmatogenous

retinal detachment surgery. *J Clin Med*. (2022) 11:6725. doi: 10.3390/jcm 11226725

35. Fallico M, Longo A, Avitabile T, Alosi P, Grillo M, Castellino N, et al. Microvascular changes after scleral buckling for Rhegmatogenous retinal detachment: an optical coherence tomography angiography study. *Diagnostics (Basel)*. (2022) 12:3015. doi: 10.3390/diagnostics12123015

36. Barca F, Bacherini D, Dragotto F, Tartaro R, Lenzetti C, Finocchio L, et al. OCT angiography findings in macula-ON and macula-OFF Rhegmatogenous retinal detachment: a prospective study. *J Clin Med*. (2020) 9:9(12). doi: 10.3390/jcm9123982

37. Nagahara M, Tamaki Y, Araie M, Eguchi S. Effects of scleral buckling and encircling procedures on human optic nerve head and retinochoroidal circulation. *Br J Ophthalmol*. (2000) 84:31–6. doi: 10.1136/bjo.84.1.31

Frontiers in Medicine

Translating medical research and innovation into improved patient care

A multidisciplinary journal which advances our medical knowledge. It supports the translation of scientific advances into new therapies and diagnostic tools that will improve patient care.

Discover the latest Research Topics

See more →

Frontiers

Avenue du Tribunal-Fédéral 34
1005 Lausanne, Switzerland
frontiersin.org

Contact us

+41 (0)21 510 17 00
frontiersin.org/about/contact

frontiers | Research Topics